Film Cooling of Turbine Blade Trailing Edges

Janendra Telisinghe
St Catherine's College
University of Oxford

Submitted in partial fulfilment of the requirements for the degree of
Doctor of Philosophy

Michaelmas 2013

Film Cooling of Turbine Blade Trailing Edges

Janendra Telisinghe

St. Catherine's College

Michaelmas 2013.

In modern gas turbine engines, film cooling is extensively used to cool the components exposed to the hot mainstream gas path. In implementing film cooling on modern gas turbine engines, the trailing edge film poses a particularly challenging design problem. From an aerodynamic point of view, the trailing edge of a blade is designed to be as thin as possible. However, this conflicts with the implementation of the cooling design. The most common method of film cooling the trailing edge is via late pressure surface discrete film cooling holes. Another method of cooling the trailing edge is by using discrete pressure surface slots. This thesis documents a comparative aerodynamic and heat transfer study of three trailing edge cooling configurations. The study was carried out using a large scale, low speed wind tunnel situated at the Southwell Laboratory. The three trailing edge cooling configurations considered were as follows. First is the common late pressure film cooling of the trailing edge via discrete film cooling holes. This configuration is designated as datum configuration. Second is the pressure surface slot coolant ejection. This configuration was designated as cast cutback configuration. The third is the pressure surface ejection via discrete film cooling holes within a step cutback. This configuration was designated the machined cutback configuration. The above configurations were incorporated into three flat plates manufactured using stereolithography. In the aerodynamic study, the static pressure distribution and discharge coefficient for the three configurations were compared. Furthermore, two dimensional total pressure measurements were carried out using a traverse mechanism downstream of the test plates. The total pressure measurements were used to compute the mixed out losses for the three configurations. It was found that the datum and machined cutback configurations have similar discharge coefficients and mixed out losses whilst the cast cutback configuration produces greater mixed out loss. The film effectiveness and heat transfer coefficient on the pressure surface downstream of the coolant ejection was obtained using a steady state heat transfer technique. The effectiveness measurements were compared with those from the literature and correlated against the two dimensional slot model. The heat transfer measurements show that the cast cutback configuration has the potential to give higher effectiveness at the trailing edge.

Acknowledgements

I would first like to thank professor Peter Ireland for giving me the opportunity to carry out this research at the Southwell Laboratory. Furthermore, I'm indebted to him for his dedication, motivation and friendship. I would also like to thank Professor Terry Jones for his time and valuable insight into blade cooling. The discussions with Professor Jones were inspiring and motivational. I would also like to thank Dr. David Gillespie for being a rock and support during the "trying times" at Southwell Laboratory, and Nigel Brett for tremendous technical and instrumentation skills in helping me set up the test facilities.

Also I would like to extend my thanks and gratitude, in no particular order, to Noel, Kenny (PokWan), Brian, Salva, Paul, Bill, Paul Cox, Rex, Laura and all others in Oxford.

My warmest thanks, gratitude and love to my wife Suzanne and my parents, for their understanding and patience. Finally, I would like to thank Rolls-Royce for funding and supporting this research.

Contents

List of Figures

List of Tables

Nomenclature

Greek

α	Slot inclination angle. eq. 2.9
β	Fitting parameter in slot model. eq. 2.9
β	Hole / slot compound angle
η	Film effectiveness. eq. 2.4
η_{ad}	Effectiveness based on adiabatic wall temperature
η_{iso}	Effectiveness based on isothermal wall temperature
γ	Ratio of specific heats
μ_c	Dynamic viscosity of coolant flow
μ_∞	Dynamic viscosity of mainstream flow
ϕ	Metal effectiveness. eq. 2.5
ρ	Density
ρ_c	Coolant flow density
ρ_∞	Mainstream density
ρ_p	Density of the flow at the mixed out plane
τ_{xx}	Shear stress in the x-direction
τ_{yx}, τ_{xy}	Shear stress in the xy-direction
τ_{yy}	Shear stress in the y-direction
τ_{yz}, τ_{zy}	Shear stress in the yz-direction
τ_{zx}, τ_{xz}	Shear stress in the xz-direction
τ_{zz}	Shear stress in the z-direction
θ	non dimensional temperature
ξ	Mixed out loss. eq. 5.21
ξ	Non dimensional distance downstream of coolant ejection. eq.2.8
ζ	Unheated starting length

Roman

A_{hole}	Cross sectional area of the coolant holes
A	Coolant cross sectional area

$\overline{P}$	Time mean averaged pressure
$\overline{T}$	Mass flow averaged cooling temperature
$\overline{u}, \overline{v}, \overline{w}$	Time mean averaged velocity components
U_c	Coolant velocity
C_1	Slot effectiveness model fitting parameter. eq. 2.10
C_2	Slot effectiveness model fitting parameter. eq. 2.10
C_d	Discharge coefficient. eq. 5.2
C_p	Specific heat capacity
Cp_c	Specific heat capacity of coolant flow
Cp_∞	Specific heat capacity of mainstream flow
C_P	Pressure coefficient. eq. 5.1
C_{PT}	Total pressure coefficient. eq. 5.4
$\dot{q}_f$	Convective heat flux in the presence of cooling. eq. 2.2
DR	Coolant to mainstream density ratio, $\frac{\rho_c}{\rho_\infty}$
f_i	CFD prediction. eq. 3.14
u', v', w'	Fluctuating part of the velocity component
f_x, f_y, f_z	Gravitational force in the x,y and z directions
H	Height of the mixed out plane
h_f	Heat transfer coefficient in the presence of film cooling. eq.2.2
Q	Total heat flux into wall
h_o	Heat transfer coefficient in the absence of cooling. eq. 2.1
h	Heat transfer coefficient
$h(\theta)$	Heat transfer coefficient
W_∞	Molecular weight of the mainstream
e	Internal energy
k	Conductivity
KE_{actual}	Actual kinetic energy. eq. 5.13
k	Fractional difference between mainstream and adiabatic wall temperature
KE_{Ideal}	Ideal kinetic energy. eq. 5.14
l	Cooling hole slot / hole length
$\dot{m}_e$	Mainstream mass flow entrained into the boundary layer
M	Mass flux ratio. eq. 2.6
$\dot{m}_{Ac}$	Measured coolant mass flow rate
$\dot{m}_c$	Coolant mass flow rate
$\dot{m}_{Ic}$	Ideal coolant mass flow rate
$\dot{m}_m$	Mainstream mass flow rate

I	Momentum flux ratio. eq. 2.12
Nu_x	Nusselt number based on distance
P_s	Static pressure
P	Coolant hole pitch. eq. 2.11
P_{om}	Total pressure of mainstream
P_{oc}	Coolant total pressure
P_p	Static pressure at the mixed out plane
Pr	Prandtl number
P	Pressure
P_∞	Static pressure of mainstream
P_{Tt}	Local measured total pressure at the traverse plane
P_{sf}	Surface static pressure
$\dot{q}$	Heat flux
$\dot{q}_o$	Convective heat flux on external surface of wall in the absence of cooling. eq. 2.1
R	Gas constant for air
Re_x	Reynolds number based on distance
Re_c	Reynolds number of the coolant
s	Slot height. eq. 2.11
SS_{diff}	Residual sum of squares
St	Stanton number
T_{aw}	Adiabatic wall temperature. eq. 2.2
T_c	Coolant temperature. eq. 2.4
T_{cr}	Temperature at which crystal changes phase
T	Temperature
T_∞	The driving gas temperature. eq. 2.1
$T_{iso,adb}$	Isothermal adiabatic wall temperature
T_{oc}	Coolant total temperature
T_{om}	Mainstream total temperature
T_p	Static temperature at the mixed out plane
$T_{rec,m}$	Mainstream recovery temperature
T_w	Wall temperature. eq. 2.1
u	Flow velocity at the traverse plane
U_∞	Mainstream velocity
u_τ	Velocity of the flow adjacent to the wall
u	Velocity of the flow in the x-direction

u_p	Flow velocity at the mixed out plane
v	Velocity of the flow in the y-direction
$\mathbf{V}$	Velocity vector in a Cartesian flow field
w	Velocity of the flow in the z-direction
V_r	Velocity ratio. eq. 2.13
W_c	Molecular weight of the coolant flow
x	Distance downstream of slot / hole
y_i	Experimental data point. eq. 3.14
Y^+	Dimensionless wall distance

Chapter 1

Introduction

1.1 Overview of turbine cooling

Modern gas turbine engine manufacturers have an increasing technological challenge to remain competitive. Not only do the modern engines need to improve in performance, but they also need to have lower fuel consumption, be reliable and conform to new regulations on emissions.

The turbine entry temperature (TET) and pressure ratio of the working fluid in a gas turbine engine is closely coupled with its specific power output and specific fuel consumption. Increasing TET reduces the specific fuel consumption whilst the increase in pressure ratio increases the specific fuel consumption. However the increase in TET at high pressure ratios results in the increased production of NOx, CO_2 and CO. The relationship between TET and pressure ratio to the specific fuel consumption, performance and resultant emissions for a modern gas turbine engine are shown in Rolls-Royce (2005).

Figure 1.1 shows a comparison of the specific power of real gas turbine engines to that of an ideal isentropic gas turbine engine and fig. 1.2 shows a diagram of a modern gas turbine engine with the fan, compressor, combustor and turbine stages highlighted. The rise in TET over the years is shown in fig. 1.3. Lakshminarayana (1996) states that, in high performance gas turbine engines, the peak temperature of the working fluid can reach nearly 2000 K at the exit of the combustor. In modern gas turbine engines, this temperature can be in excess of 2000 K. This temperature is much higher than the allowable metal temperature of the hot stage components, manufactured from current materials, so cooling is essential.

Figure 1.3 shows the evolution of turbine blade cooling technology. The blades and vanes of the early turbines (pre 1970), incorporated simple cooling designs, primarily utilising internal convective cooling to extract the heat load incident on the

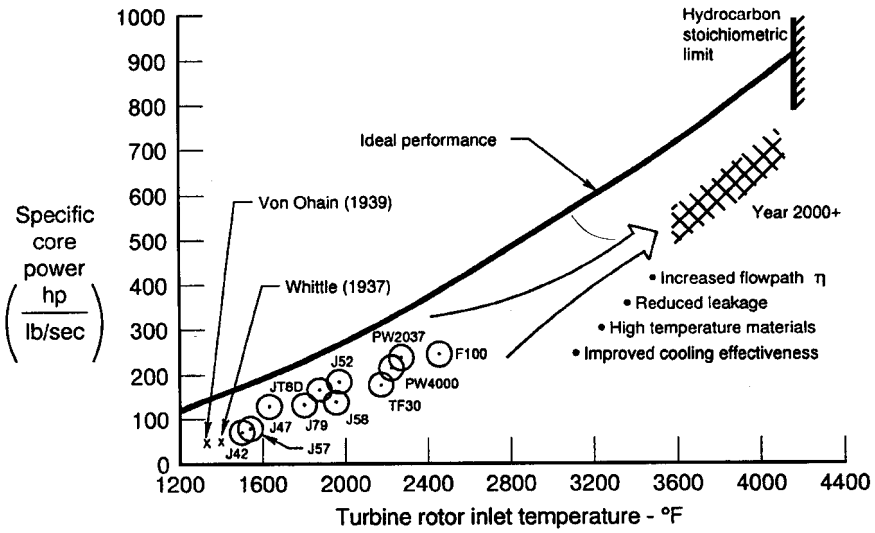

Figure 1.1: Specific power against turbine entry temperature Sautner et al. (1992) (Courtesy of Pratt & Whitney)

component surfaces. With the subsequent increases in the turbine entry temperature, more advanced cooling methodologies had to be incorporated into the design of the turbine. Currently, a combination of internal convective, impingement, film cooling and Thermal Barrier Coatings (TBC) are used to reduce the heat load and hence, extend the life of the component.

The subject of this thesis is film cooling and this is discussed in detail below. Convective cooling is achieved by passing the coolant, bled from the compressor, through passages within the turbine component. The classes of convection cooling include multi-pass, impingement and straight radial hole. A full description of the different classes of film cooling is given in Han et al. (2000). Thermal Barrier Coating (TBC) technology involves the application of a ceramic insulator to the surface of the component. The low conductivity TBC component reduces heat to the metallic turbine components.

In film cooling, the coolant air is bled from internal compartments within the blade/vane, through to the external walls to form a protective layer of cooling between the hot gas and the external component surface. As stated above, this cooling air is normally extracted from one or more stages of the compressor, and exhausted onto the external surface of the turbine via rows of discrete coolant holes. The interaction of these coolant jets with the mainstream hot gas defines a new effective gas temperature responsible for the heat flux to the surface. In this way, film cooling decreases the heat load that is carried by the component.

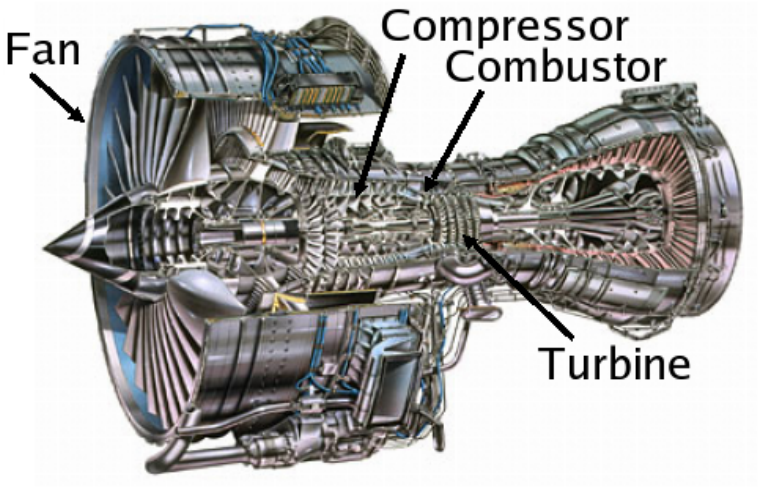

Figure 1.2: A diagram of a modern gas turbine engine for aircraft propulsion. (Courtesy of Rolls-Royce plc.)

There have been numerous research studies carried out to understand the fundamental physics of film cooling, with a view to improve the "state-of-the-art". The majority of the research has been focussed on the use of discrete film cooling holes or rows of cooling holes to achieve a protective film cooling layer on the hot gas path of the turbine surface. One of the goals of film cooling has been to achieve an ideal cooling film, which is uniform and continuous across the surface. This can be achieved by the use of a continuous slot, which is fed by a uniformly distributed cooling supply. However, in practice, the induced mechanical and thermal stresses, compounded with the fabrication constraints, prohibit such a design. In modern gas turbine engines, almost all turbine film cooling is performed by the use of discrete holes or relatively short slots. The holes can either be round or fan shaped whilst the slots have an ellipsoid cross section.

1.2 Trailing edge cooling

In implementing film cooling on modern turbines, the trailing edge film poses a particularly challenging design problem. From an aerodynamic point of view, the trailing edge of a blade is designed to be as thin as possible. However this conflicts with the implementation of the cooling design. Furthermore the cooling designs need to be robust, so that the turbine is able to operate in any service environment. Figure 1.4 (a) shows a newly machined high pressure turbine blade with drilled coolant holes whilst figures 1.4 (b) and (c) show trailing edge and pressure surface coolant holes

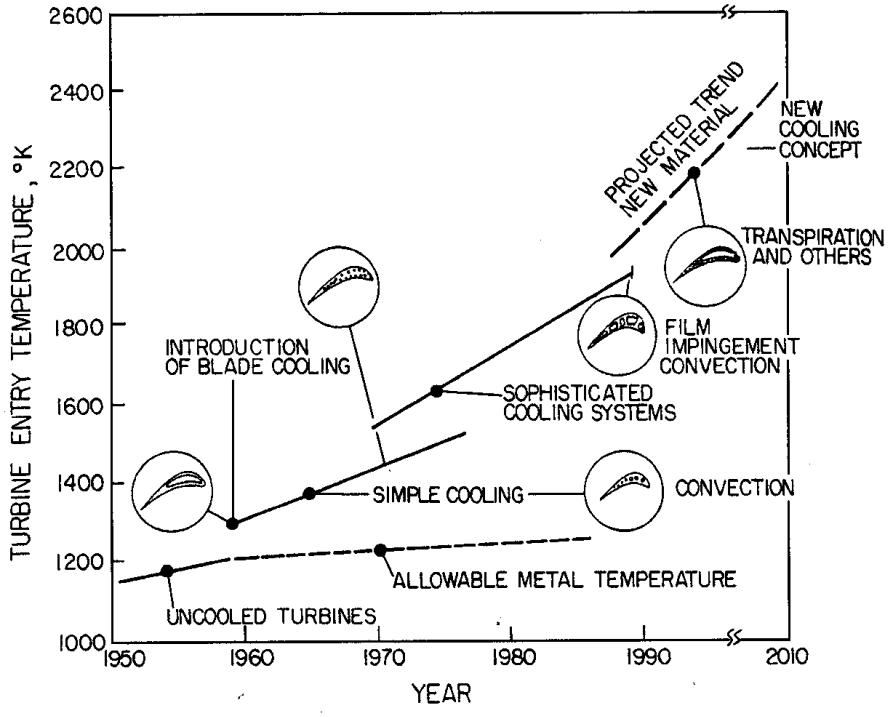

Figure 1.3: Variation of turbine entry temperature over the recent years Clifford (1985); collected in Lakshminarayana (1996)

respectively, after operating in a dusty environment. The engine had completed 2815 flight cycles.

From figure 1.4 the damage caused by operating in a sand laden environment can be seen. In this case, the pressure surface of the high pressure turbine blade, after 2815 flight cycles, is covered by a deposit of sand. The sand deposit has partially blocked the coolant hole exits at the trailing edge and pressure surface. As the pressure ratio across the coolant holes is fixed by the pressure in the internal cavity of the blade and external mainstream flow, the radical reduction in the coolant hole exit area, due to the sand blockage, would result in the decrease in mass flow rate of the coolant. Hence there would be less protective cooling film on the blade surface. Furthermore, due to the change in the exit geometry of the coolant holes, the film effectiveness would be greatly reduced downstream of the coolant holes. This would result in an increased metal temperature and hence reduced operational life of the turbine blade.

Bunker (2000) showed that, even when applying a protective thermal barrier coating on a surface with film cooling holes, the resultant partial blockage of the coolant hole would result in a dramatic reduction in the film effectiveness. The research in

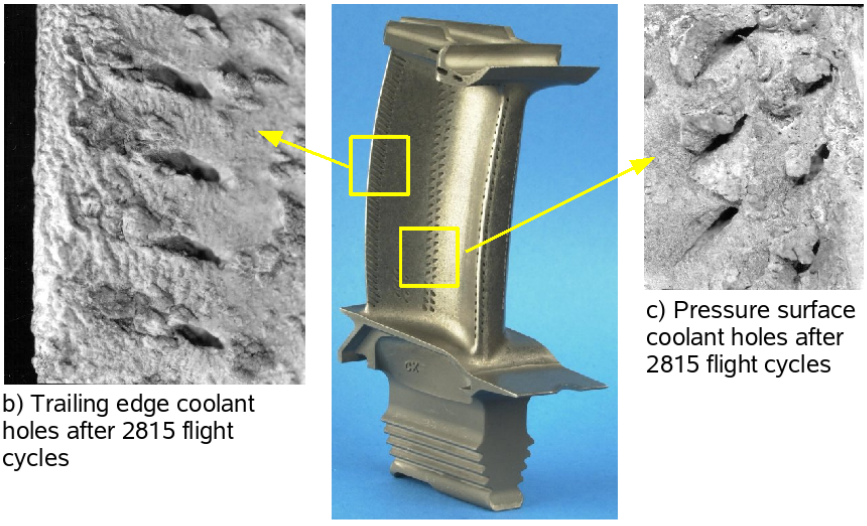

Figure 1.4: High pressure turbine blade. (a) A typical new turbine blade with drilled coolant holes (b) Close up of trailing edge coolant holes after 2815 flight cycles (c) Close up of pressure surface coolant holes after 2815 flight cycles. Images courtesy of Rolls-Royce Plc.

Bunker (2007a) shows that by shielding the film cooling exit plane in a shallow trench, a large improvement in the film cooling effectiveness was obtained.

Hence by analogy for the trailing edge coolant holes, by shielding the coolant exit plane from the mainstream flow containing pollutants such as sand, the build up of the sand at the coolant hole exit could expect to be reduced, resulting in better film effectiveness and improved operational life.

Shielding of the coolant hole exit plane is achieved by locating the coolant exit, within a slot. Figure 1.5a shows the conventional turbine blade whilst figure 1.5b shows a high pressure turbine blade with such slots on the pressure surface. Near the trailing edge, these slots form a cut-back. The slots can be either machined onto a conventional blade or included in the casting process of the blade. The cut-back near the trailing edge, shown in figure 1.5b, does not have pin fins or ribs. The coolant is fed onto the surface, from the internal chambers via discrete coolant holes. Figure 1.5c shows a high pressure turbine blade with pressure surface discrete slot ejection near the trailing edge. Like the blade shown in figure 1.5b, the discrete slot coolant exit plane is shielded from the mainstream by the cutback. There are internal ribs and pin fins within the blade to provide structural integrity and a mechanism to control the coolant mass flow. The trailing edge coolant hole ejection features as shown in figure 1.5c cannot be machined, but need to be cast during the blade manufacturing

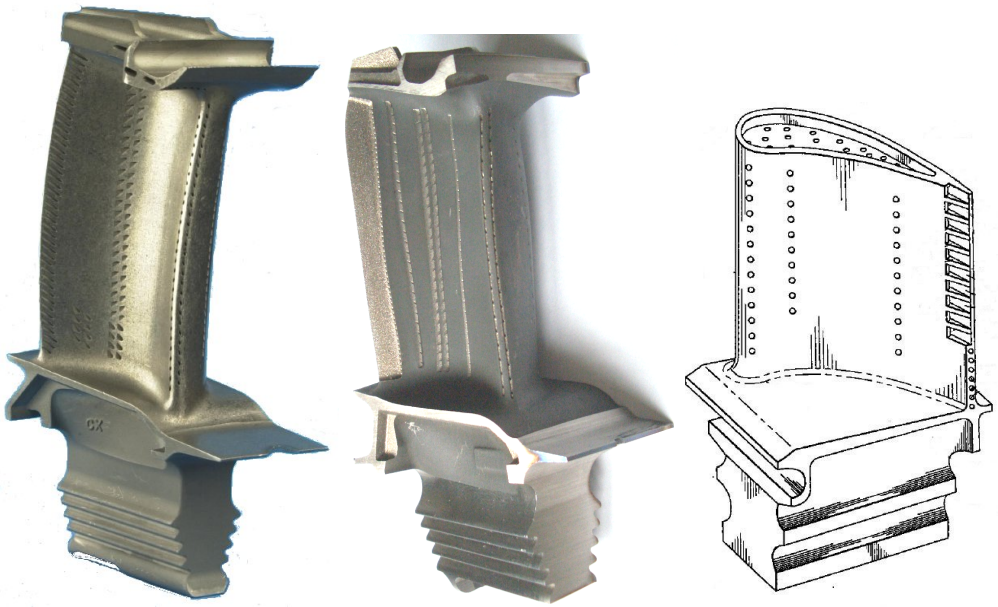

(a) Conventional High Pressure turbine blade courtesy of Rolls-Royce Plc.

(b) High Pressure turbine blade with coolant hole exit plane embedded within slot / cutback, courtesy of Rolls-Royce Plc.

(c) High Pressure turbine blade with trailing edge slot ejection from Lee (2001)

Figure 1.5: High Pressure turbine blades with conventional pressure surface, slot and cutback ejection.

stage. The cutback configuration shown in figure 1.5c is known as a "letter box" cutback configuration.

1.3 Objectives of research

The current study focuses on a large scale low speed, comparative aerodynamic and heat transfer experimental investigation of three trailing edge cooling geometries based on the trailing edge cooling configurations shown in figure 1.5. The three test plates are:

1. pressure surface near trailing edge (conventional) film cooling holes as shown in figure 1.5a, which shall be referred to as datum configuration in this thesis,

2. machined / cast cut-back pressure surface cooling system as shown in figure 1.5b, which shall be referred to as the machined cutback configuration in this thesis,

3. cast trailing edge cut-back configuration with pin fins and ribs as shown in figure 1.5c, which shall be referred to as cast cutback configuration.

The aim of the current research is to explore, in a large scale, low speed environment, the comparative difference in the aerodynamic losses and heat transfer effectiveness between the datum (i.e. pressure surface discrete cooling holes) and the machined and cast cutback trailing edge cooling configurations shown in figures 1.5b and 1.5c. The author needed to develop experimental methodologies to make this comparison, and this technique development was a key part of the work. The comprehensive set of aerodynamic and heat transfer experiments is complemented by a thorough computational study using state of the art CFD. The latter study was performed with the aim of gathering an understanding of trailing edge flow.

It must be noted that the Mach number in the vicinity of the pressure surface near trailing edge cooling ejection for a typical modern blade is approximately 0.8. The typical Reynolds number at this location varies from approximately 1.8×10^6 - 2×10^6. In the experiments documented in this thesis, the Reynolds number is matched to the engine condition, but as the experiments are low speed, the Mach number and density ratio are not matched. The research by Liess (1975) and Gritsch et al. (1998) show that the film cooling effectiveness is insensitive to Mach number. Furthermore the research by Baldauf et al. (2002) shows that matching the velocity ratio between coolant and mainstream gives good agreement in film effectiveness

at high and low density ratios. Hence the present film effectiveness measurements can be read across to engine conditions with the same velocity ratio. However the aerodynamic performance cannot be directly read across to engine conditions. It is the author's view that the trends in aerodynamic performance seen in the experimental conditions of the three trailing edge cooling designs would be similar to the trends that would be seen at engine conditions.

1.4 Thesis overview

Chapter 2 provides a summary, following a literature review, of parameters which influence film cooling, such as hole length to diameter ratio, angle of inclination and Reynolds number. The literature review of trailing edge film cooling is also summarised in this chapter.

Chapter 3 describes the numerical validation, by use of computational fluid dynamics (CFD), of a simple flat plate film cooling experiment. The experimental measurements were from Saumweber et al. (2000). The aim of this exercise was to establish a computational methodology for modelling the film effectiveness and heat transfer coefficient, which is then used to predict the flow field and film effectiveness of the three trailing edge test plates, which were the focus of this research.

Chapter 4 describes the experimental test facility used in the current research. This chapter also describes the new test plates manufactured using stereolithography and the instrumentation used in the aerodynamic and heat transfer measurements.

Chapter 5 presents the low speed aerodynamic measurements from the three test plates. The measured discharge coefficients local losses and mixed out losses are compared to the datum (conventional) trailing edge film cooling configuration.

Chapter 6 reviews the computational fluid dynamic predictions of the low speed aerodynamic measurements using the approach derived from the validation exercise in chapter 3.

Chapter 7 presents the heat transfer measurements on the pressure surface downstream of the coolant ejection plane. Again, the laterally averaged film effectiveness and heat transfer coefficient are compared to those from the datum (conventional) trailing edge film cooling configuration.

Chapter 8 details the heat transfer predictions of the three test plates using the recipe from the validation exercise shown in chapter 3.

Chapter 9 collects the conclusions from this study and gives recommendations for further work.

1.5 Summary of achievements of the research

This research has succeeded in accurately evaluating the performance of three trailing edge cooling systems of considerable interest to engine manufacturers. The research combines accurate, high spatial resolution experimental measurements with CFD prediction in order to assess the accuracy of the latter. The aerodynamic experiments showed that the cast TE system produced higher loss. The author designed and commissioned a high resolution stepper motor driven X-Y traverse system that produced total pressure loss data at high resolution, which provided considerable insight into the aerodynamics of film cooling. The film hole discharge coefficients were significantly different for the datum film cooling hole compared to the other two configurations. This difference was explained by the capping effect of the mainstream flow. RANS CFD simulations exhibited the same trends in loss coefficient as in the experiments, but were consistently higher for reasons that are explained in the thesis. The predicted discharge coefficients were within about 5% of the measurements.

The effect of wall thermal boundary condition on film cooling effectiveness has been accurately quantified and a new method of relating isothermal to adiabatic film effectiveness developed. A comparison to flat plate film cooling data in the literature enabled the author to identify the best RANS turbulence model for effectiveness and heat transfer coefficients. The author made detailed heat transfer coefficient and effectiveness measurements using a new method developed for his trailing edge research. The research showed that the cast cutback system could achieve a significantly higher effectiveness than the other two systems but at the penalty of higher coolant flow and higher aerodynamic loss. This result has directly influenced subsequent engine designs. The limitations of state of the art RANS calculations for predicting film effectiveness have been accurately quantified and this is guiding best practice for engine design within Rolls-Royce.

Chapter 2

Literature review

2.1 Introduction

In the absence of film cooling, the convective heat flux at the external surface of a wall, $\dot{q}_o$, is given by equation 2.1. Here, the hot gas temperature near the surface of the metal T_∞ is the driving gas temperature, h_o is defined as the heat transfer coefficient and T_w is the wall temperature.

$$\dot{q}_o = h_o(T_\infty - T_w) \tag{2.1}$$

With the introduction of film cooling, the driving gas temperature is the mixed hot gas and coolant temperature. This lower gas temperature, adjacent to the wall can be regarded as the adiabatic wall temperature,T_{aw}, if the wall is truly adiabatic. However, if the wall is not adiabatic, the incident heat flux, $\dot{q}_f$, on a conducting surface, due to the adiabatic wall temperature, the heat flux is given by equation 2.2.

$$\dot{q}_f = h_f(T_{aw} - T_w) \tag{2.2}$$

Straight forward algebraic manipulation can show that the ratio of the reduction in heat flux due to film cooling, to the uncooled heat flux is given by equation 2.3 as shown in Harrison (2006).

$$\frac{\Delta\dot{q}}{\dot{q}_o} = 1 - \frac{h_f}{h_o}(1 - \frac{\eta}{\phi}) \tag{2.3}$$

The definition of η is given by equation 2.4 and the definition of ϕ is given by equation 2.5.

$$\eta = \frac{T_\infty - T_{aw}}{T_\infty - T_c} \tag{2.4}$$

$$\phi = \frac{T_\infty - T_w}{T_\infty - T_c} \tag{2.5}$$

Bogard (2007a) cites 0.6 as a typical value for ϕ. h_f and h_o are nearly equal so in order to obtain a 100% reduction in heat flux, η would have to take on a value of 0.6. The importance of accurately determining η and h_f for the turbine designer can be seen from equation 2.3.

Research into film cooling has been under way for more than 35 years. The early research was not driven by gas turbine engine cooling but by research into re-entry vehicles and liquid fuelled rockets. This early film cooling utilised two dimensional slots, which could either be tangential or angled to the surface, for injection of the coolant (Bunker (2007b)). Goldstein (1971) summarises the early film cooling research undertaken, and also the early film cooling models. One early attempt at correlation, presented in Goldstein and Haji-Sheikh (1967) and summarised in Goldstein (1971), is shown in figure 2.1.

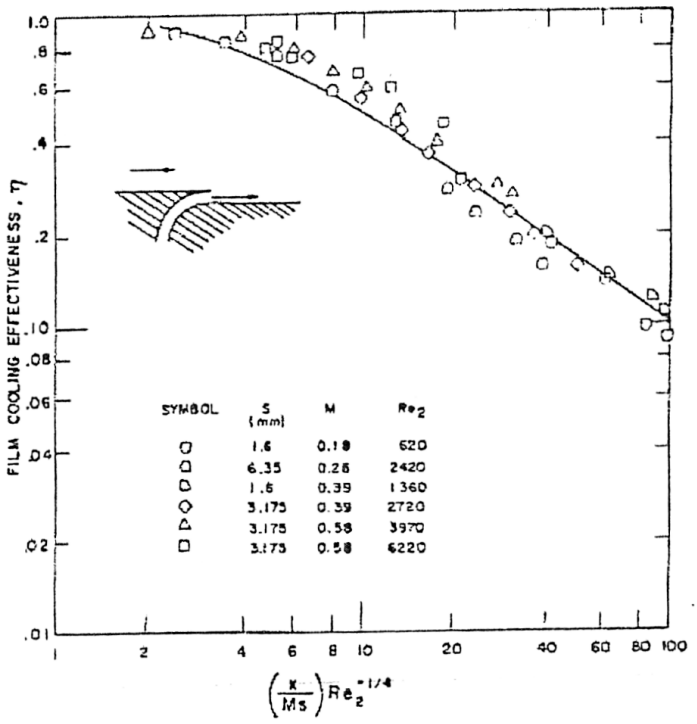

Figure 2.1: Tangential slot film cooling effectiveness, Goldstein (1971), (reproduced in Bunker (2007b))

The data shown in figure 2.1 are for a two dimensional continuous slot, with tangential ejection onto a surface and fed from a curved entry duct of large radius as

indicated in the figure. The mainstream and coolant are air and the upper surface defining the slot is a knife edge. In figure 2.1, the effectiveness of the experimental data and predictions are plotted against the product of the non-dimensional distance ($\frac{x}{s}$), which is further normalised by the mass flux ratio M and the mainstream Reynolds number based on distance downstream of the coolant ejection raised to the power -0.25. The mass flux ratio M is defined by Eqn 2.6.

$$M = \frac{\rho_c U_c}{\rho_\infty U_\infty} \tag{2.6}$$

The distance x is the distance downstream from the slot exit and s refers to the slot height. The model used by Goldstein and Haji-Sheikh (1967) was one of the first models to incorporate mass flux ratio and slot angle (α) and is given by equation 2.7

$$\eta = \frac{1.9 Pr^{\frac{2}{3}}}{1 + 0.329 \frac{Cp_\infty}{Cp_c} \frac{\mu_\infty}{\mu_c}^{0.2} \xi^{0.8} \beta} \tag{2.7}$$

where

$$\xi = \frac{x}{Ms} Re_c^{-\frac{1}{4}} \tag{2.8}$$

and

$$\beta = 1 + 1.5 \times 10^{-4} Re_c (\frac{\mu_c W_\infty}{\mu_\infty W_c}) sin\alpha \tag{2.9}$$

Bunker (2007b) shows that, for a particular film cooling application, with a fixed ratio of coolant-to-gas properties, equation 2.7 can be reduced down to equation 2.10

$$\eta = \frac{C_1}{1 + C_2 (\frac{x}{Ms})^{0.8}} \tag{2.10}$$

In discrete film cooling, the parameter s is replaced by the equivalent two-dimensional slot width given in equation 2.11 where A_{hole} and P are the hole flow cross-sectional area and pitch respectively.

$$s = \frac{A_{hole}}{P} \tag{2.11}$$

By the adjustments of the constants C_1 and C_2, this simple correlation can be used to fit many flat plate film cooling data. The constant C_1, provides the initial film effectiveness value, whilst the constant C_2 provides the rate of decay of the effectiveness downstream of the coolant holes. However, it must be noted that this model does include a few limitations. The data examples used to derive the model

were obtained from flat plate tests, where there are no pressure gradients and low mainstream turbulence. The model assumes that the coolant-to-gas properties are fixed. As the model is based upon a two dimensional slot, widely spaced discrete holes will not fit the model well. In addition the model can not provide information on the lateral variation of effectiveness. Furthermore, the model does not account for jet "blow-off", and hence is not valid for high mass flux ratios. Even with these limitations, the model can still be used to predict the film cooling effectiveness.

Figure 2.2 shows laterally averaged effectiveness for a row of cylindrical coolant holes, inclined at 30^o to the horizontal with a pitch spacing of 3d. In these experiments, Waye (2005) used fluids with density ratio of 1.3

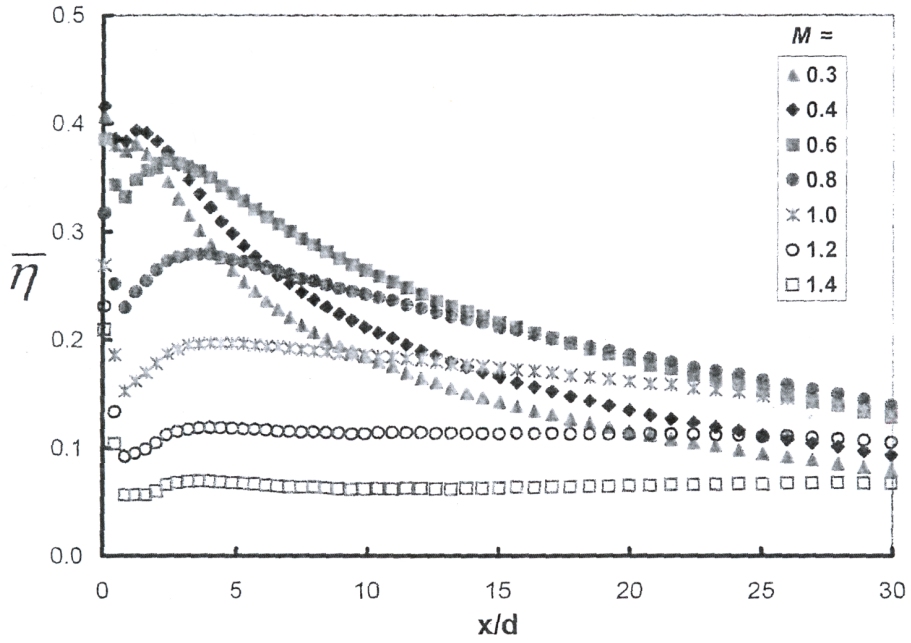

Figure 2.2: Variation of laterally averaged film effectiveness with mass flux ratio for a row of coolant holes spaced 3d apart and inclined 30^o with density ratio 1.3 (from Waye (2005))

Figure 2.3 shows the data from Waye (2005) replotted against ξ and compared with the tangential slot film cooling effectiveness correlation from Goldstein (1971).

Comparing the initial effectiveness, just downstream of the slot shown in figure 2.3, with that from discrete film cooling holes, it can be observed that the effectiveness value is considerably below 1.0 for the discrete hole cases. This is due to the absence of coolant between the coolant holes and the inclination of the coolant holes, resulting in a lower laterally averaged film effectiveness. In the slots, the coolant is fed uniformly and hence the effectiveness just downstream of the slot is near unity. For discrete

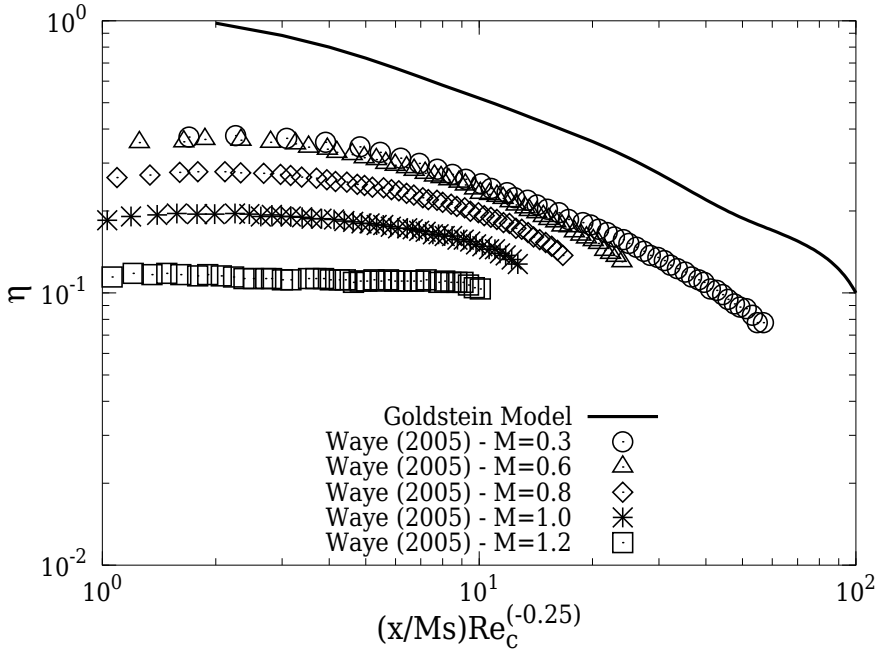

Figure 2.3: Laterally averaged film effectiveness from Waye (2005) replotted against ξ and compared with Goldstein (1971) tangential slot effectiveness.

film cooling holes, for mass flux ratios $M = 0.3$ to 0.6, the initial effectiveness value is approximately constant at 0.4. However as the mass flux ratio is increased, this initial value decreases. This decrease in effectiveness is attributed to the coolant jet lift-off (separation), from the surface just downstream of the coolant holes, allowing the mainstream to be incident on the surface. The separated coolant jet subsequently re-attaches further downstream, providing increased effectiveness values at the point of incidence (eg. $M = 0.8, x/d = 3$). Far downstream of the coolant exit, the effectiveness for lower mass flux ratio cases ($M < 0.6$) are lower than those for the higher mass flux ratio cases ($M > 0.6$). For the lower mass flux ratio cases, the coolant exiting the coolant holes has thoroughly mixed with the mainstream and hence provides very little cooling effect at the far downstream location. With the higher mass flux ratio cases, the large amount of the coolant adjacent to the wall, far downstream, would decrease the overall temperature of the wall, providing a higher effectiveness, compared with the lower mass flux ratio cases.

The jet separation and subsequent re-attachment was directly measured by Thole et al. (1992). In this experiment, the streamwise oriented holes were angled at 35^o to the horizontal. The jet separations off the surface were achieved by changing the density ratio from 1.2 to 2.0. To characterise film cooling and obtain scaling

parameters Thole et al. (1992) used three parameters, namely mass flux ratio,M, momentum flux ratio, I (equation 2.12) and velocity ratio, V_r (equation 2.13). The study noted that in film cooling, the coolant jet can take on three possible positions downstream of the coolant hole. They are fully attached, detached and re-attached, and fully detached. Figure 2.4 shows the thermal profiles along the centreline of the coolant jets, highlighting the three regimes of film cooling.

$$I = \frac{\rho_c U_c^2}{\rho_\infty U_\infty^2} \tag{2.12}$$

$$V_r = \frac{U_c}{U_\infty} \tag{2.13}$$

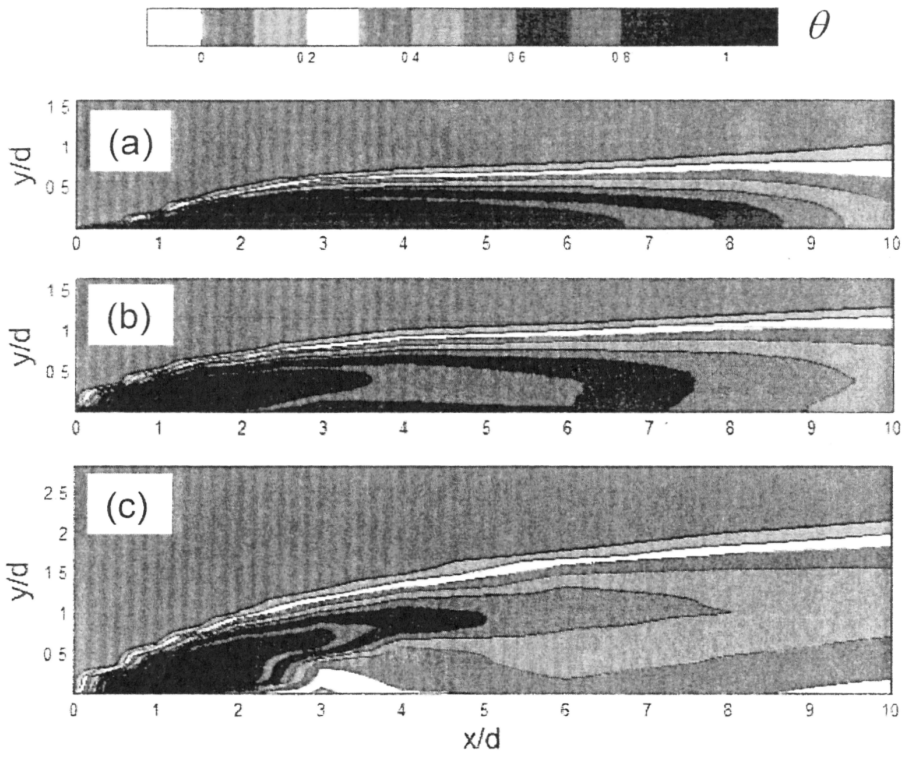

Figure 2.4: Thermal profiles along the centreline of coolant jets with (a) $I = 0.12$ "Fully attached",(b) $I = 0.5$ "Detached-reattached",(c)$I = 2$ "Fully detached" coolant jets, from Thole et al. (1992). (Reproduced in Bogard (2007a))

The best scaling parameter for film cooling was concluded in Thole et al. (1992), to be the momentum flux ratio. The three regimes occur in the following ranges of I:

- fully attached = $I < 0.4$
- detached and re-attached = $0.4 < I < 0.8$

- fully detached = $I > 0.8$

Bogard (2007a) shows that the data from Waye (2005) can also be categorised into these three regimes. However, unlike the slot effectiveness data, which collapse onto one curve when plotted in terms of $\frac{x}{Ms}$, discrete hole data do not collapse as shown in figure 2.5 (from Bogard (2007a))

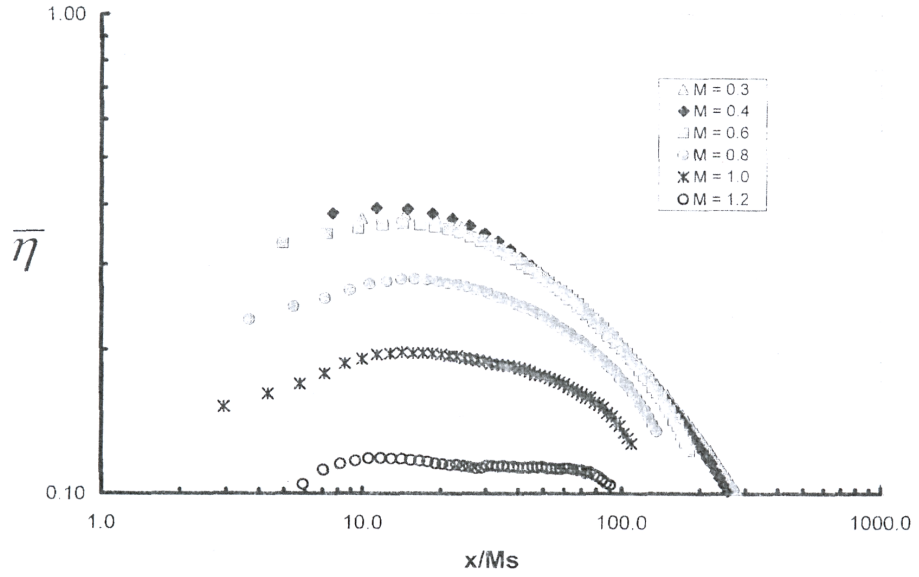

Figure 2.5: Laterally averaged film effectiveness for discrete holes presented as a function of $\frac{x}{Ms}$ from Bogard (2007a) (based on data from Waye (2005))

From figure 2.5, it can be seen that the fully attached data points do collapse into one curve. However the data from the higher mass flux ratio, which correspond to the detached - reattached and fully detached regimes, do not collapse onto a single curve. The complex 3D coolant and mainstream flow interaction in discrete film cooling results in flow separation at mass flux ratios greater than 0.6. This is not the case with slot cooling. It must be noted that the mass flux ratio at which coolant separation occurs is a function of the coolant inclination angle.

Baldauf and Schulz (2007) investigated the change in heat transfer coefficient due to a row of cylindrical holes exhausting onto a flat plate. The cooling holes were inclined at 30^o, with a hole spacing to diameter ratio of 3. The coolant to mainstream density ratio was set at 1.8. The data presented in Baldauf and Schulz (2007) were normalised with the heat transfer coefficient on a flat plate without film cooling. Figure 2.6 shows the laterally averaged heat transfer coefficient at varying mass flux rates from Baldauf and Schulz (2007).

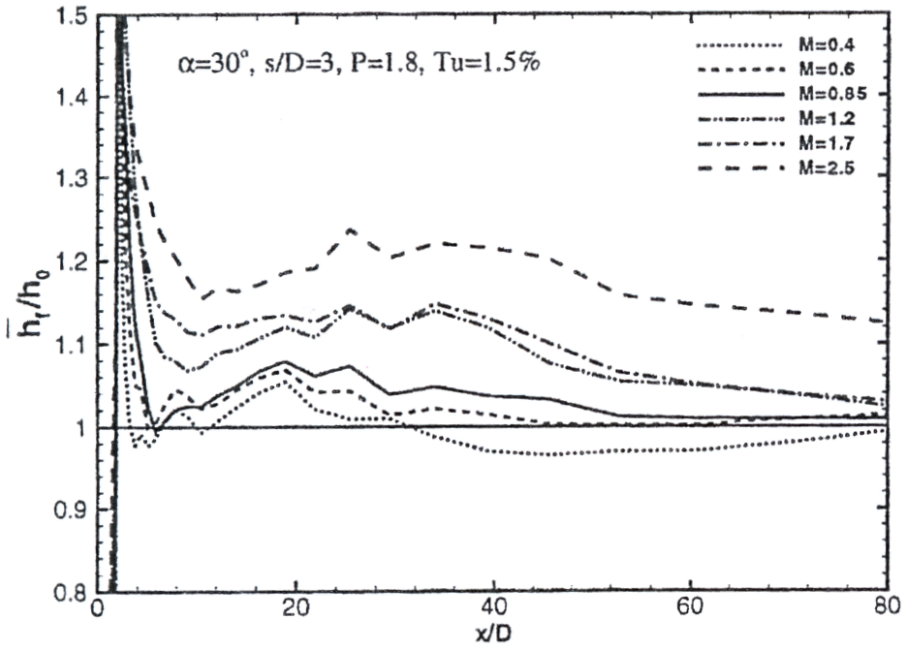

Figure 2.6: Laterally averaged heat transfer coefficient at varying mass flux rates Baldauf and Schulz (2007)

The experimental data show that there is an increase in the normalised heat transfer coefficient with increasing mass flux ratio. The sharp rise in the heat transfer coefficient at $\frac{x}{d} = 2$ is due to the experimental setup and hence should be disregarded. All mass flux ratios beyond $\frac{x}{d} = 2$ show a similar trend in the heat transfer coefficient downstream of the coolant holes. For mass flux ratios up to 0.85, which corresponds to momentum flux ratios of 0.4 and hence the fully attached regime, there is very little increase in the heat transfer coefficient from the uncooled case. The maximum enhancement is below 8% at an $\frac{x}{D}$ location of 20. With further increased mass flux ratio, the films move onto the detached-reattached and fully detached regimes. There is a significant increase in the cooled heat transfer coefficient over the uncooled value. Baldauf and Schulz (2007) suggests that the high heat transfer coefficient far downstream of the coolant holes is due to the interaction of the adjacent coolant jets, forcing the mainstream flow between the jets towards the surface.

2.2 The parameters that affect film cooling

To identify the key parameters that affect discrete film cooling holes, Baldauf et al. (2002) conducted flat plate film cooling experiments. These experiments were limited to round film cooling holes. The parameters considered were hole inclination,

coolant-to-gas density ratio, upstream turbulence intensity, pitch to diameter ratio, hole length to diameter ratio and the ratio of boundary layer thickness of the approaching flow to the film row hole diameter. Further to this set, the hole shape, the discharge coefficient and the turbulence length scale of the oncoming flow can also be considered as influential parameters of film cooling performance. A brief summary of the effect of each of these parameters on film cooling performance is discussed below.

2.2.1 Effects of length to diameter ratio

Lutum and Johnson (1998) show the effect of length to diameter ratio on film cooling for cylindrical holes. The holes were inclined to the surface at 35° with a pitch to diameter ratio of 3. The centreline and laterally averaged effectiveness downstream of the holes were studied for length to diameter ratios of 1.75 to 18. Figure 2.7 shows the results from this study.

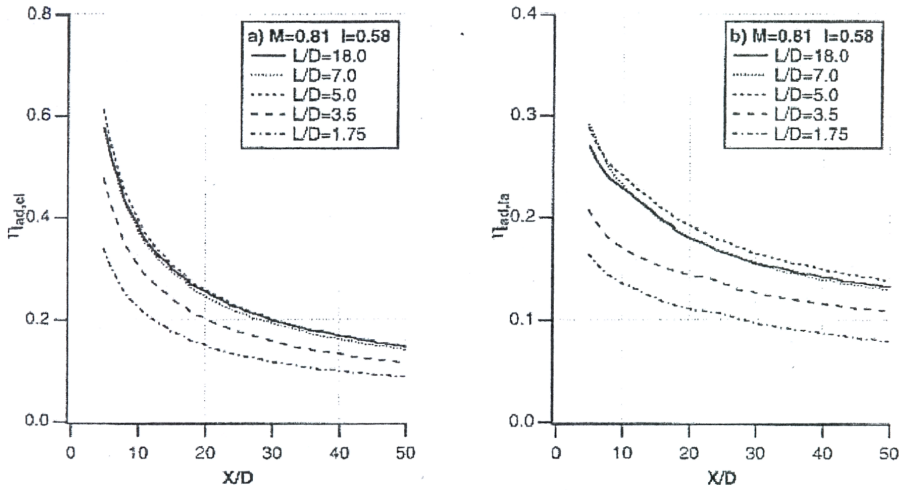

Figure 2.7: The effect of hole length to diameter ratio, Lutum and Johnson (1998)(reproduced in Bunker (2007a))

The centreline data show that the effectiveness is insensitive to length to diameter ratios larger than 5. A similar conclusion can be obtained from the laterally averaged effectiveness data. The coolant entering the hole separates at the sharp edge of the inlet. For length to diameter ratios greater than 5, the flow inside the cooling hole has sufficient length to develop downstream of the reattachment. For smaller length to diameter ratios, there is insufficient length to develop and hence entry effects are seen downstream of the coolant hole exit. Therefore, cooling hole length to diameter ratios greater than 5 are desirable in a cooling design.

Achieving such a length in practice can be difficult and Bunker (2007a) notes that the minimum acceptable length to diameter ratio is 1.5 for a circular coolant hole. This requirement comes from the film cooling hole having to act as a "short tube" instead of "port" hole with overlapping inlet and exits as found in transpirational cooling.

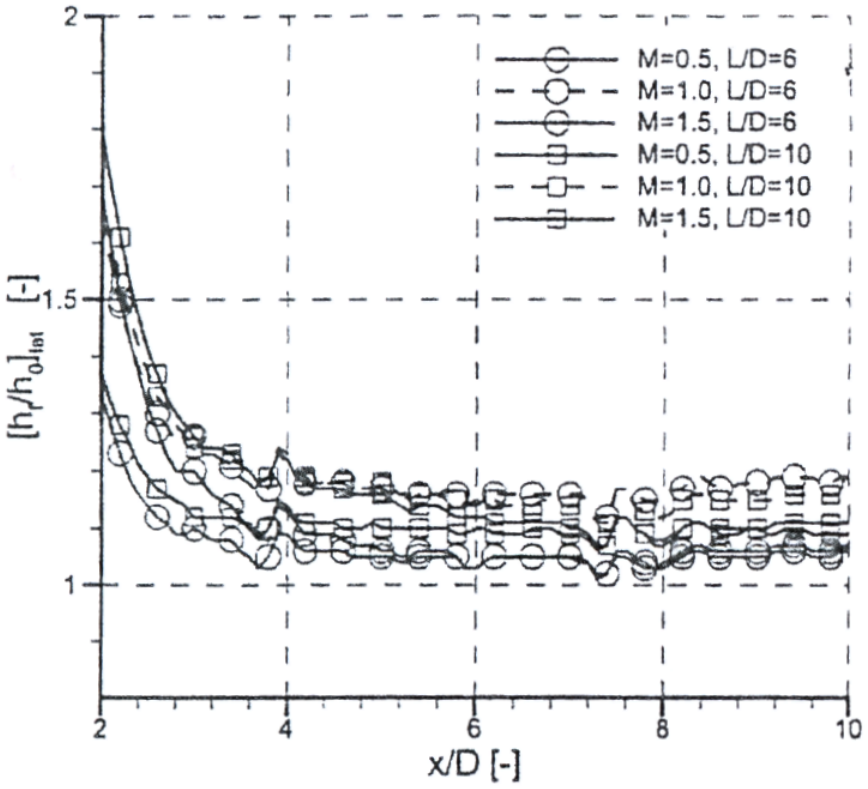

Figure 2.8: Effect of hole length on the laterally averaged heat transfer coefficient. Data from Saumweber and Schulz (2007b)

Figure 2.8 shows the effect of hole length on the heat transfer coefficient downstream of a row of cylindrical coolant holes. During the experiments, the mainstream Mach number was kept constant at 0.3 with turbulence intensity of 5.2%. The data show that there is very little effect of the hole length to diameter ratio on the heat transfer coefficient at high mass flux ratios. However, for low mass flux ratios, the increase in hole length produces a slight increase in the heat transfer coefficient downstream of the coolant hole. It is believed by the author that this increase in heat transfer coefficient could be attributed to the mainstream turbulence.

2.2.2 Effects of hole angle relative to surface

The goal of film cooling is to provide a protective coolant film on the surface downstream of the coolant holes. Hence it is evident that small angles of inclination relative to the surface would be ideal. This is not always possible in the manufacture of film cooling holes. The study by Baldauf et al. (2002) included the effects of hole inclination angle on the film cooling effectiveness. Figure 2.9 (reproduced in Bogard (2007b)) shows the spatially averaged film effectiveness plotted against the momentum flux ratio.

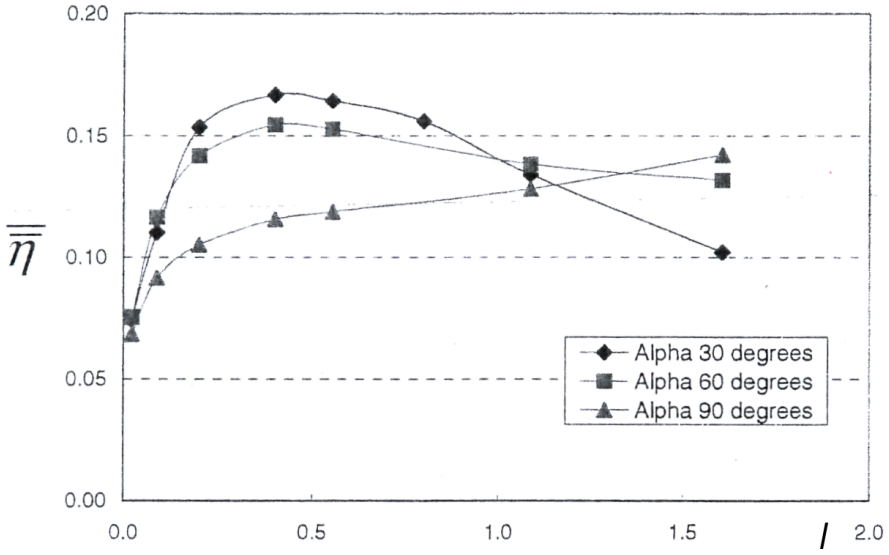

Figure 2.9: The effect of angle of inclination on film effectiveness vs momentum flux ratio, I. The data from Baldauf et al. (2002) and reproduced in Bogard (2007b).

For inclination angles of 30^o and 60^o, a momentum flux ratio of 0.4 provides the optimum film cooling effectiveness. At this momentum flux ratio, the spatially averaged effectiveness for holes normal to the surface (angle of inclination 90^o) is approximately 30% lower than the effectiveness for holes angled at 30^o. However for larger momentum flux ratios ($I > 1$), the data show that better effectiveness can be obtained from holes angled 90^o to the surface. For lower momentum flux ratios, these holes do not perform as well. Baldauf et al. (2002) attributed the increased film effectiveness performance of the 90^o coolant holes at higher momentum flux ratios to enhanced interactions of adjacent jets compared with the 30^o holes.

Figure 2.10 shows the variation of the laterally averaged effectiveness downstream of the coolant holes for a momentum flux ratio of 0.4. All three hole angles exhibit

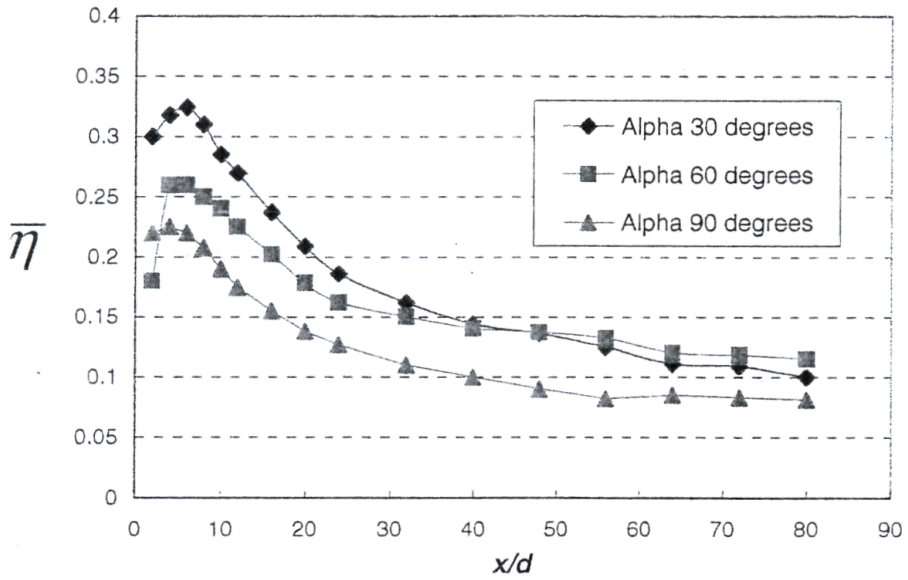

Figure 2.10: The variation of film effectiveness against $\frac{x}{d}$ for momentum flux ratio $I = 0.4$. The data are from Baldauf et al. (2002) and reproduced in Bogard (2007b).

a low effectiveness just downstream of the coolant holes. Further downstream ($2 < \frac{x}{d} < 5$), the effectiveness recovers, then subsequently decreases as $\frac{x}{d}$ increases. From the study of Thole et al. (1992), $I = 0.4$ corresponds to the detached and re-attached regime, and the film effectiveness data show this behaviour. The 60^o degree holes display very low effectiveness just downstream of the coolant holes, but recover to have an effectiveness similar to 30^o for $\frac{x}{d} > 30$. However, for the 90^o holes, the initial separation is too great for the effectiveness to recover further downstream.

Figure 2.11 shows the laterally averaged heat transfer coefficient at a steep hole inclination angle of 90^o, with a pitch to diameter ratio of 3, density ratio 1.8 and mainstream turbulence intensity of 1.5%. From comparison of the data shown in figure 2.6 and 2.11, it can be seen that most of the heat transfer enhancement occurs nearer to the hole ejection location for steep angles of ejections. For this steep angle of ejection, the enhancement of the heat transfer coefficient over the unblown heat transfer coefficient increases with increasing mass flux ratio. For low mass flux ratios, significant heat transfer coefficient enhancement (13% to 15%) is seen nearer to the hole ejection location, compared to the shallow angle ejection. For high mass flux rates, the heat transfer enhancement is twice as high as the shallow angle ejection values. Further downstream of the coolant ejection, the heat transfer coefficient drops to the level of the uncooled case.

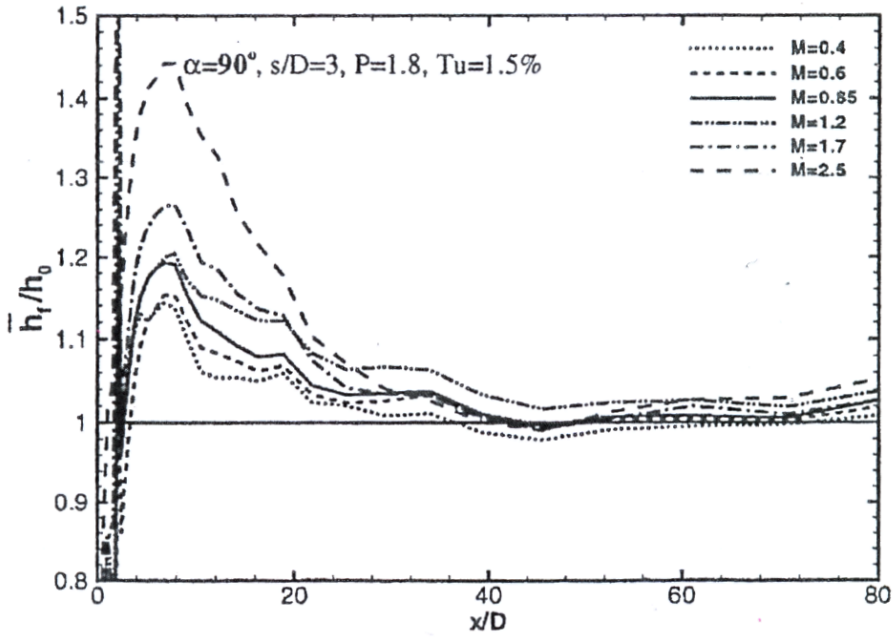

Figure 2.11: Laterally averaged heat transfer coefficient at hole inclination angle of 90^o, pitch to diameter ratio of 3, density ratio 1.8 and turbulence intensity 1.5%.

2.2.3 Effects of compound angle

Flat plate film cooling experiments, conducted in laboratories, normally have the cooling holes aligned with the mainstream direction. When the coolant holes are angled to the mainstream direction flow direction, it is referred to as compound angle ejection. Schmidt et al. (1996) measured the adiabatic film effectiveness for a compound angle of 0^o and 60^o.

From figure 2.12 it can be observed that compound angle ejection provides better film effectiveness for higher momentum flux ratios. For momentum flux ratios higher than 0.8, a study by Thole et al. (1992), showed that the coolant is largely separated for holes aligned with the mainstream (compound angle 0^o). This would result in poor effectiveness at these momentum flux ratios. However, the compound angle holes appear to remain attached to the surface, providing better film effectiveness. Bogard (2007b) states that compound angle holes present a broader profile to the mainstream. The mainstream has a large impact on the coolant jets, effectively turning the jets towards the wall.

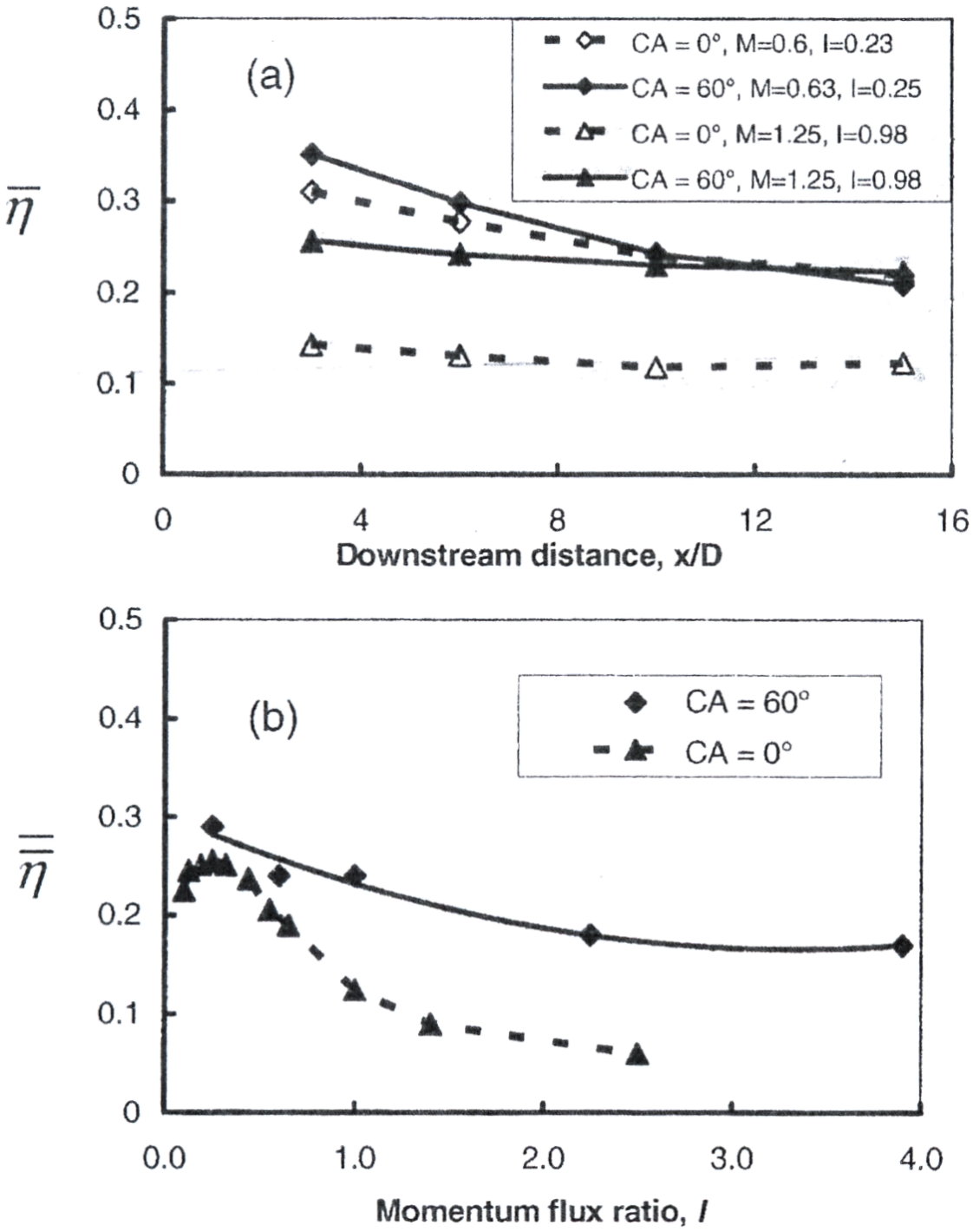

Figure 2.12: Comparison of film effectiveness for holes with compound angle of 0^o and 60^o (from Schmidt et al. (1996)). The lower figure shows the effectiveness averaged over the total length of the test section.

2.2.4 Effects of pitch to diameter ratio

Bogard (2007b) states that the spacing between coolant holes (hole pitch) found in aerofoils can range from $2d$ to $8d$. The minimum pitch is usually dictated by structural, machining and permissible coolant flow constraints. Baldauf et al. (2002) investigated rows of holes with pitch to hole diameter ratios of 2, 3 and 5. Figure 2.13 shows the film effectiveness data from Baldauf et al. (2002), spatially averaged and presented in Bogard (2007b).

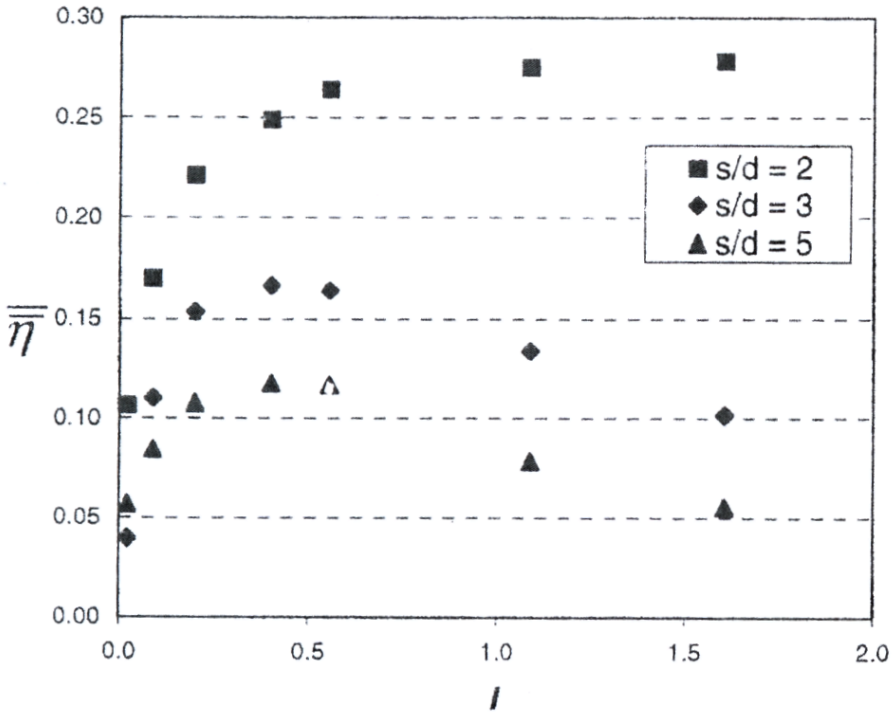

Figure 2.13: Spatially averaged film effectiveness for holes with pitches 2, 3 and 5. Data from Baldauf et al. (2002) and presented in Bogard (2007b). These holes are aligned with the flow and pitched at 30^o to the surface.

For a row of holes, with large pitch to diameter ratio, each coolant jet interacts with the mainstream in isolation. As the pitch to diameter ratio is decreased, provided the jets can still be considered to behave as though isolated, one would expect the ratios of effectiveness to follow the ratio of the hole to pitch diameter ratios. Considering the pitch to diameter ratio of 3 and 5 data presented in figure 2.13, the spatially averaged effectiveness data for a pitch to diameter ratio 3 is approximately $\frac{5}{3}$ times the data for a pitch to diameter ratio of 5. This trend was also seen in the experimental data reported by Waye and Bogard (2006), where the spatially averaged effectiveness for a

pitch to diameter ratio of 2.8 was approximately twice that of the pitch to diameter ratio 5.6.

However, the data for spatially averaged pitch to diameter ratio 2 do not conform to the above trend, but give rise to much higher effectiveness at large momentum flux ratios (greater than 1.0). At close pitch to diameter ratio, the tendency of the coolant jets to separate at high momentum flux ratio is suppressed, due to interactions of the adjacent jets, resulting in high film effectiveness.

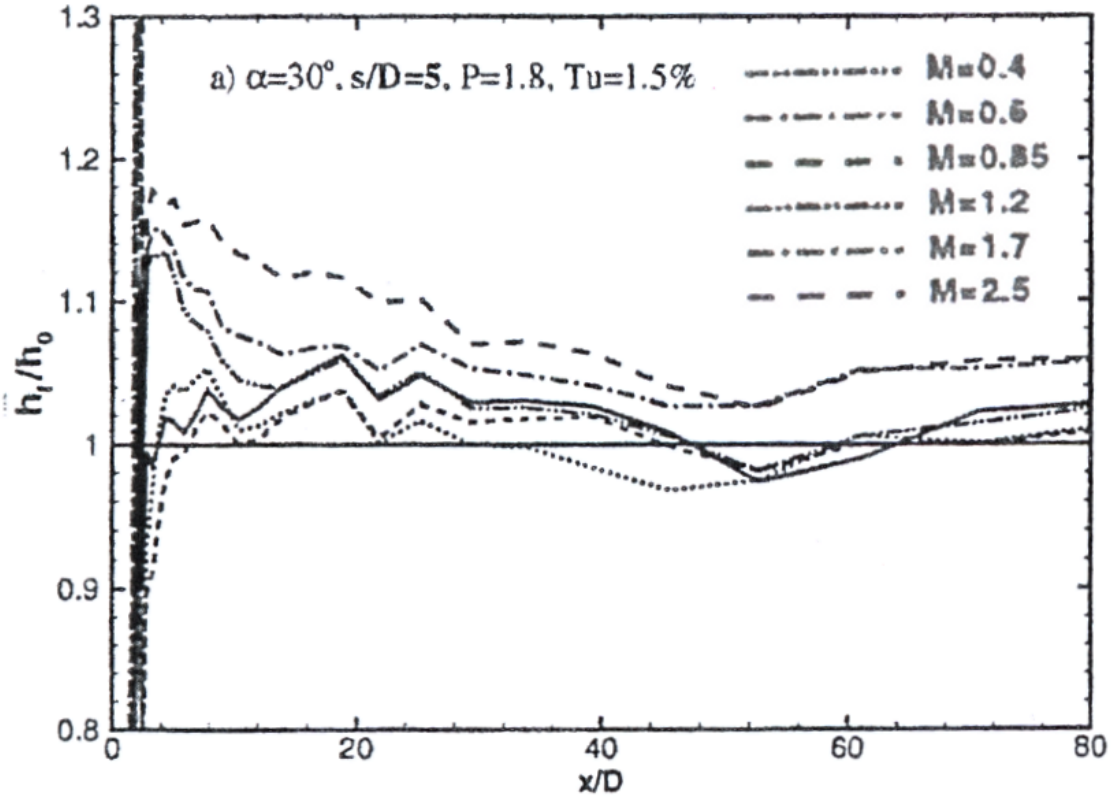

Figure 2.14: Laterally averaged heat transfer coefficient at wide hole pitch to diameter ratio from Baldauf and Schulz (2007).

Figure 2.14 shows the laterally averaged heat transfer coefficient with the same coolant ejection angle and flow conditions as shown in figure 2.6, but with a pitch to diameter ratio of 5. The heat transfer coefficient enhancement over the uncooled case for the large pitch to diameter ratio is lower than those from a geometry with a pitch to diameter ratio of 3. According to Baldauf and Schulz (2007), the lower heat transfer coefficient enhancement is due to the minimal jet to jet interaction downstream of the coolant holes and an increased proportion of undisturbed flow between the jets. However, unlike the case of the experiments with pitch to diameter

ratio of 3, the heat transfer coefficient appears to increase far downstream of the coolant holes. Also, with increasing mass flux ratio, an increase in heat transfer coefficient enhancement is observed. However, just downstream of the coolant holes, there is a greater enhancement of the heat transfer coefficient for mass flux ratios over 1.2. At these mass flux rates, Baldauf and Schulz (2007) observed jet lift off, which results in the mainstream becoming entrained downstream of the jets. This provides the heat transfer coefficient enhancement.

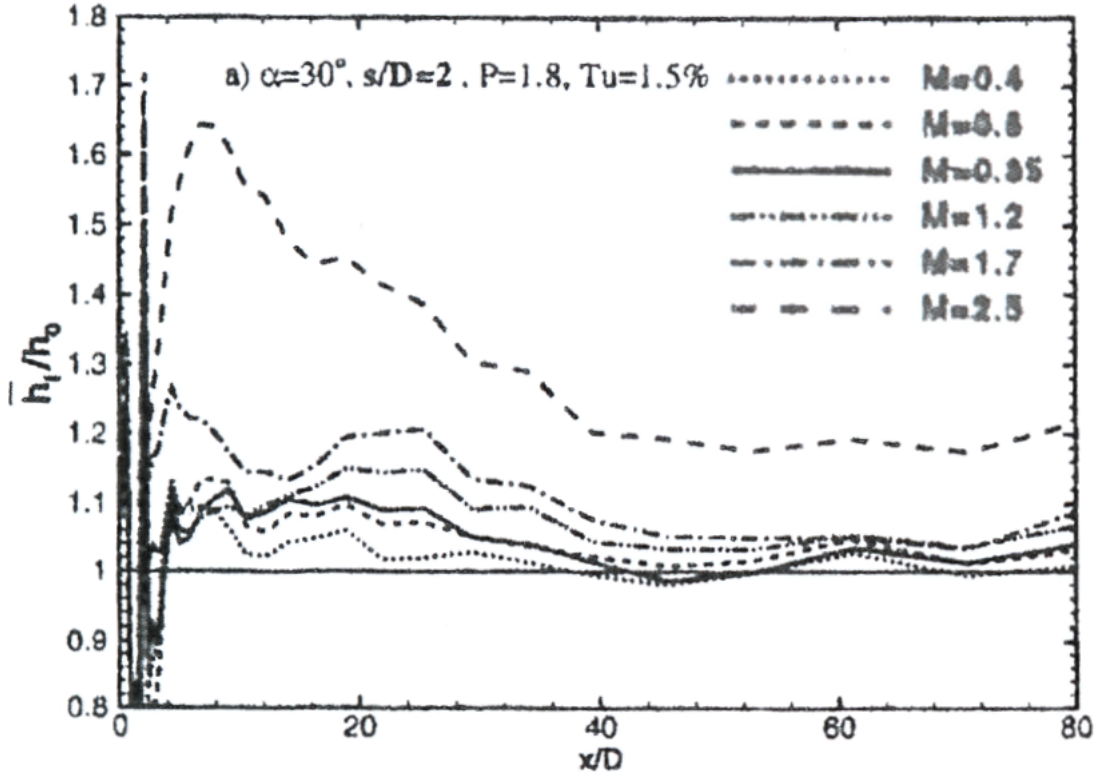

Figure 2.15: Laterally averaged heat transfer coefficient at a dense hole pitch to diameter ratio from Baldauf and Schulz (2007).

Figure 2.15 shows the laterally averaged heat transfer coefficient at a pitch to hole diameter ratio of 2. The coolant ejection angle and flow conditions are kept the same as the experimental data shown in figure 2.6. By comparing figures 2.6 and 2.15, it can be concluded that the effect of reducing the pitch to diameter ratio increases the heat transfer coefficient enhancement downstream of the coolant holes. Even with a moderate mass flux ratio of 0.6, the enhancement of the heat transfer coefficient is over 10% greater than the uncooled case. Far downstream, the heat transfer coefficient due to film cooling tends towards the uncooled value.

2.2.5 Effects of hole exit geometry

The modification of the hole exit geometry has been an effective way of improving the film effectiveness downstream of the coolant hole. These holes are commonly referred to as shaped holes or fan shaped holes. The shaping of the hole exit is obtained by introducing a lateral expansion.

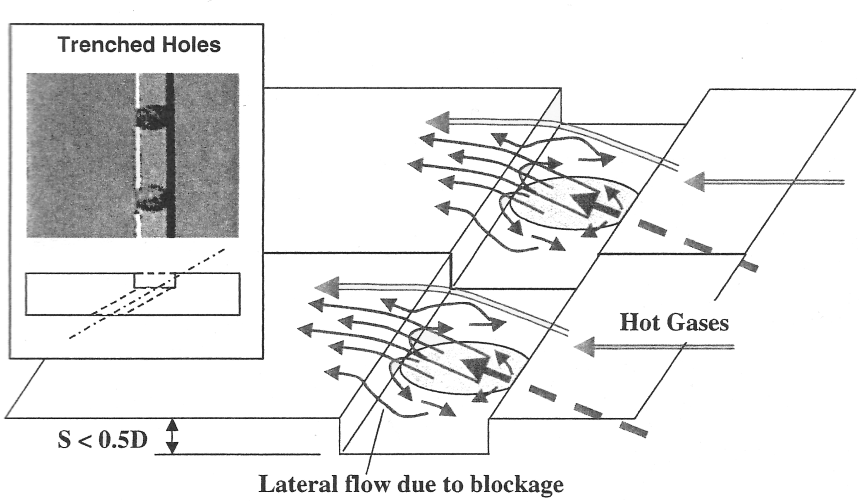

Figure 2.16: A sketch and figure showing film cooling hole embedded within the shallow trench. Reproduced from Bunker (2007a).

Another means of modification of the hole exit is to embed the exit in a shallow transverse trench. Figure 2.16 shows a sketch of such a shallow transverse trench with a cooling hole within it. Dorrington et al. (2007) studied various trench geometries including trench depth and discovered that "narrow trench" with $0.75d$ depth (S in figure 2.16) and "wide trench"with a depth of $1.0d$ produced comparable effectiveness levels with shaped hole configuration. Waye and Bogard (2006) also investigated 9 different shallow trench configurations, each with depth $0.5d$. They discovered that the critical characteristic was placing the downstream edge of the trench at the corresponding downstream edge of the coolant hole. Figure 2.17 shows the spatially averaged effectiveness levels for the baseline cylindrical holes, shaped holes, and narrow and wide trenches plotted against mass flux ratio.

For low mass flux ratios ($M < 0.5$), cylindrical holes perform better than any of the modified exit hole configurations. At these mass flux rates, the amount of coolant massflow exiting through the shaped holes may not be sufficient to fully cover the exit area, causing the freestream to interact more with the jets, resulting in lower effectiveness. As the mass flux ratio increases ($M > 0.5$), the effectiveness of the

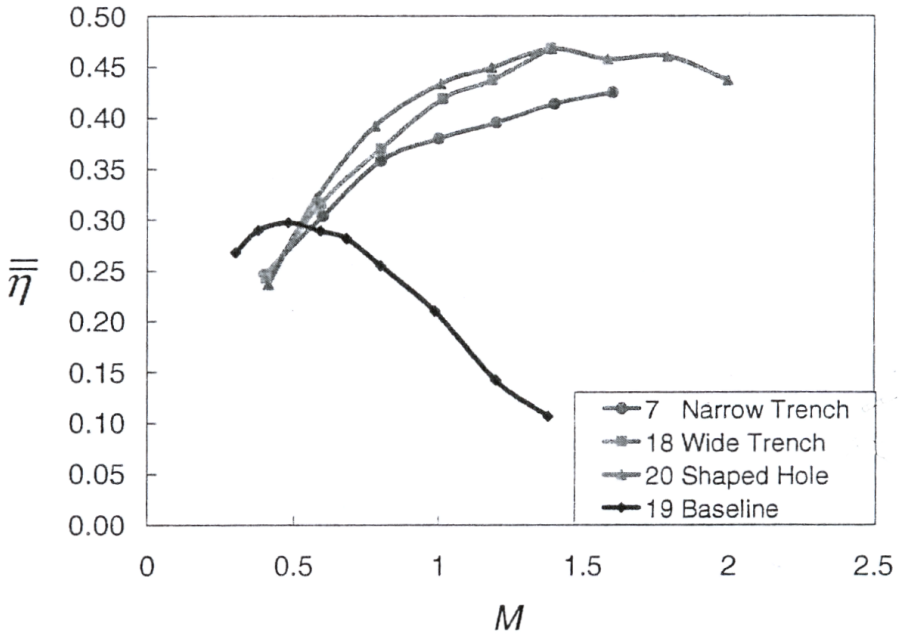

Figure 2.17: Spatially averaged film effectiveness for baseline cylindrical holes, shaped holes, and narrow and wide trenches (from Dorrington et al. (2007) and reproduced in Bogard (2007b))

cylindrical holes decreases due to the jet separation from the wall. However, the shaped hole, and narrow and wide trenches have rising effectiveness levels. It can be concluded that the hole exit modification inhibits the jet separation from the wall for large mass flux ratios.

The advantage of using trench geometries over shaped hole configurations is that the manufacturing costs are much less for the trench configurations compared with the shaped hole configurations. Furthermore the depth of the trench is shallow enough that the trench could be formed by the appropriate application of the thermal barrier coating.

2.2.6 Effects of coolant density ratio

The density ratio is defined as the ratio of the density of coolant to the density of mainstream. Sinha et al. (1991) tested film cooling effectiveness downstream of a single row of holes with varying density ratio of 1.2 to 2.0. He concluded that at low mass flux ratios the variation of film effectiveness with density ratio scaled well with mass flux ratio, whilst for higher mass flux ratio, effectiveness scaled well with momentum flux ratio.

The comprehensive study into film effectiveness by Baldauf et al. (2002) included the variation of density ratio from 1.2 to 1.8. Figure 2.18 shows the effectiveness levels from the study of Baldauf et al. (2002) plotted against mass flux ratio (a) and momentum flux ratio(b), spatially averaged over a range of $\frac{x}{d} = 2$ to 80.

From figure 2.18(a), it can be seen that the spatially averaged effectiveness for the two density ratio cases are similar for $M < 0.6$. However, for higher mass flux ratios, there is a huge deviation in the measured effectiveness. Looking at the spatially averaged effectiveness plotted against momentum flux ratio (figure 2.18(b)), the data show similar behaviour for both density ratios, whilst the maximum spatially averaged effectiveness value for density ratio of 1.2 is 10% lower than that for density ratio 1.8.

Looking closely at the laterally averaged distribution from Baldauf et al. (2002) (figure 2.19), for moderate mass flux ratio ($M = 0.6$), matching the mass flux ratio gives the same spatially averaged effectiveness. However, the peak effectiveness downstream of the hole is somewhat lower for density ratio of 1.2, compared with the density ratio of 1.8. If the velocity ratio (V_r) was matched instead of the mass flux ratio, it can be seen that the peak effectiveness would be lower, compared with the density ratio of 1.8.

For high mass flux ratios ($DR = 1.8, M = 1.0$), figure 2.19(b), matching the mass flux ratio gives a poor agreement for the laterally averaged effectiveness measurements. However, good agreement is obtained if the velocity ratio is matched.

Bogard (2007b) concludes that the correct scaling parameter must be used when scaling film cooling effectiveness from low to high density ratios.

Figure 2.20 shows the laterally averaged heat transfer coefficient measured on a flat plate with hole inclination angle of 30^o, and a pitch to diameter ratio of 3. The density ratio and turbulence intensity were kept constant at 1.2 and 1.5% respectively. Baldauf and Schulz (2007) state that the sharp rise in the heat transfer coefficient at $\frac{x}{D} = 2$ and the subsequent drop in heat transfer coefficient at $\frac{x}{D} = 3$ is due to the experimental setup and data reduction technique used in the measurement of the heat transfer coefficient. Comparing the data for density ratio of 1.8, shown in figure 2.6 with those shown in figure 2.20, it can be seen that the laterally averaged heat transfer coefficient is greater for higher density ratios and mass flux ratios. For high and low density ratios, up to mass flux ratio of 0.85, similar enhancement of the heat transfer coefficient is shown over the majority of the surface downstream of the coolant hole. With the lower density ratio and lower mass flux ratio, the heat transfer coefficient with cooling is seen to be lower than the unblown case just downstream of the coolant hole. This is not seen in the high density ratio experiments. In the low

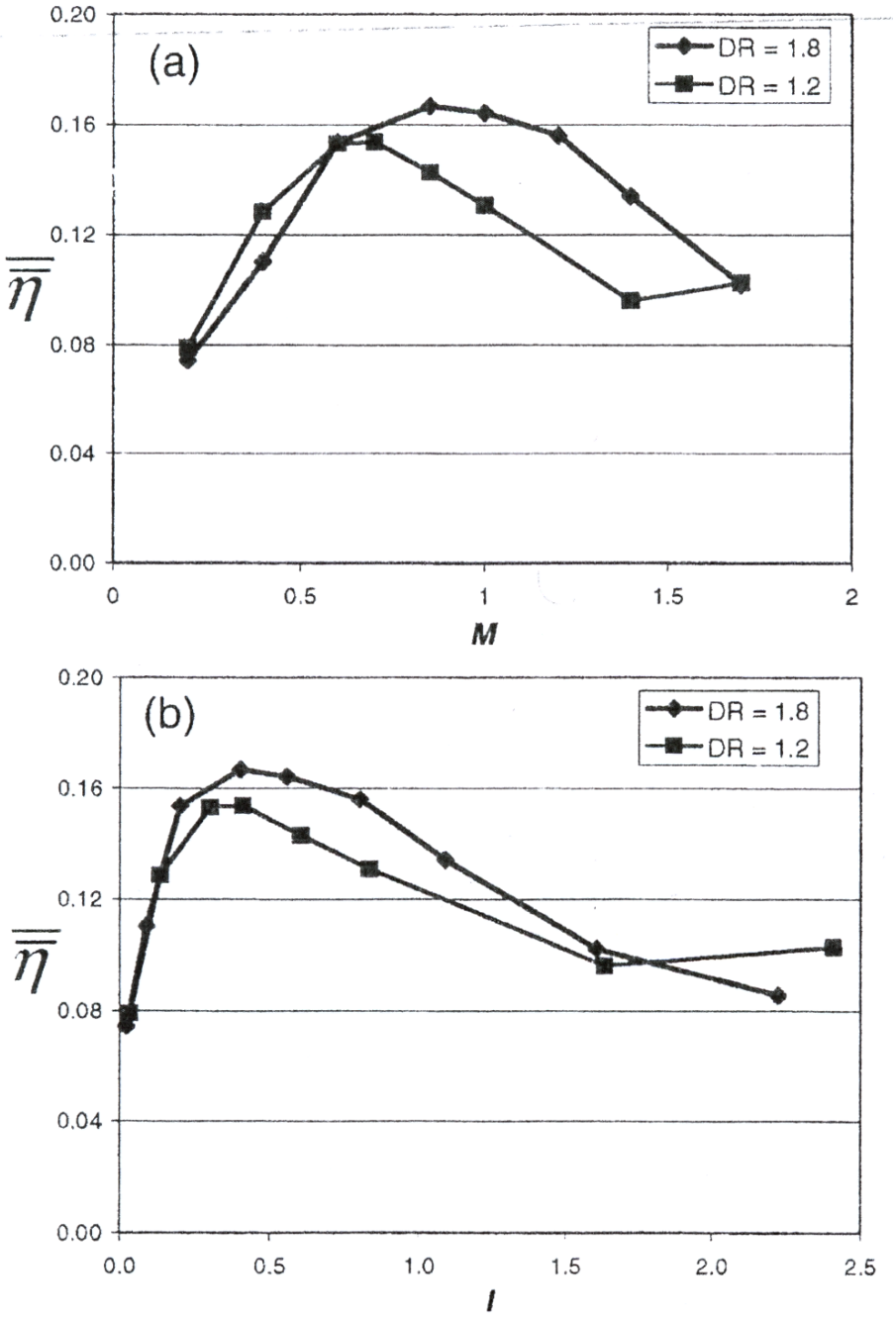

Figure 2.18: Spatially averaged film effectiveness for film cooling with density ratio of 1.2 and 1.8, plotted against (a) mass flux ratio M (b) momentum flux ratio I.

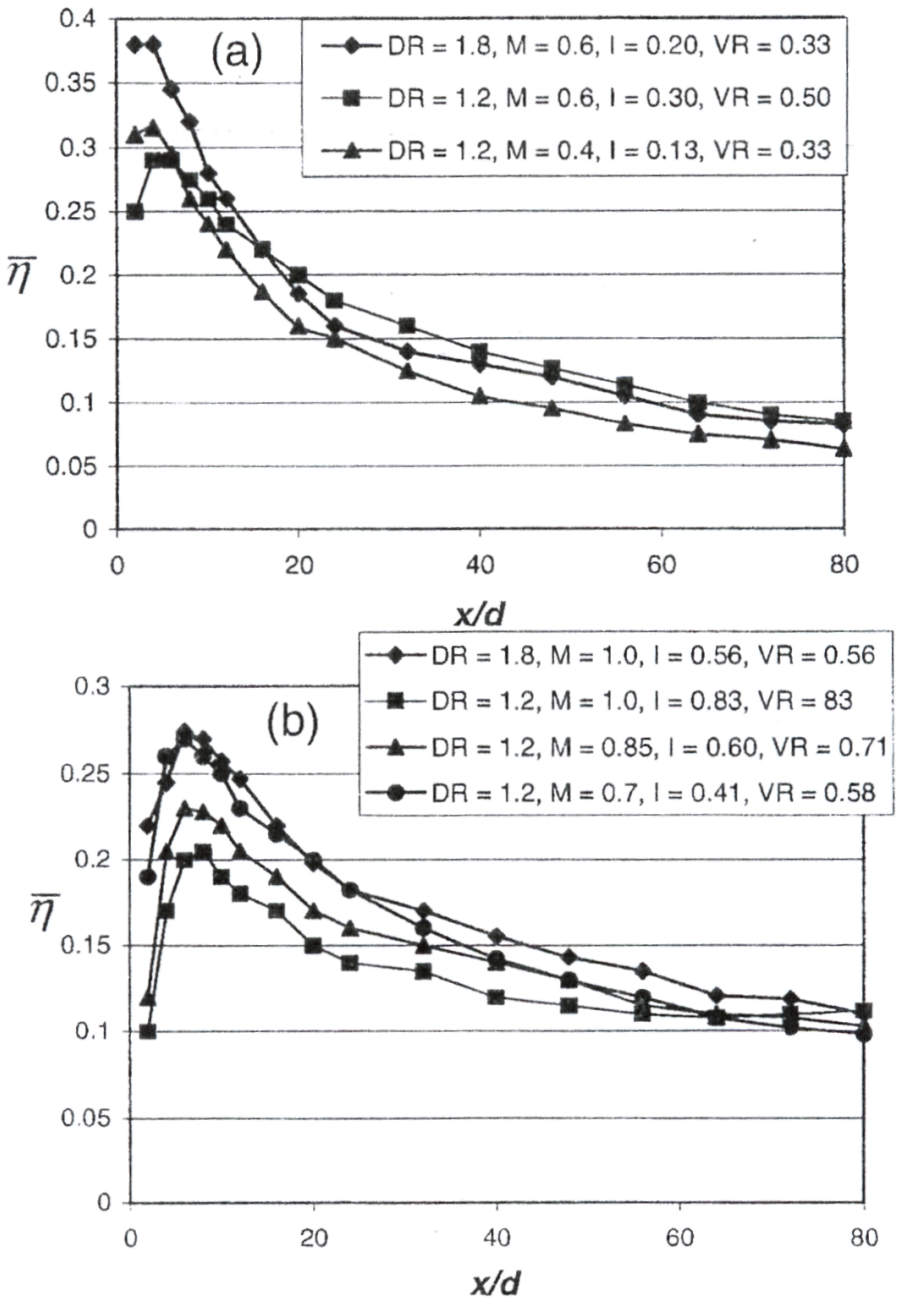

Figure 2.19: Laterally averaged film effectiveness for density ratio of 1.2 and 1.8 with matched M, I, and V_r at (a) low mass flux ratio (b) high mass flux ratio.

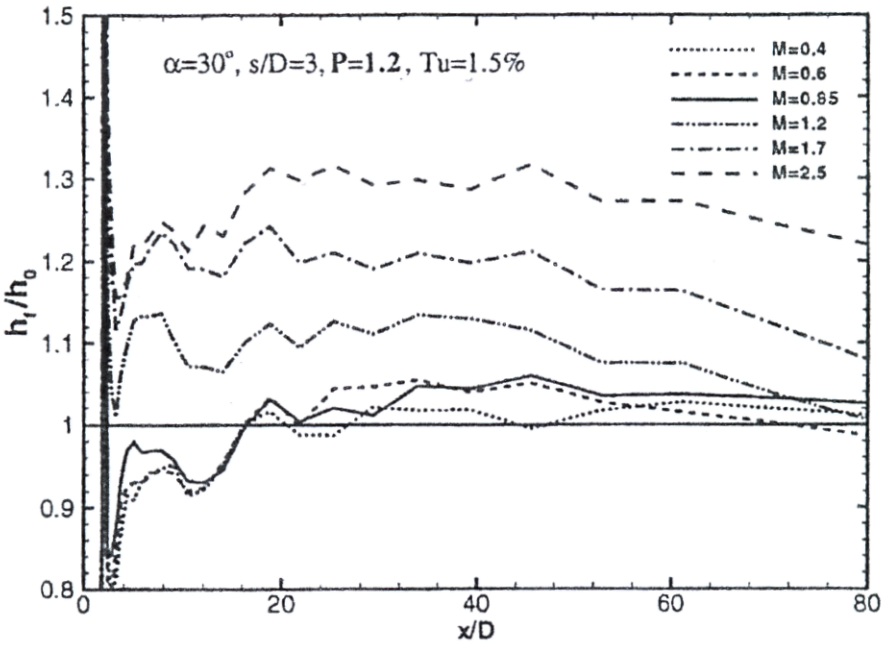

Figure 2.20: Laterally averaged heat transfer coefficient at density ratio of 1.2, hole inclination angle 30^o, pitch to diameter ratio of 3 and turbulent intensity of 1.5%. The data from Baldauf and Schulz (2007).

density ratio experiments, with increasing mass flux rate, the heat transfer coefficient enhancement increases, giving rise to about 30% enhancement at $\frac{x}{D} = 20$ and mass flux ratio of 2.5. As seen from figures 2.6 and 2.20, the enhancement of the heat transfer coefficient at high density ratio and high mass flux ratios are higher than those with low density ratio.

2.2.7 Effects of Reynolds number

Drost and Bolcs (1999) compared the film effectiveness on a simulated airfoil for a factor of three change in Reynolds number. The study used single and double rows of holes in the comparison. The study showed that the Reynolds number had a small to negligible effect on the measured film cooling effectiveness.

2.2.8 Effects of Mach number

Gritsch et al. (1998) and Liess (1975) completed experiments to study the effects of Mach number on film effectiveness. Gritsch et al. (1998) used a single row of cylindrical and shaped holes in the study with external Mach numbers of 0.3, 0.6 and 1.2. There was little difference in film effectiveness at Mach numbers of 0.3 and

0.6, but a slight increase in effectiveness levels for the cylindrical holes at external Mach number of 1.2. Liess (1975) found similar results from the studies conducted at external Mach number of 0.3, 0.6 and 0.9.

2.2.9 Effects of approach boundary layer

In an ideal uncooled turbine, the boundary layer is laminar near the leading edge, and turbulent at the trailing edge. Transition occurs in the region between the leading and trailing edge of the blade. Hence the boundary layer thickness of the approaching flow can be a fraction of the coolant hole diameter or be the same order of magnitude as the coolant hole. The study by Radomsky and Thole (2002) showed that the thickness of the boundary layer is affected by the freestream turbulence. In a simulated vane with a low freestream turbulence (0.6%), Radomsky and Thole (2002) found laminar boundary layers on most of the pressure and suction surface of the vane. For high mainstream turbulence (20%), a turbulent boundary layer was observed for most of the vane surface.

The study by Liess (1975) showed that there was very little change in the laterally averaged film effectiveness with varying boundary layer thickness, provided the ratio of boundary layer displacement thickness to hole diameter was less than 0.2. This result was confirmed by Drost and Bolcs (1999), where the approaching boundary layer displacement thickness was varied from 0.09 to 0.17. However, Drost and Bolcs (1999) did discover that the state of the boundary layer (laminar or turbulent), could have an effect on film effectiveness. Near the coolant hole, laminar boundary layers produced a 30% rise in laterally averaged film effectiveness compared with turbulent boundary layer for mass flux ratio from 0.3 to 1.5. Far downstream of the hole, there was only a slight increase in the laterally averaged film effectiveness for a laminar boundary layer.

2.2.10 Effects of freestream turbulence intensity

The effects of turbulence levels on the film effectiveness were measured by Schmidt and Bogard (1996) for streamwise oriented holes and Schmidt and Bogard (1997) for compound angled holes. The experiments were conducted on a flat plate with cylindrical holes inclined to the surface at 30^o, with pitch to diameter ratio of 6.5, and turbulence levels of 0.3%, 10% and 17%. The coolant density ratio was set to 2.0. Figure 2.21 shows a sample of the experimental data from Schmidt and Bogard (1996) and Schmidt and Bogard (1997).

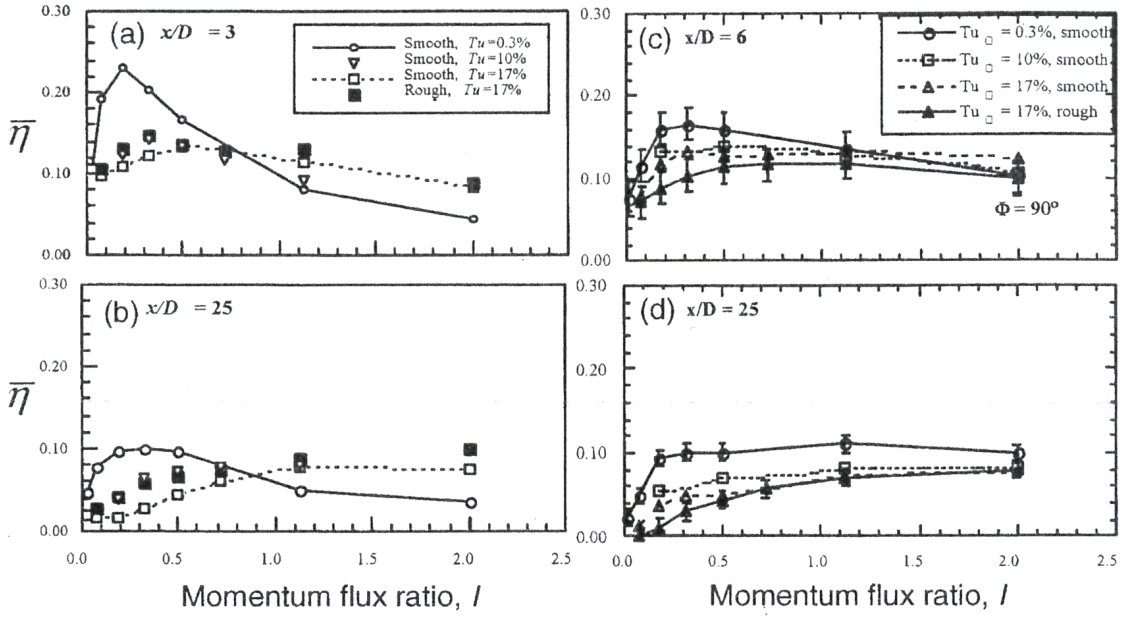

Figure 2.21: Effects of mainstream turbulence levels of 0.3%, 10%, and 17% on film effectiveness for streamwise directional holes at (a) $x/d = 3$, and (b) $x/d = 25$, and compound angled holes (c) $x/d = 6$ and (d) $x/d = 25$ (reproduced from Bogard (2007b)).

The data from the streamwise oriented hole show that for low momentum flux ratios (less than 0.8), there is a significant reduction in the laterally averaged film effectiveness with increasing turbulence intensity. However, for momentum flux ratios greater than 0.8, the low turbulence case produces laterally averaged effectiveness levels which are lower than the high turbulence cases. The low effectiveness at high momentum flux ratio and low freestream turbulence levels is due to the coolant jet separating from the surface. The increased turbulence causes some of the separated coolant to return to the surface, giving an elevated film effectiveness for high momentum flux ratios. Hence from the experiments, it can be seen that the maximum film effectiveness for high turbulence occurs at momentum flux ratio of 1.1. However, for low turbulence cases, the maximum film effectiveness occurs at momentum flux ratio of 0.2. Similar effects are seen for the compound angled film cooling experiments for momentum flux ratios less than 0.8. However, for the compound angled holes at higher momentum flux ratios, the laterally averaged effectiveness for the lower turbulence level case remains higher than the higher turbulence level conditions. This is due to the films not separating as much in the case of compound angles.

The study by Saumweber and Schulz (2007a) showed the effects of mainstream turbulence intensity on the heat transfer coefficient downstream of the cylindrical

coolant holes. Figure 2.22 shows the laterally averaged film cooling effectiveness downstream of a row of cylindrical coolant holes with varying mainstream turbulence intensities. The data were obtained at constant mainstream Mach number of 0.3

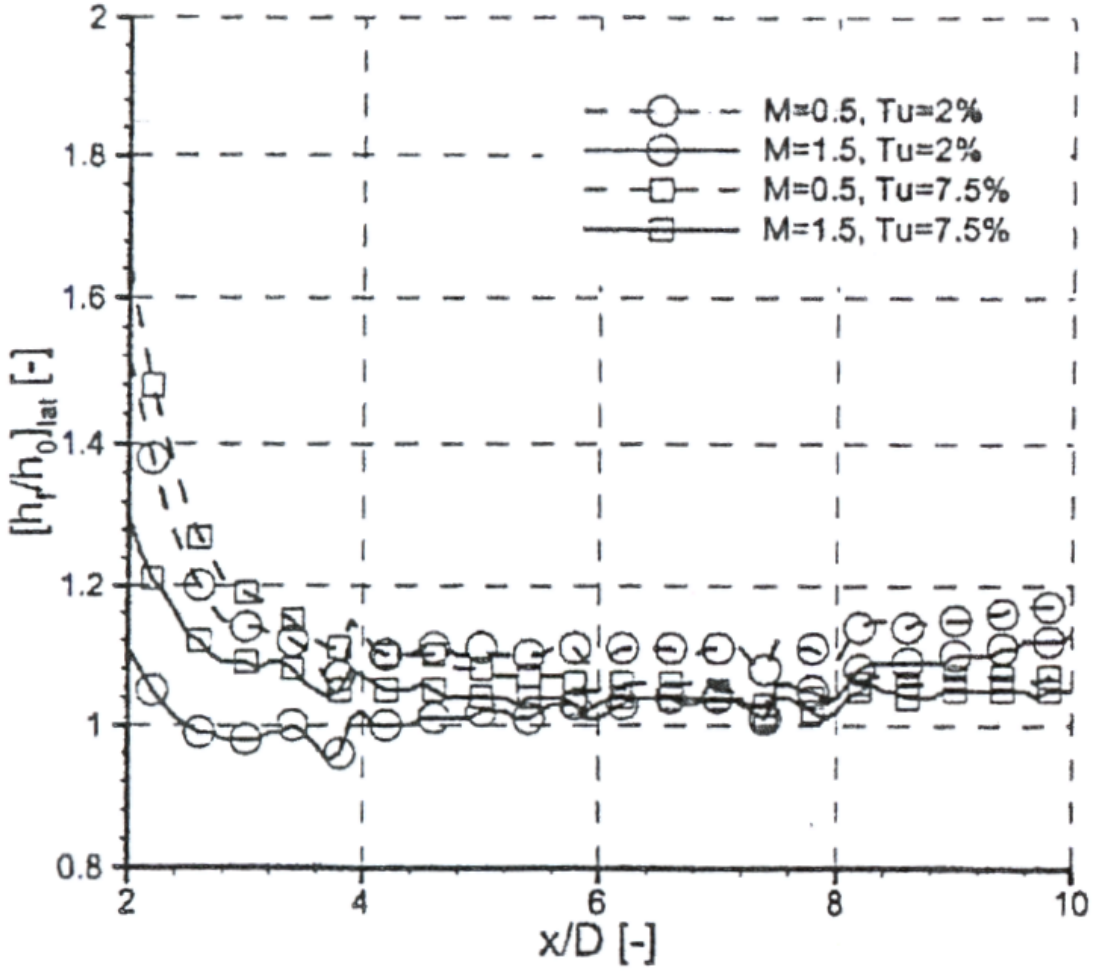

Figure 2.22: Laterally averaged heat transfer coefficients downstream of cylindrical holes at varying mainstream turbulence intensities. Data from Saumweber and Schulz (2007a)

Saumweber and Schulz (2007a) state that, with increasing turbulence intensity, the sensitivity of the heat transfer coefficient downstream of the coolant hole to the mass flux rate is reduced. This is observed from the experimental data shown in figure 2.22. The largest sensitivity in the heat transfer coefficient data is found at high mass flux ratios (mass flux ratio of 1.5) just downstream of the coolant hole. Saumweber and Schulz (2007a) state that the enhanced mixing of the coolant flow with the mainstream flow at high turbulence intensity causes the separation region to be reduced and the contact between the coolant and the wall to be intensified. This

results in a higher heat transfer coefficient downstream of the coolant wall compared with the lower turbulence intensity experiment.

2.3 Trailing edge cooling

As discussed in chapter 1, trailing edge film cooling poses a particularly challenging design problem. From an aerodynamic point of view, the trailing edge of a blade is designed to be as thin as possible. However, this conflicts with the manufacture of the requirement for cost effective cooling design. In a turbine blade the velocity of the mainstream, adjacent to the pressure surface, is lower than the velocity of the mainstream adjacent to the suction surface. Denton (1993) shows that ejecting coolant into a high speed mainstream causes an increase in entropy generation, resulting in increased losses. The increased aerodynamic losses due to film cooling ejection into a high velocity mainstream flow, for example in the case of late suction side film cooling, was experimentally shown by Jackson et al. (2000). For this reason, film cooling is not usually implemented on the late suction surface of the turbine blade, but primarily on the pressure surface or directly at the trailing edge.

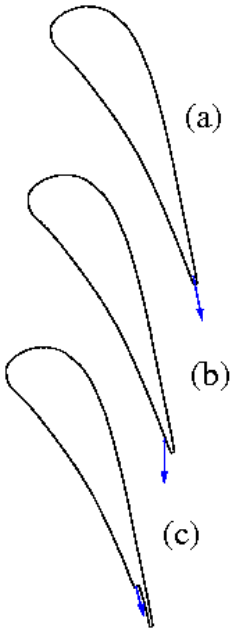

Figure 2.23: A sketch of the three common trailing edge cooling configurations. (a) Trailing edge ejection. (b) Pressure surface (upstream of trailing edge) ejection. (c) Pressure surface cutback ejection.

Figure 2.23 shows the three common methods of cooling the trailing edge. The blue arrows indicate the approximate ejection point of the coolant at or near the

trailing edges. The first method involves ejecting the coolant directly through the trailing edge (fig 2.23(a)). With this strategy, the trailing edge region is primarily cooled through internal cooling and some film cooling at the exit plane at the trailing edge. Film cooling at the trailing edge is achieved by using continuous or discrete slots, or discrete coolant holes. By having to incorporate the cooling mechanism at the trailing edge, the trailing edge would have to be thicker than an uncooled trailing edge. The second method is to use pressure side film cooling holes or slots just upstream of the trailing edge region (fig 2.23(b)) and the other, more state-of-the-art cooling concept, utilises a pressure side cutback (fig 2.23(c)). This cut-back is attained by casting the component with a shortened pressure side wall at the trailing edge with respect to the suction side wall. In the region between the two walls, a combination of pin fins, ribs and webs are used to achieve the required structural integrity of the blade and also to promote internal convective heat transfer. The above integral components also help to control the mass flow rate through the trailing edge.

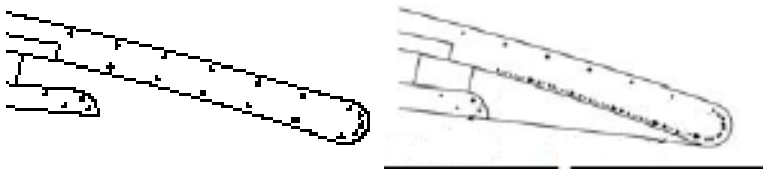

(a) "Gill" cutback trailing edge cooling configuration

(b) "Letter box" cutback trailing edge cooling configuration

Figure 2.24: "Gill" and "Letter box" trailing edge cutback configurations as defined in Fiala et al. (2008b).

,

Figure 2.24 shows two variants of the cutback trailing edge cooling configuration. Figure 2.24a shows the "Gill" cutback configuration, where the ribs and pin fins are located internally. Externally the trailing edge cutback appears as a continuous slot. Figure 2.24b shows the "Letter box" cutback configuration, where the internal ribs extend to the trailing edge. Due to these ribs, the trailing edge region does not present itself to the flow as a continuous slot, but as a number of discrete slots.

2.3.1 Aerodynamic measurements

There are numerous research reports of trailing edge ejection in which the associated losses and the film effectiveness have been studied. The early research focussed on

nozzle guide vane ejections in transonic cascades. Kapteijn et al. (1994) compared the aerodynamic performance of a transonic guide vane with coolant ejection at the trailing edge, as shown in figure 2.23(a), and a pressure surface near the trailing edge coolant ejection, as shown in figure 2.23(c). Kapteijn et al. (1994) concluded that the ejection at the pressure surface near the trailing edge causes high losses compared with ejection at the trailing edge. The vane configuration with coolant ejection through the trailing edge had a thicker trailing edge. The loss measurements of Kapteijn et al. (1994) did not take into account the total pressure of the coolant. It was also noted that, in subsonic conditions, the wakes for the pressure surface ejection mixed out faster than the wakes from coolant ejection at the trailing edge. At supersonic conditions, there was no appreciable difference. Mee (1992) compared the mixed out losses downstream in a transonic cascade with simple aerofoils having coolant ejection at the trailing edge, as in figure 2.23(a), and on the pressure surface, as in figure 2.23(b). The mixed out loss is defined as the ratio of the kinetic energy of the gas stream at the mixed out static pressure to that which can be obtained at the mixed out static pressure if the expansions from the inlet total conditions, of the mainstream and coolant, had been isentropic. Mee (1992) showed that there was no appreciable difference in the mixed out losses between the coolant ejection from the pressure surface and at the trailing edge. Mee (1992) also concludes that the experiments need to simulate the momentum flux ratios instead of the mass flux ratios when comparing losses from trailing edge region coolant ejection. By matching the momentum flux ratio and the mass flux ratio, the effects of the density ratio, between the mainstream and coolant, are also matched. Furthermore, the definition of the coolant total pressure could influence the comparison of the different coolant geometries.

Sieverding et al. (1994) also measured mixed out and total pressure losses downstream of a transonic nozzle guide vane with pressure surface slot trailing edge ejection, as shown in figure 2.23c. The conclusions from Sieverding et al. (1994) indicated that the coolant flow ejection does not produce any unusual wake flow patterns at the measurement plane. This was attributed to the rapid mixing of the mainstream with the coolant, as concluded by Kapteijn et al. (1994).

The subsonic cascade experiments of Uzol et al. (2001) showed the effects of cutback length, internal spanwise rib spacing and rib length on the discharge coefficients. The test plate simulated the coolant ejection from aerofoil as shown in figure 2.23(c). Uzol et al. (2001) concluded that the highest discharge coefficient was obtained for a cutback length, measured from the trailing edge to the pressure surface lip, to coolant

cavity height ratio of 2.4. Larger ratios (i.e. larger cutback lengths) result in smaller discharge coefficients when compared with ejection at the trailing edge, as shown in figure 2.23(a). This was attributed to high losses caused by interaction of the mainstream with the ejected coolant. It was also noted that, by having a small pitch to width ratio of ribs within the cutback cavity, comparable discharge coefficients with coolant ejection at the trailing edge were obtained. This fact was stated to be due to the coolant momentum flux at the exit plane having similar magnitude to the mainstream. Uzol and Camci (2001b) showed detailed Particle Image Velocimetry measurements conducted downstream of test blades with coolant ejection, as shown in figures 2.23(a) and (c). From the total pressure loss measurements in Uzol and Camci (2001b), it was concluded that, as the mass flux ratio increased, the total pressure loss decreased. This was due to the coolant stream filling the trailing edge wake downstream of the trailing edge. It was also observed that the total pressure increased at high mass flux ratios due to the high momentum coolant stream. It must be noted that, like Kapteijn et al. (1994), no account of the coolant total pressure was taken in the loss measurements.

Fiala et al. (2008b) compared the total pressure losses of two trailing edge cutback designs, with an uncooled blade in a low speed, large scale cascade. Again, when the losses were computed the coolant total pressure was not considered. The two trailing edge cutback coolant ejections were similar to that shown in figure 2.23(c) and figure 2.24 shows the two cutback configurations used in Fiala et al. (2008b). Figure 2.25 shows the total pressure loss downstream of the uncooled, "gill" cutback trailing edge and "letter box" cutback trailing edge configurations.

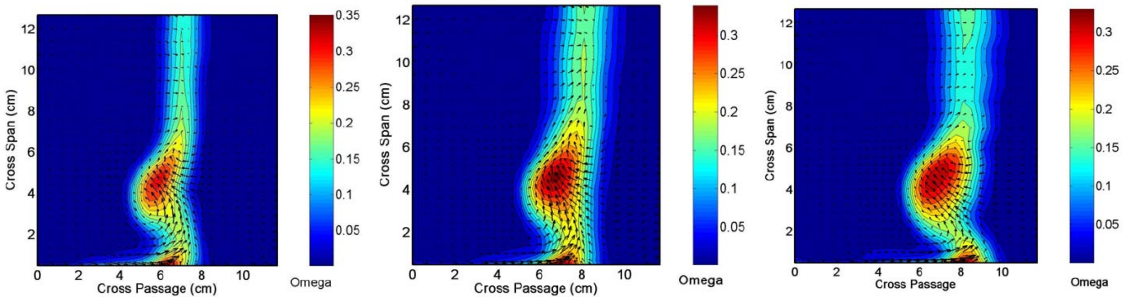

(a) Total pressure loss downstream of an uncooled blade

(b) Total pressure loss downsteam of "gill" cutback blade

(c) Total pressure loss downsteam of "letter box" cutback blade

Figure 2.25: Total pressure loss surveys reports in Fiala et al. (2008b).

The large loss core seen in figure 2.25a was attributed to the endwall loss core and was evident on all the total pressure loss surveys. Fiala et al. (2008b) observed that there was an incremental increase in the total pressure losses for the "gill" and "letter box" cutback trailing edge coolant ejections over the uncooled blade. However, of the two types of cutback, the "gill" trailing edge cutback had an incrementally larger loss of 0.2% compared with the "letter box" cutback trailing edge. Also, with increasing Reynolds number and mass flux ratio, the averaged total pressure loss was observed to decrease.

2.3.2 Heat transfer measurements

Fiala et al. (2008a) showed the heat transfer coefficient and adiabatic film effectiveness on cutback "gill" and "letter box" trailing edge cooling configurations, conducted in a large scale low speed cascade. The heat transfer measurements were conducted using steady state heat transfer method with the use of thermocouples. Fiala et al. (2008a) observed that the centreline adiabatic effectiveness levels, downstream of the cutback, on the pressure surface were similar for the two types of cutback configuration. The heat transfer coefficient was, however, slightly higher for the "gill" cutback cooling configuration. In the "letter box" cutback configuration, the adiabatic effectiveness on the rib (extending from the cutback to the trailing edge) top surface incline with the pressure surface was insensitive to external turbulence levels and mainstream Reynolds number, based on chord length. However, this adiabatic effectiveness was seen to increase with increasing mass flux ratio. The heat transfer coefficient on this surface was shown to be a function of the external Reynolds number. The rib side adiabatic effectiveness was observed to be high for low mass flux ratios and decreased with increasing mass flux ratio. The heat transfer coefficients on the rib side walls were seen to correlate with internal (coolant) and external (mainstream) Reynolds numbers.

Martini et al. (2003) report on experimental and numerical studies conducted on a low speed, large scale pressure surface cutback trailing edge cooling configuration, as shown in figure 2.23(c). The trailing edge configuration was not implemented on a blade within a cascade as in Fiala et al. (2008a), but on a flat plate. Figure 2.26a shows the experimental configuration of Martini et al. (2003). The cutback feature is stiffened by two rows of ribs, which have a pitch to rib width ratio of 2.0. As can be seen in figure 2.26a, the ribs have fillet radii at the edges. The heat transfer measurements were obtained using an infra red measurement technique. It was observed that the coolant jets, downstream of the cutback surface, coalesce into

two or three jets. Furthermore, the averaged peak adiabatic effectiveness downstream of the pressure surface cutback was no more than 0.82 for mass flux ratios from 0.55 to 1.10. This suggests that the mainstream is entrained with the coolant downstream of the cutback surface.

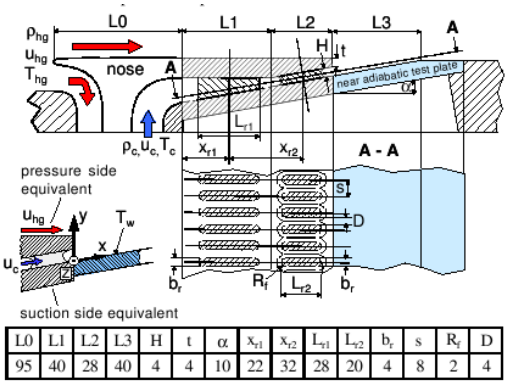

L0	L1	L2	L3	H	t	α	x_{r1}	x_{r2}	L_{r1}	L_{r2}	b_r	s	R_r	D
95	40	28	40	4	4	10	22	32	28	20	4	8	2	4

(a) Experimental setup of Martini et al. (2003)

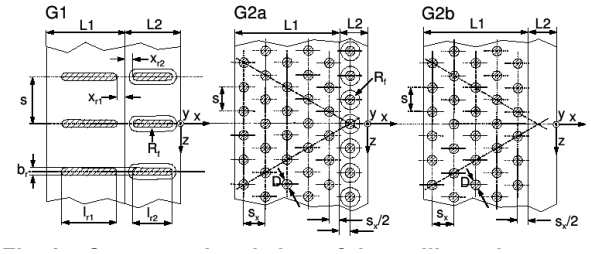

(b) Internal configuration of Martini et al. (2005)

Figure 2.26: The experimental setup of Martini et al. (2003) and new internal configuration of Martini et al. (2005).

Martini et al. (2003) concluded that the tested configuration, shown in figure 2.26a, is not a good solution for film cooling the trailing edge region due to the high temperature gradients caused by the coalescence of the coolant jets.

Martini et al. (2005) extended the research shown in Martini et al. (2003) to include pin-fin arrays, as shown in figure 2.26b, instead of the two rows of ribs, as shown in figure 2.26a. The research defined a core region where the adiabatic effectiveness was near unity, immediately downstream of the pressure surface cutback. The extent of this core region was seen to be a function of the internal arrangement of pin-fins and ribs.

Figure 2.27 shows the decay in adiabatic effectiveness downstream of the core region. It was observed by Martini et al. (2005) to be the same for all internal arrangements. Martini et al. (2005) concluded that this decay in adiabatic effectiveness downstream of the core region could be a function of the ratio of the cutback lip thickness to slot height, which was identical in all the experiments. The heat transfer coefficient far downstream of the cutback surface was observed to have a similar magnitude to that for a turbulent boundary layer on a flat plate. It was concluded that the mass flux ratio had a significant influence on the levels and trends of the heat transfer coefficient. Martini et al. (2005) also concluded that the internal pin-fin

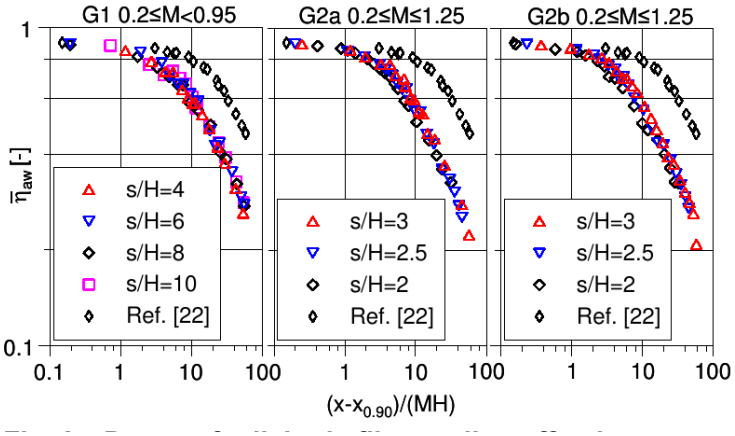

Figure 2.27: The decay of adiabatic effectiveness downstream of the core region for the three internal configurations shown in figure 2.26b. Data from Martini et al. (2005).

and rib arrangements had an influence on the heat transfer coefficient up to a length from the cutback length to slot height distance of 5.0.

2.4 Conclusions

For conventional pressure surface film cooling via discrete film cooling holes, from the literature the following can be identified as measures that would achieve better effectiveness downstream of the ejection plate.

1. A length of coolant hole to diameter ratio greater than 5.0.
2. A shallow angle of inclination, to achieve near tangential ejection onto the pressure surface.
3. Inclusion of a compound angle.
4. A small pitch to diameter ratio of the coolant holes, such as 2.0.

In the current study, the conventional (datum) pressure surface ejection incorporates the above findings. The dimensions of the datum cooling configuration are listed in table 4.2.

There have been numerous studies of the aerodynamics and heat transfer of pressure surface cutbacks of "gill" and "letter box" configurations. In the aerodynamic studies of Fiala et al. (2008b) it was found that the cutback configurations of "gill" and

"letter box" produced only an incremental change in the total pressure losses, with the losses from the "gill" configuration being slightly greater than the "letter box" configuration. In the heat transfer studies of Martini et al. (2005), it was shown that the internal configurations greatly affected the adiabatic effectiveness downstream of the coolant exit plane.

However, in the literature, there has been no research into a pressure side cutback, which is machined from a conventional blade onto a pressure surface near the trailing edge, and fed via discrete coolant holes. The coolant holes have the same configuration as the conventional (datum) trailing edge ejection, but benefit from having the coolant ejection plane shielded from the mainstream, as in the "gill" and "letter box" cutback configurations.

The current study aimed to provide a comparison of the aerodynamic and heat transfer performance of such a configuration against a "letter box" trailing edge cutback configuration and a conventional discrete coolant hole pressure ejection configuration.

Chapter 3

CFD prediction of discrete film cooling

3.1 Computational Fluid Dynamics

In computational fluid dynamics (CFD), the three fundamental governing equations of fluid flow are solved. These fundamental governing equations are

1. Conservation of mass

$$\frac{\partial \rho}{\partial t} + \nabla \cdot (\rho \mathbf{V}) = 0 \tag{3.1}$$

2. Newton's second law (momentum equation)

$$\frac{\partial (\rho u)}{\partial t} + \nabla \cdot (\rho u \mathbf{V}) = -\frac{\partial P}{\partial x} + \frac{\partial \tau_{xx}}{\partial x} + \frac{\partial \tau_{yx}}{\partial y} + \frac{\partial \tau_{zx}}{\partial z} + \rho f_x \tag{3.2}$$

$$\frac{\partial (\rho v)}{\partial t} + \nabla \cdot (\rho v \mathbf{V}) = -\frac{\partial P}{\partial y} + \frac{\partial \tau_{xy}}{\partial x} + \frac{\partial \tau_{yy}}{\partial y} + \frac{\partial \tau_{zy}}{\partial z} + \rho f_y \tag{3.3}$$

$$\frac{\partial (\rho w)}{\partial t} + \nabla \cdot (\rho w \mathbf{V}) = -\frac{\partial P}{\partial z} + \frac{\partial \tau_{xz}}{\partial x} + \frac{\partial \tau_{yz}}{\partial y} + \frac{\partial \tau_{zz}}{\partial z} + \rho f_z \tag{3.4}$$

3. Conservation of energy

$$\begin{aligned} \frac{\partial}{\partial t}\left[\rho\left(e + \frac{V^2}{2}\right)\right] + \nabla \cdot \left[\rho\left(e + \frac{V^2}{2}\right)\mathbf{V}\right] = \rho \dot{q} + \frac{\partial}{\partial x}\left(k\frac{\partial T}{\partial x}\right) \\ + \frac{\partial}{\partial y}\left(k\frac{\partial T}{\partial y}\right) + \frac{\partial}{\partial z}\left(k\frac{\partial T}{\partial z}\right) - \frac{\partial (up)}{\partial x} - \frac{\partial (vp)}{\partial y} - \frac{\partial (wp)}{\partial z} + \\ \frac{\partial (u\tau_{xx})}{\partial x} + \frac{\partial (u\tau_{yx})}{\partial y} + \frac{\partial (u\tau_{zx})}{\partial z} + \frac{\partial (v\tau_{xy})}{\partial x} + \frac{\partial (v\tau_{yy})}{\partial y} + \frac{\partial (v\tau_{zx})}{\partial z} + \\ \frac{\partial (w\tau_{xz})}{\partial x} + \frac{\partial (w\tau_{yz})}{\partial y} + \frac{\partial (w\tau_{zz})}{\partial z} + \rho \mathbf{f} \cdot \mathbf{V} \end{aligned} \tag{3.5}$$

The above equations are derived for a fluid element in a three dimensional Cartesian flow field. The vector $\mathbf{V} = u\mathbf{i} + v\mathbf{j} + w\mathbf{k}$ denotes the velocity of the fluid particle with components u, v, w and the fluid density is ρ. Equations 3.1 to 3.5 describe the instantaneous, viscous, unsteady, compressible flow field. Equations 3.2 to 3.4 are known as the Navier-Stokes equations. In the modern CFD literature (J. D. Anderson (1995)), the *Navier-Stokes equations* is taken to refer to the complete set of viscous flow equations, namely the continuity, momentum and energy equations shown above.

The *Navier-Stokes equations* are coupled nonlinear partial differential equations, and hence there is no general analytical solution (J. D. Anderson (1995)). In direct numerical simulations (DNS), the above equations are solved numerically for the complete flow field. All turbulent eddy structures of the viscous flow field are resolved. This is a computationally expensive process and even with modern advances in computing power, only very simple flow fields can be solved using DNS.

When solving flow fields of engineering interest, the instantaneous turbulent flow variables, such as the velocity components, can be decomposed into a time mean value and a fluctuating value. Taking the velocity component $u = \overline{u} + u'$, $v = \overline{v} + v'$, $w = \overline{w} + w'$ and $P = \overline{P} + P'$, the momentum equation in the x direction can be written as

$$\begin{aligned}\frac{\partial(\rho\overline{u})}{\partial t} + \nabla \cdot (\rho\overline{u}\mathbf{V}) = &-\frac{\partial\overline{P}}{\partial x} + \left[\frac{\partial\tau_{xx}}{\partial x} + \frac{\partial\tau_{yx}}{\partial y} + \frac{\partial\tau_{zx}}{\partial z}\right] \\ &- \left[\frac{\partial(\rho\overline{u'^2})}{\partial x} + \frac{\partial(\rho\overline{u'^2})}{\partial x} + \frac{\partial(\rho\overline{u'^2})}{\partial x}\right] \end{aligned} \tag{3.6}$$

Similar terms can be derived for the terms in y and z directions. The continuity and energy equations can also be re-written using the time mean values and fluctuating values of the scalar and vector fields. These equations are collectively known as the Reynolds Averaged Navier-Stokes equations (RANS). The additional terms, such as those in the final brackets on the right hand side of equation 3.6, are known as the Reynolds stresses and need to be solved. The Reynolds stresses are however usually modelled using the *Boussinesq assumption.* In this assumption, the Reynolds stresses are assumed to be linked to the velocity gradient of the flow field via the turbulent viscosity. There are numerous turbulence models used in engineering applications, from the one equation models, such as the Spalart-Allmaras turbulence model, to the many variants of the two equation k-ϵ and k-ω turbulence models.

The one equation Spalart-Allmaras model was designed specifically for aerospace applications involving wall bounded flows. In this turbulence model, the turbulence viscosity, which is used to derive the Reynolds stresses, is modelled. The length scale, related to the local shear layer thickness is not computed (Fluent^{TM} (1995)). The implementation of the model in the commercial CFD code Fluent^{TM}includes a wall function, so that a fine mesh resolution is not required near the wall. However, if a fine grid is used near the wall, the viscous region of the boundary layer in the vicinity of the wall is properly resolved.

The simplest of two equation turbulence models, is the standard k-ϵ model, proposed by Launder and Spalding (1972). By the solution of two separate equations, the turbulent velocity and length scales are independently determined. The k-ϵ model is a semi-empirical model. Fluent^{TM} (1995) provides three implementations of the k-ϵ model, namely, the standard k-ϵ model, the Re-Normalisaton Group (RNG) k-ϵ model and the realisable k-ϵ model. The RNG k-ϵ model uses a rigorous statistical technique called renormalisation group theory (Fluent^{TM} (1995)) and was proposed by Yakhot and Orszag (1986). The RNG theory provides an analytical formula for the turbulent Prandtl number, opposed to the standard model, where a constant value is used. The RNG model is purported to provide enhanced accuracy for highly swirling flows. The realisable k-ϵ model was proposed by Shih et al. (1995) and is meant to satisfy certain mathematical constraints on the Reynolds stresses, consistent with the physics of turbulent flows. The model is able to predict the spreading rate of planar and rounded jets more accurately than the standard k-ϵ model.

The standard k-ω model, is another two equation turbulence model implemented in Fluent^{TM}and is based on the Wilcox (1998) k-ω turbulence model. The implemented model incorporates modifications for the low-Reynolds number effects, compressibility, and shear flow spreading. The standard model is able to predict the free shear flow spreading rates, which are in close agreement with experiments for mixing layers, plane, round and radial jets. Fluent^{TM} (1995) claims the model is best suited for wall bounded flows and free shear flows. The shear-stress transport (SST) k-ω model, proposed by Menter (1994), is a variation of the standard k-ω model. The model effectively blends the formulation of the k-ω model in the near wall region with a variation of the k-ϵ model away from the wall. To achieve this variation, the k-ϵ model is converted into a k-ω formulation. The transformed k-ϵ model and the k-ω model are multiplied by a blending function and added together. This blending function is designed to activate the k-ω model near the wall and the transformed k-ϵ model away from the wall. It is stated in the Fluent^{TM} (1995) user guide, that the

k-ω SST model gives favourable results for flows with adverse pressure gradients and flows with transonic shock waves.

3.2 Literature survey of film cooling predictions using CFD

Many comparisons of film cooling effectiveness and heat transfer coefficient predictions with experimental data using a wide variety of turbulence models can be found in the literature. Due to the emphasis on different criteria of film cooling in the literature, there are many recommendations of different turbulence models. Furthermore, many of the studies focussed on a simple film cooling configuration, specifically a single coolant hole in a flat plate. Most of these geometries were discretized using structured hexahedral elements. Only a few examples can be found in the literature, that show predictions of film cooling performance using pure tetrahedral meshes. The earliest systematic methodology for predicting film cooling effectiveness downstream of a coolant hole, using an unstructured tetrahedral mesh, was presented by Walters and Leylek (1997). Their study proposed four critical steps necessary to predict film cooling performance downstream of a coolant hole. They were:

1. Accurate geometrical model of the physical problem.
2. A good quality grid.
3. Use of higher order discretisation scheme.
4. An effective turbulence model.

Walters and Leylek (1997) employed the above steps to predict the film effectiveness downstream of a row of coolant holes, using the k-ϵ turbulence model with standard wall functions and second order discretisation. In their study, the effectiveness levels downstream of the holes, along the centreline of the coolant hole was over predicted when compared with the experimental data, whilst the laterally averaged effectiveness was under predicted. The laterally averaged effectiveness, however, agreed closely to experimental values far downstream of the coolant hole for higher blowing rates.

Na et al. (2006) predicted film cooling effectiveness on a flat plate using the realisable k-ϵ model, the k-ω shear stress transport (SST) model and the Spalart-Allmaras (SA) turbulence model. Wall functions were not used in conjuction with the above

mentioned turbulence models. The study found that the SST model best predicted the laterally averaged effectiveness, whilst the realisable k-ϵ model best predicted the centreline effectiveness.

Harrison and Bogard (2008) used three turbulence models to predict the heat transfer coefficient enhancement and adiabatic effectiveness downstream of a coolant hole. The three turbulence models chosen were the realisable k-ϵ model, the standard k-ω model, and the Reynolds stress model. All the models were used without wall functions. The study only modelled half of a coolant hole, utilising the symmetry boundary condition to obtain the flow and thermal parameters downstream of a complete coolant hole. From the predictions of Harrison and Bogard (2008), all the turbulence models over predicted the centreline adiabatic effectiveness, whilst the standard k-ω model showed the best agreement for the laterally averaged effectiveness. All three turbulence models accurately predicted the heat transfer coefficient downstream of the coolant hole.

In the current study, four turbulence models were used by the author to predict the film cooling effectiveness and heat transfer coefficient enhancement downstream of a row of coolant holes. No symmetry boundary conditions were employed in these simulations and the full experimental domain was modelled. Two types of meshes, one structured hexahedral and the other, unstructured tetrahedral, were used to describe the fluid domain. Furthermore, the simulations were conducted with and without the use of wall functions.

3.3 Description of the experimental data

The film cooling experimental data described in this section were from the Saumweber et al. (2000). The experimental data were used to refine the CFD technique to predict the film effectiveness and heat transfer coefficient downstream of the coolant holes. The refined CFD method was applied by the author to predict the trailing edge film cooling effectiveness and heat transfer coefficient, described in section 8.

Figure 3.1 shows the experimental test section of the high pressure, high temperature test facility situated at the *Institute für Thermische Strömungsmaschinen*, in the University of Karlsruhe. The experiments were used by Schultz and his co-workers to establish the effects of engine representative turbulence intensities and length scales on the film cooling effectiveness and heat transfer coefficient downstream of cylindrical coolant holes, inclined at 30^o with the mainstream direction. The holes have a length to diameter ratio of 6 and pitch to diameter ratio of 4.

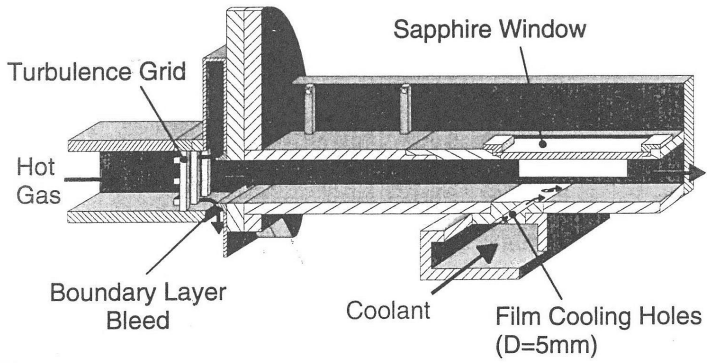

Figure 3.1: Experimental film cooling test section, reproduced from Saumweber et al. (2000)

The experimental test facility has the capability to test the effects of coolant cross flow on the film cooling effectiveness. However, for the current validation exercise, the coolant chamber was blocked off at the exit, creating a coolant plenum. The mainstream section has a rectangular cross section of $90mm \times 45mm$. The plenum section has a rectangular cross section of $75mm \times 35mm$. The mainstream boundary layer is bled off at the leading edge of the test section, as shown in figure 3.1, so as to restart the boundary layer at that point, and establish a well defined turbulent boundary layer just upstream of the coolant holes. The general operating conditions for the experiments are given in table 3.1.

Mainstream Mach number	0.3
Mainstream Reynolds number based on hole diameter	2.5×10^4
Blowing ratio	0.5
Mainstream total temperature	540 K
Coolant to mainstream total temperature ratio	0.59

Table 3.1: Experimental operating conditions for figure 3.1

Different sizes of turbulence grids were used in the experiment to understand the effects of turbulence intensity and length scale on the film cooling performance. However, for the current validation performed by the present author, the film effectiveness and heat transfer coefficient data for a turbulence intensity of 3.6% and a turbulent length scale of 2.7D were chosen. Figure 3.2 shows the experimental data reproduced from Saumweber et al. (2000).

The distance, x, indicated in figure 3.2 was measured from the downstream edge of the coolant holes. All the data reported in Saumweber et al. (2000) begin at $\frac{x}{D} = 2$. This was due to practical constraints associated with the flat plate inserts

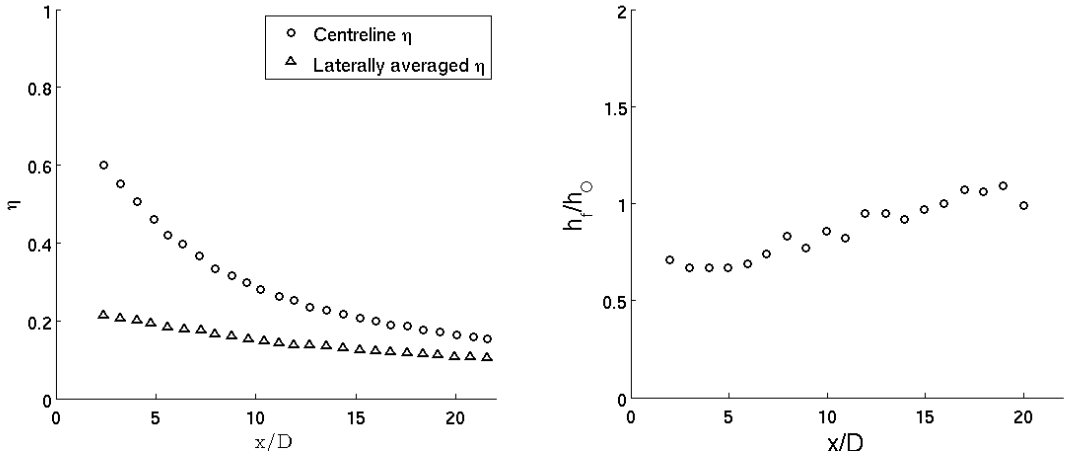

(a) Film effectiveness data Saumweber et al. (2000))

(b) Film heat transfer coefficient enhancement data Saumweber et al. (2000))

Figure 3.2: Experimental data of film effectiveness and heat transfer coefficient at turbulence intensity of 3.6% and length scale of 2.7D.

used to determine the adiabatic effectiveness and heat transfer coefficient data. To obtain the adiabatic temperature downstream of the coolant holes, the flat plate insert was manufactured from low conductivity thermoplastic material, TECAPEEK. To measure the heat transfer coefficient, the flat plate insert was machined from Titanium-Aluminium alloy. The latter test plate also included a water cooled heat exchanger to ensure that the surface of the test plate was isothermal.

For both the film cooling effectiveness and heat transfer coefficient measurements, the surface temperature was obtained using an infrared camera system. The surface temperature of the heat transfer test plate was mapped onto a finite element simulation to obtain the three dimensional surface heat flux. This was used to compute the heat transfer coefficient.

The film cooling effectiveness was computed by Saumweber et al. (2000) using equation 3.7.

$$\eta = \frac{T_{rec,m} - T_{aw}}{T_{rec,m} - T_c} \tag{3.7}$$

To determine the heat transfer coefficient, the superposition approach of film cooling, as described in Forth and Jones (1986), was used. The convective heat flux incident on the flat plate insert can be given by equation 3.8.

$$\dot{q}_f = h_f \cdot (T_{aw} - T_w) \tag{3.8}$$

The convective heat flux can also be given by equation 3.9

$$\dot{q}_f = h(\theta) \cdot (T_{rec,m} - T_w) \tag{3.9}$$

In equation 3.9, the heat transfer coefficient $h(\theta)$ is a function of the non dimensional temperature θ, given by equation 3.10.

$$\theta = \frac{T_{rec,m} - T_c}{T_{rec,m} - T_w} \tag{3.10}$$

Forth and Jones (1986) showed that the heat transfer coefficient $h(\theta)$ varied linearly with non dimensional temperature, θ. Since the convective heat flux incident on the surface given by equations 3.9 and 3.8 is the same, the equations can be combined to give:

$$h(\theta) = h_f \left(1 - \eta_{iso,adb}\theta\right) \tag{3.11}$$

$\eta_{iso,adb}$ is defined using equation 3.12.

$$\eta_{iso,adb} = \frac{T_{rec,m} - T_{iso,adb}}{T_{rec.m} - T_c} \tag{3.12}$$

The isothermal-adiabatic wall temperature, $T_{iso,adb}$, is the temperature at a location on an isothermal wall, where the heat flux onto the surface, at that point, equals zero. However, the heat flux onto the surface at locations adjacent to this point does not have to equal zero. The adiabatic wall temperature, T_{aw}, shown in equation 3.7, is the temperature at a point on the surface of an adiabatic wall. The heat flux at adjacent points must also equal zero. It must be noted that the isothermal-adiabatic effectiveness, $\eta_{iso,adb}$, is different from the effectiveness computed using equation 3.1. The difference is attributed to the temperature of the approaching boundary layer, upstream of the coolant holes. A detail explanation is included in section 3.5.2. Saumweber et al. (2000) does not account for the difference in the fluid temperatures within the oncoming boundary layer in the effectiveness and heat transfer coefficient measurements. In the measurement of the film heat transfer coefficient, Saumweber et al. (2000) assumes that the $\eta_{iso,adb} = \eta$.

3.4 CFD approach

3.4.1 Geometry and meshing strategy

Figure 3.3 shows the two computational domains used to validate the film effectiveness and heat transfer coefficient prediction methodology. Note that these sim-

ulations are of the Karlsruhe test section. The domains were created using the Ansys™ ICEMCFD™ meshing package. The dimensions for the two computation domains are shown in table 3.2.

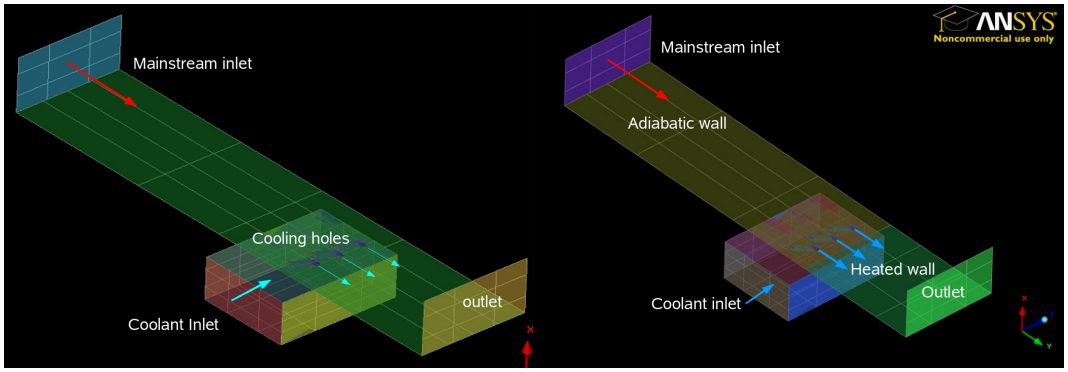

(a) Adiabatic wall computational domain (b) Isothermal wall computational domain

Figure 3.3: Computational domain for the adiabatic and isothermal wall predictions

Freestream tunnel width	90 mm
Freestream tunnel height	45 mm
Freestream tunnel length	400 mm
Plenum tunnel width	75 mm
Plenum tunnel height	35 mm
Plenum tunnel length	100 mm
Coolant hole diameter	5 mm

Table 3.2: Dimensions of test section

As stated in section 3.3, most film cooling studies used structured hexahedral meshes in the prediction of film cooling performance. In the current study, film cooling performance was predicted using both tetrahedral and hexahedral meshes. The adiabatic wall computation domain, shown in figure 3.3a, was discretised using tetrahaedral and hexahedral mesh elements. For the tetrahedral elements, the Octree algorithm, implementation in ICEMCFD™ was used. For the hex mesh, the ICEMCFD™ hexa meshing module was used. The isothermal wall computation domain, shown in figure 3.3b, was meshed only with tetrahedral elements. The aim of the current exercise was to establish the suitability of using tetrahedral meshes for the prediction of film cooling effectiveness.

To capture the boundary layer near the wall, boundary layer meshes were incorporated during the meshing process of the computational domains. To see the

difference in the predicted film effectiveness with and without wall functions, the initial cell adjacent to the wall was placed so as to have a wall $30 < Y^+ < 60$ and $Y^+ = 1$ respectively. The definition of Y^+ is given in equation 3.13. In equation 3.13, y represents the centroid of the first element from the wall surface. In the $Y^+ = 1$ and $30 < Y^+ < 60$ cases, 12 elements were used to represent the whole boundary layer region.

$$Y^+ = \frac{\rho u_\tau y}{\mu} \tag{3.13}$$

3.4.2 Turbulence models

The current study utilised four turbulence models implemented in Fluent^{TM}6.2. The four turbulence models are:

- Spalart-Allmaras 1 equation turbulence model.
- k-ϵ 2 equation turbulence model.
- Realisable k-ϵ turbulence model.
- k-ω SST turbulence model.

The first two turbulence models listed above are the simplest and are widely used in engineering applications. The performance of these turbulence models are compared against the realisable complex k-ϵ and k-ω SST turbulence models. Predictions by Na et al. (2006) showed that realisable k-ϵ best predicted the centreline film effectiveness downstream of a coolant hole, whilst laterally averaged film effectiveness downstream of the coolant hole was best predicted by the use of k-ω SST turbulence models. The current investigation also looked at the predictive capability for the local heat transfer coefficient downstream of the coolant holes.

3.4.3 Computation method

The computational domain for all simulations was initialised with the mean values of the inlet and outlet pressures and temperatures. Convergence for all the simulations was obtained using the following steps.

1. The initialised computation domain was run using an Eulean inviscid solver. The fluid properties were set to constant values and first order upwind discretisation was used for the pressure and temperature fields. The code was run until default Fluent^{TM} convergence limits were reached.

2. The desired turbulence model was chosen. A piece-wise linear interpolation was used to vary the fluid properties with temperature, apart from density. This was set to a constant value of $1.225\,\mathrm{kgm}^{-3}$. First order upwind discretisation was chosen for the turbulence equations. The solution was run until the default convergence limit was reached.

3. The density of the fluid was changed to ideal gas law and the code was run further until default convergence limits were reached.

4. Second order upwind discretisation was chosen for the pressure, temperature, and turbulence. The solution was run beyond the default convergence limits, until there was no further change in the residuals.

The mass flow rate at the outlet plane of the domain, as shown in figure 3.3, was also monitored. Figure 3.4 shows a typical mass flow rate monitor plot. Convergence was determined when the monitored massflow rate reached a constant value.

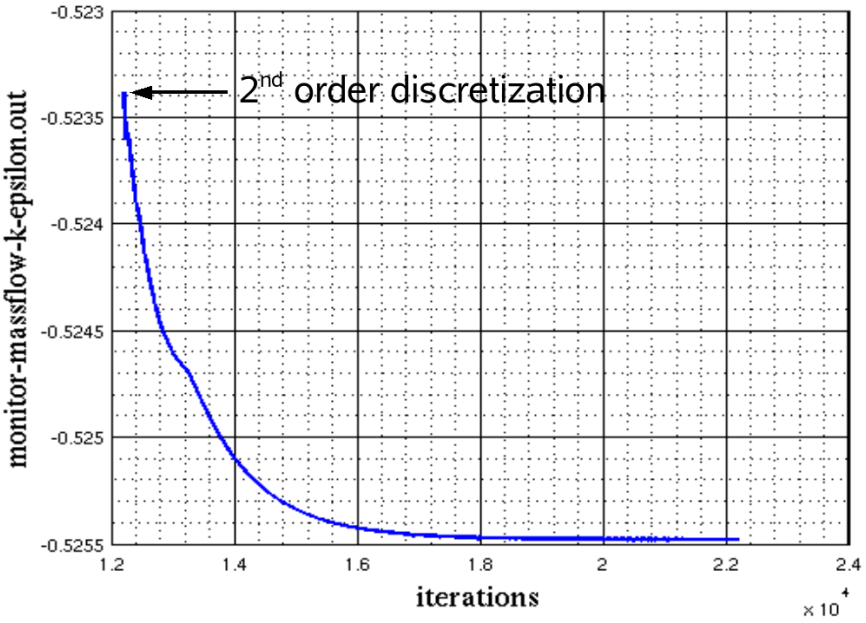

Figure 3.4: The mass flow rate at the outlet plane of the computation domain

For the heat transfer simulations, the mass flow rate at the outlet as well as the mean wall temperature downstream of the coolant holes was monitored. For all the steps mentioned above, the walls were set with an adiabatic boundary condition. Table 3.3 shows the isothermal wall temperature set on the heated wall. The corresponding θ for the set wall temperatures are also shown in table 3.3.

T_w (K)	$T_{rec,m}$ (K)	T_{tc} (K)	θ
373.95	538.9	318.6	1.34
429.30	538.9	318.6	2.01
484.65	538.9	318.6	4.01

Table 3.3: Isothermal wall temperatures set for the simulations

3.5 CFD predictions

Figure 3.5 shows the predicted flow conditions in the plenum and mainstream regions of the computation domain.

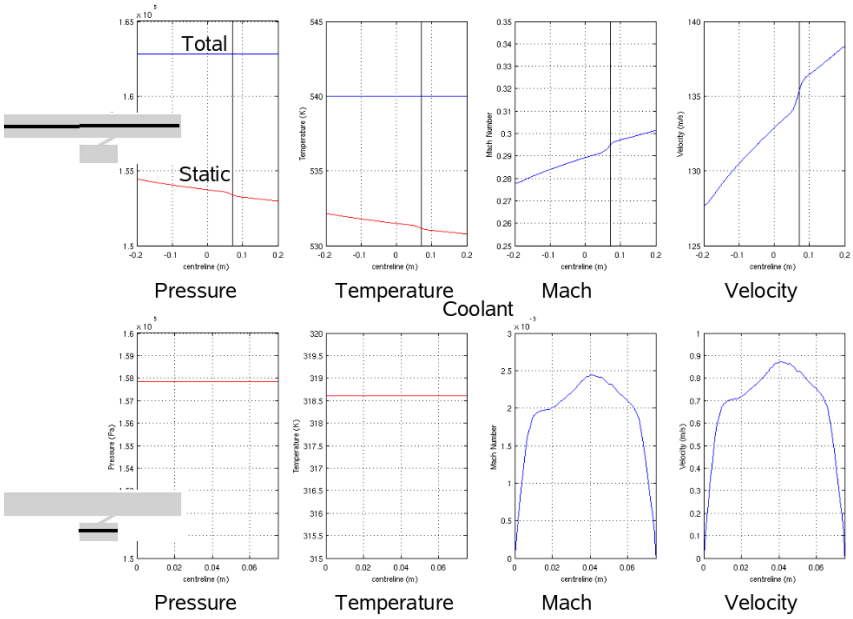

Figure 3.5: Predicted flow conditions in the plenum and mainstream flow

The four plots on the top row of figure 3.5 show the predicted pressure, temperature, Mach number and velocity plotted against the length of the mainstream part of the computation domain. The data plotted are along the mid-height of the mainstream portion of the computation domain. The x co-ordinate is measured from the inlet plane of the mainstream computation domain, located at $x = -0.2m$, to the outlet plane, located at $x = 0.2m$. The dark vertical line represents the downstream edge of the coolant hole. The total pressure and temperature along the domain is constant as expected. The decrease in static pressure is due to the pressure drop caused by the skin friction drag on the walls of the tunnel. The coolant stream, when exhausted into the mainstream, acts as a blockage to the mainstream flow path. Due to this blockage, the cross sectional area of the mainstream flow path is decreased,

resulting in the increase of the mainstream flow velocity, so as to conserve continuity. This increase in flow velocity is seen in the Mach number plot of figure 3.5. The sudden drop in static pressure, at the coolant hole location, is also due to this blockage caused by the coolant stream. A similar trend is observed with the static temperature plotted along the computation domain. The four plots on the bottom of figure 3.5 show the predicted pressure, temperature, Mach number and velocity plotted against length of the plenum domain. The data plotted are at the mid-height of the plenum part of the computation domain. Within the plenum region, the total and static pressure and temperatures are constant as expected, and the Mach number within the plenum is quite small.

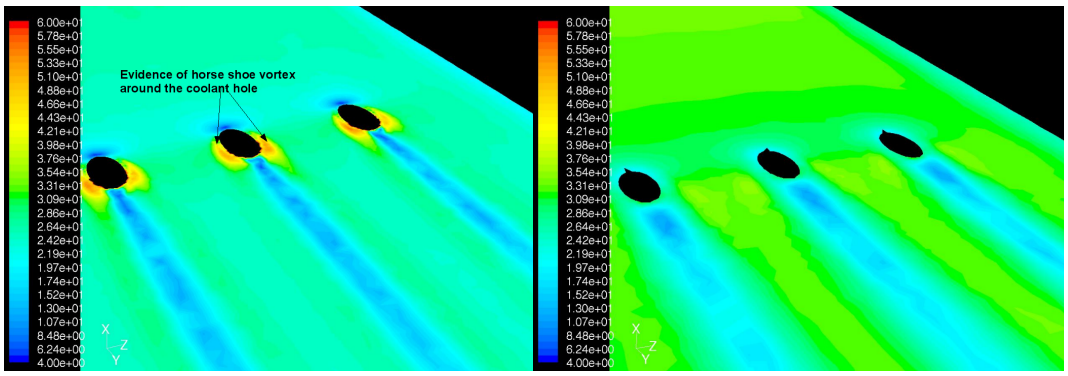

(a) $Y^+ = 01$ (b) $30 < Y^+ < 60$

Figure 3.6: Shear stress on the wall, for k-ω-SST turbulence model.

Figure 3.6 shows the typical predicted shear stress on the wall, using the $Y^+ = 1$ grid (figure 3.6a) and the $30 < Y^+ < 60$ grid (figure 3.6b), for the turbulence model k-ω SST. These plots are for the tetrahedral element grids. On both grids, there exists a low shear stress region, downstream of each coolant hole. This low shear stress is caused by the upward (away from the wall) movement of the counter rotating vortex pair, as shown in figure 3.7. There also exists, on either side of the above mentioned low shear stress region, regions of high shear stresses, when the velocity vectors of the vortex pair are tangential and near to the surface of the wall. The details of the flow structures are clearly seen in the $Y^+ = 1$ grid. This is expected as the flow in the $Y^+ = 1$ grid is resolved to the wall, whilst the flow in the $30 < Y^+ < 60$ grid is modelled using a wall function. The wall function does not capture the large shear stress adjacent to the coolant hole exits as shown in figure 3.6a.

Figure 3.7 shows typical plots of velocity vectors on a plane $\frac{x}{D} = 5$ downstream of the coolant holes. The vectors are coloured by total temperature and are plotted

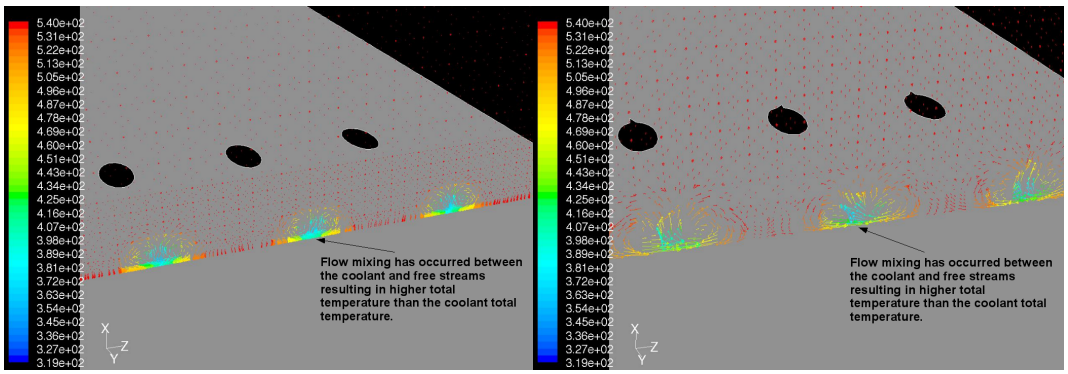

(a) $Y^+ = 01$ (b) $30 < Y^+ < 60$

Figure 3.7: Velocity vectors coloured by total temperature at the $\frac{x}{D} = 5$ plane for k-ω-SST turbulence model.

for the k-ω SST turbulence model. These plots are for the tetrahedral element grids. The counter rotating vortices can be clearly seen at this plane for both types of grids. From the total temperature contours, it can be seen that the coolant stream has mixed with the mainsteam, with the result that the lowest temperature at the plane is greater than the total temperature of the coolant supply.

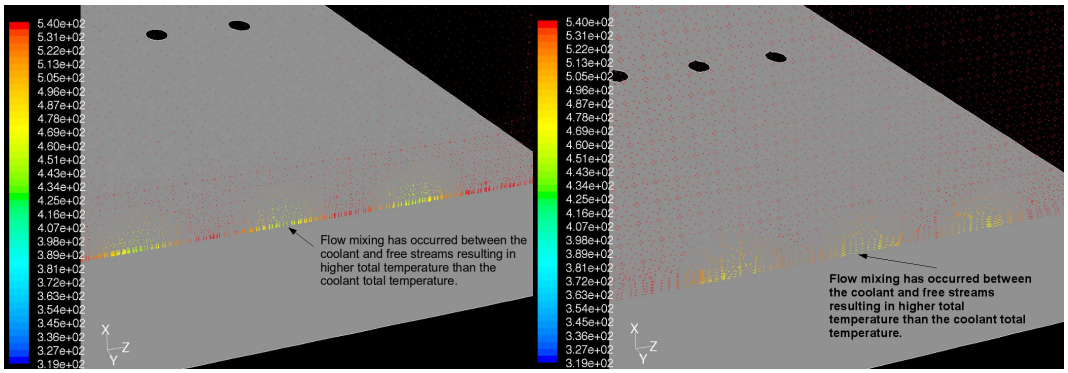

(a) $Y^+ = 01$ (b) $30 < Y^+ < 60$

Figure 3.8: Velocity vectors coloured by total temperature at plane $\frac{x}{D} = 20$ for k-ω-SST turbulence model.

Figure 3.8 shows typical plots of velocity vectors, coloured by total temperature, on a plane $\frac{x}{D} = 20$ downstream of the coolant holes. These plots are for grids with tetrahedral elements. From the colour contours, it can be seen that the coolant stream has lost most of its cooling capacity. The evidence of the counter rotating

vortex structure at $\frac{x}{D} = 20$ plane for $Y^+ = 1$ is not clearly seen. However, the vortex structure can be seen in the $30 < Y^+ < 60$ grid.

The flow features shown in figures 3.6 to 3.8 can also be seen in grids using hexahedral elements.

3.5.1 Film effectiveness prediction

3.5.1.1 Effectiveness prediction using adiabatic wall

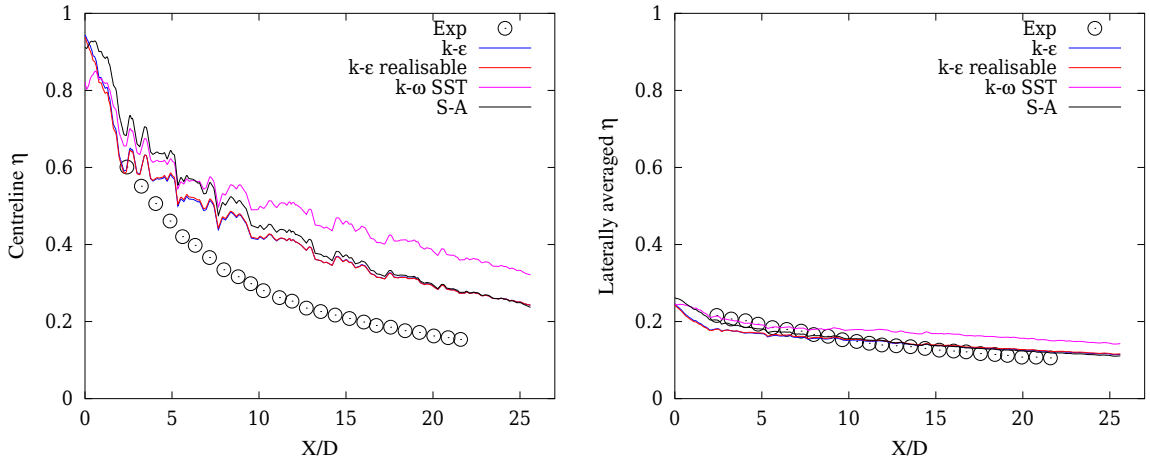

(a) Centreline η

(b) Laterally averaged η

Figure 3.9: Comparison of predicted effectiveness with experimental data from Saumweber et al. (2000) for tetrahedral mesh with $Y^+ = 1$.

Saumweber et al. (2000) reports the measured centreline and laterally averaged film cooling effectiveness. Figure 3.9 shows the predicted film effectiveness, computed using equation 3.7, for the tetrahedral element grids with $Y^+ = 1$, compared with experimental data from Saumweber et al. (2000). It can be seen that all the turbulence models provide very good agreement with the experimental data when considering the laterally averaged film effectiveness. However, all the turbulence models over predict the centreline film effectiveness, when compared with the experimental data. Similar levels of agreement between measured and computationally determined effectiveness were predicted by Harrison and Bogard (2008).

Figure 3.10 shows the film effectiveness computed for the hexahedral element grids with wall $Y^+ = 1$. Again, there is good agreement between the predicted laterally averaged film effectiveness with experimental data for all the turbulence

models. However, the centreline effectiveness is over predicted as in the case of the tetrahedral element grids.

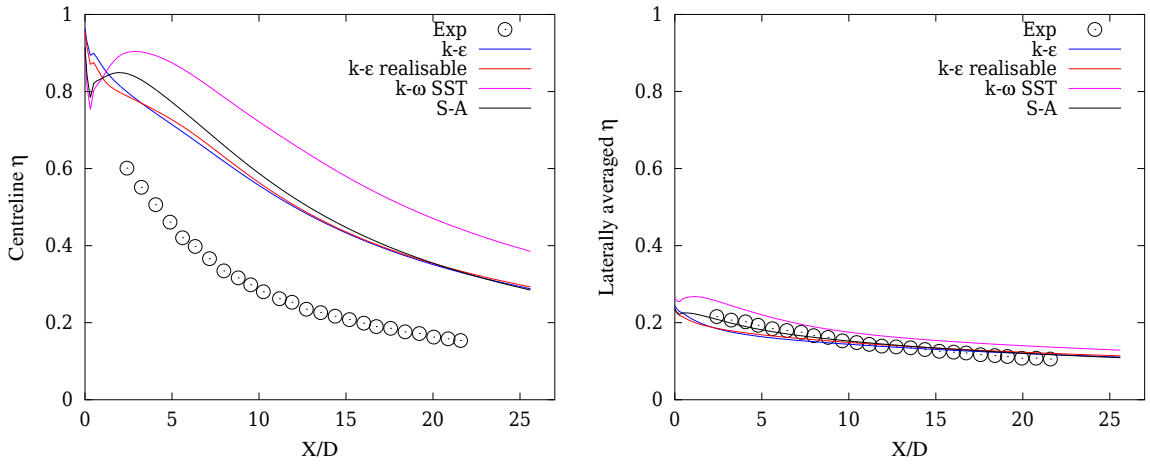

(a) Centreline η (b) Laterally averaged η

Figure 3.10: Comparison of predicted effectiveness with experimental data from Saumweber et al. (2000) for hexahedral mesh with $Y^+ = 1$.

In both grid types, the k-ω SST turbulence model over predicts the centreline and laterally averaged film effectiveness. For the tetrahedral and hexahedral element grids, the one equation Spalart-Allmaras turbulence model best predicts the laterally averaged turbulence model. The two equation k-ϵ realisable turbulence model shows close agreement to the experimental data when considering the centreline effectiveness, for both types of elements. However, the above predictions contradict the findings of Na et al. (2006), where the k-ω SST turbulence model best predicted the laterally averaged film effectiveness. The centreline film effectiveness prediction agrees with the findings of Na et al. (2006).

Figure 3.11 shows the lateral variation of the film effectiveness on the wall at $\frac{x}{D} = 5$ and $\frac{x}{D} = 20$, downstream of the coolant holes. The three peaks in effectiveness are due to the coolant stream downstream of the holes. As expected, the magnitude of the effectiveness peaks at $\frac{x}{D} = 20$ is smaller than that at $\frac{x}{D} = 5$. This reduction in effectiveness is due to the mixing of the coolant stream with the mainstream flow. From figure 3.11, it can be seen that the magnitude of the effectiveness at a point midway between the two peaks is near zero. Even though the centreline film effectiveness is over predicted when compared with experimental data, due to the effectiveness along points midway between the coolant holes being near zero, the laterally averaged

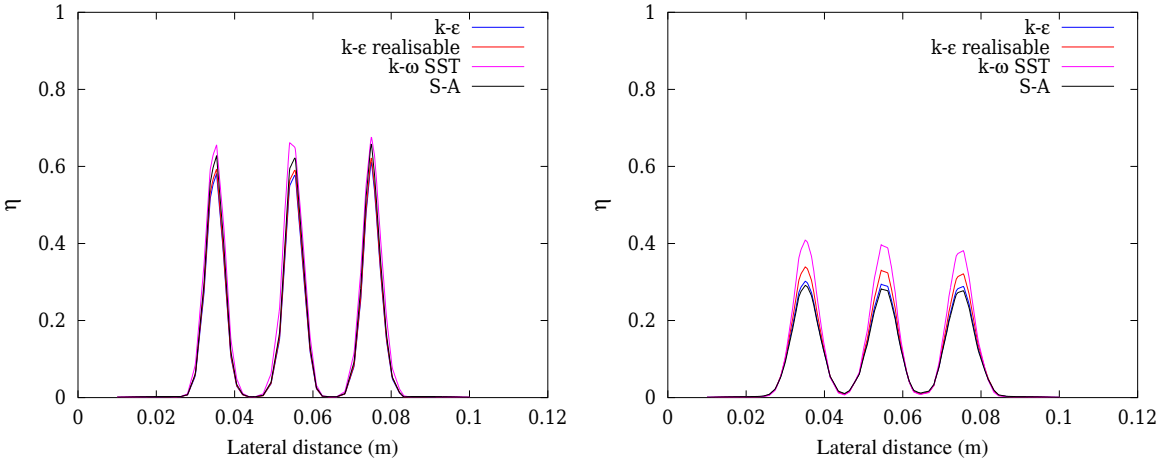

(a) Lateral variation of η at $\frac{x}{D} = 5$

(b) Lateral variation of η at $\frac{x}{D} = 20$

Figure 3.11: Lateral variation of η for tetrahedral mesh with $Y^+ = 1$.

film effectiveness predictions would be in close agreement with the experimental data, as seen in figures 3.9b and 3.10b. As stated in Harrison and Bogard (2008), the author found that the turbulence models under predict the lateral spread of the coolant stream, downstream of the coolant holes. The under prediction is due to insufficient mixing predicted by the turbulence models, between the coolant and main streams.

Figures 3.12 and 3.13 show the centreline and laterally averaged film cooling predictions, for the $30 < Y^+ < 60$ grid, compared with experimental data for the tetrahedral and hexahedral elements respectively.

It can be seen that, with wall functions enabled, the centreline effectiveness is still over predicted for the tetrahedral and hexahedral element cases. However, there is very good agreement with experimental data for the laterally averaged film effectiveness. However, unlike the $Y^+ = 1$ cases, the standard k-ϵ turbulence model best predicts the laterally averaged film effectiveness for both tetrahedral and hexahedral element grids.

To compare quantitatively the predicted results using the different turbulence models, element types and wall Y^+, the residual sum of squares between the predicted and experimental data were computed. The residual sum of squares were computed for the laterally averaged film effectiveness data. Equation 3.14 was used to compute the residual sum of squares.

$$SS_{diff} = \sum_{i=1}^{n} (y_i - f_i)^2 \tag{3.14}$$

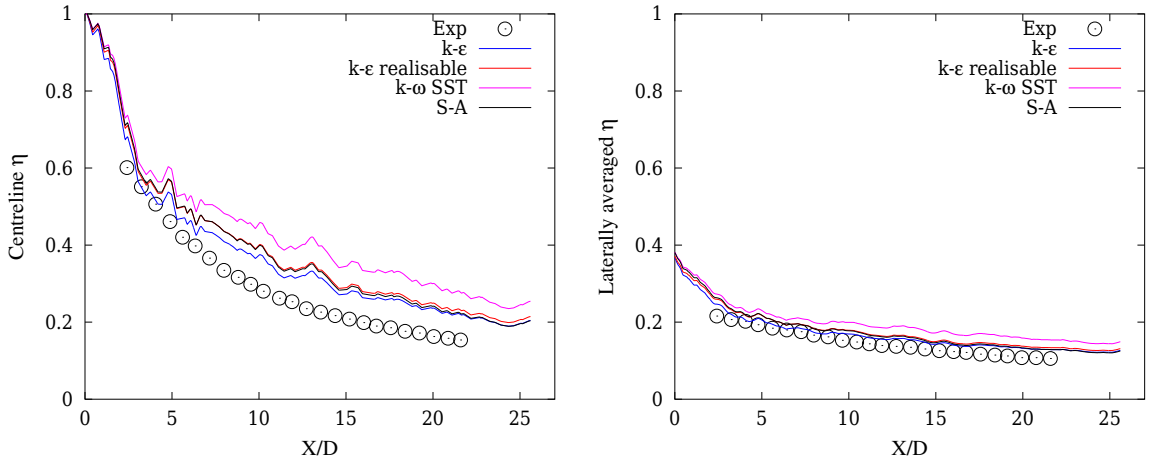

(a) Centreline η (b) Laterally averaged η

Figure 3.12: Comparison of predicted effectiveness with the experimental data from Saumweber et al. (2000) for the tetrahedral mesh with $30 < Y^+ < 60$.

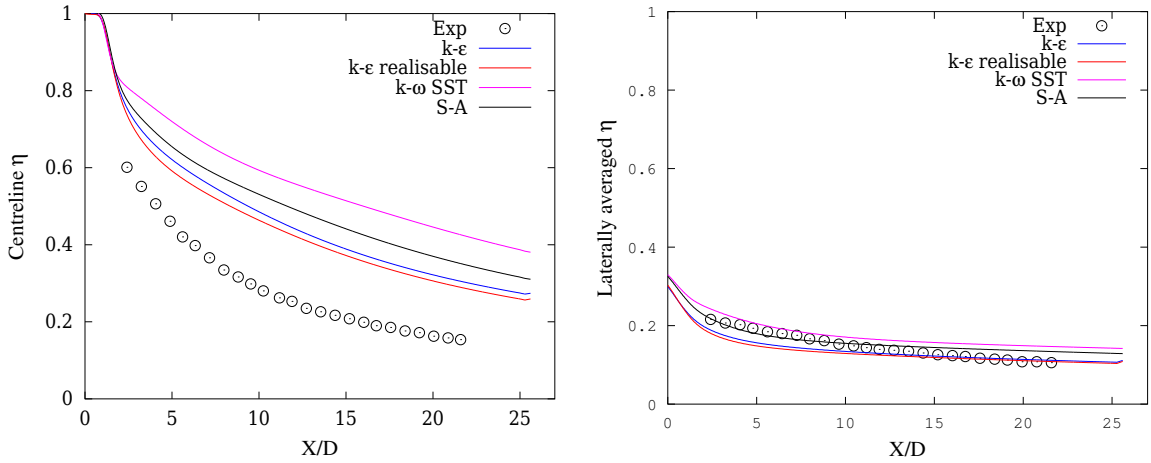

(a) Centreline η (b) Laterally averaged η

Figure 3.13: Comparison of predicted effectiveness with the experimental data from Saumweber et al. (2000) for the hexahedral mesh with $30 < Y^+ < 60$.

In equation 3.14, y_i refers to the experimental data points whilst f_i refers to the CFD prediction. To compute the residual sum of squares, initially the natural logarithm of the laterally averaged effectiveness was computed for the experimental and the CFD prediction. Figure 3.14 shows a plot of the natural logarithm of laterally averaged film effectiveness of the experimental and computational data.

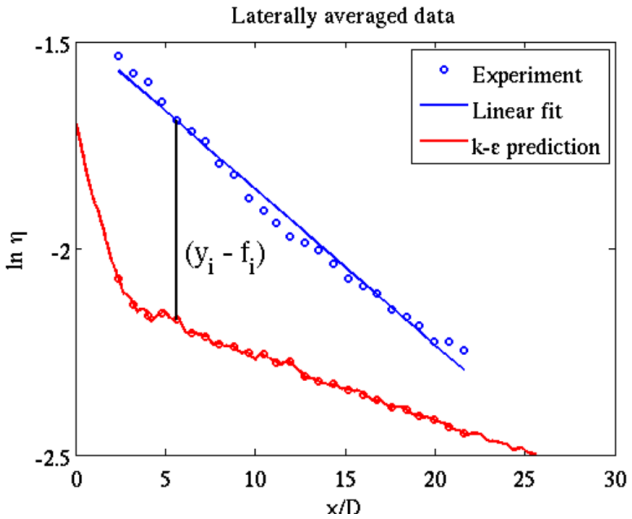

Figure 3.14: Natural logarithm of effectiveness against $\frac{x}{D}$

It is interesting to note that the gradients of the line fit of the experimental data and CFD predictions differ. This is the case for all turbulence models. The CFD predictions do not capture the decay of the effectiveness with $\frac{x}{D}$ accurately. After the natural logarithm is computed, the predicted data are interpolated to the same $\frac{x}{D}$ spacing as the experimental data. The residual sum of squares is subsequently computed using equation 3.14, where the indices i refer to each of the interpolated and experimental data points.

Figure 3.15a shows the computed sum of square differences for the turbulence models and grid types. The y-axis of figure 3.15a is the computed sum of squares whilst the x-axis is the different turbulence models. The different colours of the bars represent the differerent element types and wall Y^+ values used. It can be clearly seen that the Spalart-Allmaras turbulence model best predicts the laterally averaged film effectiveness downstream of the coolant holes for grids with $Y^+ = 1$. The standard k-ϵ turbulence model best predicts the laterally averaged film effectiveness for grids with wall Y^+ between 30 and 60. As stated in the literature, it can clearly be seen that structured hexahedral grids predict the film effectiveness more closely than the tetrahedral grids. However, it is encouraging to note that the discrepancy between

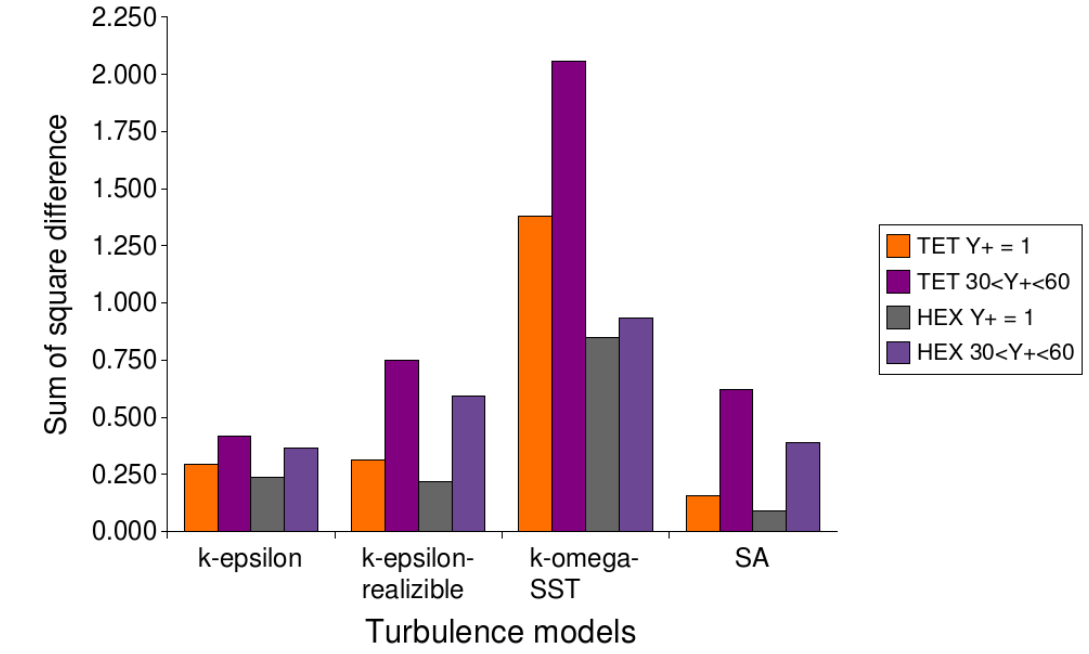

(a) Sum of square difference of log effectiveness

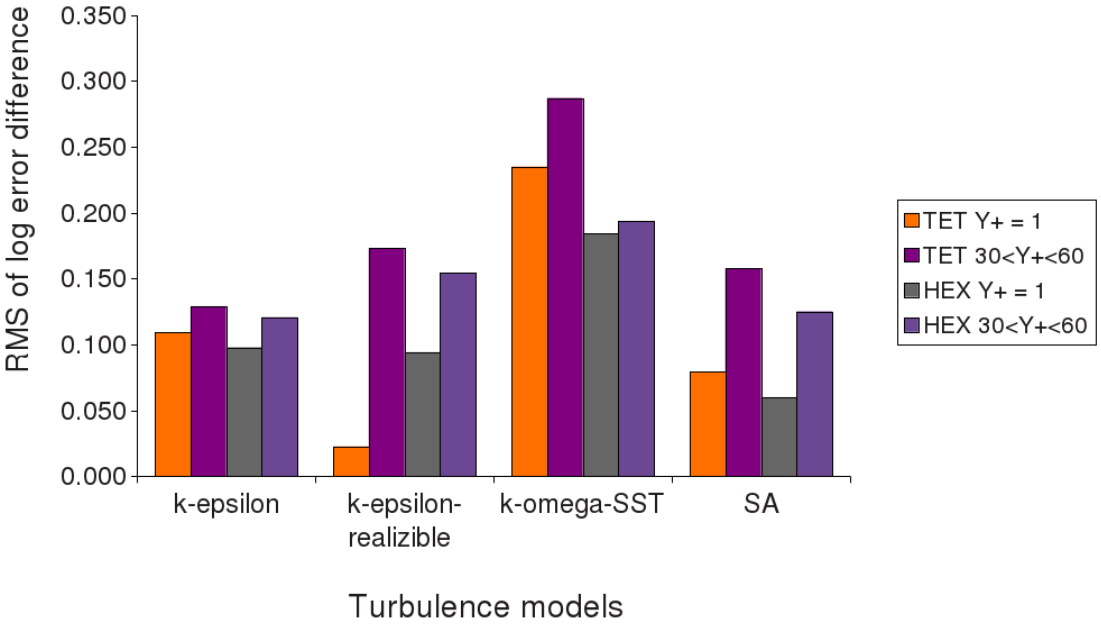

(b) Root mean square of difference in effectiveness

Figure 3.15: Sum of square and root mean square of the log effectiveness difference.

tetrahedral and hexahedral meshes are not too large and hence tetrahedral meshes with appropriate prism elements can be used to predict the laterally averaged film effectiveness downstream of the coolant holes. Figure 3.15b shows the root mean square of the differences between the log of the predicted and experimental laterally averaged effectiveness. The root mean square was computed from the log of the differences in the laterally averaged effectiveness data from $\frac{x}{D}$ of 5 to 20.

From the above predictions, it can be concluded that turbulence models can be employed to predict the laterally averaged film effectiveness. However, it would be difficult to predict the centreline effectiveness until the correct flow physics of film cooling is modelled. It can also be concluded that a pure tetrahedral mesh, with prism elements to capture the boundary layer, can be used to accurately predict the laterally averaged film effectiveness downstream of coolant holes.

3.5.1.2 Effectiveness prediction using isothermal wall

The effectiveness predictions shown in section 3.5.1.1 were computed using an adiabatic wall. Equation 3.11 shows that, by setting the wall to a uniform temperature value and leaving the gas and coolant temperatures unchanged, an effectiveness, $\eta_{iso,adb}$, can be computed. Table 3.3 shows the chosen temperature values. $h(\theta)$ was computed using equation 3.9, with the use of laterally averaged values of $\dot{q}$ and T_w. Initially the entire adiabatic wall region, as used in the adiabatic wall effectiveness computation, was set to an isothermal value. However, to best represent the experiments conducted by Saumweber et al. (2000), part of the wall was also set to an isothermal value, as shown in figure 3.3b. The extent of the heated region was estimated to be from $\frac{x}{D} = 2$ downstream of the coolant holes to the outlet plane, as shown in figure 3.3b.

Figure 3.16 shows the computed $h(\theta)$ plotted against θ at different $\frac{x}{D}$ locations. From the best line fit through the three points at each $\frac{x}{D}$ location, the x-axis intercept was also computed. This gives the reciprocal of the effectiveness. Figure 3.17 shows the predicted effectiveness using different wall boundary conditions, compared with the experimental data. The isothermal wall conditions were with and without an unheated upstream starting length.

In figure 3.17, the solid blue line represents the laterally averaged predictions from the adiabatic wall boundary conditions. The solid red line shows the laterally averaged predictions using an isothermal wall boundary condition. The isothermal boundary condition was applied to the whole wall that contained the coolant exit. The solid black line represents the predictions using an isothermal wall with an unheated

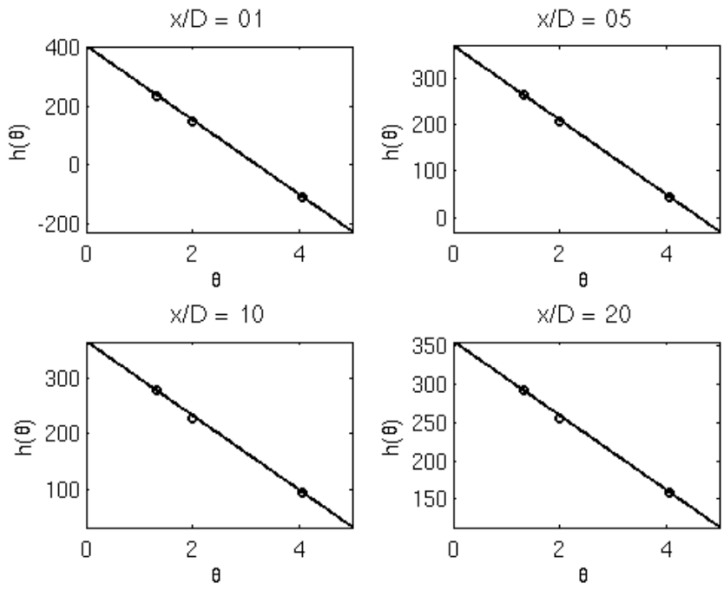

Figure 3.16: $h(\theta)$ computed using equation 3.9 against θ.

starting length (part isothermal and part adiabatic). For all turbulence models, the isothermal effectiveness without an unheated starting length predicts an increased effectiveness relative to the adiabatic wall case. The increase in effectiveness is within 10% at the far downstream location from the coolant holes. However, just downstream of the coolant hole, this discrepancy increases to over 60%.

In the case of the isothermal wall with an unheated starting length, there is very good agreement of the predicted effectiveness compared with the adiabatic wall predictions, far downstream of the coolant hole. However, near the hole, the effectiveness predicted is lower than the adiabatic wall predictions. For the Spalart-Allmaras, standard k-ϵ, and realisable k-ϵ turbulence models, the effectiveness predicted with an isothermal wall with an unheated starting length, matches the adiabatic wall effectiveness after $\frac{x}{D} = 5$. However, for the k-ω SST turbulence model, good agreement is only achieved after $\frac{x}{D} = 10$.

3.5.2 Theoretical model to predict the difference between the adiabatic and isothermal effectiveness

By considering an enthalpy balance on a control volume around the injection location of the coolant on a flat plate, the difference in the isothermal effectiveness and adiabatic effectiveness can be investigated. Figure 3.18 shows such a control volume around a coolant injection point on a flat plate. The upper horizontal surface of the

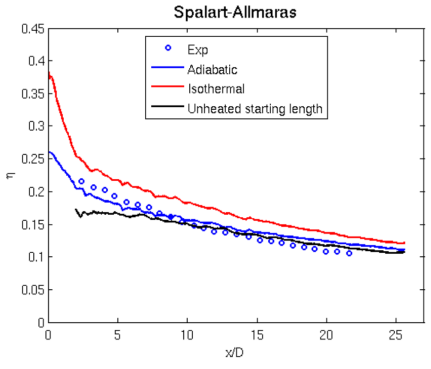

(a) Spalart-Allmaras model

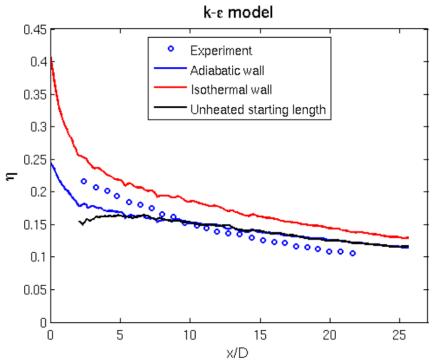

(b) Standard k-ϵ model

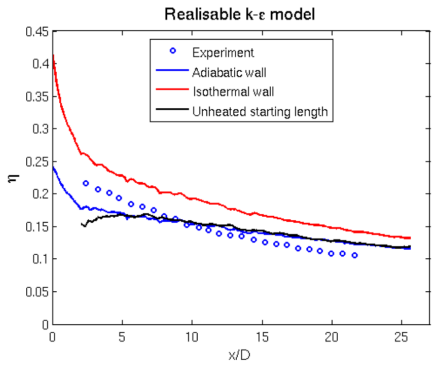

(c) Realisable k-ϵ model

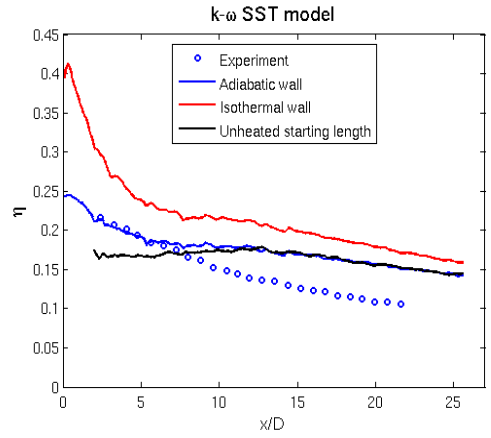

(d) k-ω SST model

Figure 3.17: Comparison of the predicted laterally averaged effectiveness using adiabatic wall and isothermal wall, with experimental data.

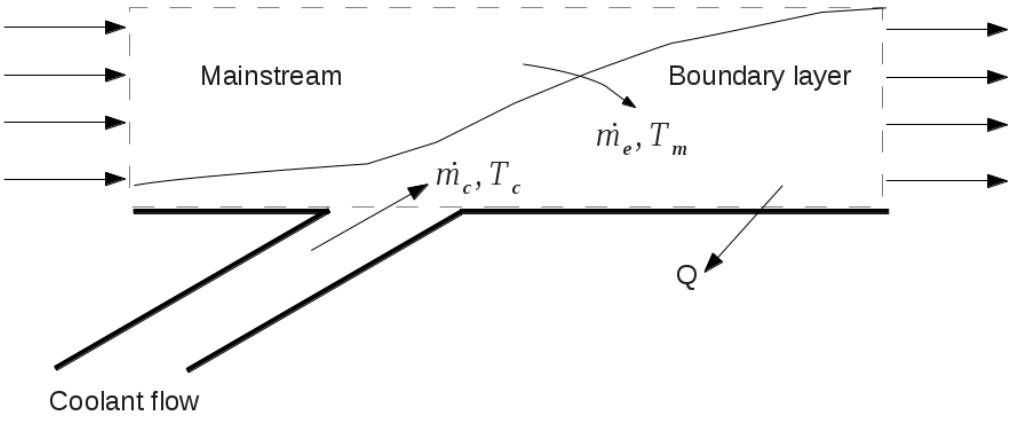

,

Figure 3.18: Diagram showing the control volume, boundary layer and coolant hole injection point on a flat plate.

control volume is defined by the streamline in the uniform mainstream. The lower horizontal surface is bounded by the wall of the model, but does not incorporate the surface within the coolant hole. It is assumed that the cooling film is confined to a discrete mixing region which is just downstream of the coolant ejection plane. The mass flow rate, $\dot{m}_c$, represents the coolant mass flow rate injected from the coolant holes. $\dot{m}_e$ represents the rate of mainstream fluid entrained from the mainstream into the boundary layer upstream and downstream of the coolant holes. It is assumed that the cooling film intermixes with this entrained mainstream flow. Equation 3.15 gives the enthalpy balance performed around the control volume.

$$\dot{m}_e C_p T_\infty + \dot{m}_c C_p T_c - Q = (\dot{m}_e + \dot{m}_c)\, C_p \overline{T} \tag{3.15}$$

In equation 3.15, Q represents the total heat transferred into the wall, up to the observation point. T_∞, T_c and $\overline{T}$ represent the mainstream, coolant and massflow averaged cooling temperatures respectively. This massflow averaged cooling temperature, $\overline{T}$, is assumed to be between the adiabatic temperature and the mainstream temperature such that the difference between the mainstream temperature and the massflow averaged coolant temperature is a fraction of the difference between the mainstream temperature and adiabatic wall temperature. This is shown in equation

3.16. The k in equation 3.16 represents this fraction, which can take a value between zero and unity.

$$T_\infty - \overline{T} = k\,(T_\infty - T_{ad}) \tag{3.16}$$

Generally, the film cooling effectiveness is defined by equation 2.4. Substituting equation 3.16 into 2.4, the general effectiveness can be given by equation 3.17

$$\eta = \frac{T_\infty - \overline{T}}{k\,(T_\infty - Tc)} \tag{3.17}$$

Considering equation 3.15, when the wall is fully adiabatic, Q is equal to zero, and the massflow averaged mean temperature is give by equation 3.18

$$\overline{T}_{aw} = \frac{\dot{m}_e T_\infty + \dot{m}_c T_c}{\dot{m}_e + \dot{m}_c} \tag{3.18}$$

By substituting equation 3.18 in equation 3.17, the fully adiabatic wall effectiveness can be evaluated. This is shown in equation 3.19.

$$\eta_{ad} = \frac{\dot{m}_c}{k(\dot{m}_e + \dot{m}_c)} \tag{3.19}$$

It can be seen that the fully adiabatic effectiveness can be expressed as a ratio of massflows. By re-arranging equation 3.19, the entrained massflow can be given as equation 3.20.

$$\dot{m}_e = \dot{m}_c \left(\frac{1}{k\eta_{ad}} - 1 \right) \tag{3.20}$$

A similar analysis can be conducted for the case when the wall is isothermal. The isothermal effectiveness can be found from equations 3.15 and 3.17, and given as:

$$\eta_{iso} = \frac{\dot{m}_c + \frac{Q}{C_p(T_\infty - T_c)}}{k(\dot{m}_e + \dot{m}_c)} \tag{3.21}$$

By subtracting equation 3.19 from equation 3.21 and substituting equation 3.20 for the entrained massflow, $\dot{m}_e$, the difference between the $\eta_{iso} - \eta_{ad}$, can be shown as:

$$\eta_{iso} - \eta_{ad} = \frac{\eta_{ad} Q}{C_p \dot{m}_c (T_\infty - T_c)} \tag{3.22}$$

It can be seen that equation 3.22 is independent of the constant k. The total heat flux, Q, incident on the surface can be calculated with equation 3.23. In equation

3.23, $\overline{St}$ represents the average Stanton number over a distance of $x0$ upstream of the coolant ejection.

$$Q = \overline{St}\rho u C_p \left(T_{ad} - Tw\right) x0 \tag{3.23}$$

Substituting equation 3.23 into equation 3.22 gives,

$$\eta_{iso} - \eta_{ad} = \frac{\eta_{ad}\overline{St}\rho u(T_{ad} - Tw)x0}{\dot{m}_c(T_\infty - T_c)} \tag{3.24}$$

Expressing the coolant mass flow $\dot{m}_c$ as $\rho u M s$, where M is the mass flux ratio and s is the equivalent two dimensional slot height of the cooling geometry, which is given by equation 2.11. The temperature T_w in equation 3.24, is the adiabatic temperature for the isothermal wall situation at the point of observation and hence $\frac{T_\infty - T_w}{T_\infty - Tc}$ is the η_{iso}, which is constant. Therefore, equation 3.24 can be re-written as follows.

$$\eta_{iso} - \eta_{ad} = \frac{\eta_{ad}\eta_{iso}\overline{St}x0}{Ms} \tag{3.25}$$

Rearranging equation 3.25, the isothermal adiabatic effectiveness can be obtained as a function of adiabatic effectiveness as shown in equation 3.26.

$$\eta_{iso} = \frac{\eta_{ad}}{(1 - \frac{\eta_{ad}\overline{St}x0}{Ms})} \tag{3.26}$$

Figure 3.19 shows the isothermal adiabatic effectiveness predicted using equation 3.26 compared with the isothermal adiabatic effectiveness predicted using Spalart-Allmaras turbulence model, as described in section 3.5.1.2. The adiabatic effectiveness used in equation 3.26 is the adiabatic effectiveness prediction using Spalart-Allmaras turbulence model and is plotted in figure 3.19.

From figure 3.19, it can be seen that good agreement is achieved between the isothermal adiabatic effectiveness predicted using equation 3.26 and the CFD analysis, confirming that the difference between the isothermal adiabatic effectiveness and adiabatic effectiveness is a result of the state of the upstream boundary layer.

3.5.3 Film heat transfer coefficient predictions

With the use of the three isothermal wall temperature predictions and equation 3.11, the film heat transfer coefficient was also computed. As laterally averaged values for $\dot{q}$ and T_w were used in the computation of $h(\theta)$, the computed h_f is laterally averaged. Saumweber et al. (2000) used the effectiveness computed from the adiabatic wall experiments and one isothermal wall condition to compute the heat transfer

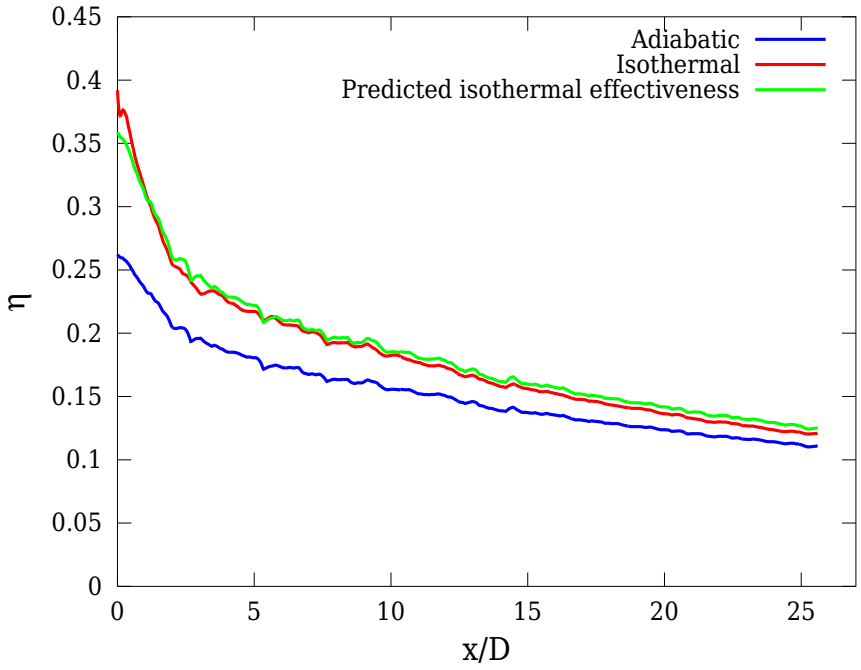

Figure 3.19: Comparison of the predicted isothermal adiabatic effectiveness from equation 3.26 with CFD

coefficient. It must be noted that the driving gas temperature for heat transfer in the cooled simulations is the mainstream coolant mixed adiabatic wall temperature adjacent to the wall.

In the current study, three isothermal wall boundary conditions were used to compute the film heat transfer coefficient. Furthermore, the film heat transfer coefficient was also computed using the predicted adiabatic film effectiveness shown in section 3.5.1.1 and one isothermal wall boundary condition, as in the research by Saumweber et al. (2000). The computed and predicted film heat transfer coefficient was normalised by the heat transfer coefficient on a flat plate without coolant. The driving gas temperature for heat transfer in the uncooled case is the gas recovery temperature. For a simple flat plate, without cooling, Kays and Crawford (1984) shows the local convective Stanton number on an isothermal wall with an unheated starting length to be given by equation 3.27.

$$StPr^{0.4} = 0.0287 Re_x^{-0.2} \left[1 - \left(\frac{\zeta}{x} \right)^{(\frac{9}{10})} \right]^{-\frac{1}{9}} \tag{3.27}$$

Equation 3.27 can be re-arranged to give the local Nusselt number as shown in equation 3.28.

$$Nu_x = 0.0287 Re_x^{0.8} Pr^{0.6} \left[1 - \left(\frac{\zeta}{x}\right)^{\frac{9}{10}}\right]^{-\frac{1}{9}} \tag{3.28}$$

Incropera and DeWitt (2001) showed that the local Nusselt number for an uncooled flat plate with an unheated starting length to be given by equation 3.29.

$$Nu_x = 0.0296 Re_x^{0.8} Pr^{0.3} \left[1 - \left(\frac{\zeta}{x}\right)^{\frac{9}{10}}\right]^{-\frac{1}{9}} \tag{3.29}$$

In equations 3.27, 3.28 and 3.29, ζ refers to the unheated starting length, upstream of the heated section, measured from the leading edge of the plate. In the above mentioned correlations, x is measured from the leading edge of the plate and not from the downstream edge of the coolant holes. Preliminary CFD predictions were carried out to compare the predicted heat transfer coefficient on a flat plate without film cooling and with an unheated starting length, to that computed from the correlations given by equations 3.28 and 3.29. The value for ζ was chosen such that the isothermal section on the wall commenced $\frac{x}{D} = 2$, measured from the downstream edge of the coolant holes. Figure 3.20 shows the predicted heat transfer coefficient on the wall compared with those computed using the correlations described in equations 3.28 and 3.29. To predict the uncooled heat transfer coefficient, a mesh using hexahedral elements, to represent the mainstream, was created. The coolant holes and the plenum were not meshed. It was assumed by the author that there would be little difference in the predicted heat transfer coefficient, using hexahedral and tetrahedral meshes.

The greatest difference in the heat transfer coefficient correlations are the exponenents of the Prandtl number. In equation 3.28 the exponent is 0.6, whilst equation 3.29 uses the exponent of 0.3. For the $Y+ = 1$, shown in figure 3.20a, the heat transfer coefficient predicted using the standard k-ϵ, realisable k-ϵ and k-ω SST turbulence models, were within 10% of the heat transfer coefficient correlation given by equation 3.29. However, the heat transfer coefficient predicted using the Spalart-Allmaras turbulence model was within 20%.

As for the case of $30 < Y+ < 60$, the predicted heat transfer coefficient using the turbulence models standard k-ϵ, realisable k-ϵ and Spalart-Allmaras are within the 10% of the flat plate heat transfer coefficient computed using equation 3.29. The k-ω SST model predicts a heat transfer coefficient greater than 10% just downstream of the heated surface. However, far downstream the heat transfer coefficient reduces to

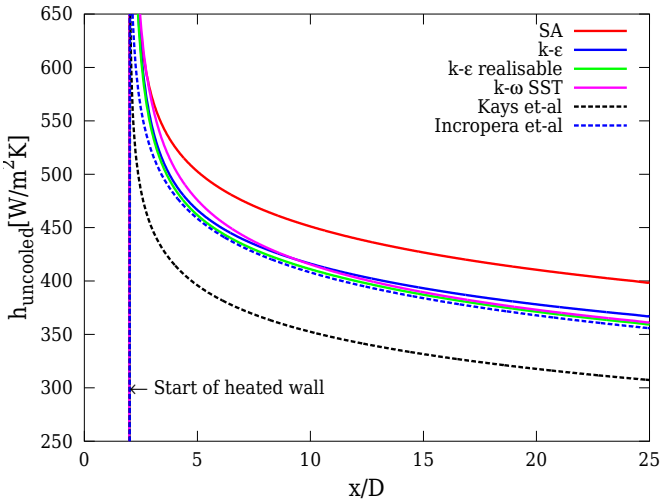

(a) The heat transfer coefficient on an uncooled flat plate with an unheated starting length. Hexahedral mesh with wall $Y^+ = 1$

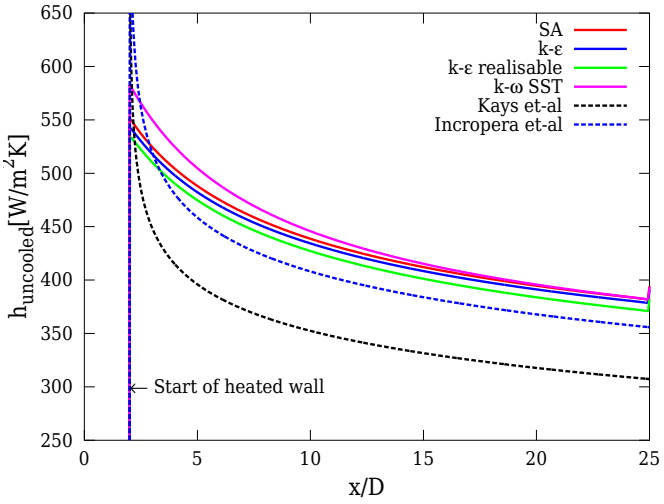

(b) The heat transfer coefficient on an uncooled flat plate with an unheated starting length. Hexahedral mesh with $30 < Y^+ < 60$

Figure 3.20: Uncooled heat transfer coefficient predictions from CFD and correlations downstream of heated wall.

the same levels as those from the standard k-ϵ, realisable k-ϵ and Spalart-Allmaras models. It is not surprising to see that the predicted uncooled heat transfer coefficient for the $30 < Y^+ < 60$ case is close for all the turbulence models, as all the turbulence models employ the use of wall functions to model the flow near the wall.

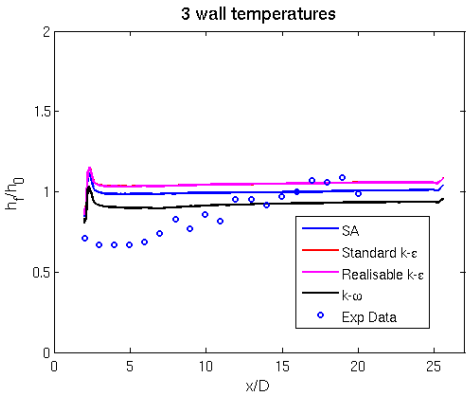

(a) h_f computed from 3 isothermal wall temperature for $Y+ \ = 1$

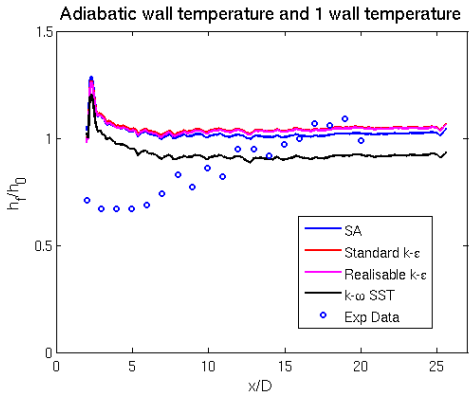

(b) h_f computed from 1 isothermal wall condition and adiabatic wall condition for $Y+ \ = 1$

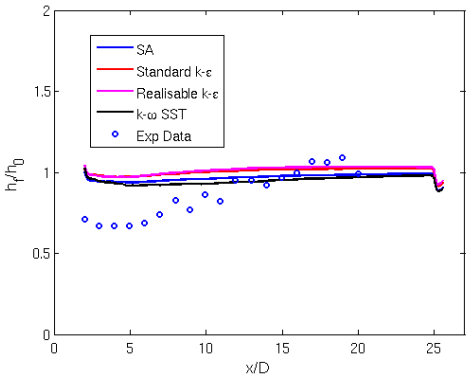

(c) h_f computed from 3 isothermal wall temperature for $30 < Y+ < 60$

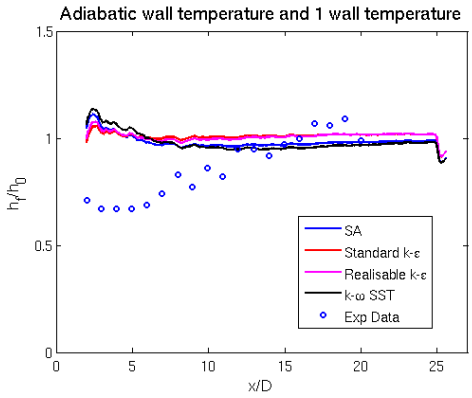

(d) h_f computed from 1 isothermal wall condition and adiabatic wall condition for $30 < Y+ < 60$

Figure 3.21: Comparison of h_f computed from 3 isothermal wall conditions and 1 isothermal wall and adiabatic wall condition.

The uncooled predicted wall heat transfer coefficient was used to normalise the predicted heat transfer coefficient with coolant, downstream of the coolant holes. $\frac{h_f}{h_O} = 1$ implies that the heat transfer coefficient of the cooled wall is equivalent to that of an uncooled wall. A value less than unity implies that the heat transfer coefficient is less than that of an uncooled plate, whilst a value greater than unity implies a heat transfer enhancement. Figure 3.21 shows the predicted film heat transfer

coefficient enhancement for all the turbulence models and the two types of tetrahedral meshes used. All turbulence models do not capture the heat transfer coefficient enhancement trends downstream of the coolant holes as shown by the experiments. There appears to be a slight rise in the predicted heat transfer coefficient enhancement downstream of the coolant holes. However, this rise in heat transfer coefficient does not match the rise in the film heat transfer coefficient from the experimental data. With wall functions, figures 3.21c and 3.21d, the differences in the predicted heat transfer coefficient enhancement using the various turbulence models are small. There is, however, some difference in the heat transfer coefficient enhancement predicted from the different turbulence models with the $Y^+ = 1$ grid. The two k-ϵ models predicted the largest enhancement, whilst the k-ω SST turbulence model predicts a lower heat transfer enhancement of the predictions from the four turbulence models.

The film heat transfer coefficients computed using the reciprocal of the adiabatic effectiveness prediction and one isothermal wall boundary condition, figures 3.21b and 3.21d, show the same trends as the three isothermal wall boundary conditions. Furthermore, after a distance of $\frac{x}{D}$ downstream of the coolant holes, there is very little difference in the predicted heat transfer coefficient enhancement computed using the two methods for all turbulence models. There is, however, a difference in the heat transfer coefficient enhancement just downstream of the coolant holes. This difference can be attributed to the state of the boundary layer of the predictions.

Figure 3.22a shows the sum of square differences computed between the experimental data and the predicted heat transfer coefficient. The heat transfer coefficient predictions were computed using the three isothermal wall boundary conditions. The sum of square errors were computed using equation 3.14 and the method described in section 3.5.1.1. However, unlike in section 3.5.1.1, the ratios of the heat transfer coefficient to that of the uncooled wall heat transfer coefficient for the CFD prediction and experiment, were used in computing the sum of square errors. Figure 3.22b shows the root mean square of the difference between the laterally averaged experimental and predicted heat transfer coefficient. This highlights the mean magnitude of the differences between the experimental and predicted heat transfer coefficients. The root mean square value was computed for the laterally averaged heat transfer coefficients from $\frac{x}{D}$ of 5 to 20. It can be seen that the k-ω SST turbulence model best predicts the experimental film heat transfer coefficient.

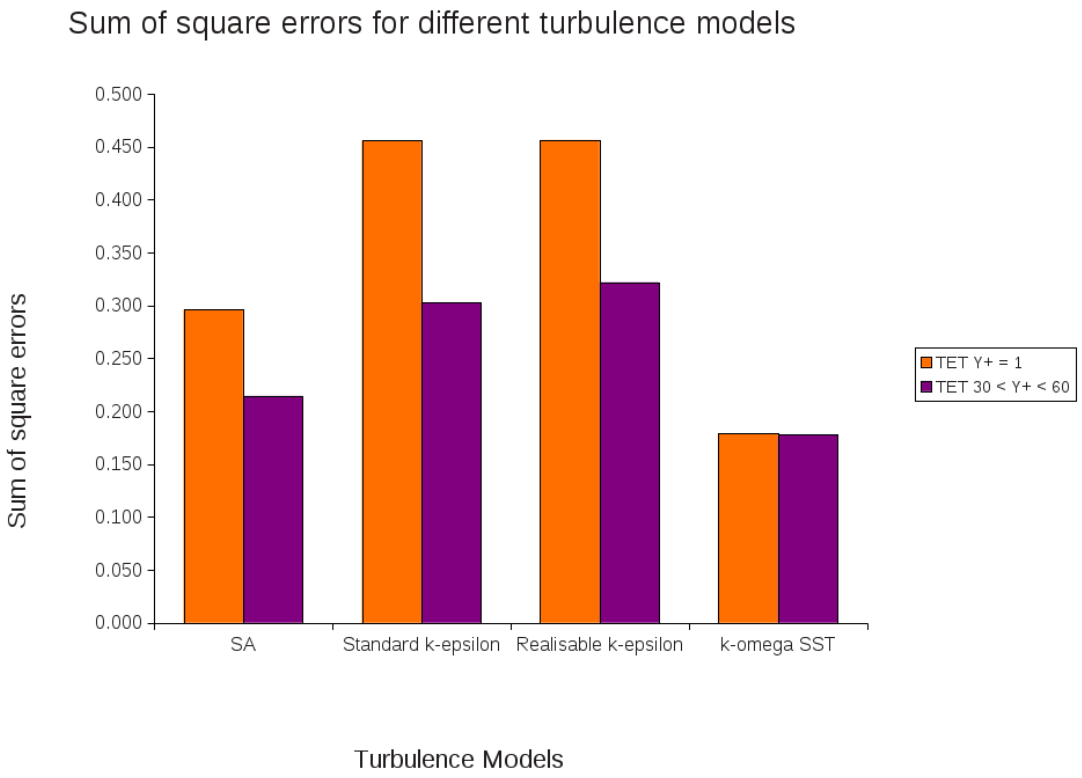

(a) Sum of square difference of the heat transfer coefficient ratio

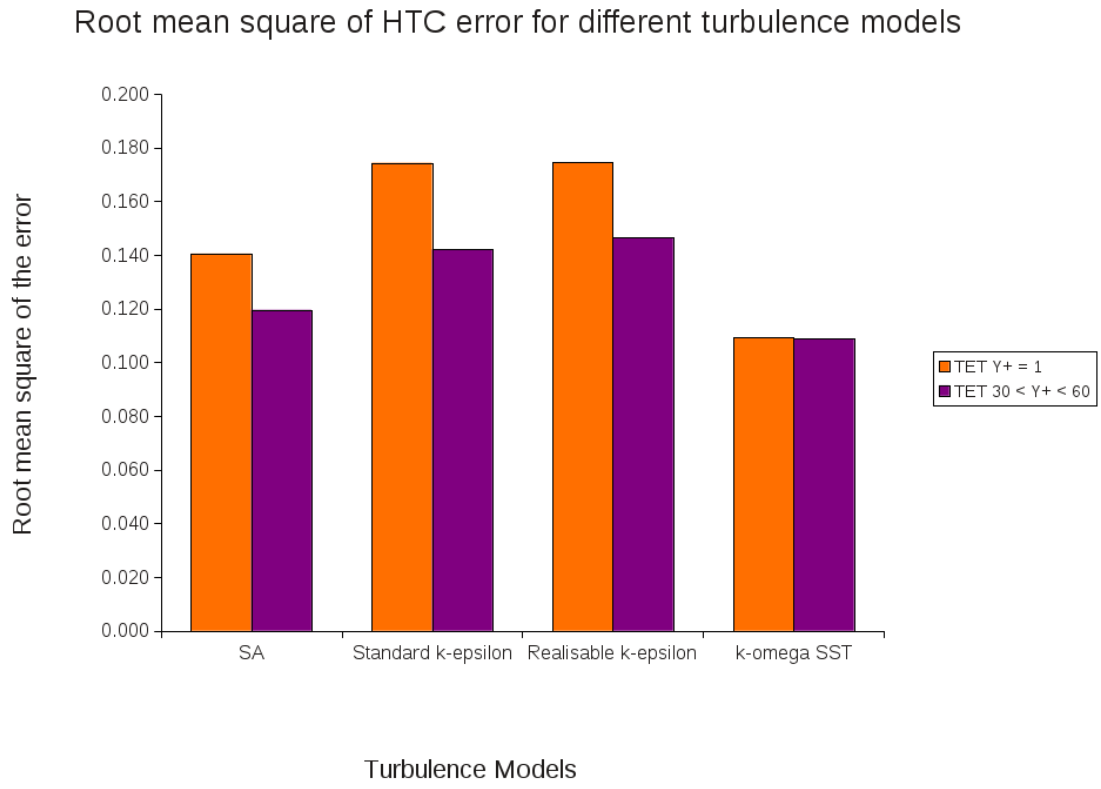

(b) Root mean square of difference in heat transfer coefficient ratio

Figure 3.22: Sum of square and root mean square of the heat transfer coefficient ratio

3.6 Conclusions

In this chapter, the film cooling effectiveness and heat transfer coefficient were predicted for a simple flat plate film cooling experiment. Four different turbulence models and two types of elements were used in the prediction for the film effectiveness.

The effectiveness was computed using an adiabatic wall, an isothermal wall and a partially isothermal wall (unheated starting length) boundary conditions. There was a difference in the predicted effectiveness using an isothermal wall and adiabatic wall. The difference was attributed to the state of the boundary layer. There was little difference between the effectiveness predicted using a partially isothermal wall and an adiabatic wall, far downstream of the coolant holes. The predicted effectiveness far downstream, using a fully isothermal wall, was shown to be 10% greater than that predicted using an adiabatic wall. Near the holes, the predicted effectiveness using an isothermal wall was seen to be about 60% greater than that predicted using an adiabatic wall. A sum of the squared differences between the effectiveness predicted using an adiabatic wall and the experimental data was computed. The effectiveness computed using hexahedral elements and the Spalart-Allmaras turbulence model provided the best prediction for the adiabatic effectiveness. The Spalart-Allmaras turbulence model with tetrahedral element mesh provided the next best prediction. Hence it can be concluded that a tetrahedral mesh can be used to predict adiabatic effectiveness. Furthermore, the Spalart-Allmaras turbulence model with $Y^+ = 1$ can be used with the tetrahedral mesh to predict the adiabatic film effectiveness downstream of the coolant holes.

The heat transfer enhancement was computed using three isothermal wall temperatures as well as using the reciprocal of the adiabatic effectiveness and one isothermal wall temperature. It can be seen that the two methods produced similar heat transfer coefficient enhancement far downstream of the coolant hole. Near the hole, due to the difference in boundary layer state, the film heat transfer coefficient computed using the reciprocal of the adiabatic effectiveness and one isothermal wall condition gives a greater value than that computed using three isothermal wall boundary conditions. It could be seen that the predicted heat transfer coefficient does not match the experimental data. There was little differences between the heat transfer coefficient predicted using different turbulence models and wall functions. However, there were difference between the predicted heat transfer coefficient from the turbulence models used with a $Y^+ = 1$ grid. The k-ω SST turbulence model with $Y^+ = 1$ provides the best agreement with the experimental data.

Turbulence model	$SS_{diff,\eta}$	**Rank** $SS_{diff,\eta}$	$SS_{diff,\frac{h_f}{h_O}}$	**Rank** $SS_{diff,\frac{h_f}{h_O}}$	**Total score**
Spalart-Allmaras	0.157	1	0.296	2	3
Standard k-ϵ	0.297	2	0.456	4	6
Realisable k-ϵ	0.312	3	0.456	3	6
k-ω SST	1.381	4	0.179	1	5

Table 3.4: The ranking of the $SS_{diff,\eta}$ and $SS_{diff,\frac{h_f}{h_O}}$ for $Y^+ = 1$

Turbulence model	$SS_{diff,\eta}$	**Rank** $SS_{diff,\eta}$	$SS_{diff,\frac{h_f}{h_O}}$	**Rank** $SS_{diff,\frac{h_f}{h_O}}$	**Total score**
Spalart-Allmaras	0.624	2	0.214	2	4
Standard k-ϵ	0.416	1	0.303	3	4
Realisable k-ϵ	0.748	3	0.322	4	7
k-ω SST	2.060	4	0.178	1	5

Table 3.5: The ranking of the $SS_{diff,\eta}$ and $SS_{diff,\frac{h_f}{h_O}}$ for $30 < Y^+ < 60$

Table 3.4 shows the summarised sum of square differences for the tetrahedral mesh with wall $Y^+ = 1$ whilst table 3.5 shows the results for a tetrahedral mesh with wall $30 < Y^+ < 60$. The sum of square differences computed for the film effectiveness and heat transfer coefficient were ranked. A rank score of 1 was given to the minimum value of the sum of square difference of the film effectiveness and film heat transfer coefficient respectively. A rank score of 4 was given to the maximum value of the sum of square difference of the film effectiveness and heat transfer coefficient. The total score was computed by the summation of the two rank scores.

From table 3.4 it can be seen that the one equation Spalart-Allmaras turbulence model is the best model to predict the film effectiveness with a tetrahedral mesh having a wall $Y^+ = 1$. The film heat transfer coefficient is best predicted by using the k-ω SST turbulence model. It can be seen that the best turbulence model to predict both the film heat transfer coefficient and film effectiveness is the one equation Spalart-Allmaras turbulence model, which provides the minimum total score.

From table 3.5, it can be seen that the standard k-ϵ turbulence model is the best model to predict the film effectiveness with a tetrahedral mesh having a wall $30 < Y^+ < 60$. The film heat transfer coefficient is best predicted using the k-ω SST turbulence model using the same mesh. From the total score, it can be seen that the best turbulence model to predict both film heat transfer coefficient and film effectiveness is either the one equation Spalart-Allmaras or the two equation standard

k-ϵ turbulence model. As the k-ω turbulence model performed poorly with this mesh in predicting the film effectiveness, the optimum turbulence model to predict both the film effectiveness and heat transfer coefficient would be the Spalart-Allmaras turbulence model.

It is surprising to see that the simple one equation Spalart-Allmaras turbulence model is the optimum turbulence model to predict the film effectiveness and film heat transfer coefficient with meshes with wall $Y^+ = 1$ and $30 < Y^+ < 60$. It must be noted that the current results are only valid for the turbulence model implemented in Fluent ^{TM}version 6.2. This validation would need to be repeated for other implementations of the turbulence model.

Chapter 4

Low speed experimental setup

4.1 Experimental facility

The current research was conducted in a low speed wind tunnel, situated in the Southwell Laboratory at the University of Oxford. Figure 4.1(a) shows the open circuit wind tunnel used in the current research. Air is drawn through a bell mouth inlet and accelerated into a rectangular test section of cross sectional area $2.25 \times 10^{-2}\,\mathrm{m}^2$, by 2 axial fans at the rear of the tunnel. The flow characteristics of the tunnel were measured and reported by Moss (1992).

Figure 4.1(b) shows an example test plate housed within the test section of the tunnel. The trailing edge cooling geometries were incorporated into such flat plates. The current study reports the results from three such test plates.

4.2 Engine aerodynamic and thermal parameter scaling to test conditions

Forth and Jones (1986) summarises the non-dimensional parameters which affect cooling performance for a flat plate with a single row of cooling holes. In order to best simulate the temperature and the velocity fields of the engine at laboratory conditions, these parameters needed to be matched. In film cooling, the heat flux incident on the surface can be shown to be a function of the parameters shown in equation 4.1.

$$\dot{q} = f\left(\rho_\infty, \rho_c, k, \mu, Cp_\infty, Cp_c, U_\infty, U_c, (T_\infty - T_w), (T_\infty - T_c), P, s, l, \alpha, \beta, x\right) \quad (4.1)$$

.

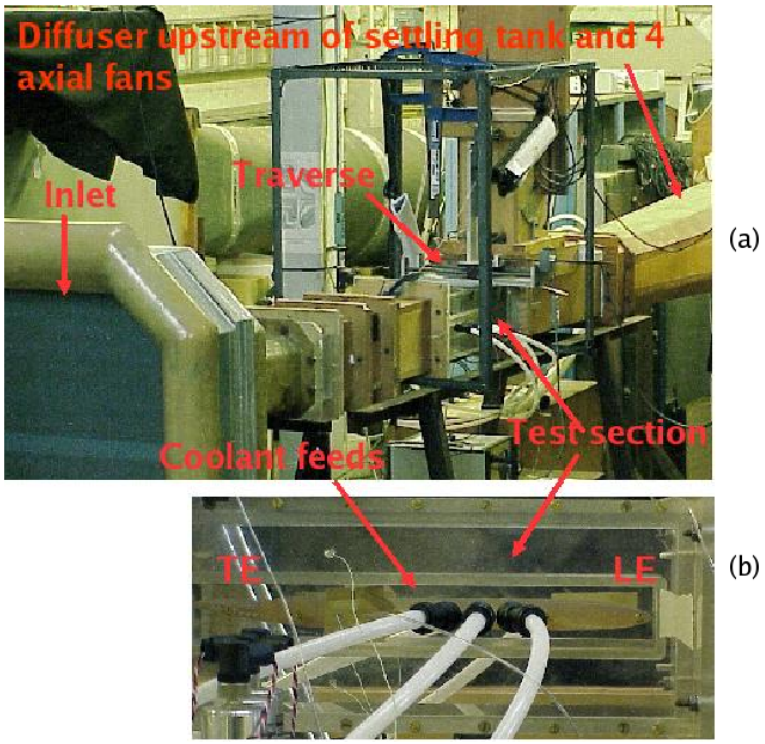

Figure 4.1: Low speed wind tunnel. (a) shows the overall wind tunnel, (b) shows an enlarged view of the test section.

Equation 4.1 shows that there are one dependent variable, sixteen independent variables and five reference dimensions. Using Buckingham (1915) theorem, twelve dimensionless groups were derived. The twelve dimensionless groups are:

- Nusselt number.
- Mainstream Reynolds number.
- Prandtl number for mainstream and coolant.
- Ratio of mainstream kinetic energy to mainstream enthalpy. This is related to the the mainstream Mach number.
- Discrete coolant hole / slot pitch to coolant hole diameter / slot height ratio.
- Discrete coolant hole / slot length to coolant hole diameter / slot height ratio.
- Distance downstream of coolant hole / slot to coolant hole diameter / slot height.
- Coolant to mainstream density ratio, DR.

- Coolant to mainstream mass flux ratio, M.
- Ratio of coolant to mainstream specific heats.
- Coolant hole / slot inclination angle.
- Coolant hole / slot compound angle.

The matching of all the above dimensionless groups would ensure that the experimentally determined heat transfer coefficient and effectiveness can be read across to the engine environment. Furthermore, the Reynolds and Mach numbers are crucial parameters that are required to be matched to ensure that the experimentally determined aerodynamic losses are applicable in the engine environment.

The current study is a comparative study of aerodynamic and heat transfer performance on three trailing edge cooling configurations described in section 1.2. The comparison is conducted in a low speed environment. The datum cooling configuration (conventional late pressure surface trailing edge ejection) was geometrically scaled from a modern gas turbine engine blade. The geometric scale factor was 10. This scale factor was chosen so that good resolution of the aerodynamic profile loss, heat transfer coefficient and effectiveness distribution downstream of coolant ejection, can be observed. Furthermore, at this scale the cooling configuration could be easily incorporated into the test tunnel without major modification. This scale factor was also used in the machined and cast cutback test plate configurations. The axial location of the cutback on the pressure surface of the machine cutback test plate was located just upstream of the trailing edge, where the coolant holes can be drilled on to the cutback face which is shielded from the mainstream. This same axial location was used for the cast cutback configuration. It must be noted that scaled machining tolerances were taken into account, when locating the axial position of the cutback. The important geometric dimensions are given in table 4.2.

The data from Moss (1992) indicated that the flow field within the tunnel test section was uniform. With the two fans running, the measured flow velocity at a point 40 mm downstream of the trailing edge and above the pressure surface was 88 m/s. This gives a Reynolds number based on plate length of 1.96×10^6 and is in the same order of magnitude to a typical gas turbine engine blade Reynolds number based on chord length at the trailing edge. Typical gas turbine engine Reynolds numbers at the trailing edge based on blade chord length can vary from 1.8×10^6 to 2.0×10^6. Even though the Reynolds numbers of the aerodynamic tests was matched close to engine Reynolds number, it must be noted that the pressure surface

boundary layer thickness at the ejection location from the tests was not matched to engine values. For the heat transfer tests due to the presence of the heater mesh and the resultant pressure drop, tunnel mean flow velocity drops to approximately 20 m/s. The mean Reynolds number based on plate length at the trailing edge is approximately 3.63×10^5. Furthermore it must be noted that the pressure surface boundary layer thickness at the ejection location from the tests was not matched to engine value. Therefore, the film effectiveness and heat transfer coefficients could not be directly read across to the engine conditions. However as the test conditions are similar between the three three trailing edge cooling configurations, the trends between the three configurations from the testing can be read across to the engine conditions.

As the experiments were carried out in a low speed wind tunnel, engine Mach number could not be matched. The average Mach number at a point 40[mm] downstream of the trailing edge and above the pressure surface was 0.3. The research by Gritsch et al. (1998) and Liess (1975) showed that there was a slight increase in the film effectiveness when the mainstream Mach number increased from 0.3 to 1.2. Therefore the trends in the measured effectiveness at Mach number 0.3 could be read across to the transonic case, provided all other dimensionless parameters are matched. However, the mixed out losses which are strong functions of the external Mach number, cannot easily be read across from the experimental conditions to engine conditions. However, the differences (deltas) in losses between the three tested configurations would be read across to the engine environment.

In the experiments documented in this thesis, the engine mass flux ratio in addition to the Reynolds number was also matched. The mass flux ratio was varied by varying the coolant mass flow. The mainstream mass flow was kept constant between the tests. However as air, with a smaller temperature difference, was used as the fluid for the mainstream and coolant, the density ratio and ratio of specific heats could not be matched. Hence the engine coolant to mainstream momentum flux ratio could not be matched at the same instance as the coolant to engine mass flux ratio.

$$I = \frac{M^2}{DR} \tag{4.2}$$

Equation 4.2 shows the relationship between the coolant to mainstream momentum flux, mass and density ratios. From equation 4.2, it can be seen that the engine momentum flux ratio could be matched with a density ratio of unity and a lower mass flux ratio than engine design conditions. Therefore, experiments were carried

out for a range of coolant to mainstream mass flux ratios so as to ensure that the engine coolant to mainstream momentum flux ratio is also matched. These tests also enabled the author to investigate the trends in aerodynamic and heat transfer performance of the three coolant systems to mass, momentum and mass flow ratios.

Dimensionless parameters	Test	Engine
Mainstream Reynolds number	2.81×10^5 - 2.0×10^6	1.8×10^6 - 2.0×10^6
Coolant to mainstream density ratio	1.1	1.7
Mass flux ratio	0.3 - 2.0	1.0
Momentum flux ratio	0.1 - 3.2	0.6
Coolant to mainstream specific heats	1.0	0.9
Mach Number	0.3	0.8
Pressure ratio	1.0 - 1.3	1.2

Table 4.1: Comparison of dimensionless parameters between test conditions and engine conditions.

4.3 Modification of test sections

The original test section, as shown in Moss (1992), housed test plates which had thicknesses of 10 mm. However, at this plate thickness, the internal flow configurations required for the trailing edge coolant geometries for the present work could not be incorporated. Hence the new test plate thicknesses were increased to 20 mm, so that the internal flow configurations could be incorporated.

The new test plates were designed with the same leading edge involute profile as those of Moss (1992). The research by Moss (1992) showed that such a profile minimised the flow separation near the leading edge. Figure 4.1(b) shows the leading edge shape incorporated into the test plate. Each plate was 330 mm long and the trailing edge cooling configurations occupied approximately 35% of the plate length, measured from the trailing edge. The test plates were 150 mm wide. The coolant plenum, for the film cooling geometries, was incorporated inside the test plates as shown in figure 4.3. The plenum is fed with six coolant inlet holes (three each on either side of the plate). The coolant is fed via six PTFE pipes from a 7 bar air line. A pressure regulator was used to regulate the mass flow rate of the coolant entering the plenum. The coolant mass flow rate was measured using a British Standard orifice meter (British Standard Institution, 1981 - BS1042). The orifice meter was placed

before the coolant distributor which split the coolant into six streams. The six PTFE tubes were connected to the coolant distributor. It must be noted that there was no heating mechanism incorporated into the coolant feed, and hence the temperature of the coolant for all the experiments was atmospheric temperature.

Each of the test plates was manufactured using a stereolithography process using epoxy resin material. For ease of instrumentation of the test plates, static pressure tappings were incorporated into the test plates at the manufacturing stage. Furthermore, straight holes were drilled through the sides of the test plates to house temperature thermocouples so as to measure the total temperature of the coolant within the plenum.

The tunnel test section was re-manufactured to house the new test plates. Two perspex side wall flanges, with holes aligned to the ends of the static tappings of the test plates, were bolted onto the test plates. This was done so that the test plates would slot into the test section via the side walls. Figure 4.1(b) shows the test plates with the side flanges housed within the test section of the tunnel.

4.4 New test plates

Figure 4.2 shows three CAD geometries of the new test plates. Figure 4.2a shows the conventional near trailing edge pressure surface (datum) film cooling geometry with 7 film cooling holes. Figure 4.2b shows the test plate with a machined cutback trailing edge film cooling configuration. The coolant is fed onto the cutback surface via 6 discrete coolant holes. Figure 4.2c shows the cast cutback film cooling configuration test plate with 3 cooling slots, separated by two lands or ribs. These ribs extend from the plenum region within the test plate to the trailing edge, as seen in figure 4.3c. This cutback configuration is known as the "letter box" configuration. The coolant holes on the datum and machined cutback test plates, figures 4.2a and 4.2b have an oval (racetrack) cross sectional profile. The exit plane cross sectional profile of the cast cutback trailing edge also has an oval (racetrack) shape.

Figure 4.3 shows the internal configurations of the new test plates. The plenum, located internally in the test plates, measures 100 mm in length, 100 mm in width and 10 mm in depth, for all three test plates. The coolant is fed via the same coolant inlet configuration, described in section 4.3, for the three test plates.

Within each plenum there are five rows of pedestal banks, with the exception of the cast-cutback test plate, which has three pedestal banks. These pedestal banks smooth the coolant from the plenum inlet to the coolant hole / slot inlet plane. Hence

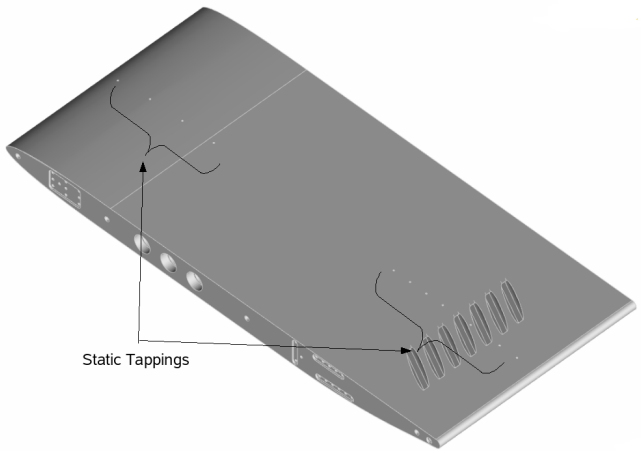

(a) Datum configuration

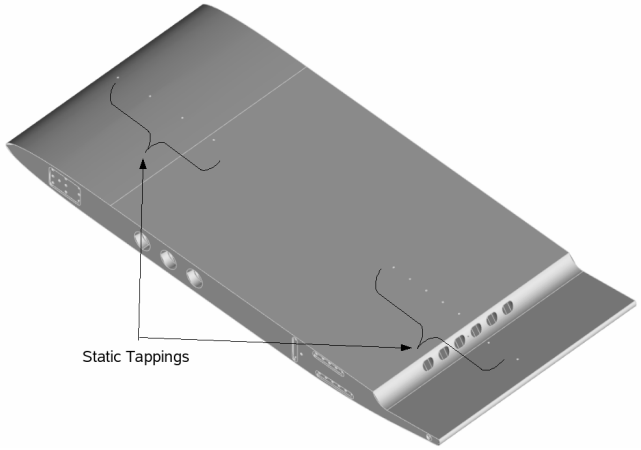

(b) Machined cutback configuration

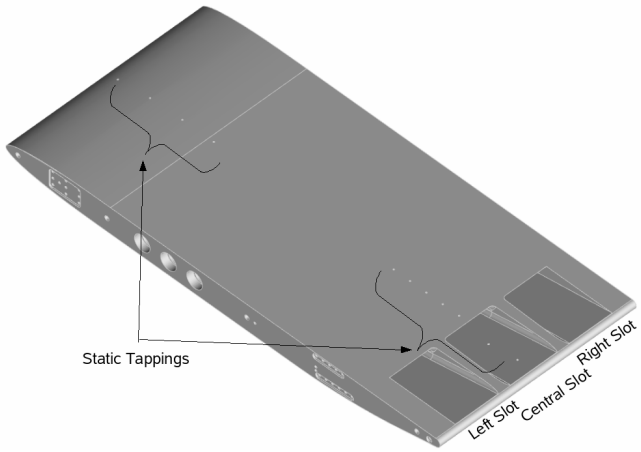

(c) Cast cutback configuration

Figure 4.2: New test plate configurations.

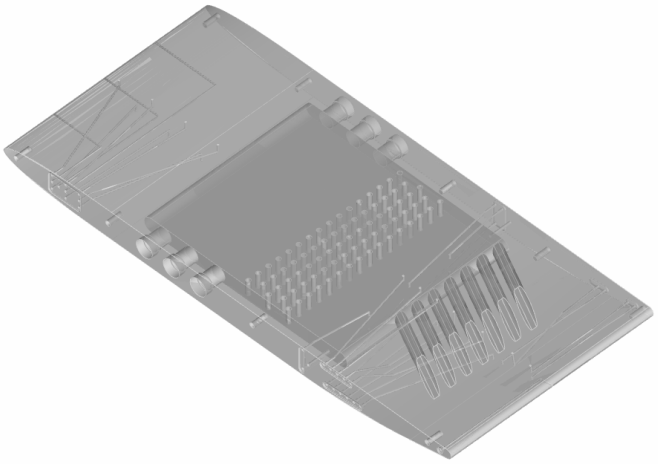

(a) Datum configuration

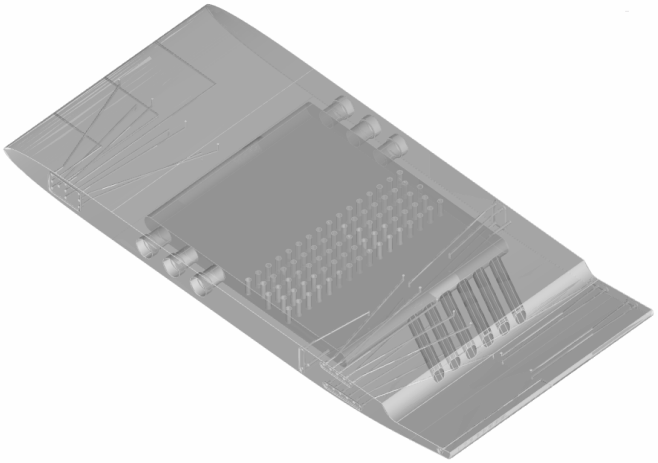

(b) Machined cutback configuration

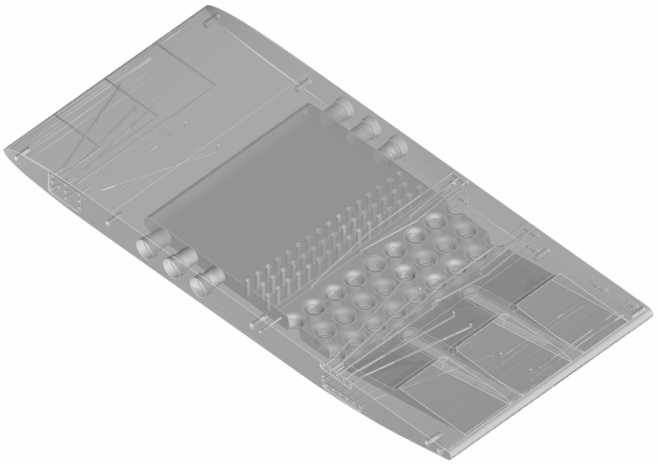

(c) Cast cutback configuration

Figure 4.3: New test plates showing internal configurations.

these pedestals are situated downstream of the plenum feed inlets but upstream of the coolant slot inlets. In the cast-cutback test plate, a further three banks of large pedestals are located downstream of the flow smoothing pedestal banks. The large pedestal banks act as blockage mechanisms, restricting the mass flow rate of the coolant, and are part of the internal cooling design.

The pedestals in the five rows of the datum, machined cutback configurations and the first three rows in the cast cutback configuration test plates are in staggered arrangements. These pedestals are cylindrical without end fillets and staggered. Each pedestal has a diameter of 3.00 mm, height of 10.0 mm and a pitch of 7.5 mm within a row. The rows of pedestals are spaced 4.50 mm apart in the axial direction. The last three rows of the cast cutback configuration test plate have cylindrical, staggered pedestals with end fillets. The nominal diameter of these pedestals are approximately 7.67 mm. The fillet radius is 2.75 mm. The pitch of these pedestals are 15.00 mm within a row. The ends of the pedestals are approximately 12.64 mm in diameter. The rows of pedestals were spaced 7.50 mm apart in the axial direction. It must be noted that the plenum cross sectional area converges as coolant passes through the last three rows of pedestal banks.

Figure 4.4 shows the cross sectional profile dimensions of the coolant holes in the datum and machined cutback test plates. The total coolant stream cross sectional area from all the holes for the datum plate is $1.720 \times 10^{-4}\,\mathrm{m}^2$ and for the machined cutback plate is equal to $1.474 \times 10^{-4}\,\mathrm{m}^2$. The hydraulic diameter for the oval (racetrack) coolant holes are approximately 5.30 mm. This results in a hole pitch to hydraulic diameter ratio of 2.00. The coolant hole length to hydraulic diameter ratio is approximately equal to 8.50 for the datum and machined cutback test plates.

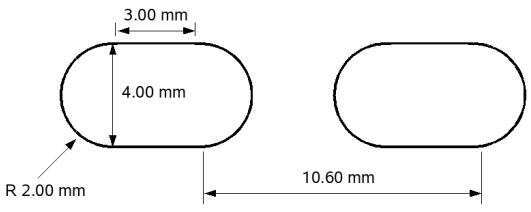

Figure 4.4: Cross sectional dimensions of oval (racetrack) coolant holes of datum and machined cutback test plates.

Figure 4.5 shows the angle of inclination (α) and compound angle (β) of the coolant holes on the machined cutback test plate. The angle of inclination (α) is the angle between the coolant hole axis and the X-Z plane, as shown in figure 4.5. The compound angle (β) is the angle between the coolant holes and the mainstream flow

direction. The hole angle dimensions are the same for the datum test plate. The coolant holes have a shallow inclination angle (α) of 8.0 ° and a compound angle (β) of 28.7 °.

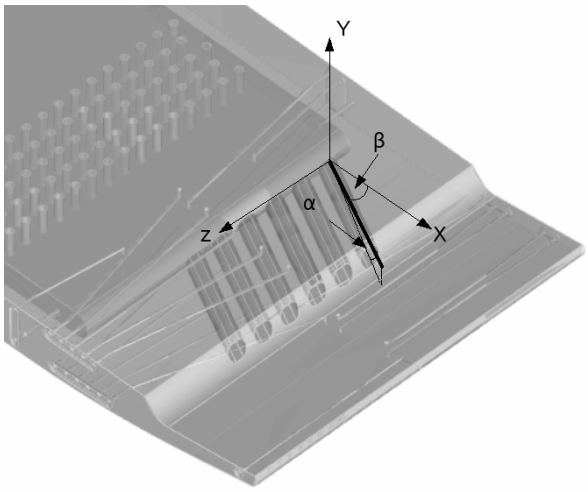

Figure 4.5: Coolant hole angle of inclination (α) and compound angle (β).

Figure 4.6 shows the cross sectional profile dimensions of the three coolant slots in the cast cutback trailing edge cooling configuration test plate. The left and right slot positions are shown in figure 4.2c. The central coolant slot has a coolant flow area of $1.816 \times 10^{-4}\,\mathrm{m}^2$. The two adjacent slots do not have the same cross sectional profile as the central slot. The total coolant flow area of the two adjacent slots is $3.266 \times 10^{-4}\,\mathrm{m}^2$. The total coolant flow area from all three slots is equal to $5.141 \times 10^{-4}\,\mathrm{m}^2$. The hydraulic diameter for the slots are approximately 9.0 mm. The slots are separated by the trailing edge ribs of the test plate which are approximately 45.0 mm apart. This results in a slot pitch to hydraulic diameter of approximately 5.0.

Figure 4.7 shows the cross section of the cast cutback test plate, taken along a plane parallel with flow direction and on the centreline of the test plate. The region shown in figure 4.7 is near the trailing edge of the test plate. From figure 4.7, it can be seen that the coolant exhausts on to the pressure surface at an angle of inclination of approximately 9.5 °. The thickness of the pressure surface lip, prior to the radius is approximately 4.2 mm.

For the cast cutback trailing edge slot cooling geometry, the pressure surface lip to slot height for the three slots is approximately equal to 0.9.

The trailing edge thicknesses for the datum (conventional) and the cast cutback trailing edge cooling configuration test plates were 6.2 mm. The machined cutback trailing edge cooling configuration test plate however had a slightly smaller trailing

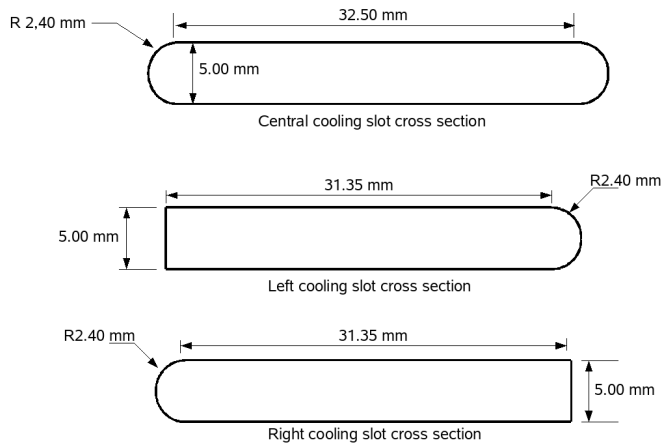

Figure 4.6: Cross sectional profile of the oval (racetrack) slots of the cast trailing edge cutback test plate. The left and right slots are shown in figure 4.2c.

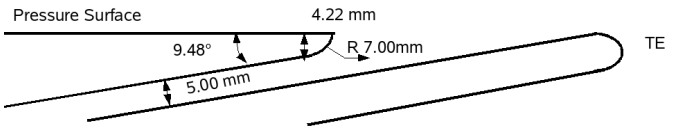

Figure 4.7: Cross section of the near TE region of the cast cutback trailing edge test plate.

edge thickness of 5.3 mm. This is expected, as the machining process of the trailing edge cutback would reduce the trailing edge thickness.

	Datum test plate	Machined-cutback test plate	Cast-cutback test plate
Coolant hole hydraulic diameter	5.3 mm	5.3 mm	9.0 mm
Hole length / Hydraulic diameter	8.5	8.5	-
Hole or slot pitch / Hydraulic diameter	2.0	2.0	5.0
Hole angle of inclination (α)	8.0 ^{o}	8.0 ^{o}	-
Hole compound angle (β)	28.7 ^{o}	28.7 ^{o}	-
Total coolant cross sectional area	1.720×10^{-4} m^2	1.474×10^{-4} m^2	5.141×10^{-4} m^2
Axial distance downstream of coolant ejection to downstream edge of pressure surface	31.20 mm	39.62 mm	50.57 mm
Cutback radius	-	10 mm	-
Cutback lip / slot height	-	-	0.86
Trailing edge thickness	6.20 mm	5.27 mm	6.20 mm

Table 4.2: Coolant hole geometry

The distance from the leading edge of all three test plates to the downstream edge of the pressure surface, prior to the start of the trailing edge curvature, was identical. For the datum test plate, the distance from the downstream edge of the coolant holes to the downstream edge of the pressure surface was approximately 31.2 mm. The distance from the upstream edge of the coolant hole to the downstream pressure surface edge was approximately 58.8 mm. For the machined cutback, the distance from the bottom of the cutback step to the downstream pressure surface edge was 39.6 mm. The distance from the top of the step to the downstream pressure surface edge was 50.4 mm. For the cast cutback test plate, the distance from the slot exit to the downstream edge of the pressure surface was approximately 50.57 mm.

The salient dimensions of the three trailing edge coolant hole test plates are summarised in table 4.2.

4.5 Instrumentation for aerodynamic measurements

Figure 4.3 shows the static tappings, of diameter 1.0 mm, which were incorporated into the stereolith plates during the stereolith process. On all three test plates there are three static tappings on the leading edge surface and a single tapping on the trailing edge surface. The trailing edge static tapping was positioned along the centreline of the test plate. A further 24 static tappings were positioned along the pressure and suction surfaces of the test plates. The internal plena of the test plates were also instrumented with static tappings. For the datum and machined cutback test plates, there were six static tappings, across the plenum, upstream of the coolant hole inlet plane. In the cast cutback test plate, there were six tappings situated across the plenum upstream of the large pedestal banks and a further six tappings, downstream of the large pedestal banks. The detailed locations of all the static tappings on the three test plates are given in Appendix A.

It must be noted that nearly all pressure and suction surface static tappings were located along the centreline of the test plates. Tapping number 25 (see table A.2) on the machined cutback test plate was situated off the centreline of the test plates. This was due to the space restrictions of the static tappings within the test plates.

Further to the test plate static tappings, six static tappings were instrumented 40.0 mm downstream of the trailing edge of the test plate. Four static tappings were also instrumented 445.0 mm upstream of the leading edge of the test tunnel. These static tappings were placed to measure the static pressure variation across the upstream and downstream planes.

All the tappings were connected via a 48 channel Scanivalve^{TM} switchbox to a differential transducer. The transducer used was a SensorTechnics^{TM} PTE5001D1A, 0 - 1 psi differential pressure transducer.

To measure the coolant and flow interaction downstream of the trailing edge, a 2D total pressure traverse system was installed. The probe tip was a circular tube of outer diameter 0.5 mm cut normal to the tube axis, and was located at a distance 40.0 mm downstream of the trailing edge. The total pressure was measured relative to a static tapping on the tunnel wall, at this axial location. It was assumed by the author that the coolant would be sufficiently mixed with the mainstream at this location, resulting in small secondary flow effects. Hence the flow field would be adequately captured by the use of a total pressure probe. A differential pressure transducer, similar to the one detailed above was used to record the data. The probe traversed an area of 1200 mm^2, gathering data from 1200 points. Each data point

within the traverse area was an average of 300 measurements. National Instruments Labview^{TM} software was used with a Measurement Labs CIO-DAS08/Jr/16-AO DAQ card to gather the data.

4.6 Instrumentation for heat transfer measurements

The heat transfer downstream of the coolant ejection was measured using a steady state heat transfer technique. In this technique, the mainstream gas temperature needed to be independently varied from a heated wall, on which heat transfer was to be measured. To facilitate this, a heater mesh, as described in Gillespie (1996), of cross sectional area $2.25 \times 10^{-2}\,\mathrm{m}^2$ was installed 40.00 mm upstream of the leading edge. The mesh was connected to a 1.5 kW DC power supply, which is capable of producing a step change in temperature of the air within the test section. The rise in temperature is approximately 20 °C.

Due to the pressure drop caused by the installed heater mesh, the Reynolds number at the trailing edge drops to a value of approximately 3.63×10^5. This is a transitional flow regime over a flat plate. To ensure that the boundary layer was turbulent at the ejection location, a boundary layer trip wire was installed on the pressure surface of the three test plates at 1.0 mm from the leading edge. The trip wire was 1.0 mm in diameter. Schlichting and Gersten (2004) showed that the critical Reynolds number based on trip wire diameter is approximately 900. Reynolds numbers higher than this would ensure a turbulent boundary layer downstream of the wire. The Reynolds number based on a trip wire diameter of 1.0 mm is approximately 1600. The distance downstream from the trip wire at which the boundary layer would be turbulent was calculated to be 25 mm using the correlations in Schlichting and Gersten (2004).

The mainstream and coolant total temperature was measured using K type thermocouples. Two thermocouples, one placed above the pressure surface and the other placed below the suction surface, were used to measure the mainstream temperature adjacent to the respective surfaces. Two further thermocouples were also placed within the plenum, to measure the coolant total temperature prior to the coolant being fed into the coolant ejection configuration of the test plates. The thermocouple beads were approximately 1.0 mm in diameter.

Furthermore, the pressure surfaces of the test plates were coated with matt black paint, prior to spraying of the liquid crystal. The matt black paint was used to enhance the colours of the liquid crystals. A single liquid crystal solution was sprayed on the

surface. An in depth detail of the heat transfer measurement techniques can be found in chapter 7. To perform an in situ calibration of the sprayed liquid crystals, two K type surface thermocouples were glued onto the pressure surface, near the region of interest.

A surface mounted Kapton insulated flexible heater from Watlow™ and Omega ™ were used to provide the necessary heated wall on which heat transfer was to be measured. The flexible heaters were connected to a SktTronic™ regulated DC power supply, with a variable output of 0-50 V/3 A. A standard digital voltmeter was used to measure the voltage and current supplied to the flexible heaterpads.

All pressure and temperature instrumentation, used in the heat transfer measurements were connected to a National Instruments™ TC-2095 32 channel isothermal terminal block. This terminal block was fed via a National Instruments™ SH96-96 cable to a National Instruments™ PCI-6220 M series DAQ data acquisition card.

4.7 Estimation of experimental errors

To estimate the experimental uncertainties due to the errors in the measured parameters, the method of small perturbation proposed by Moffat (1982) was used. In this method the effect of the errors in the measured parameters are considered in isolation. Moffat (1982) showed that, for a function $y = f(x_1, x_2, x_3, ...)$, where x_1, x_2 and x_3 are independent variables, the typical uncertainty in y can be given by equation 4.3. The worst case uncertainty is given by equation 4.4.

$$\delta y = \left\{ \left(\frac{\partial y}{\partial x_1} \delta x_1 \right)^2 + \left(\frac{\partial y}{\partial x_2} \delta x_2 \right)^2 + \left(\frac{\partial y}{\partial x_3} \delta x_3 \right)^2 + ... \right\}^{\frac{1}{2}} \tag{4.3}$$

$$\delta y = \left| \frac{\partial y}{\partial x_1} \delta x_1 \right| + \left| \frac{\partial y}{\partial x_1} \delta x_2 \right| + \left| \frac{\partial y}{\partial x_3} \delta x_1 \right| + ... \tag{4.4}$$

The partial derivatives in equations 4.3 and 4.4 were computed numerically using the central differencing method as shown in equation 4.6.

$$\begin{aligned} \frac{\partial y}{\partial x_1} &= \frac{f(x_1 + \delta x_1, x_2, x_3, ...) - f(x_1 - \delta x_1, x_2, x_3, ...)}{2\delta x_1} \\ \frac{\partial y}{\partial x_2} &= \frac{f(x_1, x_2 + \delta x_2, x_3, ...) - f(x_1, x_2 - \delta x_2, x_3, ...)}{2\delta x_2} \\ \frac{\partial y}{\partial x_3} &= \frac{f(x_1, x_2, x_3 + \delta x_3, ...) - f(x_1, x_2, x_3 - \delta x_3, ...)}{2\delta x_3} \end{aligned} \tag{4.5}$$

The computed uncertainty was normalised by the initial value of the parameter of concern to obtain a dimensionless fractional error.

In the current research, the student t-distribution was used to establish the ±95% confidence values of the measured pressures and temperatures. Furthermore, in most equations pressure and temperature differences were computed, which would cancel out any bias errors. Therefore only the random errors needed to be considered. Tables 4.3 to 4.5 show the measurement error contributions to the dimensionless error of the mixed out loss, film effectiveness and heat transfer coefficient respectively. Table 4.6 summarises the typical and worst case errors of the measured parameters.

Parameter	Units	Typical value	Measurement error	Dimensionless error
$\dot{m}_c$	kg/s	0.0571	0.000 879	0.005 74
$P_{om} - P_\infty$	Pa	5321.5	362	−0.021 91
P_∞	Pa	94 803	240	−0.005 66
P_{oc}	Pa	107 880	240	0.004 86
T_∞	K	293.1	0.3	−0.000 12
T_c	K	289.6	0.3	0.000 32
			Typical error in ζ	2.38%
			Worst case error in ζ	3.86%

Table 4.3: Typical and worst case error estimates for mixed out loss ζ.

Parameter	Units	Typical value	Measurement error	Dimensionless error
Voltage	V	5.0	0.1	0.001 59
Current	A	0.14	0.01	0.004 13
Area	m^2	6.55×10^{-4}	2.5×10^{-7}	0.0000
T_c	K	295.0	0.3	0.005 27
T_{cr}	K	304.4	0.3	−0.006 65
$T_{rec,m}$	K	302.4	0.3	0.001 38
			Typical error in η	0.97%
			Worst case error in η	1.90%

Table 4.4: Typical and worst case error estimates for film effectiveness η.

Parameter	Units	Typical value	Measurement error	Dimensionless error
Voltage	V	5.0	0.1	0.015 05
Current	A	0.14	0.01	0.054 75
Area	m^2	6.55×10^{-4}	2.5×10^{-7}	−0.000 37
T_c	K	295.0	0.3	0.025 37
T_{cr}	K	304.4	0.3	−0.032 04
$T_{rec,m}$	K	302.4	0.3	0.006 64
			Typical error in h_f	7.03%
			Worst case error in h_f	13.38%

Table 4.5: Typical and worst case error estimates for film heat transfer coefficient h_f [W/m^{2}K] .

Measured Parameter	Typical Error	Worst case error
$\dot{m}_c$	±1.54 %	±1.69 %
M	±3.74 %	±5.11 %
I	±7.17 %	±9.88 %
C_P	±0.48 %	±0.79 %
C_{PT}	±9.24 %	±13.07 %
C_d	±1.75 %	±2.01 %
ζ	±2.38 %	±3.86 %
η	±0.97 %	±1.90 %
h_f	±7.03 %	±13.38 %
Re	±3.41 %	±3.61 %

Table 4.6: Summary of typical and worst case error estimates of the measured parameters.

4.8 Summary

To carry out the comparative study on three trailing edge cooling configurations, a low speed wind tunnel at Southwell Laboratory in Oxford was modified. This chapter details the modifications which were carried out. The geometry of the datum trailing edge cooling configuration was scaled from existing turbine blade trailing edge cooling configuration. The machined and cast cutback trailing edge cooling configurations utilised the same scale factor. The test plates were manufactured using stereolithography. To aid with instrumentation, static tappings were incorporated into the test plates. The geometric features of the three configurations are summarised in table 4.2.

The experiments were carried out at low speed conditions and at a wide range of mass flux ratios. This enabled the author to match the engine mass and momentum

flux ratios. The scaling of the test section was such that the engine Reynolds number was approximately matched. Table 4.1 compares the dimensionless parameters influencing film cooling in the engine with the test conditions.

A new data acquisition system was fitted to the test tunnel with pressure transducers and thermocouples. Furthermore, a BS1042 compliant sharp edged orifice meter was installed to the tunnel to measure the coolant mass flow. Calculations were carried out to estimate the measurement uncertainty. Table 4.6 summarises the typical and worst case error estimates of the measured parameters of the tests.

Chapter 5

Low speed aerodynamic measurements

5.1 Static pressure measurements

Chapter 4 details the instrumentation implemented on the test plates and the test section. In addition to the test plate static tappings, a line of wall static tappings were included upstream and downstream of the test plates. These static tappings were included 445 mm (22.25 plate thicknesses) upstream of the leading edge and 40 mm downstream from the trailing edge of the test plate respectively. Furthermore a total pressure probe was inserted on the centreline of the tunnel, at the same location as the static tappings. Figure 5.1 shows the measured upstream total and static pressure measurements, at a mass flux ratio of zero.

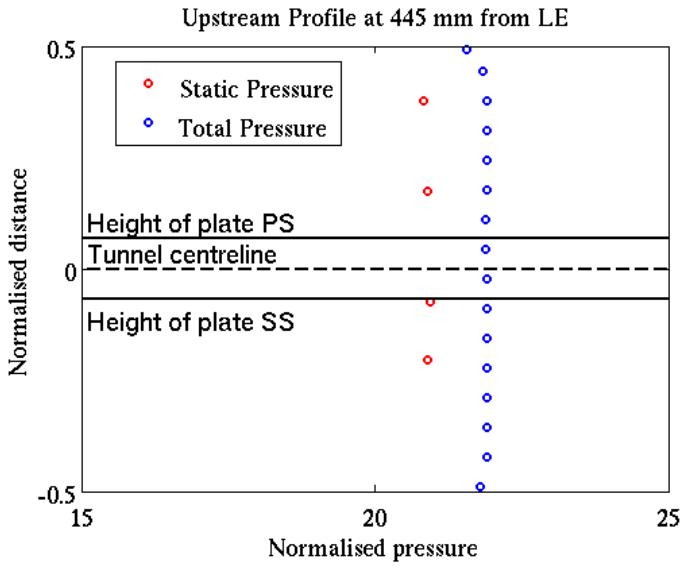

Figure 5.1: Upstream total and static pressure distribution.

The x-axis shows the normalised pressure, whilst the y-axis shows the normalised distance from the top surface to the bottom surface of the test section. The distance across the test section was normalised using the height of the test section, which was 150 mm. The absolute total and static pressure measurements were normalised by the average dynamic head. This average dynamic head was computed using the average total pressure, at a plane 445 mm upstream of the test plate, and the static pressure measurement, which was also located on the same plane and along the centreline of the tunnel. It can be seen from figure 5.1, that the total and static pressure of the upstream flow is uniform across the test section.

Moss (1992) measured the mainstream turbulence of the tunnel, using Dantec^{TM}hot wire anemometer, to be approximately 0.07%. The mainstream turbulence would be small for the heat transfer measurements due to the heater mesh, upstream of the test plates. The tests were carried out for a range of mass flux ratios from 0.3 to 2.0. For each cooling configuration, the coolant mass flow was changed whilst maintaining a constant mainstream mass flux. It must be noted that an exact match of mass flux ratios for the three configurations was not achieved. However the tested range in the mass flux ratios, for the three test configurations, was such that it encompassed the engine mass flux ratio.

Section 4.4 shows the static tappings that were installed into the three test plates. These static tappings were used to map the pressure distribution on the surface of the test plates. The pressure coefficient, C_P, was defined using equation 5.1.

$$C_P = \frac{P_{sf} - P_\infty}{P_{om} - P_\infty} \tag{5.1}$$

In equation 5.1, P_{sf} represents the measured static pressure on the surface of the test plates. P_∞ and P_{om} are the static and total pressure of the mainstream, measured 445 mm upstream of the leading edge of the test plates respectively.

Figure 5.2 shows a typical measured C_P for the machined cutback test plate at mass flux ratio 0.0. The definition of mass flux ratio is given in equation 2.6.

In figure 5.2, the Y-axis represents the coefficient of static pressure whilst the X-axis is the distance of the static tapping from the leading edge normalised against the plate length. From figure 5.2, it can be seen that the static pressure distributions on the pressure and suction surfaces are not similar, as one would expect for a symmetric plate, but vary due to the dissimilar velocities along the respective surfaces. This difference in velocities arises from two effects:

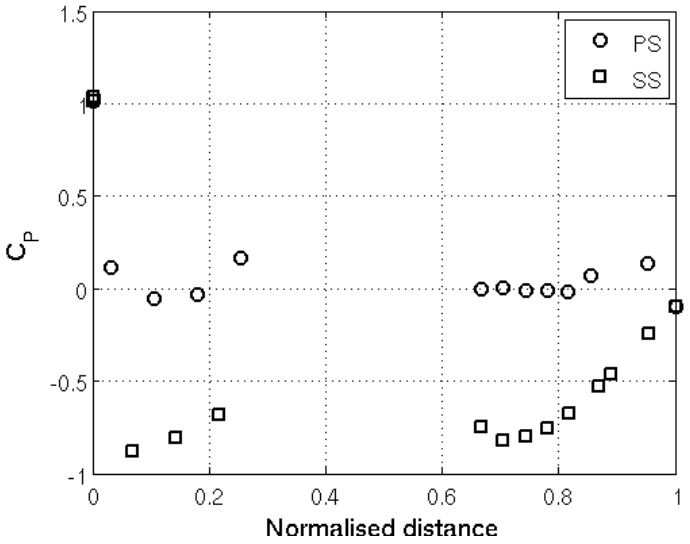

Figure 5.2: Coefficient of pressure data.

1. The asymmetry of the flat plates near the trailing edge, caused by the curvature of the suction surface towards the pressure surface (see section 4.1). This surface shape shifts the flow near the trailing edge towards the pressure surface thus restricting the pressure surface flow. Consequently the velocity is lower on the pressure surface of the plate than that on the suction surface resulting in higher pressures. It must also be noted that the asymmetry of the plate causes the trailing edge wake to be biased towards the pressure surface.

2. The coolant flow, exiting from the pressure surface causes extra blockage to the mainstream. This consequently causes the mainstream flow adjacent to the pressure surface to have a lower velocity, than that adjacent to the suction surface.

Similar trends between the pressure surface and suction surface, C_P, were observed in the datum, machined and cast cut-back plates, for all measured mass flux ratios. It was observed that the variation with mass flux ratios of the measured C_P were small, for all plates, up to the normalised distance of 0.75. Hence it can be concluded that the effect of the blockage due to the coolant over the pressure surface is small compared with the blockage caused by the curvature of the plate.

Figure 5.3 shows the variation in the coefficient of static pressure against mass flux ratio for the three test plates at the first static tapping just upstream of the coolant ejection. The first static tapping on the datum plate is located at a distance of 258.57 mm measured from the leading edge and corresponding to a normalised

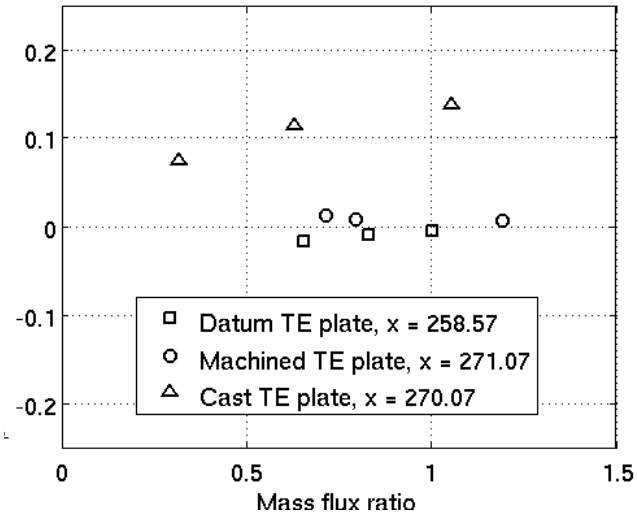

Figure 5.3: Coefficient of pressure against mass flux ratio, plotted in the y-axis, at the first static tapping upstream of the coolant ejection.

distance of 0.78. For the machined and cast cutback test plates, the first static tapping, upstream of the coolant ejection plane, is at a distance of 271.07 mm and 270.07 mm, measured from the leading edge, respectively. These correspond to a normalised distance of approximately 0.82 for both cutback test plates. It can be seen that the coefficient of pressure slightly increases for the datum and cast cutback test plates. This is attributed to the slight mainstream deceleration due to the blockage caused by the coolant stream. The coefficient of pressure for the cast trailing edge test plate has a greater value than those for the datum and machined cutback test plates. This is attributed to the coolant massflow. As the total coolant exit area of the cast cutback test plate is approximately three times greater than that for the datum and machined cutback test plates, the mass flow rate from the cast cutback test plates is greater than the mass flow rate from the machined cutback and datum test plates. This excess mass flow rate causes greater blockage to the mainstream downstream of the test plates. This blockage is seen in the surface static pressure measurements. As the mass flow rate from the machined cutback and datum test plates are similar in magnitude, the resulting blockage to the mainstream caused by the coolant would be similar. Hence the upstream static pressures have similar magnitude.

Static tapping number 22, as shown in appendix A.2, at an axial distance of 283.99 mm is located on the cutback curved surface of the machined cutback test plate. The tapping is located between the third and fourth coolant hole, from the left

as viewed in figure A.2. Figure 5.4 shows the coefficient of static pressure variation with mass flux ratio for static tapping number 22.

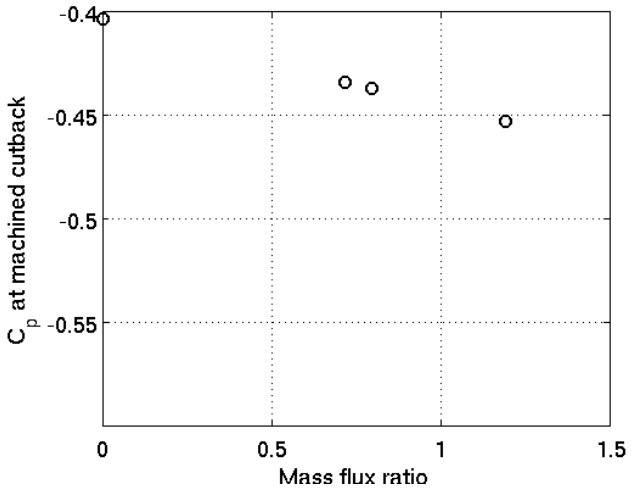

Figure 5.4: Coefficient pressure against mass flux ratio, at the machined cutback surface.

It can be seen from figure 5.4, that the coefficient of static pressure decreases with increasing mass flux ratio. This is attributed to the increased entrainment and mixing of the mainstream with the coolant. This results in a decrease in static pressure on the cutback surface (due to the increase in dynamic head caused by the increased entrained flow), giving rise to the decrease in C_p.

Static tapping number 22 on the datum cooling configuration test plate is located between two coolant holes as shown in appendix A.1. The axial distance to tapping 22, measured from the leading edge is 279.91 mm. Figure 5.5 shows the variation of coefficient of static pressure with mass flux ratio.

Again the C_p is seen to decrease with increasing mass flux ratio, and is due to the increased entrainment and mixing of the mainstream with the coolant, as in the case with the machined cutback test plate. All static tappings, downstream of the coolant ejection, for all three test plates, show the same trend as in figures 5.4 and 5.5. The increasing momentum of the coolant, with increasing mass flux ratio, decreases the surface static pressure downstream of the coolant ejection, and hence a decrease in C_p is observed.

Figures 5.6a and 5.6b show the variation in static pressure coefficient with mass flux ratio and momentum flux ratio, at the trailing edge for the datum, machined cutback and cast cutback plates. It is reassuring to note that the static pressure coefficient at the trailing edge is in the same order of magnitude as the typical values

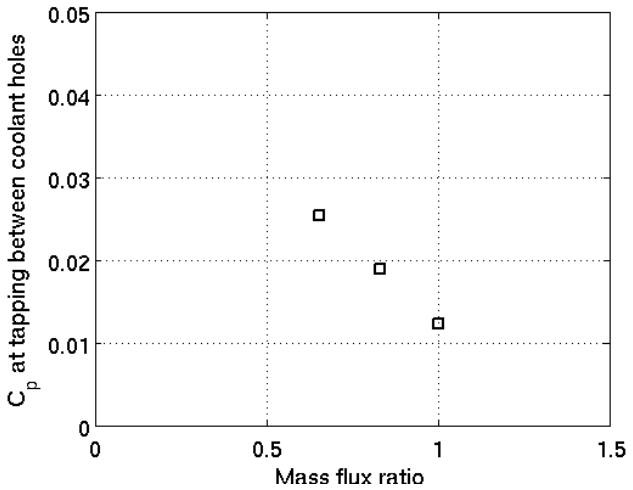

Figure 5.5: Coefficient pressure against mass flux ratio, at the machined cutback surface.

of -0.15 to -0.2, stated in Denton (1993) and measured by O'Malley et al. (1991). In figure 5.6a, it can be seen that the measured static pressure coefficients decrease with increasing mass flux ratio. This decrease in pressure coefficient can be attributed to the increased blockage effect seen by the mainstream. The blockage effect is caused by the coolant streams. The differences in the trailing edge pressure coefficients between the three plates can be attributed to the differences in the cooling geometries of the respective plates.

Figure 5.7 shows the static pressure measurements at the static tappings located 40 mm downstream of the test plates on the test section side wall. The data points in red represent the measurements when the cast cutback plate was installed in the test section, whilst the data points in black represent the measurements conducted with the datum test plate, installed within the test section. From figure 5.7, it can be seen that the static pressure is not uniform as at the upstream location, shown in figure 5.1. For both test plates, the static pressure, above the line representing the pressure surface, appears to be constant. The static pressure, below the line representing the suction surface, is lower than that on the pressure surface side, and decreases away from the suction surface. This difference in static pressure is due to the curvature of the suction surface near the trailing edge of the test plates.

It can also be seen from figure 5.7 that there is a difference in the measured static pressure between the mass flux ratios on each test plate, and also between each test plate. These are due to the interactions between the coolant and the mainstream and the blockage to the mainstream flow caused by the coolant ejection.

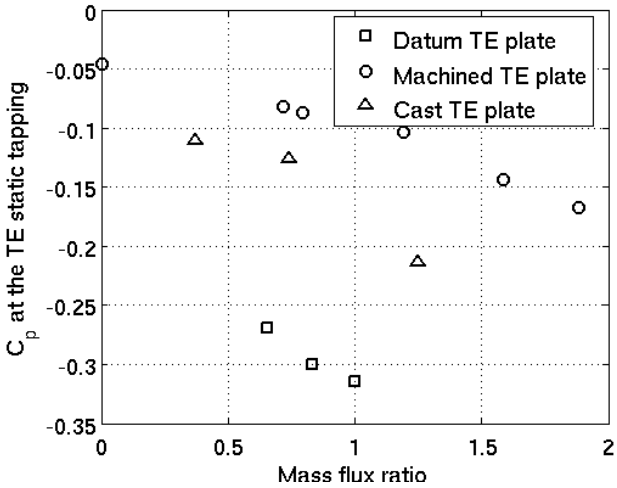

(a) C_P at TE tapping location vs Mass flux ratio

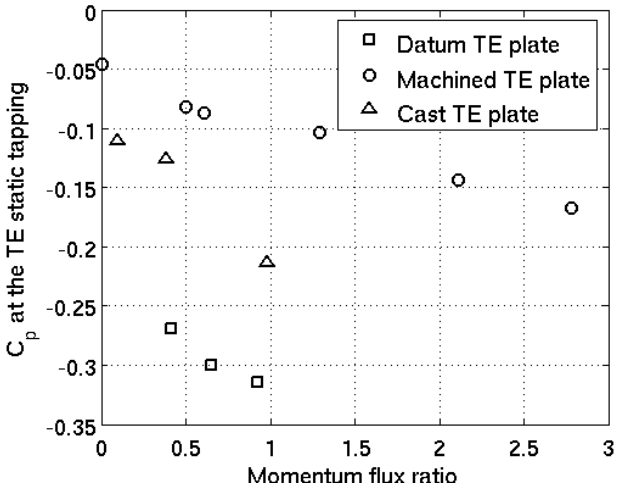

(b) C_P at TE tapping location vs Momentum flux ratio

Figure 5.6: C_P at TE tapping location.

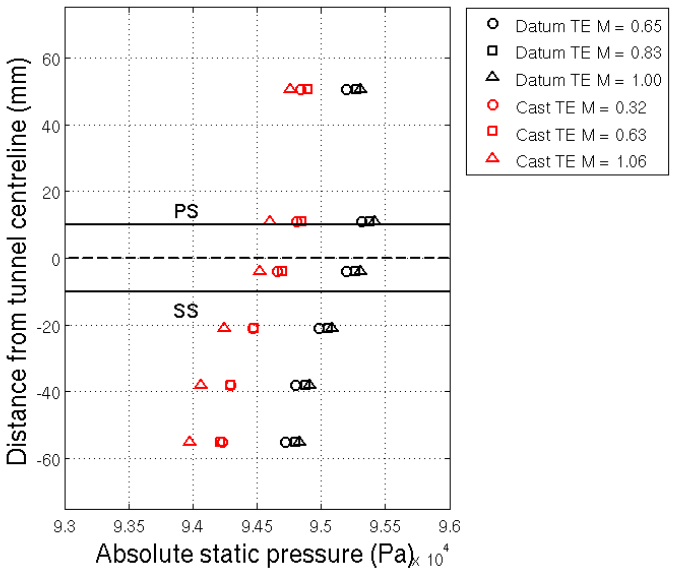

Figure 5.7: Sidewall static pressure measurements across test section 40 mm downstream of test plate trailing edge.

Downstream static pressure measurements were not obtained when the machined cutback test plate was in the test section. However, the author believes that the static pressure measurements would be similar to the datum test plate case.

5.2 Calculating discharge coefficients

The discharge coefficient is defined as the ratio between the actual / measured mass flow rate of the fluid to the ideal mass flow rate and is computed using equation 5.2. In the case of film cooling, the discharge coefficient of the cooling configuration can be computed with and without the presence of the mainstream flow. The discharge coefficient reported in this section was computed in the presence of mainstream flow.

$$C_d = \frac{\dot{m}_{Ac}}{\dot{m}_{Ic}} \tag{5.2}$$

The actual mass flow rate of the coolant, $\dot{m}_{Ac}$, was measured using a British Standard orifice meter, as mentioned in section 4.1. The ideal mass flow rate, $\dot{m}_{Ic}$, was computed from the isentropic expansion of the coolant, from the coolant total pressure within the plenum, to the exit static pressure, using equation 5.3. It must

be noted that equation 5.3 is used to compute the compressible unchoked ideal mass flow rate.

$$\dot{m}_{Ic} = \frac{AP_{oc}}{\sqrt{RT_{oc}}} \left(\frac{P_s}{P_{oc}}\right)^{\frac{1}{\gamma}} \sqrt{\frac{2\gamma}{\gamma - 1}\left[1 - \left(\frac{P_s}{P_{oc}}\right)^{\frac{\gamma-1}{\gamma}}\right]} \tag{5.3}$$

In equation 5.3, P_{oc} and T_{oc} are the total pressure and temperature of the coolant inside the plenum respectively. The total temperature was measured using two K type thermocouples. The location of the thermocouples are shown in chapter 4. There was no total pressure probe within the plena of the three test plates. Hence the mean static pressure across the plenum, upstream of the coolant hole inlets for the datum and machined cutback test plates was used as the total coolant pressure in the computation of the discharge coefficient. In the case of the cast cutback test plate the mean static pressure across the plenum, upstream of the last three pedestal banks was used to compute the discharge coefficient. It was decided to use computational fluid dynamics simulations of the test conditions to correct for the coolant total pressure. This study is shown in chapter 7.

In equation 5.3 A refers to the cross sectional area of the coolant passage. The cross sectional areas used in the discharge coefficient analysis are given in table 4.2. P_s is the static pressure just upstream of the coolant exit plane, on the pressure surface of the test plates. Table 5.1 summarises the location of these exit tappings, measured from the leading edge of the test plates.

Test plate	Location of exit static tapping from leading edge (mm)
Datum plate	258.57
Machine cutback plate	271.07
Cast cutback plate	270.07

Table 5.1: Location of exit static tapping location for the three test plates

Figure 5.8 shows the measured discharge coefficient for the three plates plotted against mass, momentum, flux and pressure ratios. It can be seen that the discharge coefficients for all three test plates are very similar. However, the cutback plates have slightly higher discharge coefficients than the datum plate. The effect of the static pressure distribution around the cooling holes at ejection, in the presence of cross flow, is a complex one, and described in detail in Rowbury et al. (2001). For lower mass flux ratios, the coolant jet, with lower momentum, is deflected or turned

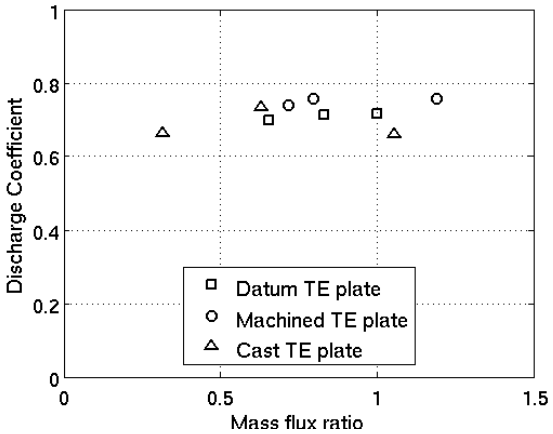

(a) Discharge coefficient vs Blowing ratio

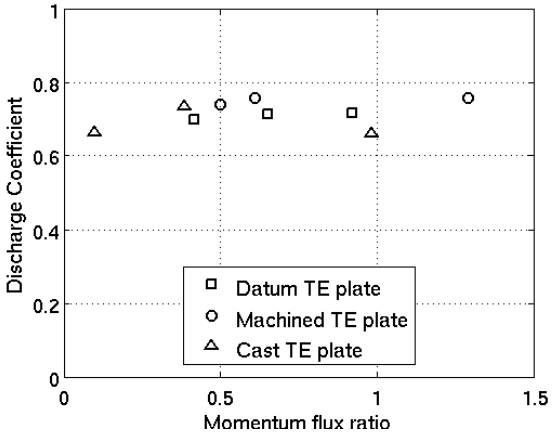

(b) Discharge coefficient vs Momentum flux ratio

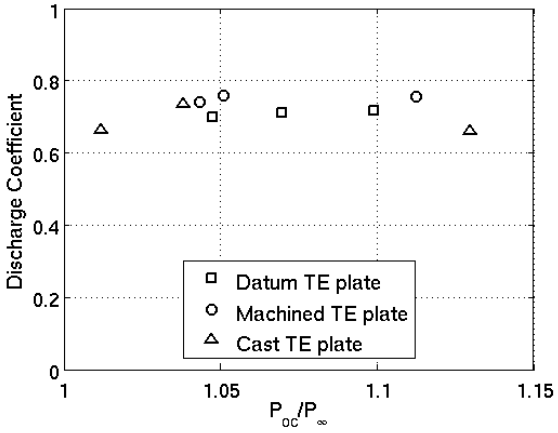

(c) Discharge coefficient vs Pressure ratio

Figure 5.8: Discharge coefficient against mass flux, momentum flux and pressure ratios.

towards the downstream surface of the coolant holes by the mainstream, and hence a "pinching" or "capping" effect of the coolant is observed. This is a well documented effect to which Rogers and Hersh (1975) proposed the "lid model". This phenomenon is also clearly shown in Fitt et al. (1985). However, for the cutback plates, the film cooling hole ejection plane is shielded from the mainstream (due to the flow separation at the cutback) and the coolant would not experience such a "pinching" or "capping" effect. Hence the discharge coefficients of the cutback configurations are slightly larger than the datum configuration as shown in figure 5.8. The research by Martini et al. (2005) shows similar trends in the discharge coefficients for the cast cutback configuration. Direct comparison of the discharge coefficient for the cast cutback configuration cannot be made with Martini et al. (2005), as the internal cooling configurations of Martini et al. (2005) were different to the current research.

At high mass, momentum and pressure ratios, the discharge coefficient appears to be independent of the plate configuration. This trend can be attributed to the coolant streams from all three test plate configurations behaving as discrete jets with high momentum. The momentum of the mainstream is not sufficiently high so as to affect the coolant flow.

5.3 Two dimensional traverse measurements

The flow profile downstream of the trailing edge was studied with the aid of a two dimensional total pressure traverse. The traverse plane is perpendicular to the tunnel flow direction, and situated 40 mm downstream of the trailing edge. Figure 5.9 shows the location of the traverse plane relative to the plate trailing edge. The positive X and Y coordinates with the origin of the traverse plane are marked in figure 5.9.

To ascertain the area of traverse, discrete line traverses were conducted at different X coordinates on the traverse plane shown in figure 5.9. The lines were 10 mm apart in the X direction. Each data point was 1 mm apart in the Y direction and was an average of 300 readings. The total pressure was recorded relative to the tunnel wall static tapping located 40 mm downstream of the trailing edge of the test plate. As the interaction of the coolant stream with the mainstream was of interest, the regions near the tunnel walls were not traversed in this study. Data along lines parallel to the Y axis were measured for the datum plate configuration over a range of Y to within 20 mm of the wall.

The line traverse data was only gathered for the datum plate configuration.

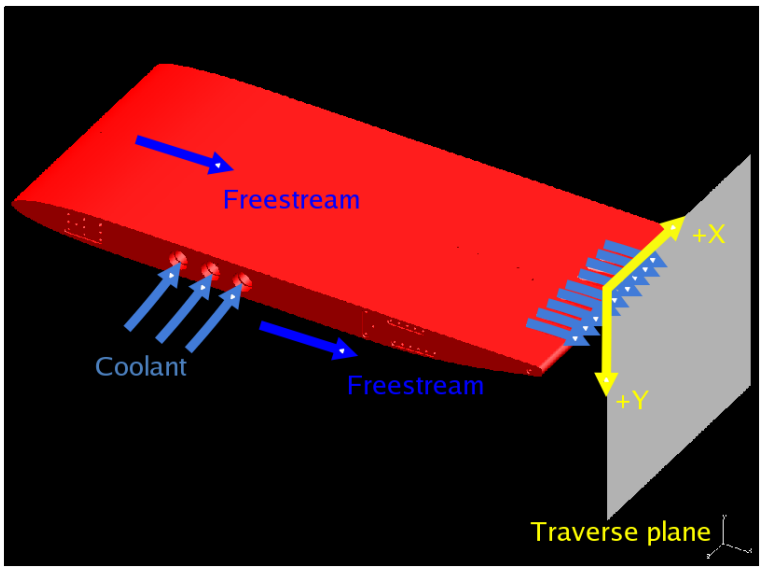

Figure 5.9: Traverse plane location 40 mm downstream of trailing edge.

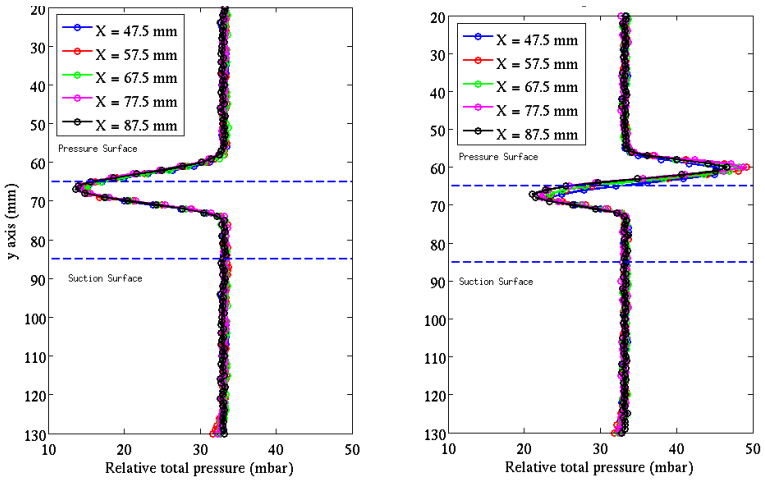

Figure 5.10: Relative total pressure (mbar) at discrete X locations on the traverse plane.

The data shown in figure 5.10 indicate that there is a variation in total pressure within the range of Y = 50 mm to Y = 80 mm. Outside of this range the variation of the total pressure was observed to be negligible. Hence, the range in the Y direction for the 2D traverse was chosen to be Y = 50 mm to Y = 80 mm. Table 5.2 shows the ranges in the X and Y direction for the three test plates. The X direction range was chosen such that the effects of the coolant stream on the mainstream from three coolant holes would be measured for the datum and machined cutback plates. In the case of the cast cut-back plate, the interaction from 1.5 slot widths would be measured.

Test plate	x min (mm)	x-max (mm)	y min (mm)	y max (mm)
Datum plate	32.0	75.0	50.0	80.0
Machine cutback plate	53.5	92.5	50.0	80.0
Cast cutback plate	35.0	100.0	50.0	80.0

Table 5.2: 2D traverse range for the three test plates.

For ease of comparison of the total pressure plots with varying mass flux ratios, the measured total pressure in the traverse plane was normalised using equation 5.4. Figures 5.11 to 5.13 show this normalised total pressure.

$$C_{PT} = 1 - \frac{P_{Tt}}{P_{om}} \tag{5.4}$$

In figures 5.11 to 5.13, a positive value (colour red) indicates loss in total pressure from mainstream value whilst a negative value indicates an increase of total pressure. The solid line in figures 5.11 to 5.13 represents the pressure surface of the test plates. The dashed line represents the test section centreline. In the figures 5.11 and 5.12, the wakes due to the coolant jets, ejected from the cooling holes, can be seen in the traverse measurements. At low mass flux ratios, the interaction between the mainstream and coolant stream causes the coolant jets to be more aligned in the direction of the mainstream flow. With increasing mass flux ratio, the coolant momentum flux ratio increases, and the coolant jets align in the direction of the coolant hole angle of inclination. On the traverse measurements, this is seen by the shifting of the wakes towards the right on the traverse plane. Furthermore, as the mass flux ratio increases, regions of large C_{PT} decrease, indicative of the wakes being filled by the coolant stream.

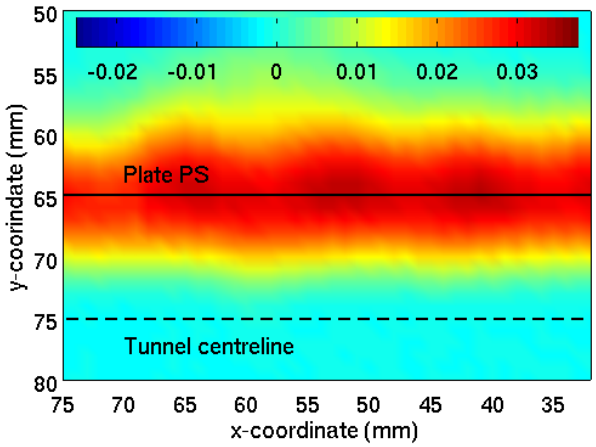

(a) Blowing ratio 0.65

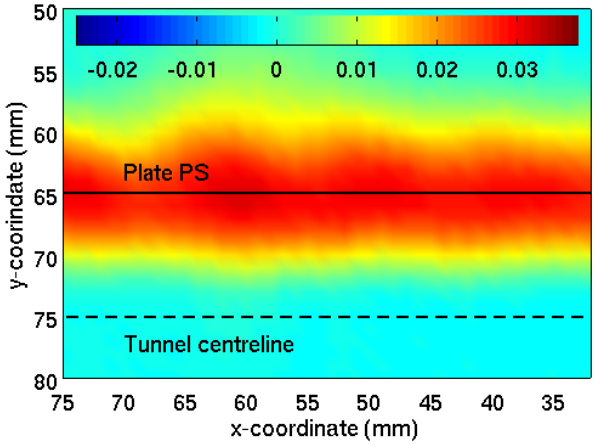

(b) Blowing ratio 0.83

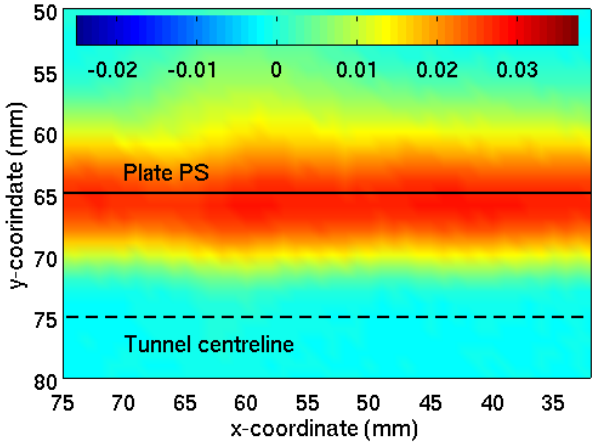

(c) Blowing ratio 1.00

Figure 5.11: 2D traverse measurements 40 mm downstream of the datum test plate.

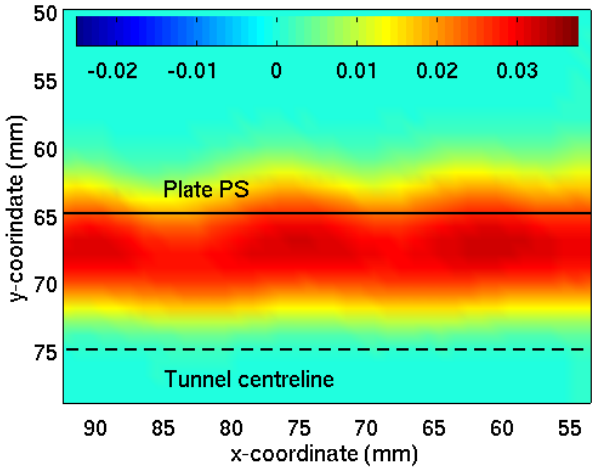

(a) Blowing ratio 0.72

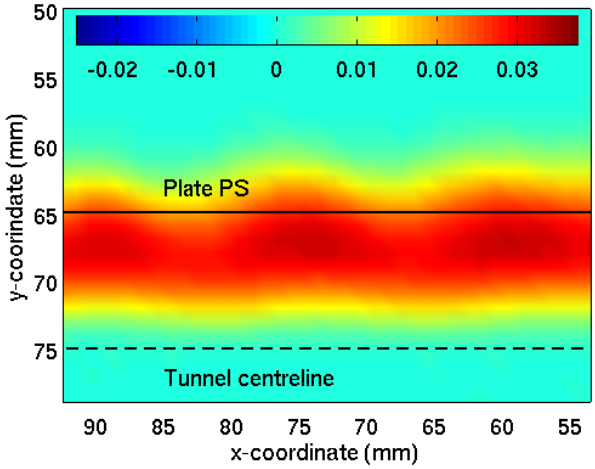

(b) Blowing ratio 0.80

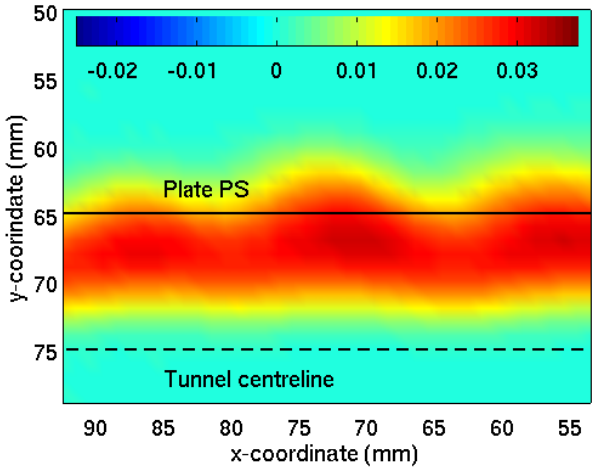

(c) Blowing ratio 1.20

Figure 5.12: 2D traverse measurements 40 mm downstream of the machined cutback test plate

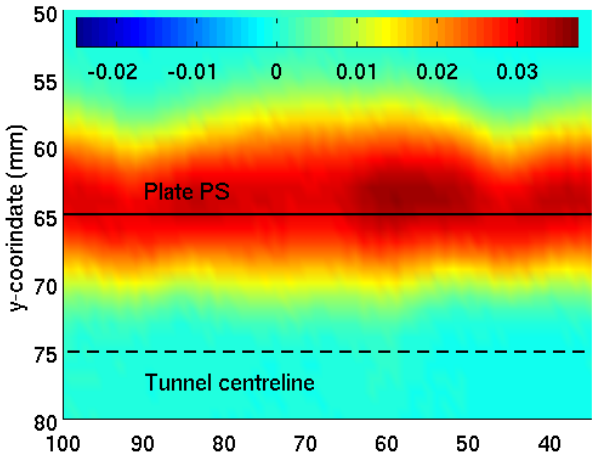

(a) Blowing ratio 0.32

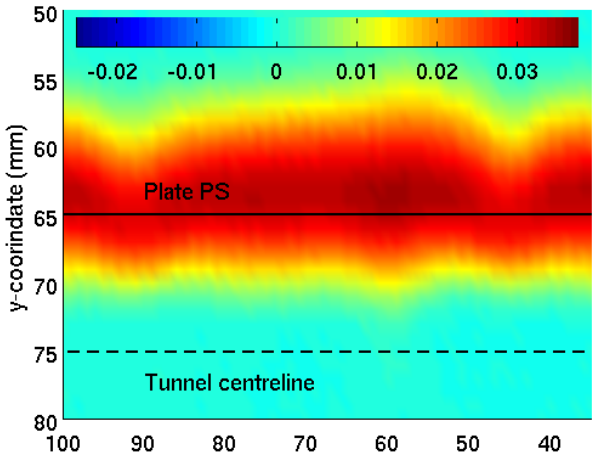

(b) Blowing ratio 0.63

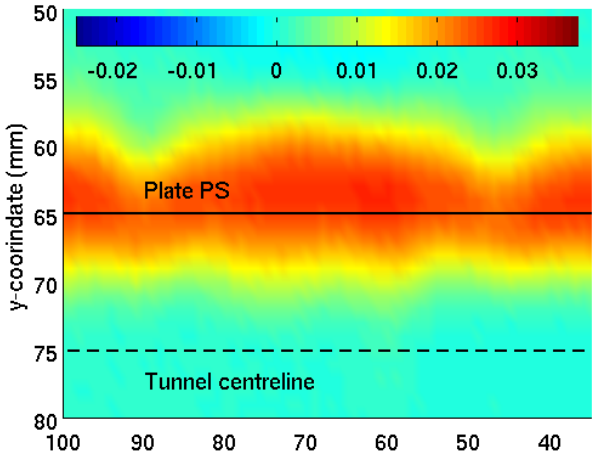

(c) Blowing ratio 1.06

Figure 5.13: 2D traverse measurements 40 mm downstream of the cast cutback test plate

Telisinghe et al. (2006) shows traverse measurements downstream of the test plates with coolant holes aligned in the direction of the mainstream flow. It can be seen from the cutback total pressure traverse measurements that the wakes are not clearly visible until mass flux ratio of 1.9. The coolant stream, in the cutback test plate case, shown in Telisinghe et al. (2006) interact with the mainstream, and mixing out within the wake caused by the pressure and suction surface of the test plate, and the cutback. However, with inclined coolant holes, this interaction is much smaller and hence the wakes due to the coolant jets are seen at a much lower mass flux ratio of 0.93.

In the cast cutback test plate traverse measurements, figure 5.13, the wakes due to the two lands, either side of the central slot, are clearly visible. As the mass flux ratio increases, C_{PT} decreases, indicating the wake due to the pressure and suction surface of the test plate and cutback, is being filled by the coolant stream.

From these plots, it can be seen that the machined cutback configuration and the datum configuration have a similar total pressure profile. The wake region for the cast cutback plate configuration is larger than the regions for the datum and machined cutback cases.

5.4 Local loss analysis

The laterally averaged C_{PT} (local total pressure ratio at the measurement plane) is shown in figure 5.14 for the three test plates. For the datum and machined cutback plates, the C_{PT} was laterally averaged over two hole pitches. For the cast cutback test plate, C_{PT} was averaged over the central slot. From figure 5.14, it can be seen that the wakes from all three test plates are biased towards the pressure surface of the test plates. This is due to the curvature of the suction surface of the test plates, towards the pressure surface.

From figure 5.14a, as the mass flux ratio is increased, the depth of the wake decreases. This is due to the coolant stream filling the wake region caused by the pressure and suction surface of the test plate. The change in depth of the wake for the machined cutback test plate shown in figure 5.14b is very small, increasing slightly when the mass flux ratio is increased from $M = 0.75$ to $M = 0.82$ ($I = 0.55$ to $I = 0.65$). The depth of the wake, however, decreases as the mass flux ratio is further increased to $M = 1.06$. A similar trend is observed in the laterally averaged C_{PT} of the cast cutback test plate, shown in figure 5.14c. The increase in C_{PT} wake depth with increasing mass flux ratio, at low mass flux ratios, was observed by Pappu

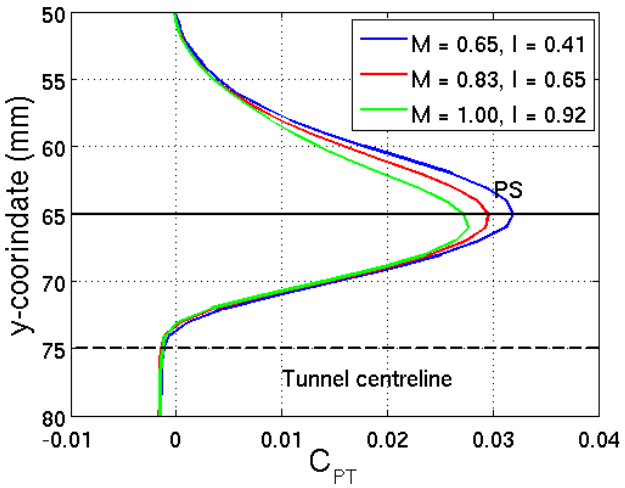

(a) Datum plate laterally averaged total pressure ratio over 2 hole pitches

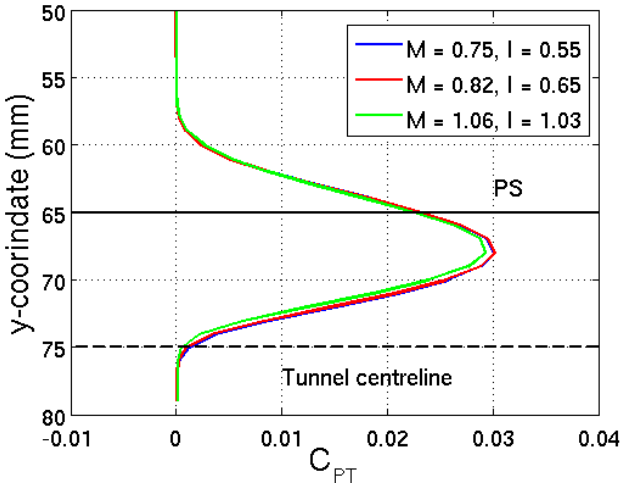

(b) Machined cutback laterally averaged total pressure ratio over 2 hole pitches

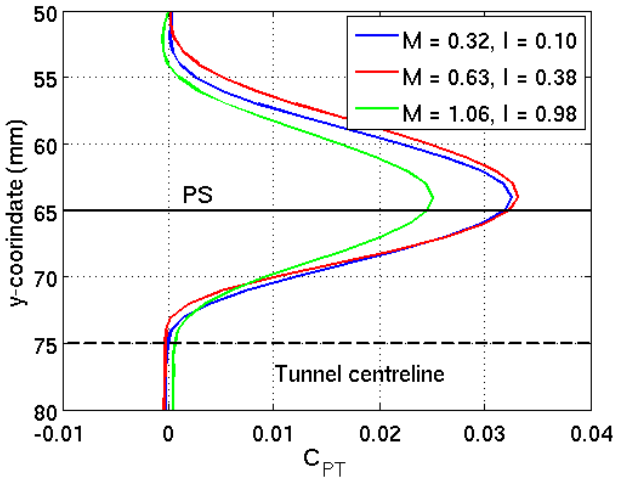

(c) Cast cutback laterally averaged total pressure ratio over 1 slot

Figure 5.14: Laterally averaged total pressure ratio for test plates.

and Schobeiri (1997) and Uzol and Camci (2001a). This increase in wake depth with increasing mass flux ratio, at low mass flux ratios was attributed to the increased mixing between the mainstream separating over the cutback edge on the pressure surface and the coolant jet shear layer. As the mass flux ratio increased further, the coolant jet total pressure fills the wake, and the increased momentum of the coolant restricts the mixing between the separated mainstream and the coolant jets. Hence the reduction in the total pressure loss C_{PT} is seen.

It must also be noted that the wake width of the C_{PT} plots for the datum and machined cutback are similar, whilst the width of the C_{PT} wake for the cast cutback is much larger. This is due to the increased mixing seen downstream of the cast cut-back plate, caused by the increased coolant exhaust area, which results in the increased coolant mass flow, compared with the datum and machined cut-back plates.

5.5 Mixed out loss analysis

The total pressure loss plots shown in the previous section indicate that the machined cutback plate and the datum plate have similar total pressure loss whilst the cast cutback plate has a much deeper wake. However, the total pressure losses do not take into account the total pressures within the coolant plena, which are dissimilar. To compare the losses due to coolant and mainstream mixing of the datum and cutback plates' geometries, a mixed out loss coefficient was computed. This loss coefficient for the three cases was determined by evaluating the kinetic energy at a mixed out plane far downstream from the traverse plane. It must be noted that the mixed out loss method shown below is based on the method shown in Mee (1992).

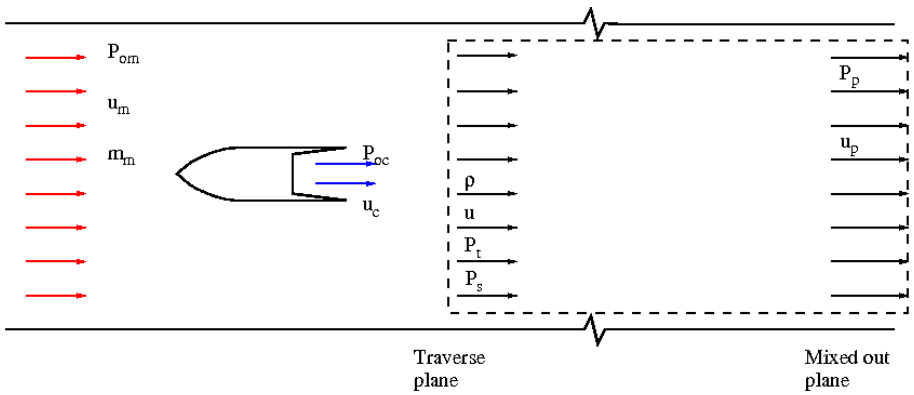

Figure 5.15: Generic trailing edge ejection.

Figure 5.15 is a schematic diagram showing the measurement plane and the mixed out plane downstream of the test plates. Assuming that

1. coolant and mainstream are ideal gases, having total temperatures T_{om} and T_{oc} respectively,
2. the static pressure P_p and temperature T_p at the mixed out plane is assumed to be constant,
3. the coolant and mainstream have completely mixed together at the mixed out plane,
4. the generic aerofoil and tunnel is assumed to be frictionless and adiabatic.

Applying the momentum equation to the control volume from traverse plane to the mixed out plane,

$$\int_{\frac{-H}{2}}^{\frac{H}{2}} \rho u^2 \, \mathrm{d}y \; - \int_{\frac{-H}{2}}^{\frac{H}{2}} \rho_p u_p^2 \, \mathrm{d}y \; = (P_p - P_s)H \tag{5.5}$$

Mass balance through the control volume gives

$$\dot{m}_m + \dot{m}_c = \rho_p u_p H \tag{5.6}$$

Re-arranging equation 5.6 and using the equation of state, the velocity at the mixed out plane can be given by

$$u_p = \frac{(\dot{m}_m + \dot{m}_c)RT_p}{HP_p} \tag{5.7}$$

Substituting equation 5.7 into equation 5.5

$$\int_{\frac{-H}{2}}^{\frac{H}{2}} \rho u^2 \, \mathrm{d}y \; - H\rho_p \left(\frac{(\dot{m}_m + \dot{m}_c)RT_p}{HP_p} \right)^2 = (P_p - P_s)H \tag{5.8}$$

Equation 5.8 can be re-arranged to give a quadratic in P_p as shown in equation 5.9, where $I = \int_{\frac{-H}{2}}^{\frac{H}{2}} \rho u^2 \, \mathrm{d}y$

$$P_p^2 H^2 - (P_s + \frac{I}{H})H^2 P_p + (\dot{m}_m + \dot{m}_c)^2 RT_p = 0 \tag{5.9}$$

The temperature at the mixed out plane is given by

$$T_p = T_{om} - \frac{u_p^2}{2C_p} = T_{om} - \frac{(\dot{m}_m + \dot{m}_c)^2 R^2 T_p^2}{2C_p P_p^2 H^2} \tag{5.10}$$

Re-arranging equation 5.10, substituting $C_p = \frac{\gamma R}{\gamma - 1}$ and dividing T_p,

$$H^2 P_p^2 \left(\frac{T_{om}}{T_p} - 1 \right) \frac{2\gamma}{\gamma - 1} - (\dot{m}_m + \dot{m}_c)^2 \, RT_p^2 = 0 \tag{5.11}$$

By adding equations 5.9 and 5.11, the static pressure at the mixed out plane can be shown to equal

$$P_p = \frac{P_s + \frac{I}{H}}{\frac{2\gamma}{\gamma-1}\left(\frac{T_{om}}{T_p} - 1\right) + 1} \tag{5.12}$$

From equation 5.12, it can be seen that the P_p is a function of T_p. Therefore through a process of iteration, the static pressure and temperature at the mixed out plane could be obtained.

The kinetic energy of the actual fluid at the mixed out plane is given by

$$KE_{actual} = (\dot{m}_m + \dot{m}_c)\frac{1}{2H^2}\left(\frac{\dot{m}_m + \dot{m}_c}{\frac{P_p}{RT_p}}\right)^2 \tag{5.13}$$

Considering the mainstream with total pressure P_{om} and total temperature T_{om} isentropically expanded to a static pressure P_p at the mixed out plane, the ideal kinetic energy is given by

$$KE_{Ideal} = \frac{1}{2}mu^2 \tag{5.14}$$

Now, the velocity could be written by

$$u^2 = M^2\gamma RT_p \tag{5.15}$$

Using the isentropic relations, the Mach number could be shown as equal to

$$M^2 = \frac{2}{\gamma - 1}\left(\left(\frac{P_{om}}{P_p}\right)^{\frac{\gamma-1}{\gamma}} - 1\right) \tag{5.16}$$

and the static temperature is equal to

$$T_p = T_{om}\left(\frac{P_s}{P_{om}}\right)^{\frac{\gamma-1}{\gamma}} \tag{5.17}$$

Substituting equations 5.15, 5.16 and 5.17 into 5.14, the ideal kinetic energy for the mainstream is given by

$$KE_{Idealmainstream} = \dot{m}_m\frac{\gamma}{\gamma-1}\frac{P_{om}}{\rho_{om}}\left(1 - \left(\frac{P_p}{P_{om}}\right)^{\frac{\gamma-1}{\gamma}}\right) \tag{5.18}$$

By using the substitution $\frac{P_p}{P_{om}} = \frac{P_{om}-(P_{om}-P_p)}{P_{om}}$ and binomial expansion, the ideal kinetic energy of the mainstream could be shown to be equal to equation 5.20

$$KE_{Idealmainstream} = \frac{\dot{m}_m}{\rho_{om}}(P_{om} - P_p)\left(1 - \frac{1}{2\gamma}\frac{P_{om} - P_p}{P_{om}} + \ldots\right) \tag{5.19}$$

Writing a similar equation for the coolant stream, the total ideal kinetic energy is given by

$$KE_{Ideal} = \frac{\dot{m}_m}{\rho_{om}}(P_{om} - P_p)\left(1 - \frac{1}{2\gamma}\frac{P_{om} - P_p}{P_{om}} + \ldots\right) + \frac{\dot{m}_c}{\rho_{oc}}(P_{oc} - P_p)\left(1 - \frac{1}{2\gamma}\frac{P_{oc} - P_p}{P_{oc}} + \ldots\right) \quad (5.20)$$

By dividing equation 5.13 by equation 5.20, the mixed out loss coefficient can be computed as shown in equation 5.21

$$\xi = 1 - \frac{KE_{actual}}{KE_{Ideal}} \quad (5.21)$$

The actual and ideal kinetic energy at the mixed out plane was evaluated over a scaled pitch height. This pitch height corresponds to the pitch of a typical turbine blade scaled on the film cooling hole diameter.

Figure 5.16 shows the mixed out loss plotted against mass flux ratio, momentum flux ratio and the coolant to mainstream mass flow rate ratio. The coolant mass flow rate was measured using an orifice meter as described in section 4.3. The mass flow rate of the mainstream was computed over a scaled pitch height as described above. As expected, the mixed out losses increase with increasing mass flux ratio as seen in figure 5.16a. The differences in mixed out losses between the datum and machined cutback test plates are marginal, with the datum test plate having slightly greater losses than the machined cutback test plate. This difference is pronounced at low mass (M = 0.6 to 0.8) and momentum flux ratios. Bogard (2007b) stated that cooling holes with compound angles presented a broader profile to the mainstream. This increased profile would result in the increased mixing of the coolant with the mainstream. With the machined cutback test plate, at low mass flux and hence low momentum flux ratios, the coolant fills the wake region caused by the mainstream separating over the pressure surface cutback, and is shown in the local loss profile for the machined cutback (figure 5.14b). As the mass flux ratio increases, the mixing of the coolant with the mainstream dominates, and hence the mixed out losses for the two plates are nearly identical.

Considering the cast cutback test plate, the local loss profiles in figure 5.14c show a much broader and deeper wake than those for the machined cutback and datum test plates. This was attributed to the increase in coolant mass flow for the cast cutback plate, when compared with the machined cutback and datum plates, resulting in

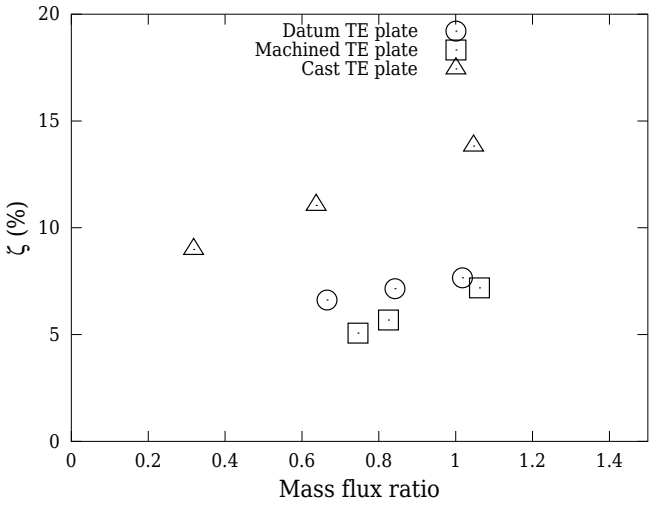

(a) Mixed out loss against mass flux ratio

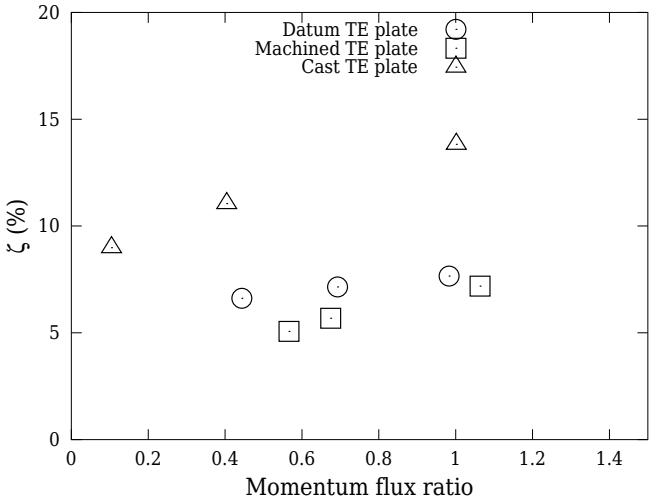

(b) Mixed out loss against momentum flux ratio

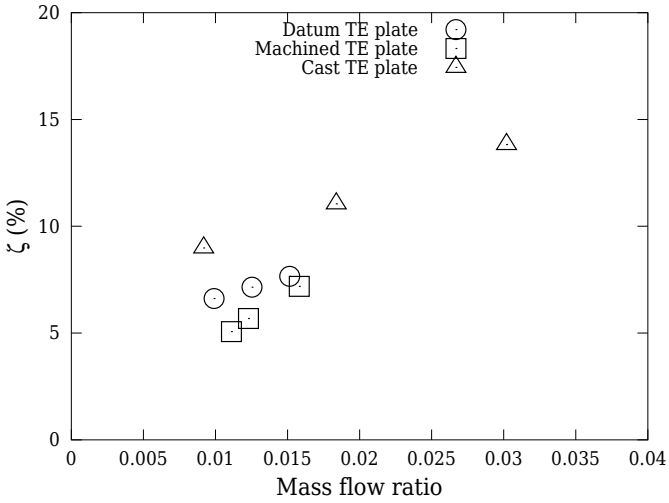

(c) Mixed out loss against coolant to mainstream mass flow ratio

Figure 5.16: Mixed out loss coefficient for the three trailing edge cooling configurations.

increased mixing. Figure 5.16 also shows that the mixed out loss for the cast cutback test plate is much greater than those for the datum and machined cutback test plates.

5.6 Conclusions

This chapter presents the low speed aerodynamic results for the three tested test plates. The discharge coefficients for the three test plates were comparable. As expected, the cutback test plates had a slightly greater discharge coefficient than the datum configuration. This was attributed to the "capping" effect experienced by the pressure surface coolant holes on the datum test plate. The machined and cast cutback test plates do not experience this "capping" effect by the mainstream.

From the traverse measurements 40.0 mm downstream of the trailing edges of the three test plates, it was observed that the wakes from the datum and machined cutback test plates were similar in width, whilst the cast cutback test plate had a larger width. From the traverse measurements shown in figures 5.11 and 5.12, the discrete coolant stream can be seen. From the traverse measurements of the cast cutback configuration, the location of the ribs, which extend towards the trailing edge, can be seen.

The local, total pressure loss profiles show that the machined cutback and datum test plates have similar sizes of wakes, whilst the cast cutback test plate has a wider and deeper wake. As the mass flux ratio increased, these wakes were filled by the coolant.

A mixed out loss was computed for the three test plates, incorporating the mainstream and coolant total pressures, unlike in the total pressure loss profiles. The mixed out losses for the datum and machined cutback test plates were similar in magnitude, with the datum test plate having slightly higher losses than the machined cutback test plate for low mass and momentum flux ratios (less than unity). At high momentum flux ratios (greater than unity), the mixed out losses for the two test plates are the same. The marginally higher mixed out loss for the datum test plate at low mass and momentum flux ratios is due to the mixing of the coolant with the mainstream. In the case of the machined cutback test plate, the coolant fills the wake region caused by the mainstream separating over the pressure surface cutback, resulting in less mixing with the mainstream flow and hence lower mixed out loss.

The mixed out loss for the cast cutback cooling configuration was greater than the datum and machined cutback cooling test plate when plotted against mass and momentum flux ratios. The mixed out losses plotted against coolant to mainstream

mass flow ratio also showed that the cast cutback configuration generated more mixed out losses compared with the machined cutback and datum cooling configurations, for a similar coolant to mainstream ratio. This increase in loss for the cast cutback configuration was attributed to the cooling configuration, which results in increased mixing of the coolant and mainstream.

Even though the discharge coefficients for the three test plates were comparable, the cast cutback test plate, with the trailing edge cooling configuration described in section 4.4, produced more loss than the machined cutback and datum cooling configurations.

Chapter 6

CFD predictions of low speed aerodynamic measurements

This chapter describes the computational fluid dynamics (CFD) predictions conducted of the low speed aerodynamic experiments. Steady CFD captures the gross flow field but is unable to resolve the small scale eddies which contribute to pressure losses in the system. The primary aim of using CFD in the current work was to visualise the steady flow field in the experiments and to aid in the understanding of the trends seen in the experimental results. The simulations also enabled the author to judge the suitability of using a commercial steady CFD code to predict the fluid measured losses in the experiment. Fluent^{TM}version 6.1.12 was used to predict the flow field of the experiments.

6.1 Geometry cleanup

The CAD geometries used to create the stereolith test plates were used in the CFD predictions of the low speed aerodynamic measurements. These geometries were directly imported into ICEMCFD^{TM}for geometry cleanup and the subsequent meshing operations. The static tappings, including all the internal pipe network, which were included in the CAD geometries of the test plates, were deleted from the CFD model. The full tunnel cross section of $2.25 \times 10^4\,\mathrm{mm}^2$ was represented around the test plate in the CFD model. The computational domain extended from 0.5 m upstream to 1 m downstream of the plate leading edge. The test section upstream of the leading edge was modelled so as to provide a development length of the flow field. The tunnel length downstream of the test plate was included so as to visualise the mixing of the coolant and mainstream.

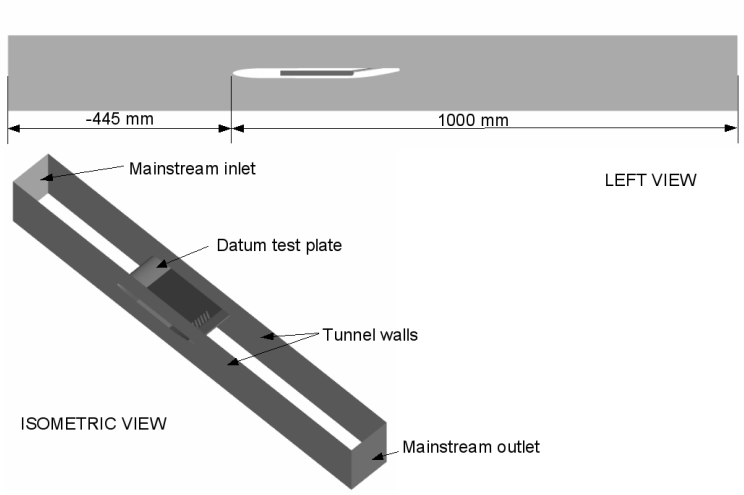

Figure 6.1: Computation domain for the datum trailing edge cooling configuration test plate

Figure 6.1 shows the isometric and left hand view of the CFD domain for the datum test plate. In the isometric view, the top and bottom walls have been removed to show the internal position of the test plate, relative to the mainstream inlet and outlet planes.

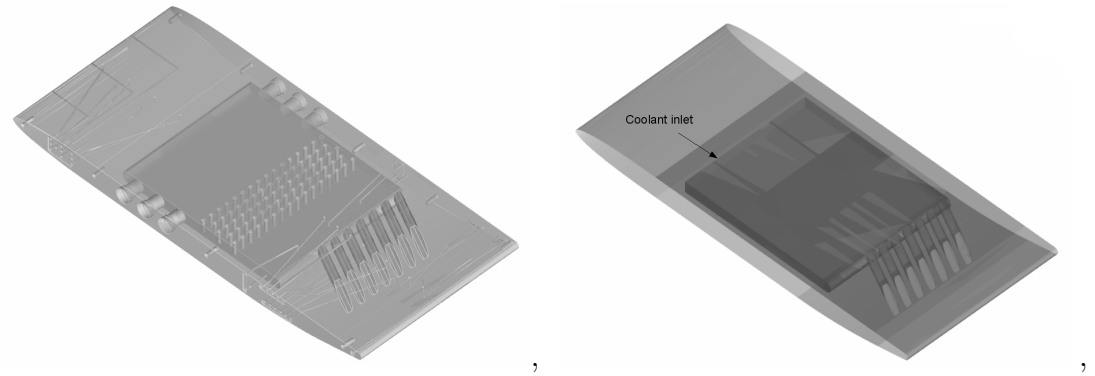

(a) Datum stereolith test plate , (b) Datum CFD test plate ,

Figure 6.2: Comparison of the stereolith and CFD datum configuration test plates.

Figure 6.2a shows the CAD geometry used in the stereolith manufacturing process of the datum cooling configuration test plate and figure 6.2b shows the CAD geometry of the datum test plate used in the CFD studies. It can be seen from figure 6.2b that the CAD model for the CFD study of the datum configuration test plate was simplified so as to minimise the number of mesh elements. Similar simplifications were carried out in the CFD studies for the machined and cast cutback cooling configurations.

Furthermore, within the plenum of the CFD test plate, the flow straightening pedestal banks, as shown in figure 6.2a, were removed from the three CFD models. The coolant inlet was changed from the plate side walls to the wall directly opposite the coolant hole inlet plane, as shown in figure 6.2b. The effect of removing the flow straightening pedestals in the CFD test plates was mitigated by the uniform coolant inlets. It must be noted that the last three rows of pedestals, shown in figure 4.3c were not removed in the simplification of the cast trailing edge cooling configuration CFD test plate, as they form part of the cast cutback trailing edge cooling configuration.

6.2 Meshing

The meshing strategy described in section 3.4.1 was employed to mesh the CFD models of the conventional, machined and cast cutback trailing edge configurations. The tunnel walls were meshed with a coarse boundary layer mesh, so as to give an approximate Y^+ value between 30 and 60. A fine boundary layer mesh was applied to the internal and external surfaces of the test plate, so as to resolve the boundary layer flows. Figure 6.3 shows the centreline cutplane of the mesh on the datum configuration CFD domain. The high density fine boundary layer mesh on the test plate walls can be seen in figure 6.3.

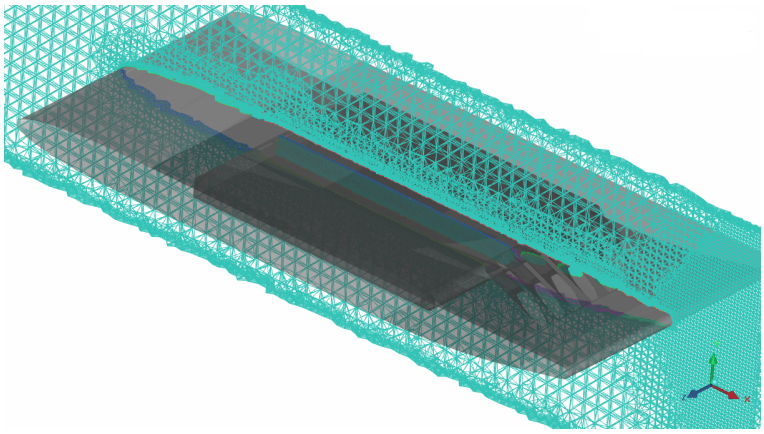

Figure 6.3: Centreline cutplane of the mesh on the datum configuration CFD domain.

As can be seen from figure 6.3, the CFD domains were meshed using unstructured tetrahedral elements. The tetrahedral element size was allowed to grow from the wall to the centre of the domain. To resolve the wake downstream of the test plate, a refined, high density tetrahedral mesh region was created for each computation

domain, as seen near the trailing edge of the test plate in figure 6.3. Each tetrahedral element within this region has an edge length of 1 mm.

6.3 Boundary conditions

In all three CFD models, pressure inlet and outlet boundary conditions were applied to the mainstream. Prescribed mass flow boundary conditions were applied to the coolant stream. Tables 6.1 to 6.3 show the boundary conditions applied to the three CFD models. The boundary condition values shown in tables 6.1 to 6.3 were derived from the experimental measurements shown in chapter 5.

Boundary conditions		Model cases		
		BR = 0.8	BR = 1.0	BR = 1.2
Operating pressure (Pa)		100385.73	100385.73	100385.73
Mainstream inlet	Total pressure (Pa)	-543.4	-735.5	-742.3
	Total temperature (K)	295.88	297.53	297.83
	Turbulence intensity (%)	4.00	4.00	4.00
	Hydraulic diameter (m)	0.150	0.150	0.150
Mainstream outlet	Static pressure (Pa)	-5699.5	-5628.8	-5596.5
	Turbulence intensity (%)	4.00	4.00	4.00
	Hydraulic diameter (m)	0.150	0.150	0.150
Coolant inlet	Mass flow rate (kg/s)	0.0121	0.0149	0.0179
	Total temperature (K)	295.11	296.25	296.64
	Turbulence intensity (%)	4.00	4.00	4.00
	Hydraulic diameter (m)	0.0185	0.0185	0.0185

Table 6.1: Boundary conditions for the datum trailing edge configuration CFD model

When applying boundary conditions for near incompressible flow fields, in Fluent™, the 'operating pressure' option is used so as to reduce numerical errors. In the current study, for the three test plates, a plane 1.0 m upstream of the test plate leading edge was chosen as the location to set the operating pressure. All pressure boundary conditions were defined relative to this plane.

Boundary conditions		Model cases		
		BR = 0.9	BR = 1.0	BR = 1.5
Operating pressure (Pa)		100385.73	100650.60	100650.60
Mainstream inlet	Total pressure (Pa)	-670	-510	-530
	Total temperature (K)	292.86	294.36	292.86
	Turbulence intensity (%)	4.00	4.00	4.00
	Hydraulic diameter (m)	0.150	0.150	0.150
Mainstream outlet	Static pressure (Pa)	-5550	-5480	-5500
	Turbulence intensity (%)	4.00	4.00	4.00
	Hydraulic diameter (m)	0.150	0.150	0.150
Coolant inlet	Mass flow rate (kg/s)	0.011517	0.012802	0.016578
	Total temperature (K)	292.51	294.36	292.26
	Turbulence intensity (%)	4.00	4.00	4.00
	Hydraulic diameter (m)	0.0185	0.0185	0.0185

Table 6.2: Boundary conditions for the machined cutback trailing edge configuration CFD model

Boundary conditions		Model cases		
		BR = 0.3	BR = 0.6	BR = 1.0
Operating pressure (Pa)		99855.99	99855.99	99723.56
Mainstream inlet	Total pressure (Pa)	-586.4	-612.6	-534.1
	Total temperature (K)	295.63	296.52	293.09
	Turbulence intensity (%)	4.00	4.00	4.00
	Hydraulic diameter (m)	0.150	0.150	0.150
Mainstream outlet	Static pressure (Pa)	-5576.6	-5533.6	-5512.3
	Turbulence intensity (%)	4.00	4.00	4.00
	Hydraulic diameter (m)	0.150	0.150	0.150
Coolant inlet	Mass flow rate (kg/s)	0.0172	0.0342	0.0571
	Total temperature (K)	294.56	293.63	289.43
	Turbulence intensity (%)	4.00	4.00	4.00
	Hydraulic diameter (m)	0.0185	0.0185	0.0185

Table 6.3: Boundary conditions for the cast cutback trailing edge configuration CFD model

As the experimental tunnel is a suction rig, all pressure boundary condition values are taken as negative. This implies that the static pressure within the tunnel cross section is lower than the ambient pressure outside the tunnel. The turbulence intensities were assumed to be 4.00% at the mainstream and coolant inlet and mainstream outlet of the CFD domain. The upstream pressure boundary conditions were determined by the total pressure measurements conducted 445 mm upstream of the leading edge of the test plates. The traverse plane static pressure measurements from the experimental rig were used to determine the downstream pressure boundary conditions. The coolant mass flow boundary condition was determined from the measured coolant flow rate.

6.4 Turbulence model computation method

For all low speed aerodynamic predictions the realisable k-ϵ model with enhanced wall functions was used. The realisable k-ϵ model is based on the standard k-ϵ model, which is one of the two oldest equation turbulence models and used frequently for the prediction of internal flows. One difference between the standard and realisable turbulence model is the prediction of the turbulence dissipation rate (ϵ). The standard k-ϵ model was reported to be poor at predicting the spreading rate of axisymmetric jets, Fluent^{TM} (1995). One reason for the development of the realisable k-ϵ model was to address this issue. Fluent^{TM} (1995) documents the other shortcomings in the standard k-ϵ model addressed by the realisable k-ϵ model. As the realisable k-ϵ model is better suited to predicting the spreading of axisymmetric jets, this turbulence model was chosen for the low speed aerodynamic predictions.

The enhanced wall function was chosen as the mesh was not uniformly refined throughout the whole computation domain. The mesh surrounding the internal flow passages and the external surfaces of the test plates was sufficiently refined such that the boundary layer flow would be resolved. The mesh surrounding the test section walls was not sufficiently refined and hence wall functions were used to predict the boundary layer flow.

For all simulations the flow was initialised and run using the procedure shown in section 3.4.3. The mass flow rate at the outlet plane was also monitored. Convergence of the simulations was determined when the mass flow rate converged to a constant value.

6.5 CFD results

6.5.1 Flow visualisation

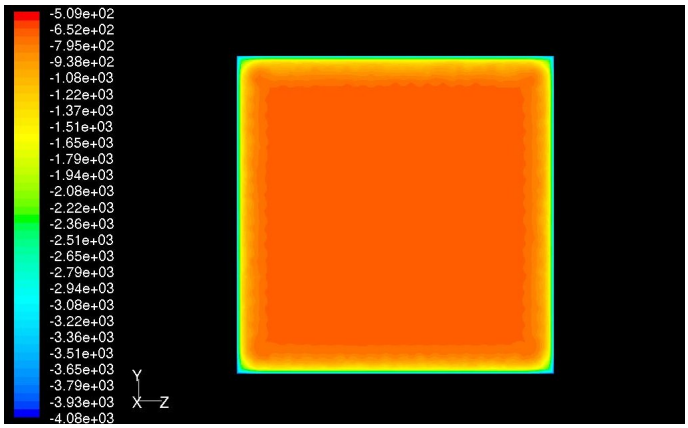

Figure 6.4: Contours of typical gauge total pressure predicted at 100 mm upstream of the test plate leading edge.

.

Figure 6.4 shows typical contours of the gauge total pressure, predicted for all CFD models, at a distance of 100 mm upstream of the test plate leading edge. It can be seen from figure 6.4 that the predicted tunnel wall boundary layer is thin.

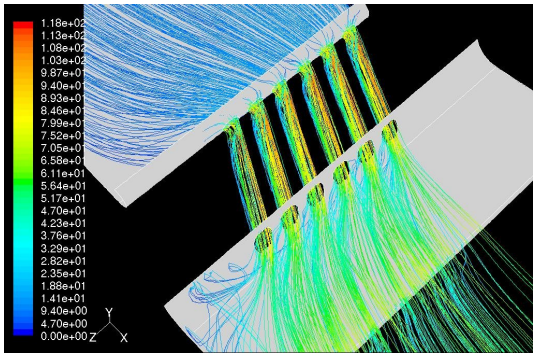

(a) Pathlines of coolant stream coloured by velocity magnitude

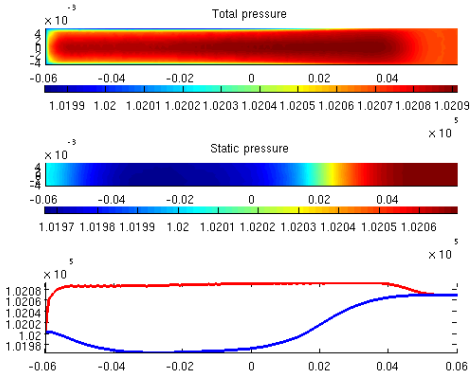

(b) Predicted coolant static and total pressure distributions across the plenum cross section at the axial location of the coolant static tappings on the stereolith plates.

Figure 6.5: Coolant path lines and pressure distributions of the machined cutback CFD domain at mass flux ratio 0.83.

Figure 6.5a shows pathlines of the coolant stream, coloured by velocity magnitude, exhausting through the coolant holes onto the machined cutback surface. Figure 6.5b shows pressure contours of the coolant at a plane located at the same axial position as the plenum static pressure tapping of the stereolith test plates. From figure 6.5a it can be seen that the coolant separates at the inlet to the coolant holes. The separation bubble causes the coolant cross sectional area to reduce and hence increase the velocity in the region of this bubble. This gradient in velocity magnitude across the coolant hole cross section is maintained until the exit plane of the coolant holes. Once the coolant exits the holes, the momentum of the mainstream is sufficiently large to turn the flow towards the axial direction. Further evidence of this is seen in figure 6.7e.

The top most figure in figure 6.5b shows the predicted plenum total pressure at the same axial position as the plenum static pressure tapping locations on the stereolith test plate. This position is 226 mm from the leading edge. The central figure in figure 6.5b shows the plenum static pressure at the same axial position described above. The X-axis of the figures in figure 6.5b is the width of the plenum, which was 100 mm. The Y-axis on the top and the central figure is the depth of the plenum, which was 10 mm. The Y-axis of the bottom figure shows the predicted pressure. It can be seen from the top and central figures, that the pressure is not constant across the width of the plenum. The red line on the bottom figure of figure 6.5b shows the total pressure across the centreline of the analysis plane and the blue line shows the static pressure across the width of the plenum wall. It can be seen from figure 6.5a and the last graph of figure 6.5b that the coolant flow is stagnant away from the coolant hole inlets, as expected. The predicted maximum difference between the coolant static and total pressure is approximately 100 Pa at the axial position plenum static pressure tapping location on the stereolith plates, which is 226 mm.

Figure 6.6a shows the pathlines of the coolant stream coloured by velocity magnitude for the cast cutback test plate. For clarity, only the plenum walls near the suction surface of the CFD test plate are shown. The pressure surface wall, just downstream of the central slot is also shown. From the pathlines upstream of the three rows of pedestals it can be deduced that the total pressure would be uniform. This is born out in the total pressure distribution plot of figure 6.6b. However, from the static pressure distribution plots of figure 6.6b, it can be seen that the effect of the pedestals can still be seen at the plane which corresponds to the plenum static tappings upstream of the large pedestal banks. The high static pressure regions seen in figure 6.6b are due to the flow curvature, caused by the pedestals. The low static

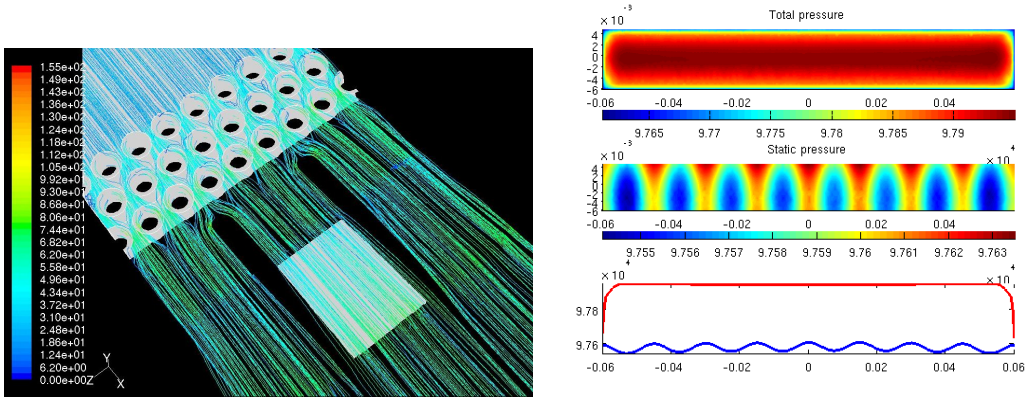

(a) Pathlines of coolant stream coloured by velocity magnitude

(b) Coolant static and total pressure distributions across the plenum at the axial location of the coolant static tappings on the stereolith test plate

Figure 6.6: Coolant path lines and pressure distribution of the cast cutback CFD domain at mass flux ratio 0.64.

pressure regions are due to the coolant flow accelerating past the gaps of the adjacent pedestals. It should also be noted from the static pressure distribution shown in figure 6.6b that the static pressure distribution is not symmetrical across the plane. This is due to the convergence of the plenum in the region of the pedestal banks. Therefore, the coolant adjacent to the plenum surface nearest to the suction surface is accelerated more than the coolant adjacent to the plenum surface nearest to the pressure surface. The red line on the last graph of figure 6.6b shows the total pressure across the cross section of the plenum, whilst the blue line shows the static pressure on the plenum wall nearest the pressure surface of the test plate. From figure 6.6b it can seen that there is an appreciable difference between the plenum total and static pressure of approximately 4.0 kPa.

Figure 6.7 shows the predicted wall shear stress on the pressure surface of the test plates, downstream of the coolant ejection. Figures 6.7a to 6.7c show the region on the pressure surface where the contoured wall shear stresses, shown in figures 6.7d to 6.7f, are contoured. Figure 6.7d also shows the wall shear stress upstream of the coolant ejection. It can be seen that the shear stress is lower near the upstream (right) edge of the coolant holes. This is because the mainstream slows down as it approaches the blockage caused by the coolant. Furthermore, the mainstream, with higher momentum than the coolant, turns the coolant jets towards the axial direction, away from the direction of the coolant hole axis. This can be clearly seen in figure

6.7e. In figure 6.7e, the separated mainstream flow region, caused by the cutback, can be seen on the pressure surface, downstream of the cutback where there are no coolant holes. The low shear stress regions are due to the separated flow impinging on the pressure surface. The high shear stresses either side of this low shear stress region are due to the mainstream accelerating along the surface. In figure 6.7f, the wall shear stress on the pressure surface downstream of the central slot is shown. The shear stress distribution clearly shows the wakes due to the pedestal banks. The high shear stress region is due to the high velocity coolant stream from the spacing between adjacent pedestals.

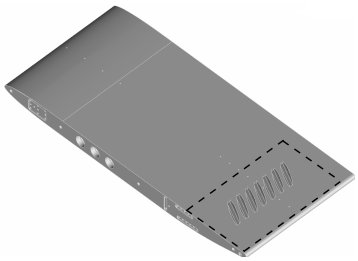

(a) Datum configuration pressure surface region

(b) Machined cutback configuration pressure surface region

(c) Cast cutback configuration pressure surface region

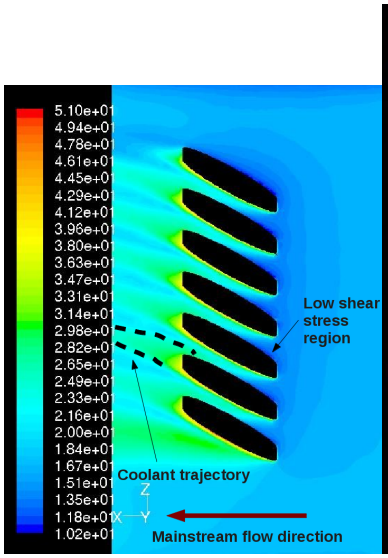

(d) Datum configuration test plate, mass flux ratio 0.83

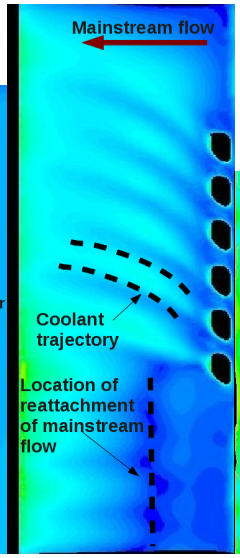

(e) Machined cutback test plate, mass flux ratio 0.83

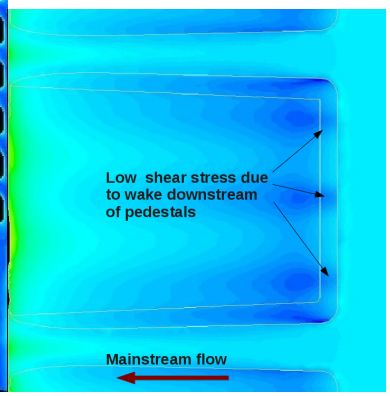

(f) Cast cutback test plate, mass flux ratio 0.64

Figure 6.7: Predicted pressure surface wall shear stress downstream of coolant ejection. The mainstream flow is from right to left for all three figures.

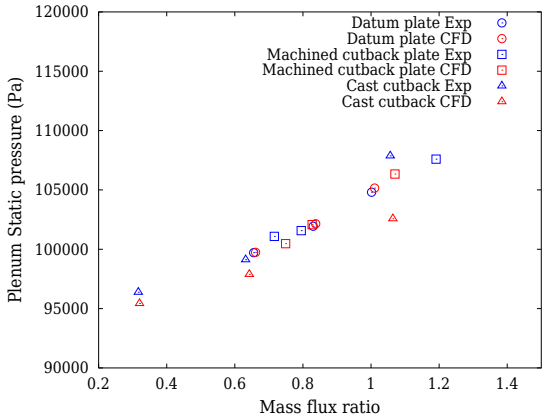

(a) Mean absolute plenum static pressure at the plenum static pressure location

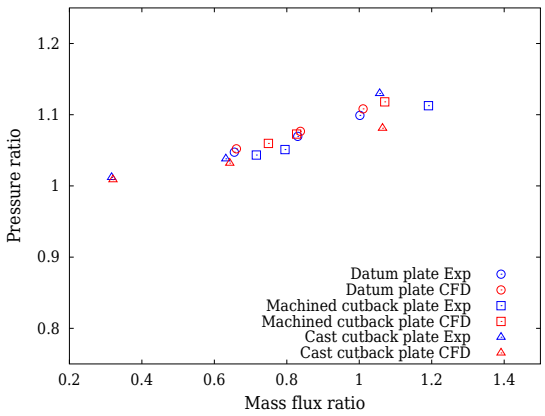

(b) Pressure ratio $\frac{P_{c,static}}{P_{exit,static}}$

Figure 6.8: Experimental and numerical mean absolute plenum static pressure and the pressure ratio. $P_{exit,static}$ is measured and predicted at the locations given in table 5.1, measured from the leading edge of the test plates.

Figure 6.8a shows the experimentally determined mean absolute static pressure, averaged across all the static tappings within the plenum, on the plenum surface compared with the plenum static pressure predicted at the same location. It can be seen that the predicted plenum static pressure is closely matched with those measured for the datum test plate. For the machined and cast cutback test plates, the plenum static pressure is under predicted, compared with the respective experimental measurements. This under prediction increases with increasing mass flux ratio. This suggests the CFD is not accurately capturing the discharge coefficient.

Figure 6.8b shows the measured coolant to exit static pressure ratio compared with those predicted for the three test plates. The predicted exit static pressure is at the same position, measured from the leading edge of the test plates, as shown in table 5.1. It can be seen that the predicted coolant to exit static pressure ratio is close to that measured for the datum test plate. However, due to the under prediction of the plenum static pressure, the predicted coolant to exit static pressure ratio for the machined and cast cutback test plates are lower than those measured.

6.5.2 Discharge coefficient predictions

The discharge coefficients for the three CFD models were predicted using equations 5.2 and 5.3. The exit static pressure used in the computation of the ideal mass flow rate, was taken from the pressure measurement along the surface of the centreline

along the test plates, at the distances given in table 5.1, measured from the leading edge. For the coolant pressure, a plane, across the plenum, at the location of plenum static tappings, was used. For the cast cutback configuration test plate, the plane was located at the static tapping location downstream of the three rows of flow smoothing pedestals, but upstream of the large pedestals. The coolant total temperature was also determined at this plane for all three test plates. The discharge coefficients were computed using the total pressure averaged across the plane within the plenum and also using the predicted average static pressures on the walls of the plenum at the tapping locations. Figure 6.9 shows the difference in the discharge coefficients using the plenum total and static pressures. From figure 6.9, it can be seen that the discharge coefficient computed using the plenum static pressure is greater than the discharge coefficient computed using the plenum total pressure. This is expected, as using the plenum static pressure, the ideal mass flow rate is computed using an underestimate of the total pressure. This results in the ideal mass flow rate computed with the plenum static pressure being lower than that computed with the plenum total pressure.

From figures 6.9a and 6.9b, it can be deduced that the effect of using the average wall static pressure at the static tapping location, instead of the plenum total pressure, to compute the discharge coefficient is very small. The differences in the discharge coefficients computed using the total and static pressures are within 1.0 %. However, for the cast cutback test plate, from figure 6.9c, it can be deduced that using the wall static pressure instead of the coolant total pressure would increase the discharge coefficient by 5.0 %. This is not surprising given the plenum pressure variation, shown in section 6.5.1.

Figure 6.10 shows the predicted discharge coefficient based on the coolant total pressure, compared to the experimentally determined discharge coefficient reported in section 5.2.

It can be concluded from figure 6.10 that for the datum and machined cutback trailing edge cooling configurations, the CFD models under predict the discharge coefficient. This under prediction is approximately 5.0 %. However, the predicted discharge coefficient for the cast cutback test plate is approximately 15.0 % greater than the experimentally determined discharge coefficient. However, it must be noted that the experimentally determined discharge coefficient was computed using plenum static pressure instead of the plenum total pressure. Therefore, the true difference is expected to be approximately 20.0 %. This suggests that the CFD model under

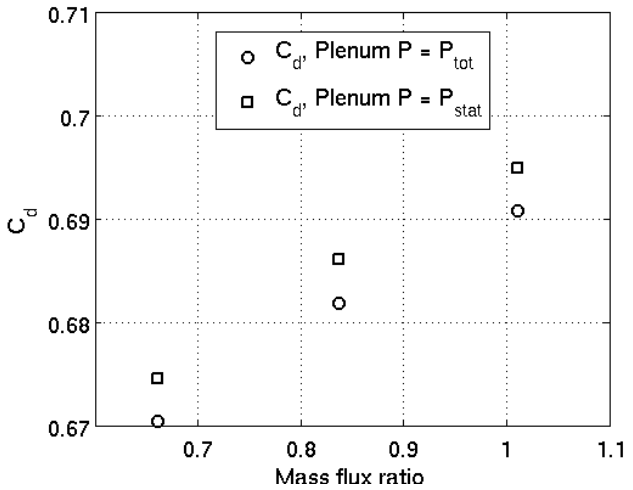

(a) Datum configuration test plate

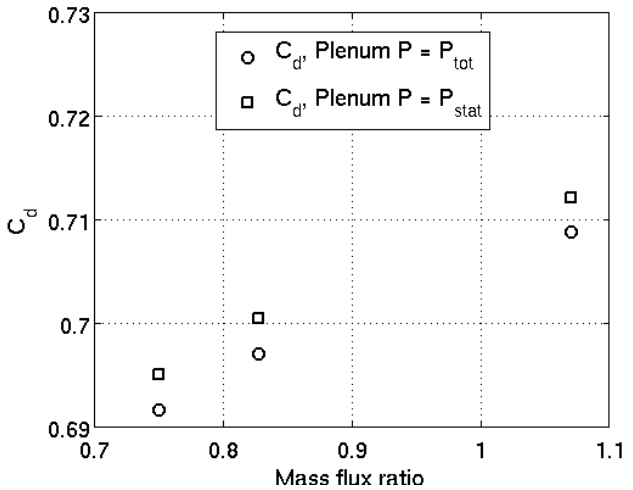

(b) Machined cutback configuration test plate

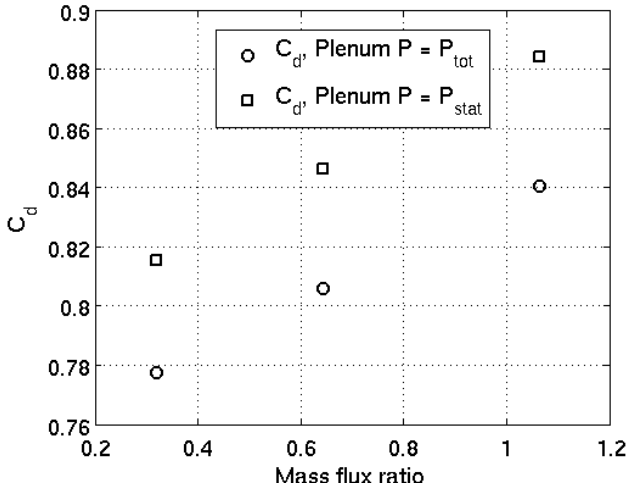

(c) Cast cutback configuration test plate

Figure 6.9: Comparison of the discharge coefficients computed using plenum total and plenum static pressure.

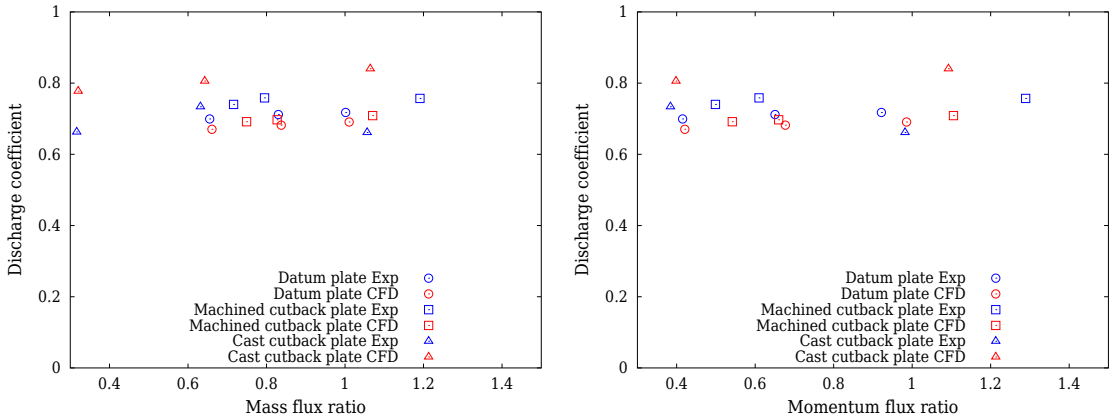

(a) Discharge coefficient against mass flux ratio (b) Discharge coefficient against momentum flux ratio

Figure 6.10: Comparison of the discharge coefficient determined from experimental and numerical analysis.

predicts the blockage due to the pedestal banks, resulting in a larger discharge coefficient.

6.5.3 CFD prediction of total pressure loss

Figures 6.11 to 6.13 show the predicted total pressure loss 40.0 mm downstream of the test plate trailing edges, compared with the experimental measurements. As stated in section 5.3, the red contour indicates a loss in total pressure whilst the blue contour indicates the increase in total pressure.

The experimental measurements shown in figures 6.11 and 6.12 show the structure of the coolant streams at the traverse plane. These structures have all together been mixed out at the traverse plane of the CFD predictions. As the mass flux ratio increases, it can be seen from the experimental and numerical predictions that the total pressure loss decreases.

From the CFD predictions of the cast cutback total pressure losses, it can be seen that the wakes from the internal pedestal banks are still visible at the traverse plane at low mass flux ratios. From the experimental measurements, the wakes from the pedestal banks appear to have been mixed out at the traverse plane. At high momentum flux ratios (M = 1.06), the strength of the coolant wakes caused by the three rows of pedestals are very strong, and influence the wake structure seen at the traverse plane.

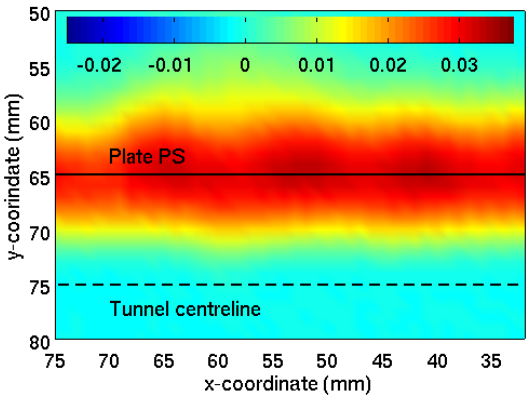

(a) Experimental measurement at mass flux ratio 0.65

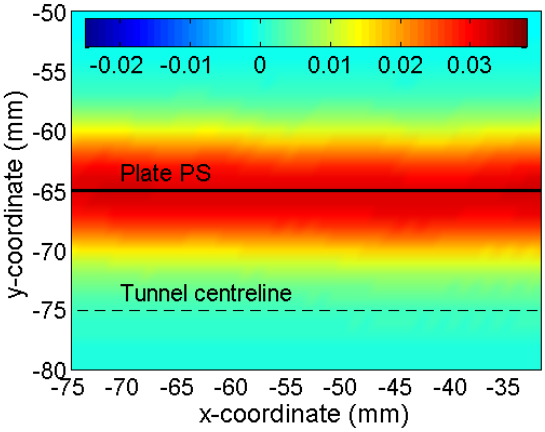

(b) CFD prediction at mass flux ratio 0.66

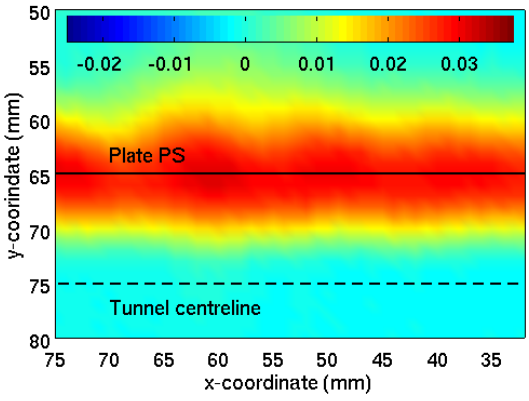

(c) Experimental measurement at mass flux ratio 0.83

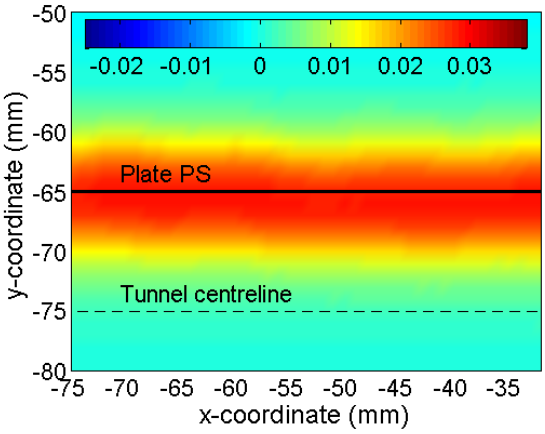

(d) CFD prediction at mass flux ratio 0.84

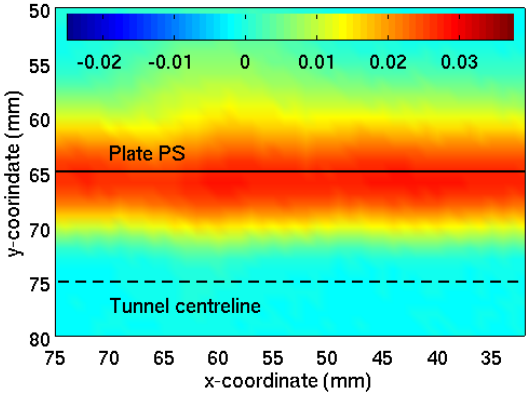

(e) Experimental measurement at mass flux ratio 1.00

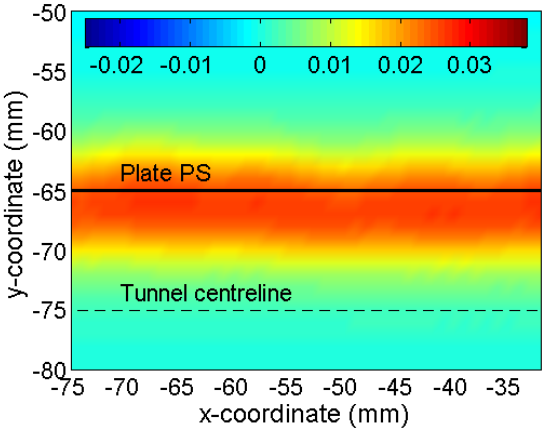

(f) CFD prediction at mass flux ratio 1.01

Figure 6.11: Comparison of the experimental and numerical total pressure loss coefficient at 40 mm downstream of datum test plate.

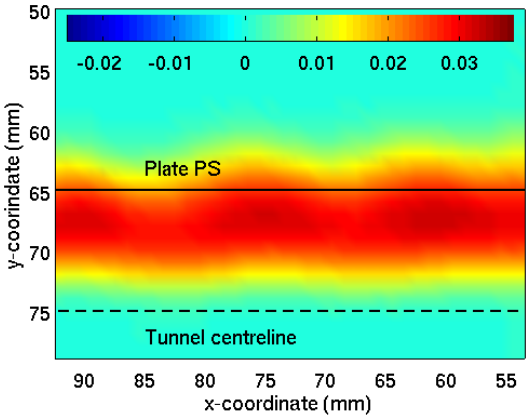

(a) Experimental measurement at mass flux ratio 0.72

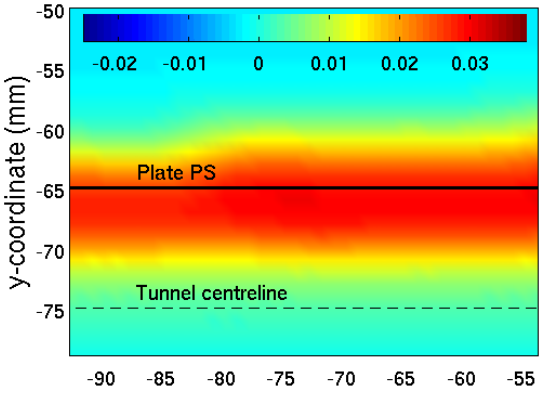

(b) CFD prediction at mass flux ratio 0.75

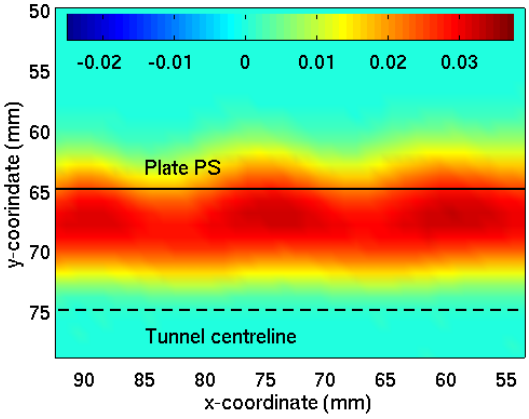

(c) Experimental measurements at mass flux ratio 0.80

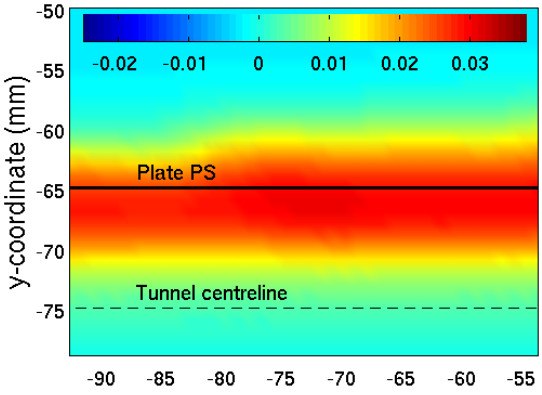

(d) CFD predictions at mass flux ratio 0.83

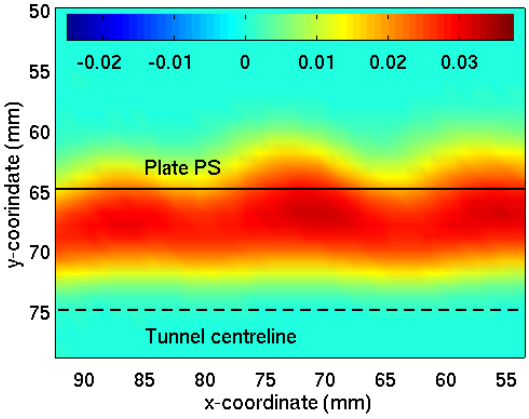

(e) Experimental measurements at mass flux ratio 1.20

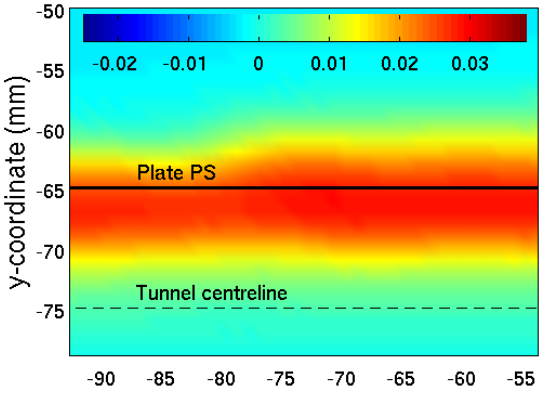

(f) CFD prediction at mass flux ratio 1.07

Figure 6.12: Comparison of experimental and numerical total pressure loss coefficient at 40 mm downstream of machined cutback test plate.

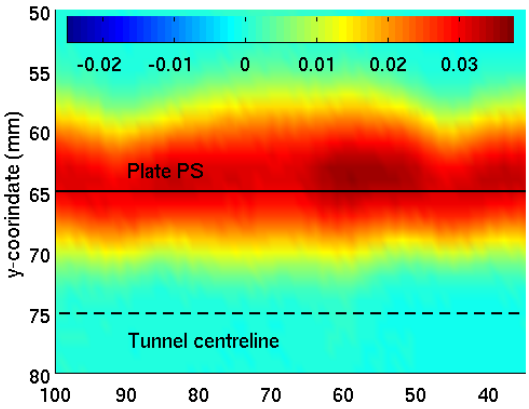

(a) Experimental measurements at mass flux ratio 0.32

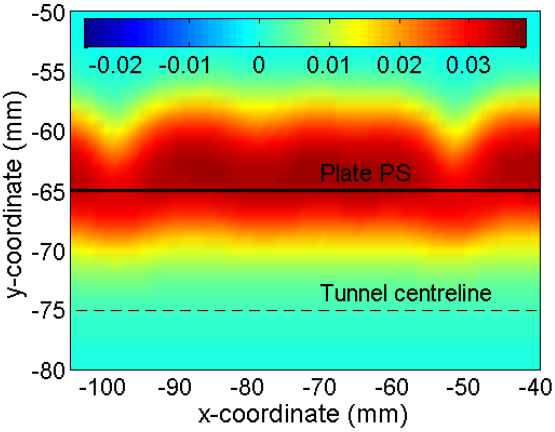

(b) CFD prediction at mass flux ratio 0.32

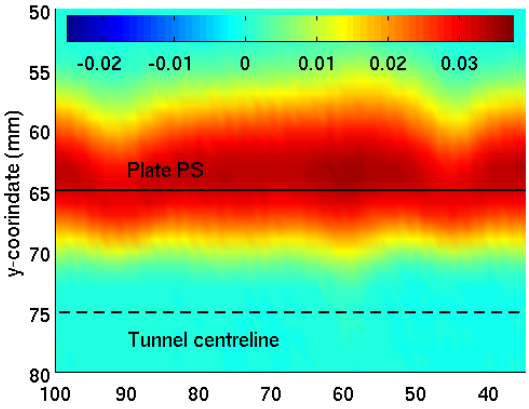

(c) Experimental measurements at mass flux ratio 0.63

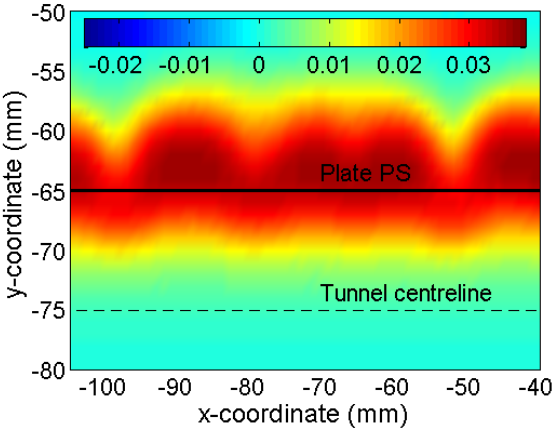

(d) CFD predictions at mass flux ratio 0.64

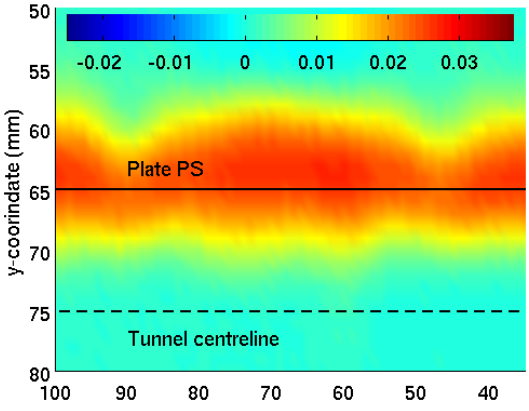

(e) Experimental measurements at mass flux ratio 1.06

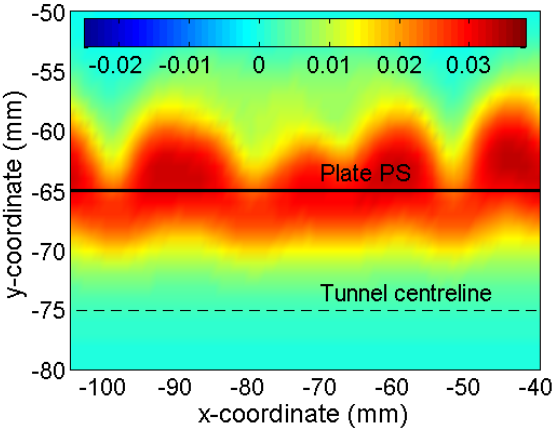

(f) CFD prediction at mass flux ratio 1.06

Figure 6.13: Comparison of experimental and numerical total pressure loss coefficient at 40 mm downstream of cast cutback test plate.

6.5.4 Mixed out loss measurements

Mixed out losses for the CFD predictions, for the three plate CFD predictions, were computed using the analysis shown in section 5.5. Figure 6.14 compares the experimentally determined mixed out loss with those predicted using CFD for the three test plates.

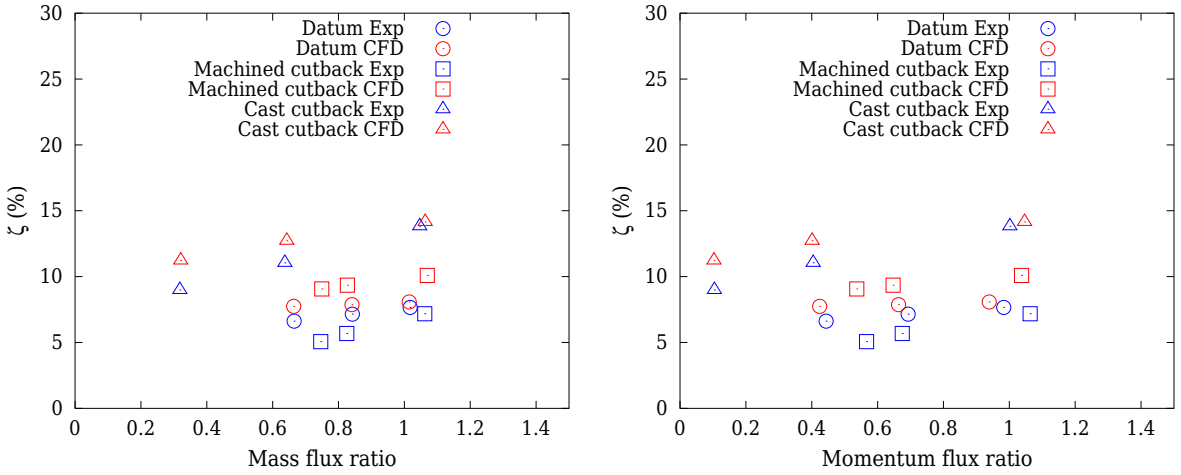

(a) Mixed out loss coefficient against mass flux ratio (b) Mixed out loss coefficient against momentum flux ratio

Figure 6.14: Comparison of experimental and numerical mixed out loss for the three trailing edge cooling configurations.

It can be seen from figure 6.14, that the mixed out losses for the three test plates are over predicted by the CFD. The mixed out losses are seen to increase with increasing mass and momentum flux ratios. For the datum and cast cutback test plates, the over prediction is greatest at low mass and momentum flux ratios. At high momentum and mass flux ratios, the experimentally determined mixed out losses are close to those predicted by CFD. For the cast cutback and datum test plates, the worst differences between the experimentally determined mixed out loss and CFD prediction are within 25.0 %. For the machined cutback test plate, the differences between the experimentally determined mixed out losses and those from the CFD are larger than 25.0 %. However, the error in mixed out loss reduces with increasing mass and momentum flux ratio. Furthermore, it can be seen that the mixed out losses predicted by the CFD for the machined cutback test plate are higher than those predicted for the datum test plate. For the experimental results, the machined cutback test plate showed a slight decrease in the mixed out losses compared with the datum test plate.

From the CFD results, it can be concluded that there is more turbulent mixing downstream of the test plates than in the experimental results. Over prediction of the mixing between the mainstream and coolant is more pronounced at lower mass and momentum flux ratios. As the mass flux ratio increases, the coolant behaves as discrete jets with sufficient momentum, such that there is less mixing with the mainstream. Hence the mixed out losses from the CFD predictions are closer to the experimental results.

6.6 Conclusions

Computational fluid dynamics was used as a means of flow visualisation and prediction of the aerodynamic performance of the three test plates. From the flow visualisation of the coolant path through the film cooling holes within the datum and machined cutback test plates, it could be seen that the coolant separated near the inlet to the coolant holes. This was as expected and has been reported in many other film cooling studies available in the literature. It was observed that a velocity gradient across the coolant hole cross section was set up due to the flow inlet flow separation. The coolant hole lengths were not sufficiently long enough to diffuse this velocity gradient. From the flow visualisation of the cast cutback test plate, the coolant was seen to accelerate past the pedestals before exiting through the slots.

From the wall shear stress plots, it was noticed that the coolant was turned towards the mainstream direction after exiting the coolant holes. Furthermore, in the datum test plate, the wall shear stress was seen to decrease upstream of the coolant holes. This was due to the deceleration of the mainstream on encountering the blockage caused by the coolant stream. From the shear stress contours on the machined cutback test plate, the extent of the separated mainstream flow due to the cutback impinging downstream of the coolant hole ejection was also observed. The cast cutback test plate did not show such evidence of the impinging mainstream. However, the evidence of the vortices caused by the pedestals was still apparent on the pressure surface downstream of the slots.

The predicted pressure distribution within the plenum showed that the static pressure was not constant across the plenum cross section for all three test plates. Furthermore the effects of the coolant holes can be seen on the static pressure at the static tapping locations within the plenum of all three test plates. Though the static pressure was not constant across the plenum, for the datum and machined cutback

test plates, the static pressures at the static tapping locations were very close to the plenum total pressure. This was not the case for the cast cutback test plate.

The predicted discharge coefficient for the datum and machined cutback test plates were close to those determined experimentally, with the predicted discharge coefficients about 5.0 % lower than those determined experimentally. The predicted discharge coefficients for the cast cutback test plate were greater than those determined experimentally. This was attributed to the lower blockage predicted by the cast cutback test plate predictions.

The predicted total pressure contours show increased mixing between the mainstream and coolant for the three test plates. However, this mixing is less pronounced at high momentum flux ratios. The mixed out loss predictions confirm the observations from the total pressure loss contours. The predicted mixed out losses were over predicted for all three test plates, but share the same trends with increasing mass and momentum ratios as the experimental data.

Chapter 7

Low speed heat transfer measurements

7.1 Introduction

This chapter describes the steady state heat transfer method used to establish the film effectiveness and heat transfer coefficient on the pressure surface of the test plates. The film effectiveness and heat transfer coefficient were only measured within the region from the coolant ejection plane to the trailing edge, on the pressure surface of the test plates. The steady state heat transfer technique was used to measure these film effectiveness and heat transfer coefficients for each of the three test plates.

7.2 Steady state heat transfer method

In the steady state heat transfer method, a variable heat source in conjunction with a hot mainstream gas temperature was used to measure the surface temperature and heat transfer coefficient, on the pressure surface of the test plate. For a heat source, a flat surface heater pad was used. Figure 7.1 shows examples of the heater pads used in the current research. The heater pads incorporate a serpentine track, which when connected to a constant power source produces a constant heat flux.

Figure 7.2 shows the schematic of the setup for the steady state heat transfer experiments. A square portion of the pressure surface, from the coolant holes / slot ejection plane to the trailing edge, was machined from the test plates and replaced by a section of foam material from Rohacell^{TM}. The heater pads, manufactured from Watlow^{TM} and Omega^{TM}, were placed above the Rohacell^{TM} but installed flush with the test plate surfaces, so as not to disturb the boundary layer over the pressure surface. Table 7.1 shows the heater pads used for the three test plates and the area of

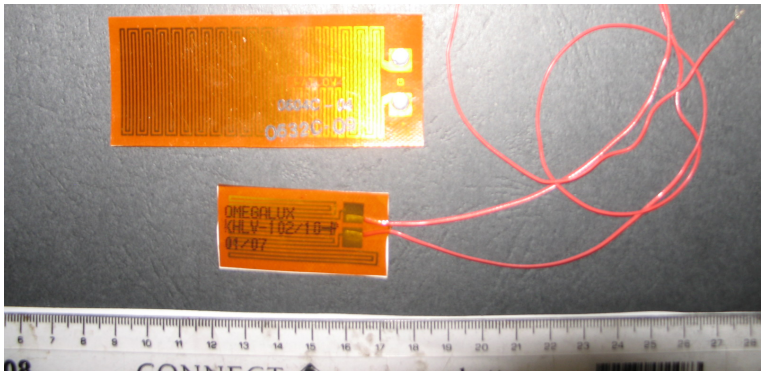

Figure 7.1: Examples of surface mounted heater pads used in the current research.

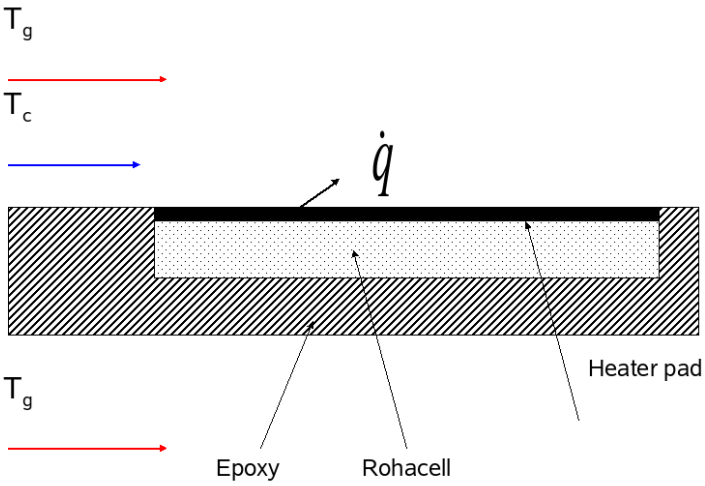

Figure 7.2: Schematic diagram of the setup of the steady state heat transfer method.

the applied heat flux. The power to the heater pads was supplied by a conventional bench top DC power supply.

Test plate	Manufacturer	Heated area (m^2)
Datum test plate	Watlow^{TM}heaterpad	2.440×10^{-3}
Machined cutback test plate	Watlow^{TM}heaterpad	6.545×10^{-4}
Cast cutback test plate	Omega^{TM}heaterpad	3.476×10^{-3}

Table 7.1: Area of the heater pads used in the steady state heat transfer method.

All of the test plates were painted with black paint and a single narrow band liquid crystal BM/R30C1W/S40 was used. Figure 7.3 shows the regions downstream of the coolant ejection planes of the test plates, where the Rohacell^{TM} inserts and the heater pads were installed. The yellow lines in figure 7.3 shows the perimeter of the Rohacell^{TM}. The red lines show the perimeter of the heater pads.

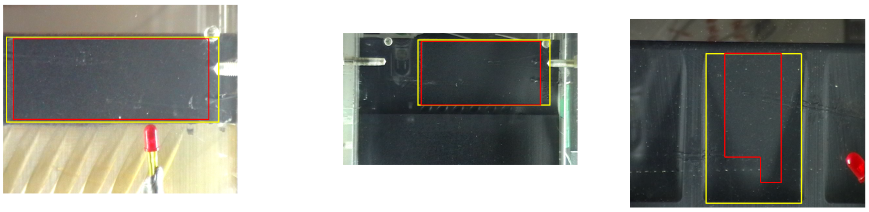

(a) Datum test plate (b) Machined cutback test plate (c) Cast cutback test plate

Figure 7.3: Perimeter of the Rohacell^{TM}and heater pads on the three test plates. The yellow lines indicate the perimeter of the Rohacell^{TM}. The red lines indicate the perimeter of the heater pads.

From the three test plate geometries, it can be seen that the heater pads do not extend all the way to the trailing edge. This was due to limitations of the Rohacell^{TM} installation. Furthermore, from figure 7.3c, it can be seen that the heater pad used for the cast cutback test plate from Omega^{TM} did not have a rectangular area. Furthermore, the heater pads from Watlow^{TM} had a small rectangular region with no copper tracks. The areas with the copper tracks produce a constant heat flux and hence the areas without copper tracks did not have a uniform heat flux. However, the heater pads were situated on the surface such that the non-uniform heated areas

were situated away from the region of interest. The in situ calibration of the liquid crystal is described in section 7.2.1. Figure 7.4 shows the liquid crystal colour play with only the heater pad switched on. There is no mainstream or coolant gas. Figure 7.4 shows the uniformity of the heat flux from the heater pad with the exception of the small rectangular region with no copper tracks.

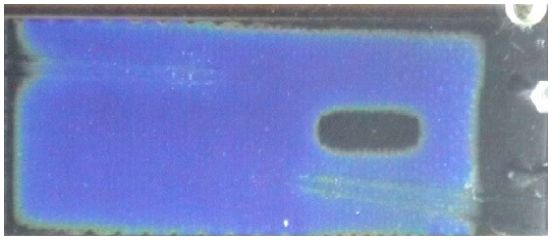

Figure 7.4: Heat pad mounted on the machined cutback surface and coated with black paint and single narrow band liquid crystal. Crystal colour play shows uniform heat flux produced by the heater pad with the exception of the small rectangular region with no copper tracks.

The heat flux from the heater pad is given by equation 7.1

$$\dot{q} = h\left(T_{cr} - T_{aw}\right) \tag{7.1}$$

In equation 7.1, T_{cr} is the temperature at which the single narrow band liquid crystals change phase, and T_{aw} is the adiabatic wall temperature. h is the heat transfer coefficient which is a function of the flow field.

Equation 3.7 can be re-arranged to give the adiabatic wall temperature T_{aw} as

$$T_{aw} = T_{rec,m}\left(1 - \eta\right) + \eta T_c \tag{7.2}$$

In equation 7.2, $T_{rec,m}$ is the mainstream recovery temperature. Substituting equation 7.2 into equation 7.1 and re-arranging it, the heat flux from the heater pad can be shown to be given by equation 7.3.

$$\dot{q} = -h\left(1 - \eta\right)T_{rec,m} + h\left(T_{cr} - T_c\eta\right) \tag{7.3}$$

Equation 7.3 expresses the heat flux $\dot{q}$ as a linear function of the mainstream gas temperature $T_{rec,m}$. The gradient A of this function is given by equation 7.4.

$$A = -h\left(1 - \eta\right) \tag{7.4}$$

The y-axis intercept B is given by equation 7.5.

$$B = h\left(T_{cr} - T_c\eta\right) \tag{7.5}$$

Dividing equation 7.4 by equation 7.5, the film effectiveness can be computed by equation 7.6.

$$\eta = \frac{1 + \left(\frac{A}{B}\right) T_{cr}}{1 + \left(\frac{A}{B}\right) T_c} \tag{7.6}$$

Substituting equation 7.6 into equation 7.5, the heat transfer coefficient can also be computed.

Hence by independently varying the heat flux from the heater pad and the mainstream gas temperature, whilst keeping the coolant gas temperature fixed, and plotting the variation of heat flux against the mainstream gas temperature to compute the gradient and intercept, the film effectiveness and heat transfer coefficient could be computed.

7.2.1 Calibration of liquid crystals

The narrow band liquid crystal that was sprayed on to the test plates was calibrated in situ within the test tunnel. Two Omega$^{\text{TM}}$ flat surface K-Type thermocouples were glued onto the surface of the heater pad to measure the local surface temperature. The thermocouples were glued onto the external heater pad surface prior to being painted black and then coated with liquid crystals.

The power to the heater pads was adjusted so that the full colour play of the liquid crystals could be observed. The colour play was recorded on a Panasonic$^{\text{TM}}$ video recorder. Simultaneously, the surface temperature signals from the surface mounted K-Type thermocouples were recorded via the data acquisition system described in section 4.6.

Figure 7.5 shows a typical green intensity signal and the hue signal, captured from the Panasonic$^{\text{TM}}$ video camera, plotted against the measured surface temperature. The green and hue signals are from an average of 6 pixels surrounding the tip of the surface mounted thermocouples. Table 7.2 shows the manufacturer's liquid crystal transition temperature for the liquid crystal coatings used.

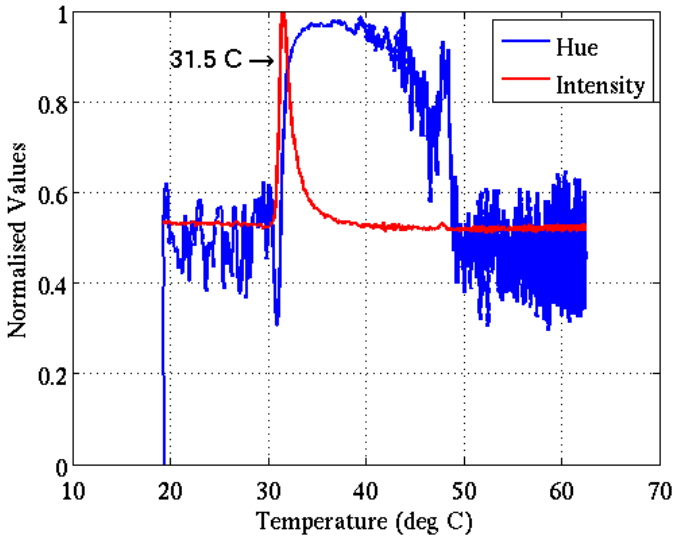

Figure 7.5: Liquid crystal event temperature for steady state heat transfer experiment.

Test plate	Crystal transition temperature (°C)
Datum test plate	31.1
Machined cutback test plate	31.5
Cast cutback test plate	31.2

Table 7.2: Crystal transition temperature.

7.2.2 Experimental procedure

The experimental procedure of the steady state heat transfer method is as follows

1. The mainstream gas temperature is set to a value by varying the Drake™ power supply.

2. The DC power supply to the heater pad is set so as to obtain a colour change of the liquid crystals.

3. An image of the heated surface with liquid crystal colour change, the power setting of the DC power supply to the heater pad, and the mainstream gas temperature are recorded.

4. The power to the heater pad is progressively varied until complete coverage liquid crystal colour contour moves across the full extent of the heated surface of the test plate.

5. The mainstream gas temperature is changed and the above procedures 1 to 4 are repeated.

Figure 7.6 shows still images of the pressure surface cut-back on the machined cutback test plate. From figure 7.6a, the extent of the Watlow^{TM} heater pad as well as the location of the Omega^{TM} surface mounted thermocouple can be seen. In figure 7.6(a) the DC power supply to the heater pad has not been set to obtain a colour change of the liquid crystals.

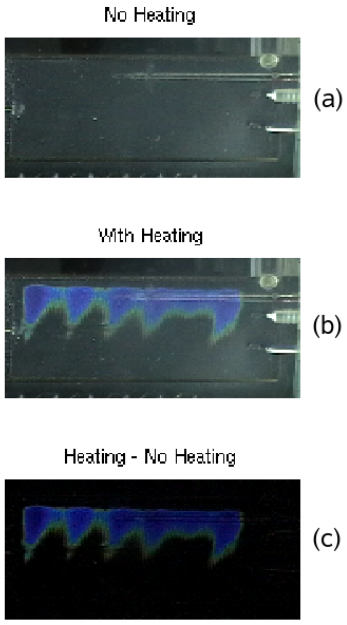

Figure 7.6: Still images of the machined cutback TE test plate with (a) no heat flux from heater pad, (b) heat flux from heater pad and (c) heated plate - unheated plate.

Figure 7.6b shows the colour play of the liquid crystal on the surface of the test plate with the heater pad turned on. To enhance the contrast of the colour of the liquid crystals the still image of the test plate with the heated surface was subtracted from the original still image of the unheated surface. Figure 7.6c shows such an image.

Figure 7.7a shows the decomposition of figure 7.6 into the hue, saturation and intensity components.

By using threshold values of hue and intensity, determined from a sample of images, a cropping mask was created for all images, to extract the contours where the largest change in hue signal with temperature is observed. Figure 7.7b shows such an extracted contour.

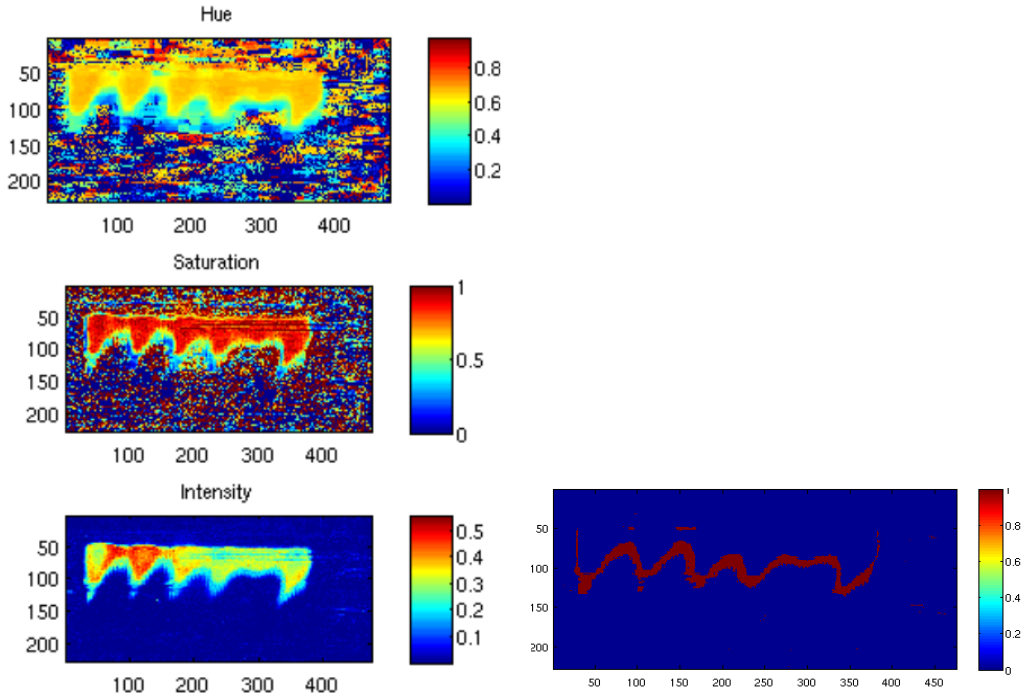

(a) Decomposition image to hue, saturation and intensity of the heated - unheated images

(b) Contour of greatest change in hue with temperature

Figure 7.7: Decomposition of the image to its constituent hue, saturation and intensity signal to identify the region of highest change in hue with temperature.

Each extracted contour was assigned its corresponding power (heat flux) from the DC power supply. Hence for a given mainstream gas temperature, contours of heat flux on the cutback surface were obtained. By using equation 7.3 and computing the slope and y-intercept, the film effectiveness and heat transfer coefficient were calculated.

For the heat transfer tests three mass flux ratios were targeted. For the datum and machined cutback configurations, mass flux ratios of 0.6, 0.8 and 1.0 were targeted. These are the typical mass flux ratios for discrete film cooling holes seen on engine turbine blade / vane at the late pressure surface. For the casts cutback test plate mass flux ratios of 0.3, 0.6 and 1.0 were targeted, as these are the expected range in mass flux ratios for a cast cutback slot arrangement in a engine turbine blade / vane. It must be noted that for the machined cutback test plate the lowest measured mass flux ratio was 0.72. Due to the heater mesh installed upstream of the test plates, the Reynolds number from the aerodynamic measurements, detailed earlier in this thesis,

could not be matched. Section 7.2.3 shows the calculated Reynolds number for the heat transfer measurements.

7.2.3 Experimental results

Figure 7.8 shows the contours of film effectiveness downstream of the film cooling ejection of the three test plates. In all of the figures, the trailing edge is located near the top whilst the coolant ejection plane is located near the bottom of the figures. Figures 7.8a to 7.8c show the film effectiveness for the datum test plates. Figures 7.8d to 7.8f show the effectiveness downstream of the machined cutback test plate. Figures 7.8g to 7.8i show the film effectiveness for the cast cutback test plate. In all three test plates, the range of cover of the liquid crystal contours extracted during the processing phase, on the test plates, determines the region of effectiveness data. Hence the range of cover of the effectiveness contours does not necessarily match the area of the heated surface,

In figure 7.8b, the rectangular high film effectiveness region near the trailing edge is due to an interpolation caused by the rectangular region devoid of uniform heat flux, found on the Watlow^{TM}heater pad. The region of high film effectiveness just downstream of the coolant ejection plane of the cast cutback test plate is also attributed to the above error.

From figures 7.8a to 7.8c, the high film effectiveness regions due to the coolant ejection via coolant holes can be observed. It can be observed that the trajectory of the coolant exhausting from each coolant hole is more in line with the mainstream flow direction rather than the inclination angle of the coolant holes. These high effectiveness regions are consistent with the high wall shear stress regions (see figure 6.7), predicted using steady CFD, downstream of the coolant holes. However, the contours downstream of the cast cutback trailing edge do not show evidence of the presence of upstream pedestal banks as seen in the pressure surface wall shear stress contours, shown in figure 6.7. The CFD predictions shown in chatper 6 are from a steady CFD calculation. The vortex shedding downstream of the pedestals is an unsteady phenomenon. Hence it is not surprising that the wakes due to the pedestals, seen from the wall shear stress contours on the pressure surface, are not evident in the film effectiveness contours downstream of the coolant ejection plane.

Figure 7.9 shows the contours of the heat transfer coefficient downstream of the film cooling ejection plane for the three test plates. Figures 7.9a to 7.9c show the heat transfer coefficient downstream of the datum test plate. Figures 7.9d to 7.9f show the heat transfer coefficient downstream of the machined cutback test plate. Figures 7.9g

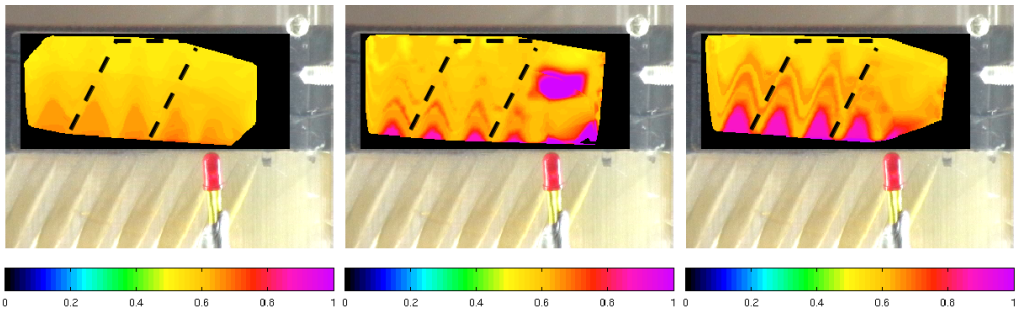

(a) Datum test plate η at M = 0.64, Re = 3.57×10^5 (b) Datum test plate η at M = 0.80, Re = 3.66×10^5 (c) Datum test plate η at M = 0.96, Re = 3.64×10^5

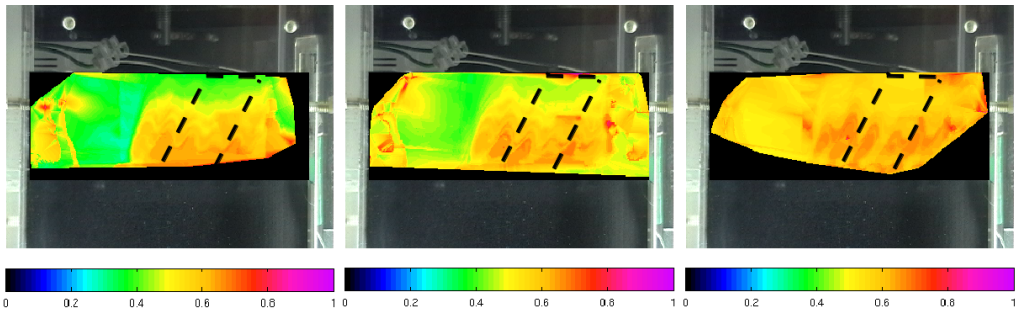

(d) Machined cutback test plate η at M = 0.72, Re = 2.87×10^5 (e) Machined cutback test plate η at M = 0.80, Re = 2.85×10^5 (f) Machined cutback test plate η at M = 1.12, Re = 2.81×10^5

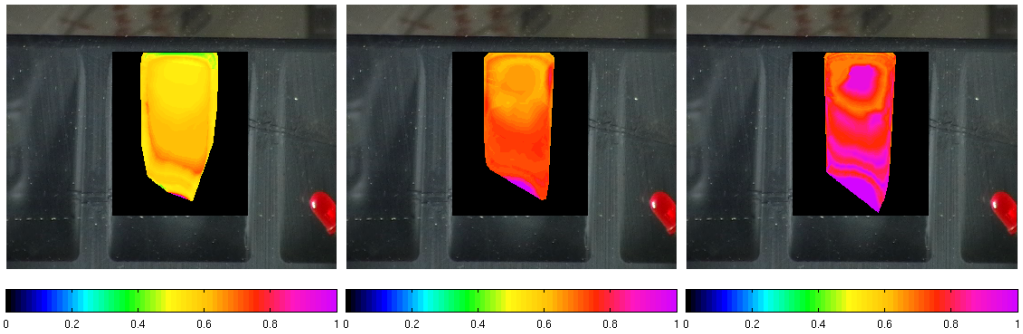

(g) Cast cutback test plate η at M = 0.30, Re = 3.77×10^5 (h) Cast cutback test plate η at M = 0.60, Re = 3.73×10^5 (i) Cast cutback test plate η at M = 1.00, 3.71×10^5

Figure 7.8: Film effectiveness downstream of the ejection plane.

to 7.9i show the heat transfer coefficients downstream of the cast cutback test plate. From figures 7.9a to 7.9b, it can be seen that there is heat transfer augmentation just downstream of the datum coolant holes due to the ejected coolant. However, at the highest mass flux ratio of 0.96, the heat transfer augmentation just downstream of the coolant ejection is lower than that at 0.64. This trend is observed when coolant jets separate and re-attach downstream of coolant ejection due to high momentum flux ratios, as seen in the experiments of Thole et al. (1992). However, in the current experiments, the momentum flux ratios are not high enough to cause jet separation and re-attachment downstream of coolant ejection. The low heat transfer coefficient at high mass flux ratio, just downstream of the coolant ejection is caused by the coolant jet separation due to the Rohacell^{TM} insert, which presents a step to the coolant flow. The coolant separates at the insert edge, nearest the coolant exit location and re-attaches downstream. It must also be noted that the measured heat transfer coefficient for the datum configuration, at the three measured mass flux ratios are within the measurement errors of the experiment shown in table 4.6. The heat transfer coefficient contours on the machined and cast cutback configuration, shown in figure 7.9, do not exhibit the above trend.

Figures 7.10 to 7.12 show the laterally averaged film effectiveness and heat transfer coefficient downstream of the cooling hole ejection plane. In figures 7.10 to 7.12 the downstream edge of the coolant holes as well as the trailing edge of the plates are marked. For the datum and machined cutback test plates, film effectiveness and heat transfer coefficient were laterally averaged over two coolant hole pitches. This laterally averaged region is shown in figures 7.8 and 7.9 as the area enclosed within the dashed lines. For the cast cutback test plate, the film and heat transfer coefficient was averaged across the central slot to the edge of the heater pad.

From figure 7.10a it can be seen that for the datum trailing edge ejection, as expected, the laterally averaged film effectiveness downstream of the coolant ejection increases with increasing mass flux ratio. Near the trailing edge, film effectiveness appears to be independent of the mass flux ratio, as the mass flux ratio increases above 0.80. The measured heat transfer coefficients at the three mass flux ratios were within the measurement errors. Hence no discernable trend with mass flux ratio can be observed.

From figure 7.11a it can be seen that the laterally averaged film effectiveness for the machined cutback test plate is independent of mass flux ratio, until approximately one hydraulic diameter downstream of the coolant ejection plane at the cutback. Beyond the hydraulic diameter of one, the laterally averaged film effectiveness increases with

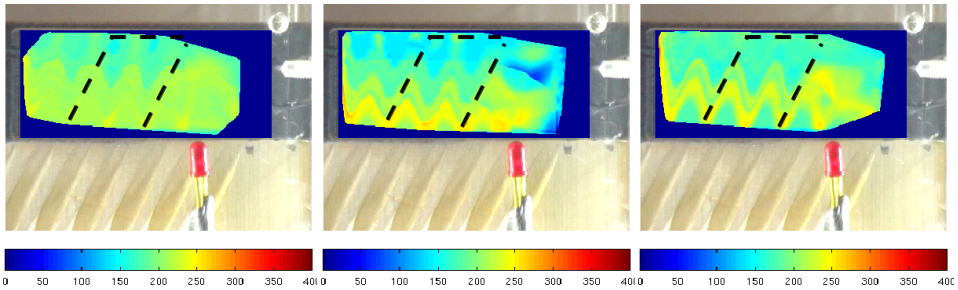

(a) Datum test plate h_f at M = 0.64, Re = 3.57×10^5

(b) Datum test plate h_f at M = 0.80, Re = 3.66×10^5

(c) Datum test plate h_f at M = 0.96, Re = 3.64×10^5

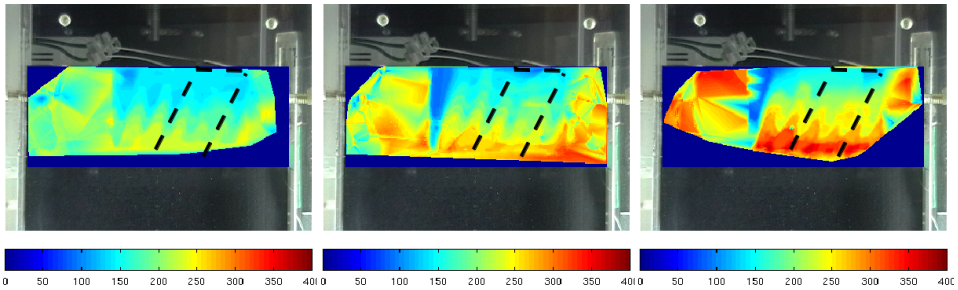

(d) Machined cutback test plate h_f at M = 0.72, Re = 2.87×10^5

(e) Machined cutback test plate h_f at M = 0.80, Re = 2.85×10^5

(f) Machined cutback test plate h_f at M = 1.12, Re = 2.81×10^5

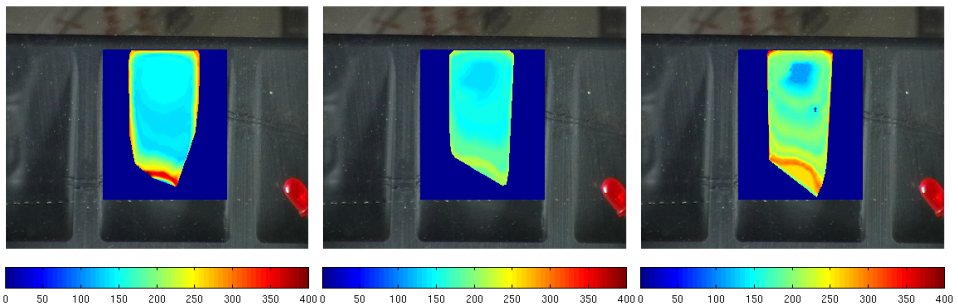

(g) Cast cutback test plate h_f at M = 0.30, Re = 3.77×10^5

(h) Cast cutback test plate h_f at M = 0.60, Re = 3.73×10^5

(i) Cast cutback test plate h_f at M = 1.00, Re = 3.71×10^5

Figure 7.9: Film heat transfer coefficient, h_f, (W/m^2K) downstream of the ejection plane

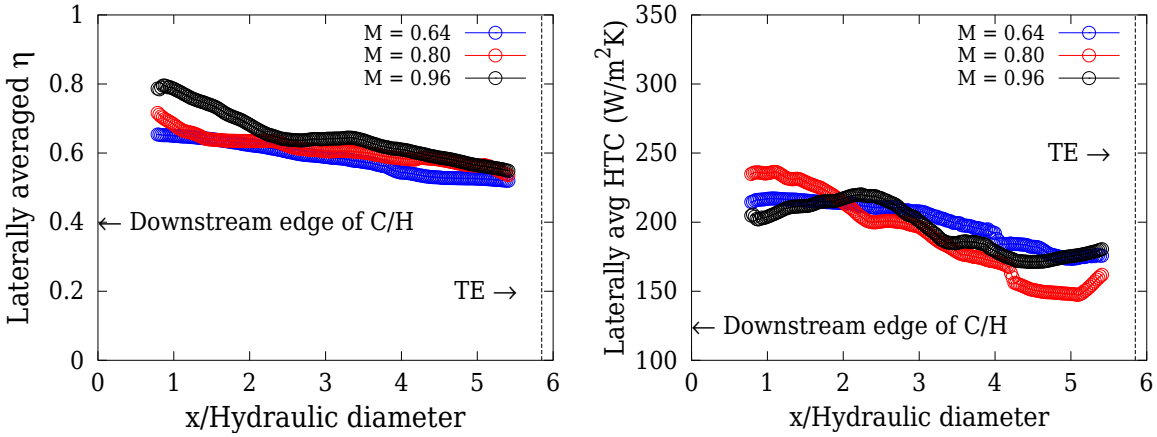

(a) Laterally averaged film effectiveness η

(b) Laterally averaged surface heat transfer coefficient

Figure 7.10: Laterally averaged, over two hole pitches, film effectiveness and surface heat transfer coefficient downstream of the datum pressure surface coolant holes.

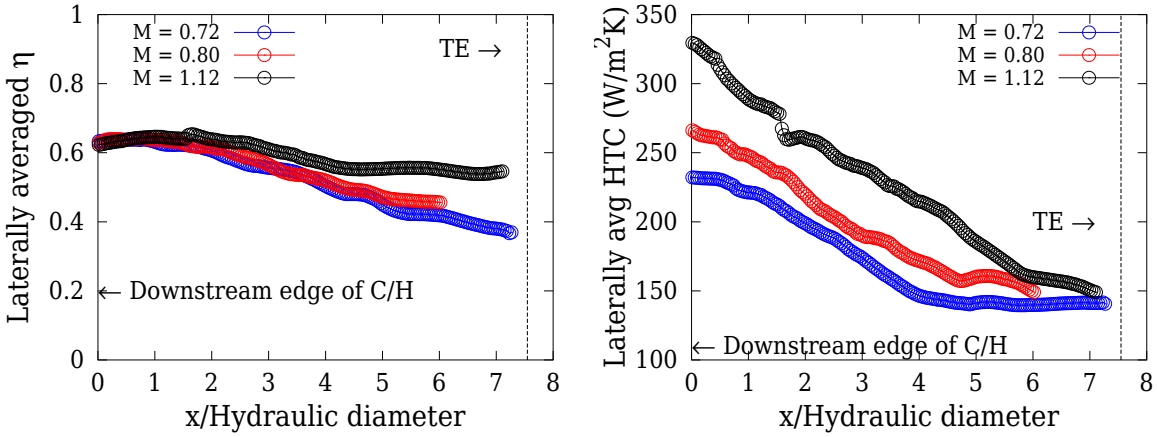

(a) Laterally averaged film effectiveness η

(b) Laterally averaged surface heat transfer coefficient

Figure 7.11: Laterally averaged, over two hole pitches, film effectiveness and surface heat transfer coefficient downstream of the machined cutback coolant holes.

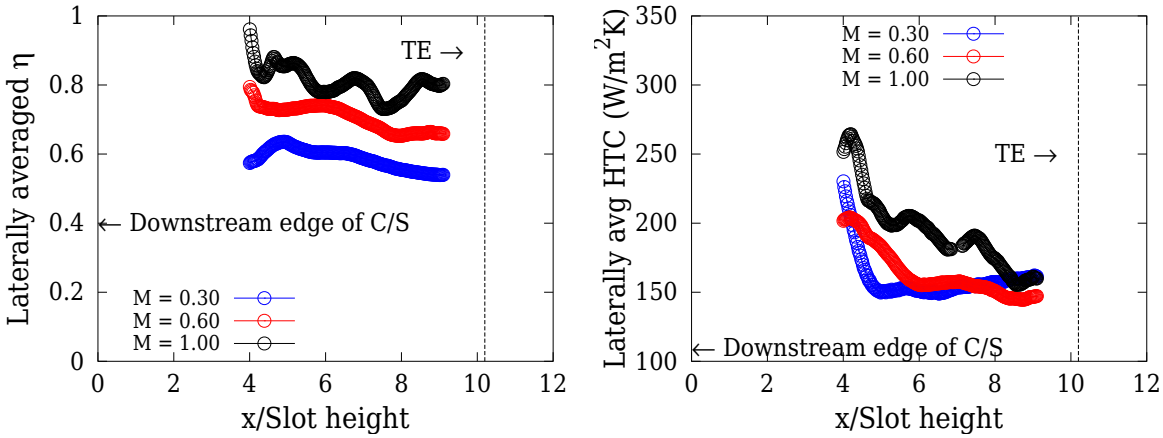

(a) Laterally averaged film effectiveness η

(b) Laterally averaged surface heat transfer coefficient

Figure 7.12: Laterally averaged, across the central hole slot, film effectiveness and surface heat transfer coefficient downstream of the cast cutback slot.

increasing mass flux ratio as expected. It must be noted that the rate of decay of film effectiveness downstream of the coolant ejection is lower at the higher mass flux ratio. At lower mass flux ratio, the coolant jets have lower momentum and hence mix with the mainstream. However, at high mass flux ratios, due to the high momentum of the coolant, the coolant jets do not completely mix with the mainstream. Hence the decay of film effectiveness with respect to distance downstream of ejection is less when compared with the laterally averaged film effectiveness at lower mass and momentum flux ratios. From figure 7.11b, it can be seen that with increasing mass flux ratio, there is an increase in the heat transfer coefficient on the pressure surface downstream of the cutback. The decay of heat transfer coefficient with distance downstream of the coolant ejection appears to be consistent for all mass flux ratios.

For the cast cutback test plate it can be seen from figure 7.12a that the film effectiveness increases with increasing mass flux ratio. Furthermore, comparing the film effectiveness on the cast cutback test plate with that on the machined cutback test plate, at a mass flux ratio of 1.00 (mass flux ratio of 1.12 on the machined cutback test plate), it can be concluded that the film effectiveness is greater on the cast cutback test plate. This is not surprising as the coolant is fed continuously within the central slot region. Hence there is less mixing of the coolant with the separated mainstream. From figure 7.12b it can be concluded that the heat transfer coefficient increases with increasing mass flux ratio. At a mass flux ratio of 1.00 on

the cast cutback test plate (mass flux ratio of 1.12 on the machined cutback test plate), the heat transfer coefficient near the trailing edge of the coolant ejection plane is comparable. However, there is insufficient data on the cast cutback test plate just downstream of the coolant ejection, due to the heater pad configuration (see figure 7.3), to make a comparison of the heat transfer coefficient with the machined cutback test plate.

At a mass flux ratio of 0.80, comparing the film effectiveness from the datum and machined cutback test plates, it can be seen that the film effectiveness levels on both test plates, just downstream of the coolant ejection, are comparable. Further downstream from the coolant ejection, the film effectiveness on the datum test plate decays whilst the effectiveness on the machined cutback test plate remains approximately constant. This is because the coolant jets from the machined cutback test plate are shielded from the mainstream due to the mainstream separating over the cutback surface. In the datum test plate, as the coolant jets exhaust from the coolant holes, they mix with the mainstream. Hence the film effectiveness decays with distance from the coolant exit plane. It must, however, be noted that the coolant holes on the machined cutback are discrete holes and hence there would be some mainstream entrainment with the coolant jets. Therefore the film effectiveness just downstream of the coolant ejection is not unity. Moving further towards the trailing edge, the decay in film effectiveness on the machined cutback test plate is greater than that on the datum test plate. This is due to the enhanced mixing of the coolant jets with the separated mainstream. Considering the heat transfer coefficient, there is higher heat transfer just downstream of coolant ejection on the machined cutback test plate when compared with the datum test plate. The decay in heat transfer coefficient is, however, greater on the machined cutback test plate, when compared with the datum test plate. This, again, is due to the enhanced mixing of the coolant jets with the separated mainstream on the machined cutback test plate.

Figure 7.13 shows the comparison of the laterally averaged effectiveness at $\frac{x}{D}$ of 4 and 5 for the three tested cooling configurations. The laterally averaged effectiveness data are plotted against mass flow ratio. For the cast cutback configuration, the laterally averaged effectiveness was plotted at a distance of 4 and 5 times the slot height downstream of the coolant flow ejection plane.

From the trends in the variation of the laterally averaged effectiveness against mass flow ratio, at low mass flow ratios and at $\frac{x}{D}$ of 4 or 5 downstream of the coolant ejection, it can be seen that the datum configuration provides the same effectiveness with a lower coolant mass flow. However, with the increasing mass flow ratio of

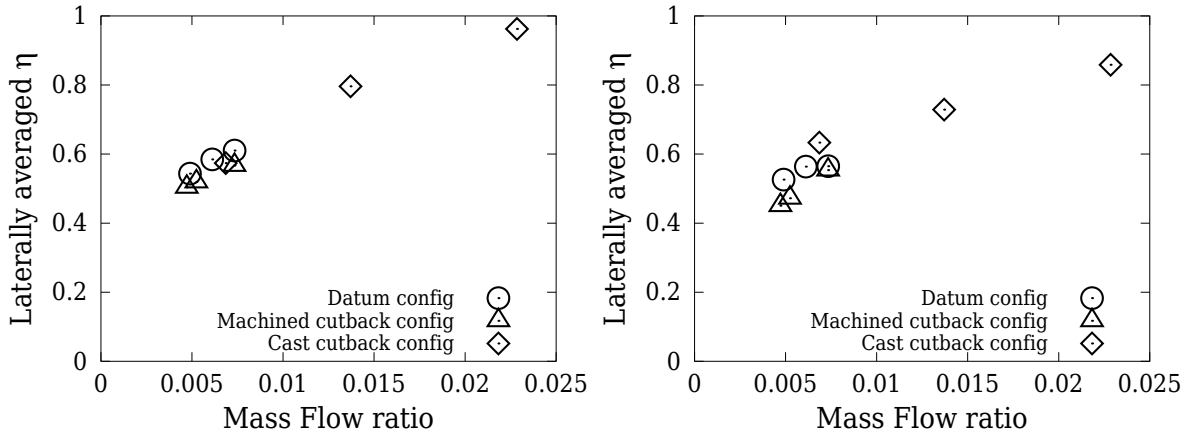

(a) Laterally averaged film effectiveness η at $\frac{x}{D} = 4$(b) Laterally averaged film effectiveness η at $\frac{x}{D} = 5$

Figure 7.13: Comparison of the laterally averaged effectiveness against mass flow ratio at $\frac{x}{D}$ of 4 and 5.

the coolant, the cast cutback configuration shows the potential to provide the better laterally averaged effectiveness.

7.3 Comparison of experimental data

Figure 7.14 shows the laterally averaged effectiveness data from the current research compared with the experimental data from Waye (2005), Martini et al. (2005) and the slot correlation from Goldstein and Haji-Sheikh (1967). The Goldstein Model shown in figure 7.14 was derived from the experimental data measured downstream of a continuous slot, with a sharp pressure surface lip thickness. The coolant was fed via a large curved entry duct, providing a uniform flow downstream of the coolant ejection. This is an ideal slot ejection configuration, where the effectiveness downstream of ejection gradually decays from unity.

Comparing the laterally averaged effectiveness from Goldstein and Haji-Sheikh (1967) with the cast cutback configuration and the experimental results from Martini et al. (2005), the effects of the internal configuration on the downstream laterally averaged effectiveness can be seen. The three slot geometric configurations, G1, G2a and G2b from Martini et al. (2005) are illustrated in figure 2.26b. The trailing edge internal configuration of the cast cutback test plate in the current research is approximately a combination of G1 and G2a test configurations of Martini et al. (2005). The experimental results from the cast cutback configurations for mass flux

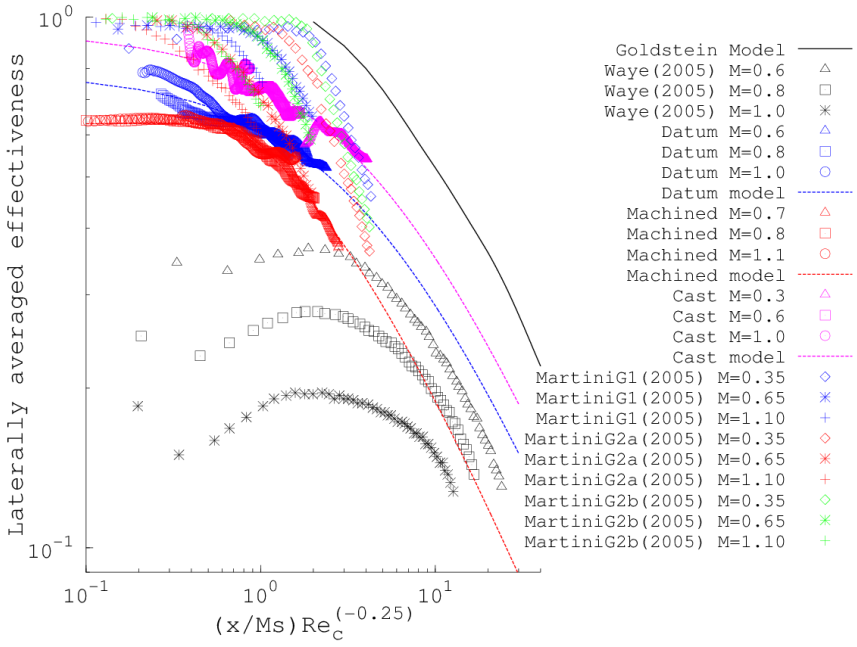

Figure 7.14: Laterally averaged film effectiveness data from datum, machined and cast cutback compared with Goldstein and Haji-Sheikh (1967), Waye (2005) and Martini et al. (2005).

ratios of 0.6 and 1.0 are similar to those from Martini et al. (2005) at mass flux ratios of 0.65 and 1.10. However, at the lowest tested mass flux ratio, the effectiveness from the cast cutback configuration does not have a similar trend to those from Martini et al. (2005). The discrepancies in the rate of the decay of the laterally averaged effectiveness between the cast cutback configuration and the tests from Martini et al. (2005) can be attributed to the differences in the density ratio and the ratio of pressure surface lip thickness to slot height. The three slot configurations of Martini et al. (2005) had a pressure surface lip thickness to slot height ratio of 1.0 and the tests were carried out at engine representative density ratios of 1.5 to 1.7. In contrast, the pressure surface lip thickness to slot height ratio of the cast cutback test plate was approximately 0.86 and the tests were carried out at density ratio of unity. For the same mass flux ratio, a density ratio of greater than unity results in a velocity ratio lower than that for a case with density ratio of unity. Hence the coolant and the mainstream flows would have dissimilar velocities, increasing the mixing between the two streams. A large pressure surface lip thickness will also cause eddies to separate off the lip and readily mix downstream with the coolant flow. Therefore the cause of the rapid decay in the laterally averaged effectiveness of Martini et al. (2005),

compared with the cast cutback configuration, is attributed to the difference in the density ratio and pressure surface lip thickness.

The laterally averaged effectiveness from Waye (2005) is from experiments with discrete film cooling holes inclined at 30 ° and having a spacing of three hole pitches. For similar mass flux ratios, the datum configuration, has a higher laterally averaged effectiveness. This higher effectiveness is due to the combination of favourable hole inclination angle, hole length, spacing and compound angle in the datum configuration, resulting in the coolant flow exhausting onto the pressure surface as tangentially as possible.

Figure 7.14 also shows models, in the form of equation 2.10, fitted to the datum, machined and cast cutback laterally averaged effectiveness data. The parameters used for the fitting are given in table 7.3.

Plate Configuration	Parameter C_1	Parameter C_2
Datum	0.9976	0.2779
Machined cutback	1.1739	0.6189
Cast cutback	1.1922	0.2658

Table 7.3: Slot model parameters for datum, machined cutback and cast cutback configuration.

7.4 Conclusions

A steady state heat transfer technique was used to measure the film effectiveness and heat transfer coefficient on the pressure surface of the test plates downstream of the trailing edge ejection. Laterally averaged film effectiveness and heat transfer coefficients on the pressure surface, downstream of the film cooling ejection plane were computed. It must be noted that, for the datum and machined cutback test plates, laterally averaged film effectiveness and heat transfer coefficients were computed over two hole pitches. For the cast cutback test plate, the laterally averaged film effectiveness and heat transfer coefficient were computed across the central slot region.

Comparing the laterally averaged film effectiveness from the three test plates, it can be concluded that generally the film effectiveness increases with increasing mass flux ratio, as expected. Just downstream of the coolant ejection, the film effectiveness

for the datum test plates is greater than that for the machined cutback test plate. This is due to the fact that, in the machined cutback test plate, the coolant is ejected away from the pressure surface and impinges further downstream on the pressure surface. The slight rise in the laterally averaged effectiveness on the machined cutback test plate, further downstream from the coolant ejection plane, is due to the reattachment of the coolant jets. In the case of the datum test plate, the notably high coolant effectiveness region observed just downstream of the coolant ejection location is due to the coolant exhausting on the pressure surface.

Moving further towards the trailing edge, along the pressure surface, the coolant mixes with the mainstream and hence a reduction in the film effectiveness with distance is observed on all three test plates. Near the trailing edge, the film effectiveness level at a mass flux ratio of 0.80 is approximately 0.58 for the datum test plate and 0.40 for the machined cutback test plate. At a lower mass flux ratio of 0.60, the film effectiveness on the cast cutback test plate at the trailing edge is approximately 0.6. However, it must be noted that the lower mass flux ratio of 0.6 in the cast cutback test plate corresponds to approximately twice the mass flow rate of the machined cutback test plate. Hence it is not surprising that the effectiveness is higher on the cast cutback test plate. The trends in the laterally averaged effectiveness with mass flow ratio also show that the cast cutback configuration has the potential to provide higher effectiveness than the datum and machined cutback configurations with high mass flow ratios.

For the datum test plate, the measured heat transfer coefficients at the three mass flux ratios were within the measurement errors of the experiment. Hence no discernable trend could be observed. For the machine and cast cutback test plates, higher heat transfer coefficient levels were achieved with higher mass flux ratios. This is not surprising, as increases in mass flux ratio increase the momentum of the coolant jets, resulting in higher velocity and hence higher heat transfer coefficients. Far downstream from coolant ejection, the heat transfer coefficient reached similar values for all mass flux ratios.

Chapter 8

CFD predictions of low speed heat transfer measurements

This chapter describes the computational fluid dynamics predictions conducted on the low speed heat transfer experiments. Fluent^{TM}version 6.1.12 was used to predict the film effectiveness and heat transfer coefficient on the pressure surface near the trailing edge of the test plates. The boundary conditions and geometry were chosen to match the experiments described in chapter 7.

8.1 Model and mesh generation

The computational domain created for the aerodynamic predictions described in chapter 6 was modified and used to generate the heat transfer predictions. The surface downstream of the film cooling ejection plane was segregated from the pressure surface of the test plates within the computational domain. This was done so that the heat flux from the heater pad could be represented in the computational predictions. Figure 8.1 shows the heated wall segments on the pressure surface at which constant heat flux boundary conditions were applied.

The meshes for the three computation domains were created using the process defined in chapter 6. Care was taken to ensure that the mesh was uniform across the boundaries of the segmented surface. This was to ensure that discontinuities at the boundary did not the cause errors.

8.2 Boundary conditions

Tables 8.1 to 8.3 show the boundary conditions applied to the three CFD models used for the prediction of the heat transfer experiments. The boundary condition

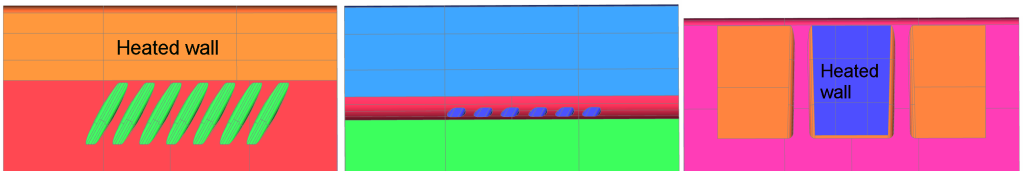

(a) Datum test plate heated wall (b) Machined cutback test plate heated wall (c) Cast cutback test plate heated wall

Figure 8.1: Segregated pressure surface sections for the datum, machined cutback and cast cutback test plate CFD models. A constant heat flux boundary condition was applied at the heated surfaces indicated.

values shown in tables 8.1 to 8.3 were derived from the experimental measurements described in chapter 7.

Boundary conditions		Model cases		
		M = 0.64	M = 0.80	M = 0.96
Operating pressure (Pa)		100915.47	101710.08	101710.08
Mainstream inlet	Total pressure (Pa)	-1322.65	-1319.18	-1320.30
	Total temperature (K)	309.70	308.78	308.92
	Turbulence intensity (%)	4.00	4.00	4.00
	Hydraulic diameter (m)	0.150	0.150	0.150
Mainstream outlet	Total pressure (Pa)	-1525.31	-1528.66	-1528.25
	Turbulence intensity (%)	4.00	4.00	4.00
	Hydraulic diameter (m)	0.150	0.150	0.150
Coolant inlet	Mass flow rate (kg/s)	0.00255	0.00290	0.00367
	Total temperature (K)	297.00	297.30	296.99
	Turbulence intensity (%)	4.00	4.00	4.00
	Hydraulic diameter (m)	0.0185	0.0185	0.0185
Heaterpad heat flux	qdot01 (W/m^2)	204.28	254.73	314.67
	qdot02 (W/m^2)	408.56	509.46	629.35
	qdot03 (W/m^2)	762.82	840.79	891.72

Table 8.1: Boundary conditions for datum trailing edge configuration CFD model.

As stated in section 6.3, the mainstream inlet total pressures were derived from measurements just upstream of the test plate. It must, however, be noted that this

Boundary conditions		Model cases		
		M = 0.72	M = 0.80	M = 1.12
Operating pressure (Pa)		101974.95	100518.17	101974.95
Mainstream inlet	Total pressure (Pa)	-1321.03	-1332.48	-1325.30
	Total temperature (K)	304.35	305.49	308.12
	Turbulence intensity (%)	4.00	4.00	4.00
	Hydraulic diameter (m)	0.150	0.150	0.150
Mainstream outlet	Total pressure (Pa)	-1523.40	-1537.00	-1523.40
	Turbulence intensity (%)	4.00	4.00	4.00
	Hydraulic diameter (m)	0.150	0.150	0.150
Coolant inlet	Mass flow rate (kg/s)	0.00233	0.00261	0.00348
	Total temperature (K)	296.80	296.93	297.13
	Turbulence intensity (%)	4.00	4.00	4.00
	Hydraulic diameter (m)	0.0185	0.0185	0.0185
Heaterpad heat flux	qdot01 (W/m^2)	354.88	330.88	324.93
	qdot02 (W/m^2)	709.76	661.75	649.86
	qdot03 (W/m^2)	6468.23	1120.00	1235.17

Table 8.2: Boundary conditions for machined cutback trailing edge configuration CFD model.

Boundary conditions		Model cases		
		M = 0.30	M = 0.60	M = 1.00
Operating pressure (Pa)		99326.25	99326.25	99326.25
Mainstream inlet	Total pressure (Pa)	-1280.29	-1284.23	-1281.12
	Total temperature (K)	309.22	307.89	306.63
	Turbulence intensity (%)	4.00	4.00	4.00
	Hydraulic diameter (m)	0.150	0.150	0.150
Mainstream outlet	Total pressure (Pa)	-1499.57	-1499.26	-1495.28
	Turbulence intensity (%)	4.00	4.00	4.00
	Hydraulic diameter (m)	0.150	0.150	0.150
Coolant inlet	Mass flow rate (kg/s)	0.0032	0.0071	0.0125
	Total temperature (K)	295.57	295.67	295.08
	Turbulence intensity (%)	4.00	4.00	4.00
	Hydraulic diameter (m)	0.0185	0.0185	0.0185
Heaterpad heat flux	qdot01 (W/m^2)	392.00	682.00	1245.00
	qdot02 (W/m^2)	784.00	1023.00	1596.00
	qdot03 (W/m^2)	1492.00	1378.00	2109.00

Table 8.3: Boundary conditions for cast cutback trailing edge configuration CFD model.

total pressure was measured downstream of the heater mesh, which was installed upstream of the test plate leading edge. The mainstream total temperatures shown in tables 8.1 to 8.3 were set to equal thermocouple measurements of the mainstream flow over the pressure surface of the test plates.

The mainstream outlet static pressure was matched to the tunnel side wall static tapping measurements 372.0 mm downstream from the leading edge of the test plate. This was the same plane on which the traverse measurements were conducted.

The measured heat flux from the heater pads on the three experimental test plates were used as heat flux boundary conditions on the segmented surface of the CFD domains. In the heat transfer experiments, the mainstream gas temperature, along with the heater pad heat flux, was varied to obtain the heat transfer coefficient and the film effectiveness. The mainstream gas temperature was varied so that the temperature distribution over the heated surface could be determined using a single liquid crystal coating. For the CFD analysis, the full temperature distribution over the heated surface is predicted, and hence only the heat flux on the segmented surface needed to be varied.

Apart from the mainstream and coolant inlet, the mainstream outlet and the segmented surface, each of the other surfaces was set as an adiabatic wall. For the initial heat transfer computational run, the segmented wall was also set as an adiabatic wall. For subsequent runs, the heat fluxes shown in tables 8.1 to 8.3 were matched.

8.3 Turbulence model computation method

From the conclusions shown in section 3.6, the Spalart-Allmaras turbulence model is the best choice to predict film cooling effectiveness and heat transfer coefficients. As the generated mesh was sufficiently refined, the Spalart-Allmaras turbulence model was chosen to predict the heat transfer experiment. It must, however, be noted that the tunnel wall mesh was not refined. Hence the tunnel wall adiabatic temperatures would not be accurately captured. However, the tunnels walls are far away from the region of interest and hence inaccuracies in the wall temperature would not influence the flat plate predictions.

For all simulations the flow was initialised and run using the procedure shown in section 3.4.3. The mass flow rate at the outlet plane was also monitored. Convergence of the simulations was identified when the mass flow rate reached a constant value.

8.4 CFD results

Figure 8.2 shows the film effectiveness distributions from the steady computational fluid dynamics predictions for the three test plate models. The effectiveness contours shown in figure 8.2 are from the coolant ejection plane to the trailing edge. Figures 8.2a to 8.2c show the predicted effectiveness contours on the datum test plate model. Figures 8.2d to 8.2f show the predicted effectiveness contours on the machined cutback test plate. Figures 8.2g to 8.2i show the predicted effectiveness contours on the cast cutback test plate. The predicted contours are plotted across the width of the test plate models from the datum and machined cutback test plates, shown in figures 8.2a to 8.2f. In the case of the cast cutback test plate, the predicted film effectiveness contours are shown across the central slot region of the model.

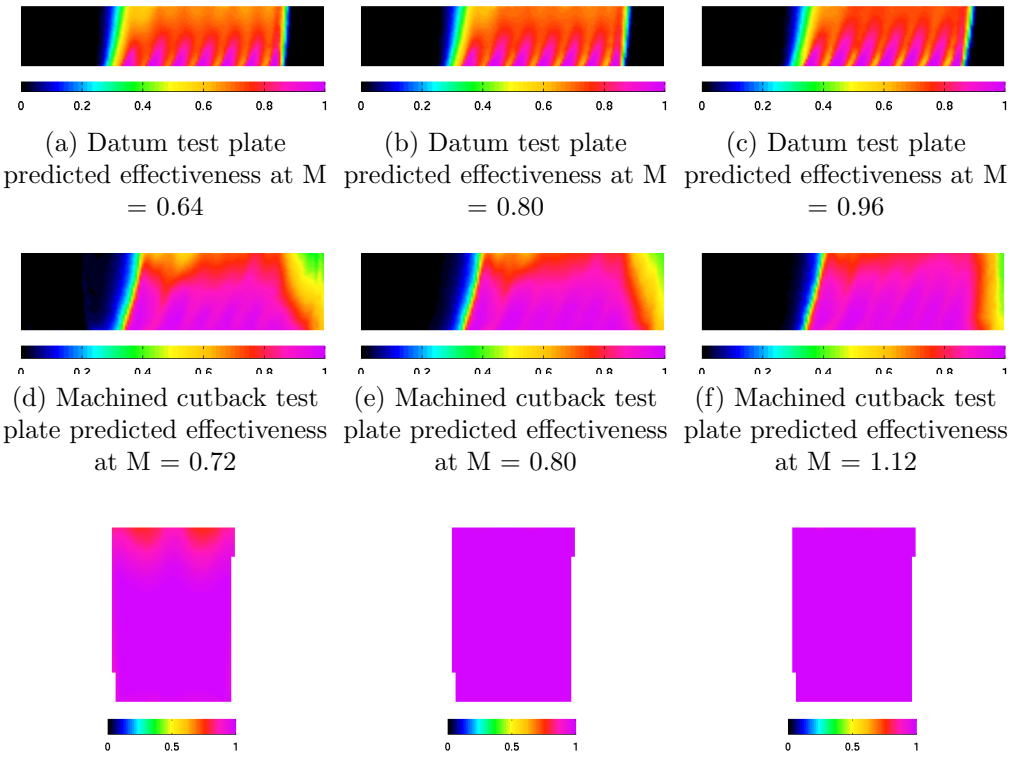

(a) Datum test plate predicted effectiveness at M = 0.64

(b) Datum test plate predicted effectiveness at M = 0.80

(c) Datum test plate predicted effectiveness at M = 0.96

(d) Machined cutback test plate predicted effectiveness at M = 0.72

(e) Machined cutback test plate predicted effectiveness at M = 0.80

(f) Machined cutback test plate predicted effectiveness at M = 1.12

(g) Cast cutback test plate predicted effectiveness at M = 0.30

(h) Cast cutback test plate predicted effectiveness at M = 0.60

(i) Cast cutback test plate predicted effectiveness at M = 1.00

Figure 8.2: Predicted film effectiveness, downstream of the coolant ejection on the three test plates.

From figures 8.2a to 8.2c it can be seen that the predicted film effectiveness downstream of the seven coolant holes shows similar trends to that measured from the low

speed heat transfer experiments. The predicted coolant jets are seen to turn, from the angle of ejection, to the mainstream flow direction as seen in the experiments. However, from the contour plots it can be seen that the predicted high film effectiveness, just downstream of the coolant ejection, extends further towards the trailing edge, when compared with the experimentally determined film effectiveness. This observation is also seen in the predicted film effectiveness downstream of the machined and cast cutback test plate models. It appears that the mixing of the coolant jets with the mainstream is underpredicted in the CFD predictions.

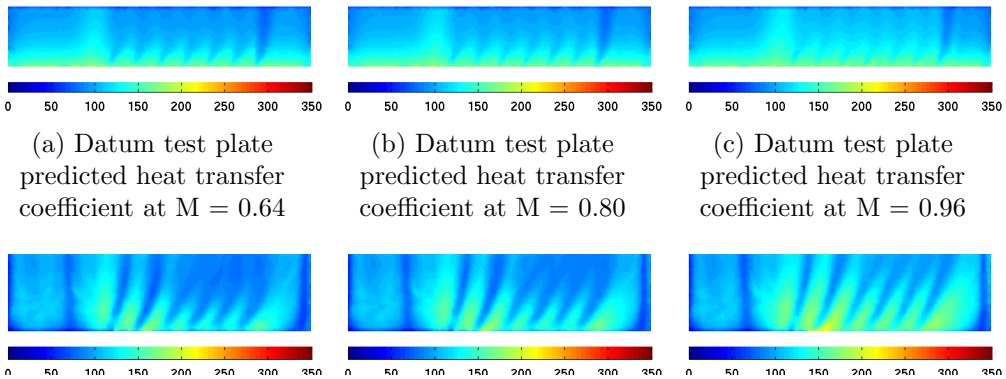

(a) Datum test plate predicted heat transfer coefficient at M = 0.64

(b) Datum test plate predicted heat transfer coefficient at M = 0.80

(c) Datum test plate predicted heat transfer coefficient at M = 0.96

(d) Machined cutback test plate predicted heat transfer coefficient at M = 0.72

(e) Machined cutback test plate predicted heat transfer coefficient at M = 0.80

(f) Machined cutback test plate predicted heat transfer coefficient at M = 1.12

(g) Cast cutback test plate predicted heat transfer coefficient at M = 0.30

(h) Cast cutback test plate predicted heat transfer coefficient at M = 0.60

(i) Cast cutback test plate predicted heat transfer coefficient at M = 1.00

Figure 8.3: Predicted heat transfer coefficient, downstream of the coolant ejection on the three test plates.

Figure 8.3 shows the predicted heat transfer coefficients downstream of the coolant ejection on the three test plate models. From the contours of the heat transfer coefficients shown in figures 8.3a to 8.3f, it can be seen that the coolant jets exhausting from the coolant holes are turned in the direction of the mainstream, as seen in the experimental measurements. In figures 8.3g to 8.3i the wake structures caused by the

upstream pedestal banks are seen in the contours on the pressure surface of the cast cutback test plate model.

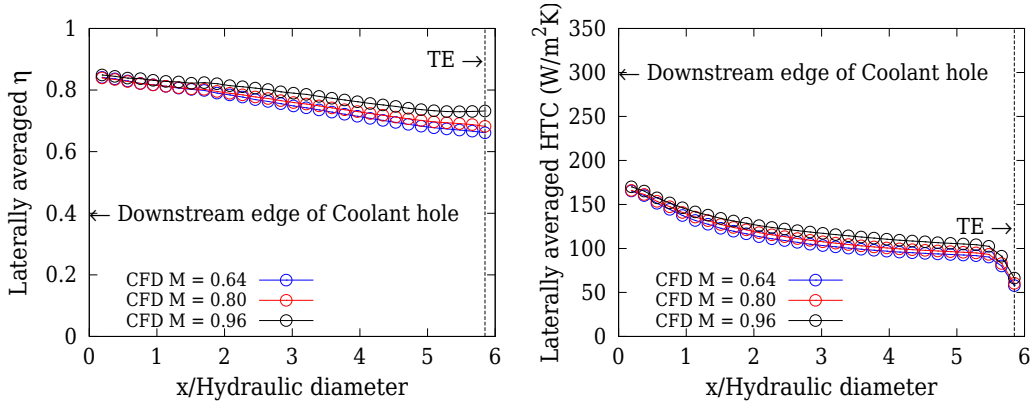

(a) Datum test plate laterally averaged effectiveness

(b) Datum test plate laterally averaged heat transfer coefficient

Figure 8.4: Predicted laterally averaged film effectiveness and heat transfer coefficient on the pressure surface, downstream of the coolant ejection, on the datum test plate

Figures 8.4 to 8.6 show the predicted laterally averaged film effectiveness and heat transfer coefficient downstream of the coolant ejection. In the case of the datum and machined cutback test plate, the film effectiveness and heat transfer coefficients were averaged across two hole pitches. In the case of the cast cutback test plate, the predicted film effectiveness and heat transfer coefficients were averaged across the central slot.

8.5 Comparison of the CFD predictions with experimental data

Figures 8.7 to 8.9 show the laterally averaged film effectiveness and heat transfer coefficient from the experimental measurements compared with the CFD predictions. From the figures, it can be seen that the CFD over predicts the laterally averaged film effectiveness and under predicts the laterally averaged heat transfer coefficient, for all the three cooling configurations.

It can be seen from figure 8.7a that the predictions of the laterally averaged film effectiveness for the datum configuration follow the same trends as the experimental measurements. Furthermore, the predictions reasonably capture the decay of the

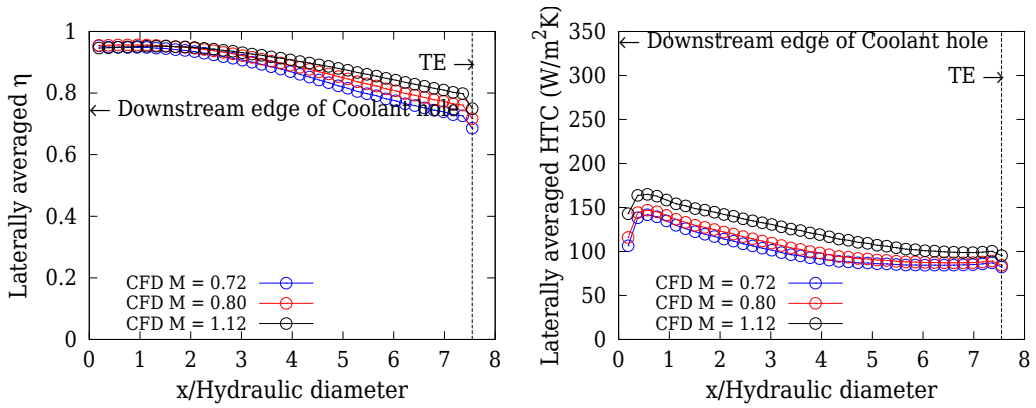

(a) Machined cutback test plate laterally averaged effectiveness

(b) Machined cutback test plate laterally averaged heat transfer coefficient

Figure 8.5: Predicted laterally averaged film effectiveness and heat transfer coefficient on the pressure surface, downstream of the coolant ejection, on the machined cutback test plate

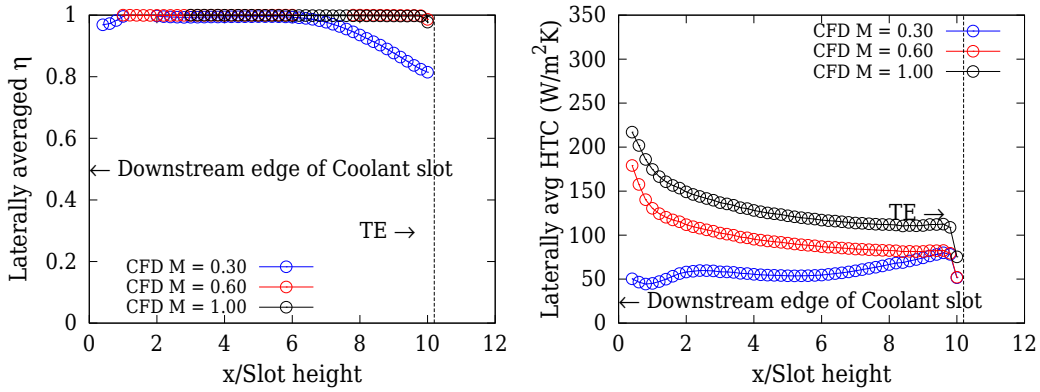

(a) Cast cutback test plate laterally averaged effectiveness

(b) Cast cutback test plate laterally averaged heat transfer coefficient

Figure 8.6: Predicted laterally averaged film effectiveness and heat transfer coefficient on the pressure surface, downstream of the coolant ejection, on the cast cutback test plate

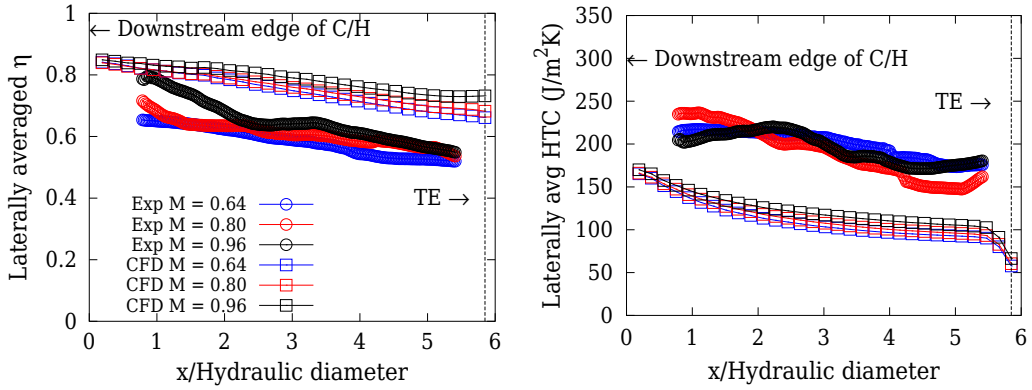

(a) Datum test plate laterally averaged effectiveness

(b) Datum test plate laterally averaged heat transfer coefficient

Figure 8.7: Comparison between the predicted and experimental, laterally averaged film effectiveness and heat transfer coefficient on the pressure surface, downstream of the coolant ejection, on the datum test plate.

laterally averaged effectiveness with distance downstream of the coolant ejection. In figure 8.7b it can be seen that the trends in the experimental data are not captured within the CFD predictions.

In figure 8.8a, it can be seen that the CFD predicts the effectiveness trend of the mainstream flow separation at the cutback, and subsequent re-attachment downstream on the pressure surface, as seen in the experimental measurements. However, the CFD under predicts the interaction of the coolant with the mainstream, in the vicinity of the pressure surface cutback and hence the predicted effectiveness is close to unity. This under prediction of the interaction of the mainstream flow with the coolant flow is seen in the trends of the heat transfer coefficient predictions shown in figure 8.8b. The heat transfer coefficients predicted by the CFD are lower than the measurements.

From figure 8.9, it can be seen that the film effectiveness and heat transfer coefficient predictions, for the cast cutback configuration, under predict the mainstream and coolant interaction downstream of the exit plane of the coolant. However, in figure 8.9a it can be seen that, at the lowest mass flux ratio, the decay in the film effectiveness, caused by the enhanced mixing of the mainstream and coolant, seen in the measurements at a distance of seven hydraulic diameters downstream of the coolant ejection, is captured in the CFD prediction. The expected rise in heat transfer coefficient due to the mixing, from seven hydraulic diameters downstream of the coolant ejection to the trailing edge, is seen in figure 8.9b.

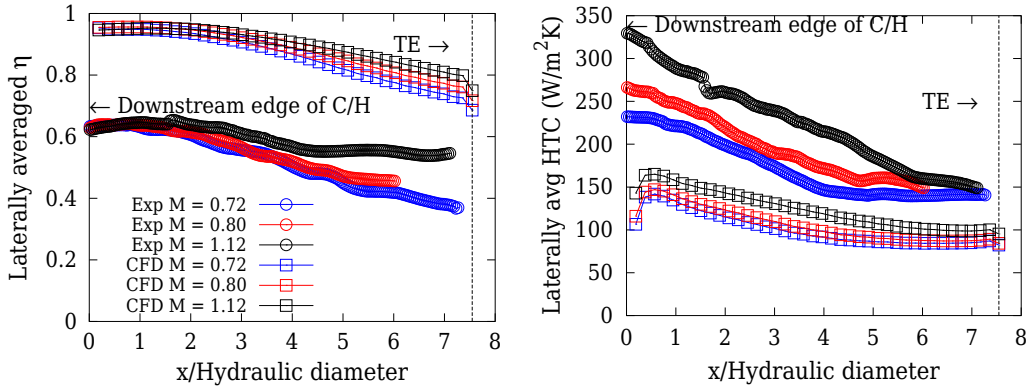

(a) Machined cutback test plate laterally averaged effectiveness

(b) Machined cutback test plate laterally averaged heat transfer coefficient

Figure 8.8: Comparison between the predicted and experimental, laterally averaged film effectiveness and heat transfer coefficient on the pressure surface, downstream of the coolant ejection, on the machined cutback test plate.

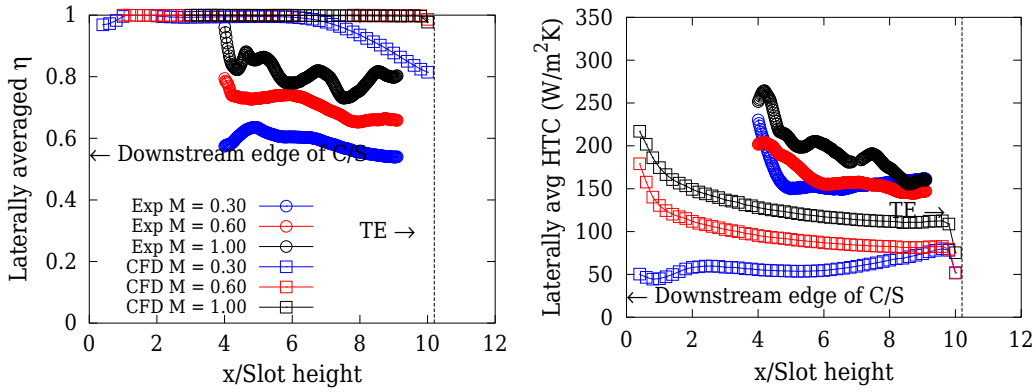

(a) Cast cutback test plate laterally averaged effectiveness

(b) Cast cutback test plate laterally averaged heat transfer coefficient

Figure 8.9: Comparison between the predicted and experimental, laterally averaged film effectiveness and heat transfer coefficient on the pressure surface, downstream of the coolant ejection, on the cast cutback test plate.

However, at higher mass flux ratios, the experimental trends are not captured in the CFD predictions. It appears that the coolant flow in the CFD predictions has sufficient momentum, as a result of incorrect prediction of the internal blockage, and is able to cool the pressure surface downstream of the coolant ejection up to the trailing edge.

8.6 Conclusion

This chapter documents the results from low speed, steady computational fluid dynamic predictions of the film effectiveness and heat transfer coefficient on the pressure surface of the datum, machined cutback and cast cutback test plate models. The predicted effectiveness and heat transfer coefficient contours, on the pressure surface, were compared with the measured contours shown in chapter 7. Laterally averaged film cooling effectiveness and heat transfer coefficients were computed from the predictions for the three test plates.

The predicted film effectiveness and heat transfer coefficient contours for the datum and machined cutback test plate configurations show similar trends to those measured using the steady state heat transfer technique. However, the predicted and measured contours of the cast cutback test plate do not show similar trends. In the CFD predictions, the wakes due to the upstream pedestal banks are visible on the pressure surface of the test plates. These wakes are not visible on the measured film effectiveness and heat transfer coefficient contours.

Comparing the magnitudes of the laterally averaged film effectiveness from the measurements and CFD predictions, it can be concluded that the mixing of the mainstream with the coolant is less pronounced in the CFD predictions. This is not surprising as the CFD predictions were obtained using a steady solver. Despite the above discrepancies, the predicted laterally averaged film effectiveness downstream of the film cooling ejection shows similar behaviour to that measured for the datum and machined cutback test plate configurations. In the predictions for the machined cutback configuration, it can be seen that the film effectiveness is not a function of the mass flux ratio until a distance of approximately 1.5 hole diameters downstream of the coolant ejection plane. This behaviour is seen in the laterally averaged film effectiveness measurements, though due to the enhanced mixing of the mainstream with the coolant, the distance is approximately 1.0 hole diameters downstream of the coolant ejection.

Comparing the magnitudes of the predicted and measured laterally averaged heat transfer coefficients for the datum and machined cutback test plates, it can be seen that the laterally averaged heat transfer coefficients are under predicted. This under prediction is due to the lower mixing predicted in the simulations. However, the trends seen in the measurements are visible in the predictions. In the datum configuration, the measured film heat transfer coefficient at the highest tested mass flux ratio was lower than the heat transfer coefficient at the lowest tested mass flux ratio, just downstream of the coolant ejection.

In the case of the cast cutback configuration, the CFD predictions show very little difference, as the blowing ratio is varied, in the laterally averaged film cooling effectiveness downstream of the coolant ejection. At the lowest simulated mass flux ratio, the laterally averaged effectiveness is seen to decay before the trailing edge. This is not the case with the measured laterally averaged film effectiveness for the cast cutback test plate. Comparing the measured and predicted film effectiveness contours, it can be seen that there is no evidence of the wakes due to the pedestal banks, which are seen in the predictions but not in the measurements. This can be attributed to the unsteady interactions of the mainstream with the coolant stream, downstream of the coolant ejection in the test plate, which are not captured by the steady CFD predictions. Comparing the measured and predicted laterally averaged heat transfer coefficients, it can be concluded that the unsteady interactions of the mainstream with the coolant produce higher heat transfer coefficients in the measurements which are not captured in the CFD predictions.

Therefore from the CFD investigations it can be concluded that trends in the film effectiveness and heat transfer coefficient can be predicted for the datum and machined cutback configurations using the steady CFD solver. However, to predict the absolute magnitudes, the simulations would need to be run using an unsteady solver. In the case of the cast cutback configurations, due to the unsteadiness, even the trends were not predicted accurately.

Chapter 9

Conclusions and recommendations for further work

9.1 Conclusions

The current thesis documents the comparative studies which have been carried out on three trailing edge configurations in a large scale, low speed wind tunnel. The three configurations studied were:

1. Pressure surface ejection via discrete film cooling holes near the trailing edge.
2. Pressure surface ejection via a machined cutback near the trailing edge. The coolant is fed via discrete coolant holes.
3. Pressure surface ejection via a cast cutback, near the trailing edge with internal pin fins and ribs. This configuration is known as the "letterbox" in literature.

The literature survey of film cooling with discrete cooling holes shows that a cooling arrangement with the following four points produces better effectiveness downstream of coolant ejection.

1. Length of coolant hole to coolant hole diameter ratio greater than 5.0.
2. Shallow angle of inclination to achieve a near tangential ejection with respect to the surface downstream.
3. Inclusion of a compound angle.
4. Small hole pitch to coolant hole diameter ratio. This is to achieve a near continuous coolant ejection.

The conventional pressure surface test plate used in the current study incorporated the above four points in its configuration. The literature documents numerous research into near trailing edge, pressure surface coolant ejection from cutback "gill" and "letterbox" configurations. These configurations are normally manufactured through casting. The literature showed that there was a small increase in the total pressure losses, with the "gill" configuration having a greater total pressure loss compared with the "letterbox" configuration. The numerous heat transfer studies into the above two configurations showed that the heat transfer coefficient and adiabatic film effectiveness downstream of the cooling configurations were greatly affected by the internal cooling arrangement.

To establish a computational fluid dynamics methodology for modelling film cooling effectiveness and the heat transfer coefficient, the experimental data from Saumweber et al. (2000) were used. The experiments gave film effectiveness and heat transfer coefficients downstream of cylindrical film cooling holes on a flat plate. The study showed that the Spalart-Allmaras turbulence model can be used to predict the film effectiveness and heat transfer coefficients downstream of film cooling holes, even when the fluid domain is meshed with tetrahedral elements.

The low speed aerodynamic and heat transfer experiments, documented in this research, were carried out in the test tunnel used by Moss (1992). Chapter 4 documents the modifications carried out on the test tunnel. Three new test plates were manufactured using stereolithography and incorporating static pressure tappings. These test plates comprised of the following cooling arrangements:

1. Datum configuration test plate with seven cooling holes ejecting onto the pressure surface.

2. Machined cutback configuration test plate with a pressure surface cutback fed with six discrete film cooling holes.

3. Cast cutback configuration test plate with three coolant slots separated by two ribs. Upstream of the slots and within the plenum are three banks of pedestals.

Figures 4.3 and 4.2 show the internal and external CAD representations of the three new geometries. Table 4.2 summarises the geometries of the cooling hole configurations on the three test plates.

The three tested cooling configurations had similar discharge coefficients, with the cutback cooling configurations being slightly greater than the datum configuration. This discrepancy was attributed to the "capping" effect experienced by the pressure

surface coolant holes on the datum test plate. The two dimensional traverse measurements carried out downstream of the test plates showed the wake structure due to the coolant configurations and trailing edges. The width of the wakes from the datum and machined cutbacks were similar, whilst the cast cutback configuration had a larger width. The local, total pressure loss profiles indicated that the machined cutback and the datum test plates have similar size of wakes, whilst the cast cutback test plate had wider and deeper wakes. As the mass flux ratio was increased the wakes downstream of the three test plates were filled by the coolant.

Mixed out losses for the three cooling configurations were calculated incorporating the coolant and mainstream total pressures, unlike the total pressure loss profile calculations. The mixed out losses for the datum and machined cutback cooling configurations were similar in magnitude, with the datum configuration having slightly higher losses than the machined cutback configuration for low mass and momentum flux ratios (less than unity). At high momentum flux ratios (greater than unity), the mixed out losses for the two configurations are the same. The marginally higher mixed out loss for the datum configuration at low mass and momentum flux ratios, is due to the mixing of the coolant with the mainstream. In the case of the machined cutback configuration, the coolant fills the wake region caused by the mainstream separating over the pressure surface cutback, resulting in less mixing with the mainstream flow and hence lower mixed out loss. The mixed out loss for the cast cutback cooling configuration was greater than the datum and machined cutback cooling configurations when plotted against mass and momentum flux ratios. The mixed out losses plotted against coolant to mainstream mass flow ratio, also showed that the cast cutback configuration generated more mixed out losses compared with the machined cutback and datum cooling configurations, for a similar coolant to mainstream ratio. This increase in loss for the cast cutback configuration was attributed to the cooling configuration, which results in increased mixing of the coolant and mainstream.

Computational fluid dynamics (CFD) was used as a means of flow visualisation and prediction of the aerodynamic performance of the three cooling configurations. Fluent ^{TM} CFD solver with realisable k-ϵ turbulence model was used in the study. The CFD predictions showed that for the datum and machined cutback cooling configurations, the coolant hole lengths were insufficient to diffuse the velocity gradient within them. This velocity gradient was caused by the coolant flow separating at the inlet to the coolant holes. In the predictions for the cast cutback configuration, the coolant is seen to accelerate past the pedestals before exiting through the slots. The wall shear stress predictions for the datum and machined cutback configurations

showed that the coolant flow trajectory is turned towards the mainstream direction downstream of coolant ejection. Furthermore, in the case of the machined cutback configuration, the downstream wall shear stress contours show the extent of the separated mainstream flow due to the pressure surface cutback. In the cast cutback configuration, the downstream predicted wall shear stress contours show evidence of vortices caused by the upstream pedestals.

The discharge coefficient from CFD predictions for the datum and machined cutback cooling configurations were close to those determined experimentally. However, the predicted discharge coefficient for the cast cutback configuration was greater than those determined experimentally and this was attributed to the lower blockage predicted by the CFD for the cast cutback cooling configuration. The predicted total pressure contours show increased mixing between the mainstream and coolant for the three cooling configurations. This was borne out in the mixed out loss predictions when compared with the experiments. However, it must be noted that the mixed out loss predictions share the same trends with increasing mass and momentum ratios as the experimental data.

The film effectiveness and heat transfer coefficients on the pressure surface downstream of the coolant ejection were measured using a steady state heat transfer technique. The technique enabled contours of film effectiveness and heat transfer coefficients to be computed downstream of the coolant ejection. Laterally averaged film cooling effectiveness and heat transfer coefficients were also computed for the three cooling configurations. For the datum and machined cutback test plates, laterally averaged film effectiveness and heat transfer coefficients were computed over two hole pitches. For the cast cutback test plate, the laterally averaged film effectiveness and heat transfer coefficient were computed across the central slot region.

Comparing the laterally averaged film effectiveness from the three test plates, it can be concluded that generally the film effectiveness increases with increasing mass flux ratio, as expected. Just downstream of the coolant ejection, the film effectiveness for the datum and cast cutback test plates are greater than that for the machined cutback test plate. This is due to the fact that in the machined cutback test plate, the coolant is ejected away from the pressure surface and impinges further downstream on the pressure surface. The slight rise in the laterally averaged effectiveness on the machined cutback test plate, further downstream from the coolant ejection plane, is due to the reattachment of the coolant jets. In the case of the datum and cast cutback test plates, the higher coolant effectiveness region observed just downstream of the coolant ejection location is due the coolant exhausting on the pressure surface.

Moving further towards the trailing edge, along the pressure surface, the coolant mixes with the mainstream and hence a reduction in the film effectiveness with distance is observed on all three test plates. Near the trailing edge, the film effectiveness levels for the datum configuration at mass flux ratio of 0.80 are comparable to cast cutback configurations at a mass flux ratio of 0.30. The effectiveness levels for the machined cutback configuration at mass flux ratio of 0.80 is lower than the datum and cast cutback configuration. This is not surprising, as the lower effectiveness is the result of the enhanced mixing between the coolant and the mainstream, the latter of which separates at the pressure surface cutback and re-attaches downstream of the cutback. The aforementioned extra mixing between the mainstream and coolant is also present in the cast cutback configuration. However, it must be noted that the coolant massflow rate, at the lowest tested mass flux ratio for the cast cutback configuration, is approximately twice the mass flow rate in the machined and datum configurations at mass flux ratio of 0.80. This higher massflow enables the local gas temperature adjacent to the pressure surface, in the region near the trailing edge of the cast cutback temperature to be lower than in the machined cutback configuration, and hence have better effectiveness when compared with the machined cutback configuration.

With the measured heat transfer coefficients, for the machined and cast cutback test plates, higher heat transfer coefficient levels were achieved with higher mass flux ratios. This is not surprising as increases in mass flux ratio increase the momentum of the coolant jets, resulting in higher velocity and hence higher heat transfer coefficients. However, for the datum configuration, the measured heat transfer coefficient at the tested mass flux ratios are within the measurement errors and hence no discernible trend with mass flux ratio could be observed.

Steady computational fluid dynamics was used to predict the film effectiveness and heat transfer coefficient downstream of the coolant ejection. The predictions captured the general trends seen in the experiment measurements. However, the steady solver was unable to capture the magnitudes of the experimental film effectiveness and heat transfer coefficient. The flow field downstream of film cooling is highly unsteady and hence it is the author's opinion that an unsteady prediction is required to capture the magnitudes of the film effectiveness and heat transfer coefficients.

The findings of the research documented in this thesis show that a cutback configuration shields the coolant ejection plane from the mainstream unlike the datum configuration. It can be concluded that a cooling configuration such as the cast cutback configuration will be required to cool the next generation of turbine blade

trailing edges so as to withstand the ever increasing turbine entry temperatures in excess of 2000 K. This is because the aforementioned configuration enables the cooling designer to easily direct a larger mass flow rate of coolant, compared with the other two configurations, at the trailing edge. However, due to this large coolant flow rate, the cast cutback configuration would have greater mixed out loss compared with the datum and machined cutback configurations, which would result in higher specific fuel consumption.

Even though the machined cutback configuration discussed in this thesis shields the coolant ejection plane from the mainstream and produces a small increase in the mixed out loss compared with the datum configuration, the effectiveness at the trailing edge is lower than the datum configuration. Due to the low effectiveness this configuration would not be ideal to cool the trailing edge on the next generation of turbine blades operating in temperatures in excess of 2000 K. However, the machined cutback configuration would be a low cost modification to the current turbine blade trailing edge cooling configuration which would shield the coolant exit from the mainstream and hence prevent the excessive blockage of the coolant exit plane when operating in a sand laden environment. It is the author's opinion that the effectiveness at the trailing edge would be greater for a machined cutback configuration operating in a sand laden environment compared with a datum configuration operating in the same environment.

9.2 Recommendations

The author would like to recommend the following:

1. A sensitivity study of the aerodynamic and heat transfer performance of the three configurations to density ratio and Mach number.

2. A study of the change in the heat transfer and aerodynamics of the three configurations due to rotation.

3. Optimisation of the internal and external arrangement of the cast cutback configuration to improve the mixed out losses.

4. Effectiveness and heat transfer predictions on the rib side walls of the cast cutback configuration.

5. Hot wire measurements, downstream of the trailing edge of the cast cutback configuration to understand the unsteady flow characteristics.

6. Unsteady CFD predictions to better capture the heat transfer and film effectiveness downstream of the cutback configurations.

Appendix A

Static tapping locations

A.1 Datum trailing edge cooling configuration test plate

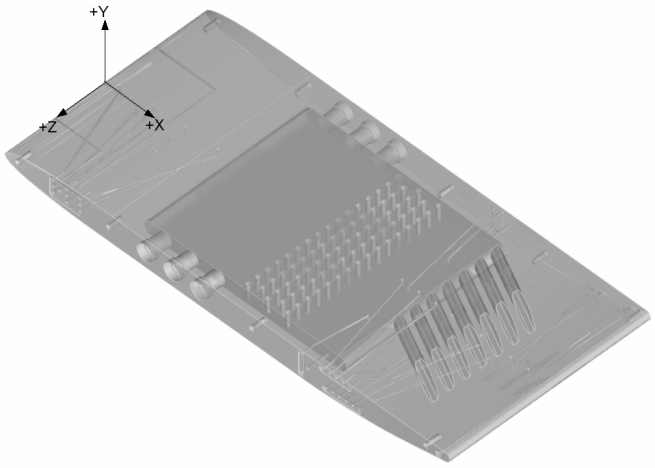

Figure A.1: Datum test plate

Figure A.1 shows the datum trailing edge cooling configuration test plate with the static tappings. Table A.1 shows the co-ordinates of the instrumented static tappings along the test plate. The origin of the co-ordinates are at the centreline of the test plate as shown in figure A.1.

Tapping number	Tapping description	Co-ordinates		
		X	Y	Z
1	Left side of leading edge	0.00	0.00	38.00
2	Centre of leading edge	0.00	0.00	0.00
3	Right side of leading edge	0.00	0.00	-37.00
4	Pressure surface along centreline	10.20	5.57	0.00
5	Suction surface along centreline	22.60	-7.77	0.00
6	Pressure surface along centreline	34.82	8.96	0.00
7	Suction surface along centreline	47.25	-9.61	0.00
8	Pressure surface along centreline	59.50	9.90	0.00
9	Suction surface along centreline	71.50	-10.00	0.00
10	Pressure surface along centreline	83.50	10.00	0.00
11	Pressure surface along centreline	221.07	10.00	0.00
12	Pressure surface along centreline	233.57	10.00	0.00
13	Pressure surface along centreline	246.07	10.00	0.00
14	Pressure surface along centreline	258.57	10.00	0.00
15	Pressure surface along centreline	279.91	10.00	0.00
16	Suction surface along centreline	221.07	-10.00	0.00
17	Suction surface along centreline	233.51	-10.00	0.00
18	Suction surface along centreline	246.07	-10.00	0.00
19	Suction surface along centreline	258.57	-10.00	0.00
20	Suction surface along centreline	270.93	-6.94	0.00
21	Suction surface along centreline	287.93	-4.46	0.00
22	Pressure surface along centreline	279.91	10.00	0.00
23	Pressure surface along centreline	302.07	10.00	0.00
24	Suction surface along centreline	294.75	-3.25	0.00
25	Pressure surface along centreline	315.35	10.00	0.00
26	Suction surface along centreline	316.76	1.19	0.00
27	Trailing edge along centreline	332.00	0.00	0.00
28	Plenum, +Z side, near pressure surface	225.50	5.00	30.00
29	Plenum, +Z side, near suction surface	225.50	-5.00	30.00
30	Plenum, along centreline near Pressure surface	225.50	5.00	0.00
31	Plenum, along centreline near Suction surface	225.50	-5.00	0.00
32	Plenum, -Z side, near pressure surface	225.50	5.00	30.00
33	Plenum, -Z side, near suction surface	225.50	-5.00	-30.00

Table A.1: Static tapping location on Datum trailing edge cooling configuration

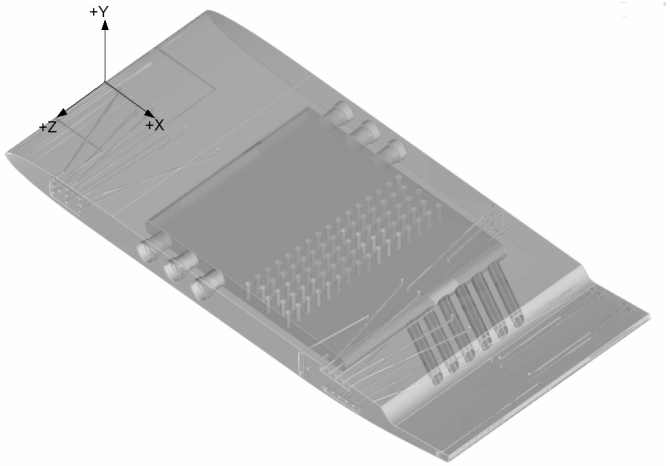

Figure A.2: Machined cutback trailing edge cooling test plate

A.2 Machined cutback trailing edge cooling configuration

Figure A.2 shows the machined cutback trailing edge cooling configuration test plate with the static tappings. Table A.2 shows the co-ordinates of the instrumented static tappings along the test plate. The origin of the co-ordinates are at the centreline of the test plate as shown in figure A.2.

A.3 Cast cutback trailing edge cooling configuration

Figure A.3 shows the cast cutback trailing edge cooling configuration test plate with the static tappings. Table A.3 shows the co-ordinates of the instrumented static tappings along the test plate. The origin of the co-ordinates are at the centreline of the test plate as shown in figure A.3.

Tapping number	Tapping description	Co-ordinates		
		X	Y	Z
1	Left side of leading edge	0.00	0.00	37.50
2	Centre of leading edge	0.00	0.00	0.00
3	Right side of leading edge	0.00	0.00	-37.50
4	Pressure surface along centreline	10.67	5.59	0.00
5	Suction surface along centreline	23.05	-7.77	0.00
6	Pressure surface along centreline	35.32	8.96	0.00
7	Suction surface along centreline	47.75	-9.61	0.00
8	Pressure surface along centreline	60.00	9.90	0.00
9	Suction surface along centreline	72.00	-10.00	0.00
10	Pressure surface along centreline	84.00	10.00	0.00
11	Pressure surface along centreline	221.57	10.00	0.00
12	Pressure surface along centreline	234.07	10.00	0.00
13	Pressure surface along centreline	246.57	10.00	0.00
14	Pressure surface along centreline	259.07	10.00	0.00
15	Pressure surface along centreline	271.07	10.00	0.00
16	Suction surface along centreline	221.57	-10.00	0.00
17	Suction surface along centreline	234.07	-10.00	0.00
18	Suction surface along centreline	246.57	-10.00	0.00
19	Suction surface along centreline	259.57	-10.00	0.00
20	Suction surface along centreline	271.42	-6.94	0.00
21	Suction surface along centreline	288.43	-4.46	0.00
22	Pressure surface along centreline	283.99	10.00	0.00
23	Pressure surface along centreline	294.01	10.00	0.00
24	Suction surface along centreline	295.25	-3.25	0.00
25	Cutback pressure surface along centreline	316.22	5.00	0.00
26	Suction surface along centreline	317.26	1.19	0.00
27	Trailing edge along centreline	332.00	0.00	0.00
28	Plenum, +Z side, near pressure surface	226.48	5.00	30.00
29	Plenum, +Z side, near suction surface	226.48	-5.00	30.00
30	Plenum, along centreline near Pressure surface	226.48	5.00	0.00
31	Plenum, along centreline near Suction surface	226.48	-5.00	0.00
32	Plenum, -Z side, near pressure surface	226.48	5.00	30.00
33	Plenum, -Z side, near suction surface	226.48	-5.00	30.00

Table A.2: Static tapping location on Machined cutback trailing edge cooling configuration

Tapping number	Tapping description	Co-ordinates		
		X	Y	Z
1	Left side of leading edge	0.00	0.00	37.50
2	Centre of leading edge	0.00	0.00	0.00
3	Right side of leading edge	0.00	0.00	-37.50
4	Pressure surface along centreline	10.20	5.59	0.00
5	Suction surface along centreline	23.55	-7.77	0.00
6	Pressure surface along centreline	34.82	8.96	0.00
7	Suction surface along centreline	47.25	-9.61	0.00
8	Pressure surface along centreline	60.00	9.90	0.00
9	Pressure surface along centreline	84.00	10.00	0.00
10	Suction surface along centreline	72.00	-10.00	0.00
11	Pressure surface along centreline	221.07	10.00	0.00
12	Pressure surface along centreline	233.57	10.00	0.00
13	Pressure surface along centreline	246.07	10.00	0.00
14	Pressure surface along centreline	258.57	10.00	0.00
15	Pressure surface along centreline	271.07	10.00	0.00
16	Suction surface along centreline	221.07	-10.00	0.00
17	Suction surface along centreline	233.51	-9.82	0.00
18	Suction surface along centreline	246.07	-9.25	0.00
19	Suction surface along centreline	258.57	-8.28	0.00
20	Suction surface along centreline	270.93	-6.95	0.00
21	Suction surface along centreline	287.93	-4.46	0.00
22	Cutback pressure surface along centreline	293.58	4.15	0.00
23	Suction surface along centreline	294.75	-3.25	0.00
24	Cutback pressure surface along centreline	315.72	7.85	0.00
25	Suction surface surface along centreline	316.76	1.19	0.00
26	Trailing edge along centreline	332.00	0.00	0.00
27	Plenum, +Z side, near pressure surface downstream of large pedestals	242.70	1.26	36.33
28	Plenum, -Z side, near pressure surface downstream of large pedestals	242.70	1.26	-36.18
29	Plenum, along centreline, near pressure surface downstream of large predestals	242.70	1.26	0.00
30	Plenum, +Z side, near suction surface downstream of large pedestals	242.70	-6.26	36.33
31	Plenum, -Z side, near suction surface downstream of large pedestals	242.70	-6.26	-36.33
32	Plenum, along centreline, near suction surface downstream of large pedestals	242.70	-6.26	0.00
33	Plenum, +Z side, near pressure surface upstream of large pedestals	189.70	4.88	36.33
34	Plenum, along centreline, near pressure surface upstream of large pedestals	189.70	4.87	0.265

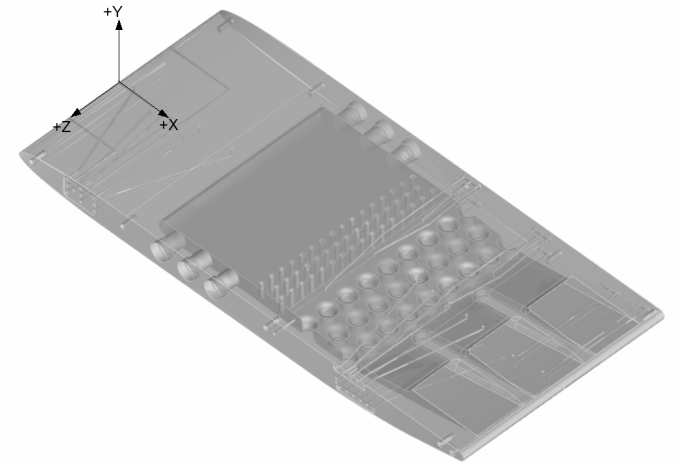

Figure A.3: Cast cutback trailing edge cooling test plate

35	Plenum, -Z side, near pressure surface upstream of large pedestals	189.70	4.88	-36.44
36	Plenum, +Z side, near suction surface upstream of large pedestals	189.70	-6.00	36.44
37	Plenum, -Z side, near suction surface upstream of large pedestals	189.70	-6.00	-36.18
38	Plenum, along centreline, near suction surface upstream of large pedestals	189.70	-6.00	0.00

Table A.3: Static tapping location on cast cutback trailing edge cooling configuration

Bibliography

S. Baldauf and A. Schulz. Flat plate film heat transfer augmentation. In *Film Cooling Science And Technology For Gas Turbines: State-Of-The-Art Experimental And Computational Knowledge*, 2007. von Karman Institute Lecture Series VKI-LS 2007-06, 16-20 April 2007, Brussels.

S. Baldauf, M. Scheurlen, A. Schulz, and S. Wittig. Correlationof filme cooling effectiveness from thermographic measurements at engine like conditions. In *Proceedings of the ASME Turbo Expo 2002: Power for Land, Sea and Air*, 2002. Amsterdam, Netherlands (2002-GT-30180).

D. G. Bogard. Fundermentals of film effectiveness performance. In *Film Cooling Science And Technology For Gas Turbines: State-Of-The-Art Experimental And Computational Knowledge*, 2007a. von Karman Institute Lecture Series VKI-LS 2007-06, 16-20 April 2007, Brussels.

D. G. Bogard. Geometric and flow influences on film effectiveness. In *Film Cooling Science And Technology For Gas Turbines: State-Of-The-Art Experimental And Computational Knowledge*, 2007b. von Karman Institute Lecture Series VKI-LS 2007-06, 16-20 April 2007, Brussels.

E. Buckingham. Model experiments and the form of empirical equations. *Journal of turbomachinery - transactions of ASME*, 37:263–296, 1915.

R. S. Bunker. Effect of partial coating blockage on film cooling effectiveness. In *Proceedings of the ASME Turbo Expo 2000: Power for Land, Sea and Air*, 2000. Munich, Germany (2000-GT-0244).

R. S. Bunker. Turbine engine film cooling constraints. In *Film Cooling Science And Technology For Gas Turbines: State-Of-The-Art Experimental And Computational Knowledge*, 2007a. von Karman Institute Lecture Series VKI-LS 2007-06, 16-20 April 2007, Brussels.

R. S. Bunker. Turbine engine film cooling design and applications. In *Film Cooling Science And Technology For Gas Turbines: State-Of-The-Art Experimental And Computational Knowledge*, 2007b. von Karman Institute Lecture Series VKI-LS 2007-06, 16-20 April 2007, Brussels.

R. J. Clifford. Rotating heat transfer investigations on a multipass cooling geometry. *AGARD*, CP 390, 1985.

J. D. Denton. Loss mechanisms in turbomachines. *Journal of Turbomachinery - Transactions of the ASME*, 115(4):621–656, 1993.

J. R. Dorrington, D. G. Bogard, and R. S. Bunker. Film effectiveness performance for coolant holes embedded in various shallow trench and crater depressions. In *Proceedings of the ASME Turbo Expo 2007: Power for Land, Sea and Air*, 2007. GT-2007-27992.

U. Drost and A. Bolcs. Investigation of detailed film cooling effectiveness and heat transfer distribution on a gas turbine airfoil. *Journal of Turbomachinery*, 121: 233–242, 1999.

N. J. Fiala, I. Jaswal, and F. E. Ames. Letterbox trailing edge heat transfer - effects of blowing rate, reynolds number and external turbulence on heat transfer and film cooling effectiveness. In *Proceedings of the ASME Turbo Expo 2008: Power for Land, Sea and Air*, 2008a. Berlin, Germany (GT2008-50474).

N. J. Fiala, J. D. Johnson, and F. E. Ames. Aerodynamics of a letterbox trailing edge - effects of blowing rate, reynolds number and external turbulence on aerodynamic losses and pressure distribution. In *Proceedings of the ASME Turbo Expo 2008: Power for Land, Sea and Air*, 2008b. Berlin, Germany (GT2008-50475).

A. D. Fitt, J. R. Ockendon, and T. V. Jones. Aerodynamics of slot-film cooling: theory and experiment. *Journal of fluid mechanics*, 160:15–27, 10 1985. ISSN 1469-7645.

Fluent^{TM}. *Fluent 6.2 User Guide*. Fluent Inc, 1995.

C. J. P. Forth and T. V. Jones. Scaling parameters in film-cooling. In C.-L. Tien, V. P. Carey, and J. K. Ferrell, editors, *Heat transfer 1986; Proceedings of the Eighth International Conference*, pages 1271–1276, 1986.

D. R. H. Gillespie. Intricate internal cooling systems for gas turbine blading. DPhil thesis, University of Oxford, 1996.

R. J. Goldstein. Film cooling. *Advances in Heat Transfer*, 7:321–379, 1971.

R. J. Goldstein and A. Haji-Sheikh. Pediction of film cooling effectiveness. In *Japan Society of Mechanical Engineers, semi-Int. Symposium*, pages 213–218, 1967.

M. Gritsch, A. Schulz, and S. Wittig. Adiabatic wall effectiveness measurements of film-cooling holes with expanded exits. *Journal of Turbomachinery*, 120:549, 1998.

Je-Chin Han, Sandip Dutta, and Srinath V Ekkad. *Gas turbine heat transfer and cooling technology*. Taylor and Francis, 2000.

K. L. Harrison. *Computational and experimental study of film cooling performance including shallow trench configurations*. PhD thesis, University of Texas, Austin, Texas, 2006.

K. L. Harrison and D. G. Bogard. Comparison of rans turbulence models for prediction of film cooling performance. In *Proceedings of the ASME Turbo Expo 2008: Power for Land, Sea and Air*, 2008. GT-2007-51423.

F. P. Incropera and D. P. DeWitt. *Introduction to heat transfer*. John Wiley & sons, 4th edition, 2001.

JR. J. D. Anderson. *Computational fluid dynamics : The basics with applications*. McGraw-Hill, 1995. ISBN 0-07-001685-2.

D. J. Jackson, K. L. Lee, P. M. Ligrani, and P. D. Johnson. Transonic aerodynamic losses due to turbine airfoil, suction surface film cooling. volume 122, pages 317–326, 2000.

C. Kapteijn, J. Amecke, and V. Michelassi. Aerodynamic performance of a transonic turbine guide vane with trailing edge coolant ejection: Part 1 - experimental approach. 1994. The Hague, Netherlands (94-GT-288).

W. Kays and M. Crawford. *Convective heat and mass transfer*. McGraw-Hill Education, 2nd edition, 1984.

B. Lakshminarayana. *Fluid Dynamics and Heat Transfer of Turbomachinery*. John Wiley, 1996.

B. E. Launder and D. B. Spalding. *Lectures in mathematical model of turbulence.* Academic Press, 1972.

Ching-Pang Lee. Turbine blade trailing edge cooling opennings and slots, 01 2001. URL `https://register.epo.org/application;jsessionid=F63599CEA42E4A1AC93623B2D9EE8344.RegisterPlus_prod_0?number=EP00305460&tab=main`.

C. Liess. Experimental investigation of film cooling with injection from a row of holes for the application to gas turbine blades. *Journal of Turbomachinery*, 97:21–27, 1975.

E. Lutum and B. V. Johnson. Influence of the hole length-to-diameter ratio on film cooling with cylindrical holes. In *Proceedings of the ASME Turbo Expo 1998: Power for Land, Sea and Air*, 1998. Stockholm, Sweden (1998-GT-10).

P. Martini, A. Schultz, and S. Witting. Experimental and numerical investigation of trailing edge film cooling by circular coolant wall jets ejected from a slot with internal rib arrays. In *Proceedings of the ASME Turbo Expo 2003: Power for Land, Sea and Air*, 2003.

P. Martini, A. Shculz, and H. J. Baurer. Film cooling effectiveness and heat transfer on the trailing edge cut-back of gas turbine airfoils with various internal cooling designs. In *Proceedings of the ASME Turbo Expo 2005: Power for Land, Sea and Air*, 2005. Reno-Tahoe, Nevada, (GT2005-68083).

D. J. Mee. Techniques for aerodynamic loss measuremen of transonic turbine cascades with trailing edge region coolant ejection. In *Proceedings of the ASME Turbo Expo 1992: Power for Land, Sea and Air*, 1992. Cologne, Germany (92-GT-157).

F. R. Menter. Two-equation eddy-viscosity turbulence models for engineering applications. *American Institute of Aeronautics and Astronautics*, 32:1598–1605, 1994.

R. J. Moffat. Contributions to the theory of single sample uncertainty analysis. *Journal of Fluid Engineering*, 104, 1982.

R. W. Moss. The effects of turbulence length scale on heat transfer. DPhil thesis, University of Oxford, Department of Engineering Science, 1992.

S. Na, B. Zhu, M. Bryden, and T. I-P Shih. Cfd analysis of film cooling. In *American Institute of Aeronautics and Astronautics*, 2006. AIAA 2006-0022.

K. O'Malley, A. D. Fitt, T. V. Jones, J. R. Ockendon, and P. Wilmott. Models for high-reynolds-number flow down a step. *Journal of fluid mechanics*, 222, 1991.

K. R. Pappu and M. T. Schobeiri. Optimising for trailing edge ejection mixing losses: a theoratical and experimental study. *ASME paper number 97-gt-523*, 1997.

R. W. Radomsky and K. A. Thole. Detailed boundary layer measurements on a turbine stator vane at elavated freestream turbulence levels. *Journal of Turbomachinery*, 124:107–118, 2002.

T. Rogers and A. S. Hersh. The effects of grazing flow on the steady state resistance of square edged orifices. *American institute of aeronautics and astronautics, 2nd aero-acoustics conference*, 1975.

Rolls-Royce. *The Jet Engine*. Rolls-Royce PLC, 2005.

D. A. Rowbury, M. G. Oldfield, and G. D. Lock. Large scale testing to validate the influence of external cross flow on the discharge coefficients of film cooling holes. *Journal of turbomachinery - Transactions of the ASME*, 2001.

C. Saumweber and A. Schulz. Airfoil film heat transfer and effects of approach conditions. In *Film Cooling Science And Technology For Gas Turbines: State-Of-The-Art Experimental And Computational Knowledge*, 2007a. von Karman Institute Lecture Series VKI-LS 2007-06, 16-20 April 2007, Brussels.

C. Saumweber and A. Schulz. Effects of film hole shaping and freestream conditions on heat transfer augmentation and discharge coefficients. In *Film Cooling Science And Technology For Gas Turbines: State-Of-The-Art Experimental And Computational Knowledge*, 2007b. von Karman Institute Lecture Series VKI-LS 2007-06, 16-20 April 2007, Brussels.

C. Saumweber, A. Schulz, and S. Wittig. Effects of turbulence intensity on film cooling. Technical Report C3/Karlsruhe/2/ed1, TATEF, 2000.

M. Sautner, S. Clouser, and J. C. Han. Determination of surface heat transfer and film cooling effectiveness in unsteady wake flow conditions. *AGARD*, CP 527:1–12, 1992.

H. Schlichting and K. Gersten. *Boundary layer theory*. Springer-verlag, 2004.

D. Schmidt, B. Sen, and D. Bogard. Film cooling with compound angle holes: Adiabatic effectiveness. *Journal of Turbomachinery*, 118:807–813, 1996.

D. L. Schmidt and D. G. Bogard. Effects of free-stream turbulence and surface roughness on film cooling. In *Proceedings of the ASME Turbo Expo 1996: Power for Land, Sea and Air*, 1996. 96-GT-462.

D. L. Schmidt and D. G. Bogard. Effects of free-stream turbulence and surface roughness on laterally injected film cooling. *Proceedings of the 32nd national heat transfer conference*, 12, 1997. HTD-vol.350.

T.-H. Shih, W. W. Liou, A. Shabbir, Z. Yang, and J. Zhu. A new $k - \epsilon$ eddy viscosity model for high reynolds number turbulent flows - model development and validation. *Computers Fluids*, 24:227–238, 1995.

C. H. Sieverding, T. Arts, R. Denos, and F. Martelli. Investigation of the flow field downstream of a turbine trailing edge cooled nozzle guide vane. 1994. The Hague, Netherlands (94-GT-209).

A. Sinha, D. Bogard, and M. Crawford. Film cooling effectiveness downstream of single row of holes with variable density ratio. *Journal of Turbomachinery*, 113: 442–449, 1991.

J. C. Telisinghe, P. T. Ireland, T. V. Jones, D. Barrett, and C. Son. Comparative study between a cutback and conventional trailing edge film cooling system. *Proceedings of ASME Turbo Expo 2006: Power for Land, Sea and Air*, 3, 2006.

K. A. Thole, A. Sinha, D. G. Bogard, and M. E. Crawford. Mean temperature measurements of jets with a crossflow for gas turbine film cooling applications. *Rotating machinery transport phenomena*, 1992.

O. Uzol and C. Camci. Aerodynamic loss characteristics of a turbine blade with trailing edge coolant ejection: Part 2 - external aerodynamics, total pressure losses and predictions. *Journal of turbomachinery - transactions of ASME*, 2001a.

O. Uzol and C. Camci. Aerodynamic loss characteristics of a turbine blade with trailing edge coolant ejection: Part 2 - external aerodynamics, total pressure losses and predictions. *Journal of turbomachinery - transactions of ASME*, 123:249–257, 2001b.

O. Uzol, C. Camci, and B. Glezer. Aerodynamic loss characteristics of a turbine blade with trailing edge coolant ejection: Part 1 - effects of cutback length, spanwise rib spacing, free-stream reynolds numbber and chordwise rib length on discharge coefficient. *Journal of turbomachinery - transactions of ASME*, 123:238–248, 2001.

D. K. Walters and J. H. Leylek. A systematic computational methodology applied to a three-dimensional film-cooling flowfield. *Journal of Turbomachinery*, 119:777–785, 1997.

S. K. Waye. *Film cooling effectiveness of suction side axial holes, compound angle holes and axial holes embedded within an overlying transverse trench.* PhD thesis, University of Texas, Austin, Texas, 2005.

S. K. Waye and D. G. Bogard. High resolution film effectivess measurements of axial holes embedded in a transverse trench with various trench configurations. In *Proceedings of the ASME Turbo Expo 2006: Power for Land, Sea and Air*, 2006. 3rd-6th June 2006, Barcelona, Spain (GT-2006-90226).

D. C. Wilcox. *Turbulence modelling for CFD.* DCW Industries Inc., 1998.

V. Yakhot and S. A. Orszag. Renormalization group analysis of turbulence: I. basic theory. *Journal of scientific computing*, 1:1–51, 1986.